Josephson photonics : microwave generation & amplification in the quantum regime

Florian Blanchet

Communauté UNIVERSITÉ Grenoble Alpes

THÈSE

Pour obtenir le grade de

DOCTEUR DE LA

COMMUNAUTE UNIVERSITE GRENOBLE ALPES

Spécialité : **Physique de la Matière Condensée et du Rayonnement**

Arrêté ministériel : 25 mai 2016

Présentée par

Florian Blanchet

Thèse dirigée par **François LEFLOCH,** CEA Grenoble et encadrée par **Max HOFHEINZ,** Professeur agrégé, Institut Quantique Sherbrooke

préparée au sein du **Laboratoire PHotonique, ELectronique et Ingéniérie QuantiqueS**
dans **l'École Doctorale Physique**

Photonique Josephson : génération & amplification micro-ondes en régime quantique

Josephson photonics: Microwave generation & amplification in the quantum regime

Thèse soutenue publiquement le **17 décembre 2018**, devant le jury composé de :

Monsieur Philippe JOYEZ
Ingénieur Chercheur, CEA Saclay, Rapporteur
Monsieur Christopher EICHLER
Senior Scientist, ETH Zürich, Rapporteur
Monsieur Olivier BUISSON
Directeur de Recherche, Institut Néel Grenoble, Président
Madame Julia MEYER
Professeur des Universités, CEA Grenoble, Examinateur

Acknowledgements

Je tiens tout d'abord à remercier l'ensemble du jury : M. Philippe Joyez, M. Christopher Eichler, M. Oliver Buisson et Mme Julia Meyer; pour avoir accepter de participer à ma défense de thèse, et pour les discussions et questionnements pertinents qui ont eu lieu à cette occasion.

Si j'ai pu effectuer ma thèse à Grenoble c'est avant tout grâce à Max qui m'a fait confiance pour participer à ce projet. Les membres du groupe, passés et présents, ont su être d'une grande aide pendant ces trois années et sont devenus des amis plus que des collègues. Salha qui m'a accompagné pour prendre en main nos expériences et en comprendre la physique. Mes co-bureau successifs, Dibyendu puis Romain A., pour les discussions quasi-quotidiennes qui ont permis de dissiper des doutes et d'avancer quand ce fût nécessaire, ainsi que la grande mémoire de Romain qui a plus d'une fois été d'un grand renfort – que ce soit sur des choses importantes ou beaucoup plus futiles. Je n'oublie pas Frédéric G. et Jean-Luc sans qui la réalisation des dispositifs aurait été bien plus périlleuse, les conseils et retours ont toujours été des plus pertinents. Merci aussi à M. Juha Leppäkangas, M. Fabien Portier et M. Nicolas Roch avec qui nous avons collaboré pendant ma thèse.

Ca a été plaisant de travailler dans ce laboratoire où l'ambiance est bienveillante et l'ensemble des personnes accueillantes. La diversité des activités a offert de nombreuses discussions et une ouverture sur d'autres sujets qui, j'en suis convaincu, m'ont été plus que profitables. En particulier, les remarques de Claude et François L. lors des répétions pour les conférences qui ont contribué à m'apporter le recul nécessaire. François L. qui a toujours fait ce qu'il fallait pour s'assurer que la thèse se déroule dans les meilleures conditions possibles. Jean-Pascal qui m'a à plusieurs reprises rendu plus simple pas mal de procédures – pour moi qui ai tendance à repousser les tâches administratives le plus tard possible et plus encore. Et l'ensemble des permanents du laboratoire : Romain M., Vincent, Marc, Xavier, Alexandre P., Frédéric P – et son duo avec Claude lorsqu'il est question de parler du service informatique, Louis, Pierre, Silvano, Christophe, Georg et Daniel.

Ces années à Grenoble ont aussi été marquées par les doctorants et post-doctorants qui m'ont accompagné, les plus anciens qui étaient là à mon arrivée Salha, Alexandre A., Loic, Dibyendu, Dharam, Patrick, Juan-Carlos, Anaïs. Puis ceux qui sont arrivés juste après moi : Anthony toujours motivé pour passer une bonne soirée – sauf quand il a lessive – regarder un film (on aura fini par le voir ton Sin City) ou coincher jusqu'au petit matin avec Alexis et Quentin. Estelle très motivée pour aller grimper – bientôt ton premier 7a? – ou essayer de nouveaux jeux. Thomas, cet inconditionnel des montagnes, que ce soit pour grimper, randonner, skier, ... et le premier motiver pour faire un gros repas. Romain A. bien trop enjoué et exigeant lorsqu'il est question de faire un tarot, et mis à part une aversion pour le bloc, un compagnon de grimpe. Florian V. toujours motivé pour réunir les doctorants, aussi bien au laboratoire qu'en dehors, pour voir un film, jouer, sortir, manger. Ainsi que les doctorants arrivés peu avant mon départ : Tom, Cécile, Julia, Agostino, Alessandro. Les Doctoriales et formations m'ont aussi offert de belles rencontres, Lynda et Solveig avec qui j'ai partagé la rédaction et préparation propres à la fin de thèse.

Un remerciement particulier à Salha sans qui ma thèse et ces années à Grenoble auraient été bien différentes. Tout d'abord pour m'avoir si bien accompagné au début, et pour tous les moments où l'on s'est soutenu par la suite. Je ne pensais pas travailler autant en binôme en commençant ma thèse, et encore moins y trouver quelqu'un avec qui je travail aussi bien. Et par-dessus tout, j'ai trouvé une amitié qui n'a cessé de grandir pour être aujourd'hui une amie avec qui le temps passe si vite et sur laquelle je sais pouvoir compter. Pour terminer par le plus important, merci à mes parents pour m'avoir donné le gout des sciences, encouragé à vouloir comprendre « Comment ca marche ? » et toujours soutenu dans mes choix. Merci aux soutiens de mes parents, mes frères – Aurélien et Léo – et ma famille.

Florian

A mes parents, Maryse & Tony
A papy Bébert

Introduction

This thesis presents advances in the field Josephson photonics. It focuses on two questions:

- How can non-classical photon sources be built and how non-classical can they be?
- Can useful amplification be achieved and what are its limits?

Both are continuations of previous works done by, respectively, A. Grimm [*Grimm15*] and S. Jebari [*Jebari17*].

The field of Josephson photonics is about the interplay between *Coulomb blockade* (CB) and *circuit Quantum Electrodynamic* (cQED). The first one emerged in the sixties and studies Coulomb interaction effects in tunnelling. The second one emerged in 2004 [*Blais04*] thanks to the advances in nano-fabrication and cryogenic microwave technology. It studies interaction between microwave fields and non-linear circuits forming two-level systems – often called artificial atoms – interacting in the same way as photons and atoms in cavity quantum optics.

Scientific context

The field of cQED has recently made tremendous progress to the point where it is now arguably the most advanced platform for quantum computing [*Devoret04*; *Blais07*; *Clarke08*]. Compared to the QED regime of quantum optics, cQED uses superconducting microwave resonators to replace optical cavities and Josephson junctions to replace atoms. These artificial atoms have much stronger electric dipole moments than real atoms and come with wires attached, allowing for the incredible design flexibility.

However, if we consider that cQED is one domain of quantum optics brought to the microwave regime, what about the regime of itinerant photons, which comes first to mind when thinking about quantum optics? It concerns photons in the form of wave packets propagating rather than photons confined in cavities. This regime of itinerant photons is so far much less developed in quantum microwaves. Usually cQED is used to reach this regime by coupling the cavity to a transmission line so that the cavity quantum state leaks out [*Houck07*; *Bozyigit11*; *Eichler11*]. In order to detect quantum states, this process can also be reversed and used to catch itinerant states [*Yin13*]. However, this cQED approach has some limitations.

Bandwidth is limited: In order for cQED to work, the coupling between the artificial atom and the cavity must be much stronger than the coupling to the transmission line, this is the so-called strong-coupling regime [*Wallraff04*; *Blais04*]. This limits the achievable bandwidth of cQED devices working with itinerant photons to be much lower than the non-linearity of the artificial atoms. This is a severe technical limitation for some applications, but also prevents cQED from addressing one fundamental aspect of quantum mechanics: Non-locality [*Aspect82*b; *Aspect82*a]. The bandwidths of cQED imply photon wave-packets have sizes of the order of 10 m or more, whereas the experimental space at the low temperatures is limited to few 10 cm. All cQED experiments so far are therefore local.

Frequency range is limited: The cQED approach is limited by the plasma frequency of the Josephson junction. This frequency typically cannot be pushed significantly beyond 1/3 of the superconducting gap.

Accurately shaped control signals are required: The cQED approach relies on unitary operations on the artificial atom using accurately calibrated microwave pulses. These pulses require significant hardware overhead and make the design of complex circuits a very challenging task.

Catching an itinerant photon in a cavity is difficult: When a quantum state is generated using cQED, the leaky cavity generates an exponentially decaying envelope. Catching an itinerant photon is the time-reversed process and therefore requires a time-reversed envelope, i.e. it must be exponentially growing [*Cirac97*]. Therefore, with fixed coupling between the cavity and a transmission line a photon released from one cavity cannot be caught completely in another one, the coupling between the incoming photon and an artificial atom is therefore weaker than for emission, because at no point in time the photon is fully confined in the cavity.

The goal of this thesis is to explore what the field of Josephson photonics has to offer in order to overcome these limitations, both for the generation of quantum states and for amplification. In particular, we explore if broadband non-classical microwave states can be generated from a simple DC bias, in particular a bright single photon source, and if a DC powered amplifier can operate at the quantum limit.

Single Photon Source

While microwave generators are good coherent sources, non-classical ones are useful for long distance transfer of quantum information in cQED. Consequently, development of single photon sources is an active field both in cQED [*Houck07*; *Hoi13*; *Pechal14*; *Sathyamoorthy16*] and in Josephson photonics [*Souquet14*; *Dambach15*; *Leppäkangas15*]. However, these are theoretical proposals. Experimental implementations started with the implementation of [*Leppäkangas15*] presented in this work and [*Dambach15*] in parallel at CEA Saclay [*Rolland16*; *Rolland18*].

Moreover, such non-classical photons are a candidate to implement quantum cryptographic protocols [*Ekert91*; *Bennett14*] or quantum computers [*Knill01*]. So far the second one has not been deeply explored, but the first ones are already implemented in optics and deployed by companies.

Quantum-limited amplifier

Quantum mechanics predicts a fundamental limit on amplifier performance [*Heffner62*; *Caves82*] through an Heisenberg-like uncertainty principle: a signal can be amplified or be faithfully transmitted without additional noises, but not both; a fine-tuning of the noise then requires a well-defined complementary mode called *idler*. Moreover, *Superconductor Insulator Superconductor* (SIS) structures had been proposed to reach this limit already early on [*Lee82*].

However, many of amplifiers based on a Josephson junction are limited – see above – by the usage of a *Radio Frequency* (RF) pump [*CastellanosBeltran09*; *Astafiev10*; *Bergeal10*a; *Bergeal10*b; *Macklin15*]. When not, they use a resistive shunt that gives an undefined *idler* mode [*Ribeill11*; *Hover12*] and are far from the quantum limit. See [*Jebari17*] for a short review of the different working principles (figure 1).

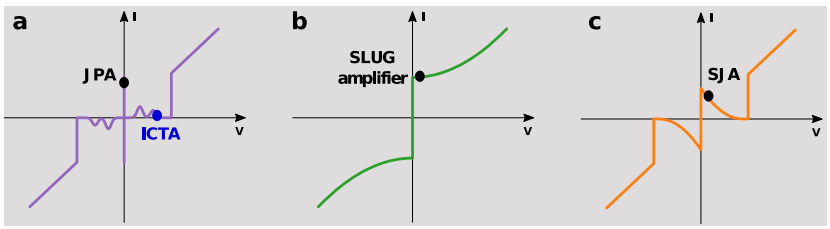

Figure 1: **S. Jebari's review** of amplifier working principles (image from [*Jebari17*]). ***Panel a:*** IV characteristic of an unshunted Josephson junction. ***Panel b & c:*** IV characteristic of a shunted Josephson junction. The different working points are shown on the different IV characteristics.

From Coulomb blockade to dynamic Coulomb blockade

When a small conducting island exists between two electrodes, electrons can flow between the two electrodes by tunnelling successively from the first electrode to the island and from the island to the second electrode. However, Coulomb repulsion between electrons can forbid an electron to tunnel. This phenomenon is called *Coulomb blockade* and takes place when the charging energy $e^2/2C$ is larger than the particle energy eV_b and thermal energy $k_B T$, where C is the capacity of the island and V_b the bias between the island and the electrode.

As capacitance has to be small, in order to reach this limit C. A. Neugebauer and M. B. Webb did the first observation in granular ultra-thin films [*Neugebauer62*]. Then it was observed in junctions with superconducting particles in oxide barrier [*Zeller69*]. When fabrication methods had been advanced enough, islands were designed at will [*Fulton87*], together with theoretical background [*Likharev88*], more devices were developed and used to tune electron tunnelling and study it [*Pothier91*].

Coulomb blockade also plays a role when there is no island but a single junction. In that case, explored in late eighties [*Delsing89*; *Geerligs89*] and known as *dynamic Coulomb blockade*, inelastic tunnelling happens only when the energy of a particle can be dissipated in the electromagnetic environment. Let's consider the case where the electromagnetic environment consists of a single mode at ω_0. In that case $eV_b \geq \hbar\omega_0$ is required for inelastic tunnelling. As a consequence conduction channels due to inelastic tunnelling are closed when the bias is decreased below $\hbar\omega_0/e$, and a dip is observed in the differential conductance (figure 2).

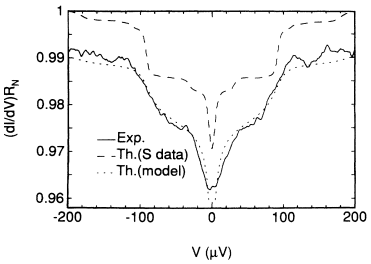

Figure 2: **Differential conductance** as a function of the voltage bias for a normal junction (image from [*Holst94*]). A dip at zero bias is visible (see text).

T. Holst et al. observed the case of a Josephson junction with an electromagnetic environment reduced, on purpose, to a single mode resonator [*Holst94*]. Now the particles are Cooper pairs and are condensed. Each tunnelling Cooper pair has an energy $2eV_b$ to dissipate, which can happen only when $2eV_b = \hbar\omega_0$. Then, they observed peaks in the current – see figure 3 – instead of the differential conductance dip. Moreover, the *P*-theory developed meanwhile [*Averin90*; *Girvin90*; *Ingold91*; *Ingold92*] gives tools to quantitatively explain the results. Note also that early theoretical works [*Averin85*; *Likharev85*; *Likharev88*] predicted charge and discharge oscillations – called Bloch oscillations – of the junction capacitance, that is similar to dynamic Coulomb blockade.

Josephson photonics

Thanks to new microwave techniques, experiments focusing on the microwaves radiated by such inelastic tunnelling processes [*Basset10*; *Hofheinz11*; *Pashkin11*] can now be conducted. Those experiments measure the current as [*Holst94*] (see also figure 3) but also wire the device to measure the emitted microwave signal[1]. The results (see figure 4) show a correlation between the Cooper pair current flowing through such a device and the microwave photons radiated at ω_0. This correlation is consistent with the interpretation of Cooper pairs tunnelling by giving their energy to the electromagnetic environment in the form of photons.

These experiments focussed on the creation of photons from a DC-biased Josephson junction. Then other studies, theoretical [*Armour13*; *Gramich13*; *Armour15*] and experimental [*Altimiras14*; *Houle17*], were conducted to study more complex electromagnetic environments (like two resonators or strong

[1] Coaxial cables and fast acquisition board for example.

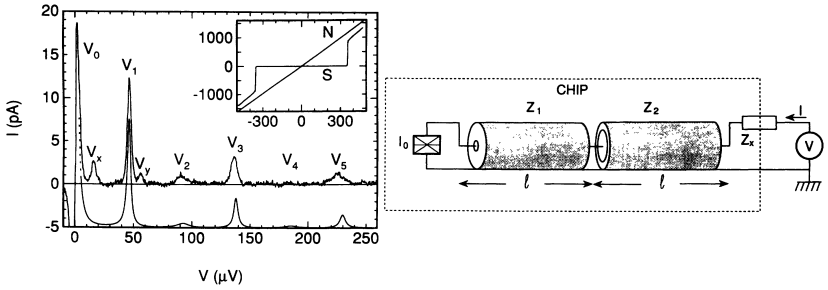

Figure 3: **T. Holst's experiment in 1994** (images from [*Holst94*]). ***Right scheme*** shows the device made of stepped quarter-wave TLs forming a resonator with a low quality factor and a Josephson junction biased by a DC voltage source. ***Left figure*** shows the current through the device as a function of the applied voltage. ***Inset*** the usual IV characteristics of a Josephson junction (N indicates normal state, S superconducting one). ***Main*** zoom below the gap in superconducting state. In addition to the super-current at zero bias there is also a finite Cooper pair current at $(2n+1)\,\hbar\omega_0/2e$ corresponding to a tunnelling Cooper pair giving its energy as form of a photon at $(2n+1)\,\omega_0$, the different modes of the resonator.

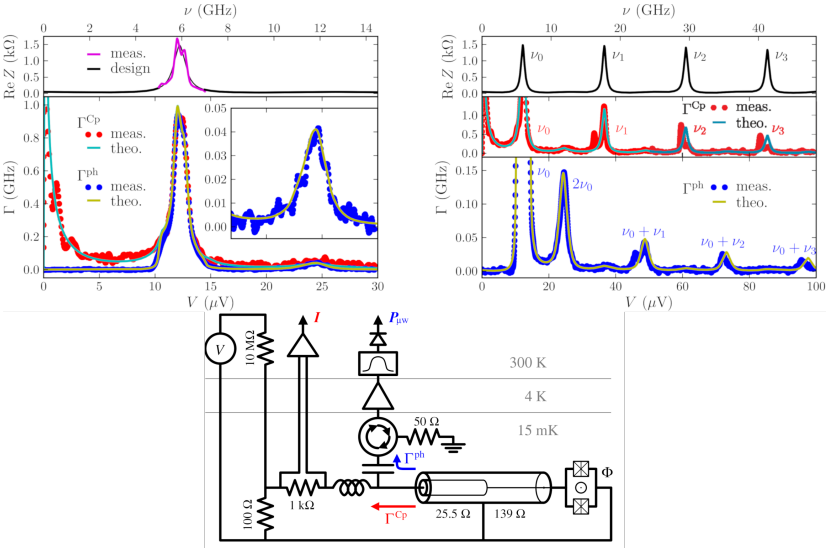

Figure 4: **M. Hofheinz' experiment in 2011** (images [*Hofheinz11*]) ***bottom scheme*** shows how the previous experiment is updated with a bias-tee to spit DC & RF components, both are then measured. ***Top left figure*** shows how the Cooper pair current (in red) and the photon rate (in blue) are effectively correlated in agreement with the explanation that a tunnelling Cooper pair gives its energy to a photon. ***Top right figure*** shows other process where more than one photon is created.

coupling) or out-of-equilibrium system (strong critical current). In particular, the photonic aspect has then been addressed in terms of input photons using *Input Output Theory* (IOT) [*Leppäkangas14*b; *Mora17*; *Leppäkangas18*]. These proposals have shown that *Josephson photonics* is a fertile place to implement and study any kind of photonic devices in the microwave domain: Sources, amplifiers, converters, detectors.

This thesis presents results about such a *non-classical source* & a *parametric amplifier*.

Thesis goals – *Josephson photonics: Microwave generation & amplification in the quantum regime*

Non-classical radiation

As explained previously, a DC-biased Josephson junction coupled to a microwave resonator produces microwave photons: To tunnel through a Josephson junction biased at V_b, a Cooper pair has to give its energy $2eV_b$ to the resonator in the form of n photons of energy $\hbar\omega_0$; so the tunnelling is only possible if $2eV_b = n\hbar\omega_0$. It results in a Cooper pair current, and microwave radiation.

If the tunnelling events of Cooper pairs are independent, i.e. there are no memory effects at low frequencies, and higher order processes are negligible, which is the case when $Z_0 \ll R_Q/\pi$ where Z_0 is

the resonator characteristic impedance and $R_Q \equiv h/4e^2 \simeq 6.453\,\mathrm{k\Omega}$ is the quantum of resistance[2], statistics of emitted photons will also be independent: The device forms a coherent source of photons [*Hofheinz11*; *Grimm15*] – like a laser [*Cassidy17*].

In this work, we study what happens when the first condition is broken at will by adding an RC circuit in series with the resonator. It introduces a memory effect for Cooper pairs: A Cooper pair will charge the capacitor which influence further tunnelling for a time $\simeq RC$ until the capacitor relaxes via the resistor. The influence is easy to understand from an energetic point of view:

- When the capacitor is empty, a tunnelling Cooper pair has to charge the capacitor with the energy $(2e)^2/2C$, and eventually creates n photons of (total) energy $n\hbar\omega_0$. Consequently, for such a process the bias has to be $2eV_b = (2e)^2/2C + n\hbar\omega_0$
- When the capacitor is already charged with one Cooper pair, a second tunnelling Cooper pair has to charge the capacitor with the energy $(2\cdot e)^2/2C - (2e)^2/2C = 3(2e)^2/2C$, and eventually creates m photons of (total) energy $m\hbar\omega_0$. Consequently, for such a process the bias has to be $2eV_b = 3\cdot(2e)^2/2C + m\hbar\omega_0$

If the bias voltage is chosen to create one photon at the first tunnelling event, then depending on C, either the second event is impossible energetically or $m = 0$, see also figure IV.9. In any case no photon can be emitted. Finally, if the resonator relaxes faster than the capacitor, i.e. $Q/\omega_0 \ll RC$ where Q is the resonator quality factor, only one photon is created and goes out of the resonator before the capacitor relaxes and allows further tunnelling and creation of a new photon. Photons are emitted one by one. The device therefore acts as a *single photon source*.

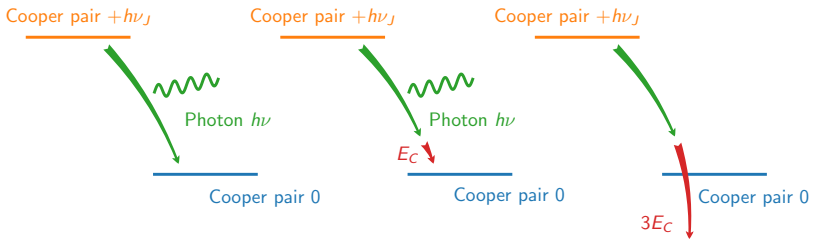

Figure 5: **Blocking mechanism.** ***Left diagram:*** Initial situation. Tunnelling happens when the Cooper pair energy $h\nu_J$ and photon energy $h\nu$ are equal. Then each tunnelling Cooper pair gives a photon. ***Centre diagram:*** Same process in presence of a high impedance RC circuit where a charging energy E_C is required for a Cooper pair to tunnel and charge the capacitor, while dissipating the remaining energy as a photon. ***Right diagram:*** When the capacitor is already charged, the charging energy to pay is now $3E_C$, consequently energies are not balanced any more blocking further tunnelling.

The photon statistics of a source are characterised by the second-order correlation function $g^{(2)}$ [*Glauber63*] defined as:

$$g^{(2)} \equiv \frac{\langle a^\dagger a^\dagger a a\rangle}{\langle a^\dagger a\rangle^2} \tag{1}$$

This quantity can discriminate classical from quantum statistics:

- For a coherent field $|\alpha\rangle$, it is $\alpha^4/\left(\alpha^2\right)^2 = 1$;
- For a Fock state $|n\rangle$, $g^{(2)} = n(n-1)/n^2 = 1 - 1/n$;
- For a thermal state $\propto \sum_n e^{-n\hbar\beta\omega_0}|n\rangle\langle n|$ at temperature β, $g^{(2)} = 2$

The value $g^{(2)} = 1$ is the boundary between classical and quantum states. The optical Hanbury Brown-Twiss experiment is the most intuitive to understand $g^{(2)}$: The field is split in two with a beam splitter, then the field is measured on each path. It gives the probability to measure a photon on a path –

[2] This condition is discussed in chapter V.

labelled D_1 – knowing a photon is also measured on the other path – labelled D_2 – $p(D_1|D_2)$ using *Single Photon Detector* (SPD) and coincidence circuits (see figure 6). Then this probability is compared to the bare probability to measure a photon on the path D_1, $p(D_1)$: This ratio is $g^{(2)}$. The boundary $g^{(2)} = 1$ means these two probabilities are equals $p(D_1|D_2) = p(D_1)$, which is the definition of two independent events. However, in the microwave domain SPD do not yet exist and, therefore, our measurement is rather based on the measurement of field amplitudes proportional to the field operator $a^\dagger$ & a in equation 1 as proposed by M. Da Silva [*daSilva10*].

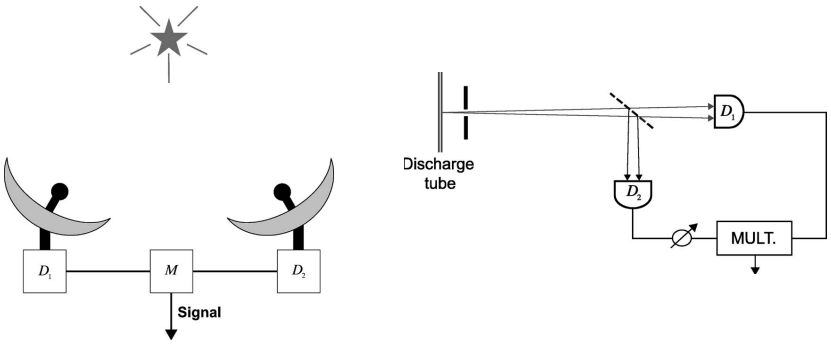

Figure 6: **Photon correlation measurement using Hanbury Brown-Twiss setup** (image [*Glauber06*]). ***Left scheme*** is used in astronomy, the radiation coming from a celestial object is detected at two different points and coincidences are then computed. ***Right scheme*** is used in optics, a light source is split in two and SPD are used on each path to measure coincidences (see text).

In the thesis, experimental results of such a source are reported. Results are also compared to previous theoretical work by J. Leppäkangas [*Leppäkangas15*]. Moreover, theoretical background using P-theory is derived and used to develop an analytic method to extract quantitative insights from experimental data. An alternative method for obtaining single photons based on Franck-Condon blockade by using a high impedance resonator has been explored in parallel [*Souquet14*; *Dambach15*; *Rolland18*].

Quantum-limited amplification

Amplification based on Josephson photonics can be achieved by increasing the bias of the Josephson junction from $2eV_b = \hbar\omega_0$ to $2eV_b = \hbar\omega_0 + \hbar\omega_1$ where ω_1 is a second resonator frequency[3]. In that case, a Cooper pair tunnelling through the Josephson junction has to create a photon in each resonator.

An *ad hoc* Hamiltonian is $e^{-i\omega_J t} a_0^\dagger a_1^\dagger + \mathfrak{h.c.}$ where $\hbar\omega_J \equiv 2eV_b$, this is a *parametric* interaction where a pump oscillating at frequency ω_J excites two modes a lower frequencies $\omega_{0/1}$. Early derivations [*Mollow67*a; *Mollow67*b] show that it gives rise to amplification. Such a device is then a parametric amplifier.

A more intuitive way to picture this amplifier is to consider this process where a Cooper pair gives rise to photons as a radiative transition. An input field will then accelerate this process through stimulated emission: A incoming photon at a frequency involved in the radiative transition will transmit, if possible, its properties to the photon created by the radiative transition, see figure 7. It is a coherent amplification of the input field.

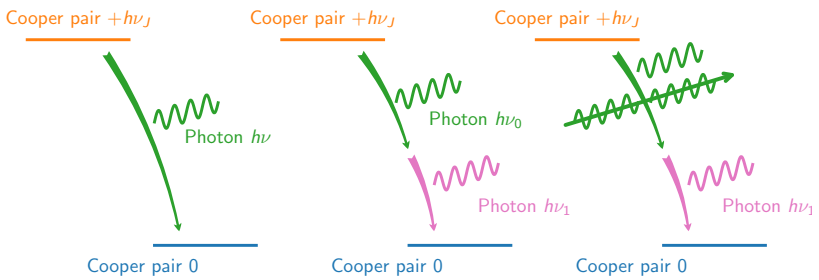

Figure 7: **Amplification process.** ***Left diagram:*** The initial situation (see above). ***Centre diagram:*** Situation where a Cooper pair tunnels and create two photons, one at ν_0 and one at ν_1, this process is visible on figure 4 at 50 µV. ***Right diagram:*** Same process with an additional input photon at ν_0, resulting in stimulated emission and amplification.

In this thesis, theoretical characteristics of the parametric amplification for Josephson photonic devices are derived. Connexion between P-theory and IOT are made and properties are derived:

[3] It includes the degenerate case $\omega_0 \simeq \omega_1$ where there is a single physical resonator.

Input added noise: Parametric amplification is a mechanism where the quantum limit derived by C. Caves [*Caves82*] can be reached. However, in the case of Josephson photonics phase noise of the pump must be considered.

Gain-bandwidth product: How high gain reduces the effective bandwidth, i.e. over which range of frequencies the amplifier can be operated;

Compression point: The maximum power that can be amplified with this mechanism.

Experimental results of such a device are shown and compared to theoretical results. Finally, a future design overcoming some defects is proposed.

Outline

Chapter I: Inelastic Cooper Pair Tunnelling

The first chapter introduces two complementary theories of *Inelastic Cooper Pair Tunnelling* (ICPT) which aim to describe how Cooper pairs can tunnel though the Josephson junction depending on the surrounding electromagnetic environment:

- The so-called P-theory [*Ingold91*; *Nazarov13*], which can be seen as a generalisation of the Fermi golden rule;
- The IOT which gives more information about how energies can be dissipated though the environment.

The chapter also gives limitations of both theories.

We then derive the *Power Spectral Density* (PSD) and parametric amplification [*Clerk10*] (described by gain and noise [*Caves82*]) generated by ICPT. Each of them is first introduced with simple classical pictures before using quantum models.

The chapter ends with a memento on the Caldeira-Leggett [*Caldeira83*] model which is a powerful tool to deal with arbitrary complex electromagnetic environments. Moreover, it also describes how we can determine some properties – described by its P-function – of a complex environment made of many well-know simple environments.

Chapter II: Experimental setup

The second chapter describes all different experimental setups used to characterise our devices. 4 K techniques for device screening, He dilution fridge, its electronics, as well as computing code developed to perform and analyse measurements.

4 K is an easily reachable temperature using liquid He, and is low enough to roughly characterise material properties of our samples and properties of our structures: Josephson junctions & resonators. When it is characterised and if it is compliant with our design, the device is cooled to 12 mK with our He dilution fridge.

The main measurement system of the 12 mK platform is a high speed digitiser (AlazarTech ATS9373) used to exact correlation properties of the field coming from the sample [*daSilva10*]. This chapter gives theoretical and technical details about the scheme of this setup.

Finally, the chapter describes how measurements are performed and analysed. A flexible framework has been developed in `python`:

- A data structure compatible with all our measurement, and future measurements;
- A control structure – and associated driver objects – to describe how a measurement should be performed;
- A *Graphical User Interface* (GUI) to visualise our data using various filters.

Chapter III: Sample design and fabrication

The third chapter is succinct and describes how our samples are fabricated. A first section describes how the NbN/MgO/NbN trilayer is sputtered and etched to form Josephson junctions, transmission lines and other structures. A section is dedicated to building blocks of our designs and the limits they impose on the electromagnetic environment we can synthesise.

Chapter IV: Non-classical radiation

The fourth chapter is focused on the building of a source of anti-bunched photons using ICPT. A first section describes how the sample is designed to engineer the ICPT process to build a photon source operating in the quantum regime (figure IV.9). Then PSD is measured and the P-theory is used to characterise the sample:

- The critical current;
- The thermodynamic temperature;
- The impedance seen by the Josephson junction.

Finally, two operating modes are explored, free-running and on-demand. The first one corresponds to the operating mode for which the sample was designed. The second one exploits an unexpected behaviour: A high critical current allows to escape from ICPT regime to reach a dark regime where the sample essentially behaves as a resistor. The chapter describes this second regime and how it can be used to generate photons on-demand. In both cases, PSD and $g^{(2)}$ are measured to characterise the sample.

Chapter V: Quantum-limited amplification

The fifth chapter is focused on quantum-limited amplification based on ICPT. A first section describes how the ICPT process can be engineered to allow for amplification (figure 7). Some drawbacks and solutions are identified.

Finally, theoretical derivations of characteristics of such amplifiers, as bandwidth and compression point, are derived and compared to experimental results from one of the designs. To characterise our amplifiers, both gain and PSD are measured and used to also extract quantum limit and input added noise, which is a measure of how close the amplifier operates to the quantum limit ([*Caves82*]). Our results indicate that ICPT can lead to near quantum-limited amplification when voltage noise is mastered.

References

[*Altimiras14*] Carles Altimiras et al. "Dynamical Coulomb Blockade of Shot Noise". *Phys. Rev. Lett.* **112**, 236803 (2014),

Cited on page 3.

[*Armour15*] A. D. Armour, Björn Kubala, and Joachim Ankerhold. "Josephson Photonics with a Two-Mode Superconducting Circuit". *Phys. Rev. B* **91**, 184508 (2015),

Cited on page 3.

[*Armour13*] A. D. Armour et al. "Universal Quantum Fluctuations of a Cavity Mode Driven by a Josephson Junction". *Phys. Rev. Lett.* **111**, 247001 (2013),

Cited on page 3.

[*Aspect82*a] Alain Aspect, Jean Dalibard, and Gérard Roger. "Experimental Test of Bell's Inequalities Using Time-Varying Analyzers". *Phys. Rev. Lett.* **49**, 1804–1807 (1982),

Cited on page 1.

[*Aspect82*b] Alain Aspect, Philippe Grangier, and Gérard Roger. "Experimental Realization of Einstein-Podolsky-Rosen-Bohm Gedankenexperiment: A New Violation of Bell's Inequalities". *Phys. Rev. Lett.* **49**, 91–94 (1982),

Cited on page 1.

[*Astafiev10*] Oleg V. Astafiev et al. "Resonance Fluorescence of a Single Artificial Atom". *Science* **327**, 840–843 (2010), pmid: 20150495

Cited on page 2.

[*Averin90*] D. V. Averin, Yuli V. Nazarov, and A. A. Odintsov. "Incoherent Tunneling of the Cooper Pairs and Magnetic Flux Quanta in Ultrasmall Josephson Junctions". *Physica B: Condensed Matter*. LT-19 **165-166**, 945–946 (1990),

Cited on page 3.

[*Averin85*] D. V. Averin, A. B. Zorin, and K. K. Likharev. "Bloch Oscillations in Small Josephson Junctions". *Sov. Phys. JETP* **61**, 407–413 (1985),

Cited on page 3.

[*Basset10*] J. Basset, Hélène Bouchiat, and R. Deblock. "Emission and Absorption Quantum Noise Measurement with an On-Chip Resonant Circuit". *Phys. Rev. Lett.* **105**, 166801 (2010),

Cited on page 3.

[*Bennett14*] Charles H. Bennett and Gilles Brassard. "Quantum Cryptography: Public Key Distribution and Coin Tossing". *Theoretical Computer Science*. Theoretical Aspects of Quantum Cryptography – celebrating 30 years of BB84 **560**, 7–11 (2014),

Cited on page 2.

[*Bergeal10*a] Nicolas Bergeal et al. "Analog Information Processing at the Quantum Limit with a Josephson Ring Modulator". *Nature Physics* **6**, 296–302 (2010),

Cited on page 2.

[*Bergeal10*b] Nicolas Bergeal et al. "Phase-Preserving Amplification near the Quantum Limit with a Josephson Ring Modulator". *Nature* **465**, 64–68 (2010),

Cited on page 2.

[*Blais04*] Alexandre Blais et al. "Cavity Quantum Electrodynamics for Superconducting Electrical Circuits: An Architecture for Quantum Computation". *Phys. Rev. A* **69**, 062320 (2004),

Cited on page 1.

[*Blais07*] Alexandre Blais et al. "Quantum-Information Processing with Circuit Quantum Electrodynamics". *Phys. Rev. A* **75**, 032329 (2007),

Cited on page 1.

[*Bozyigit11*] Deniz Bozyigit et al. "Antibunching of Microwave-Frequency Photons Observed in Correlation Measurements Using Linear Detectors". *Nature Physics* **7**, 154–158 (2011),

Cited on page 1.

[*Caldeira83*] A. O Caldeira and A. J Leggett. "Quantum Tunnelling in a Dissipative System". *Annals of Physics* **149**, 374–456 (1983),

Cited on pages 7, 23, 38.

[*Cassidy17*] M. C. Cassidy et al. "Demonstration of an Ac Josephson Junction Laser". *Science* **355**, 939–942 (2017), pmid: 28254938

Cited on page 5.

[*CastellanosBeltran09*] M. A. Castellanos-Beltran et al. "Bandwidth and Dynamic Range of a Widely Tunable Josephson Parametric Amplifier". *IEEE Transactions on Applied Superconductivity* **19**, 944–947 (2009),

Cited on page 2.

[*Caves82*] Carlton M. Caves. "Quantum Limits on Noise in Linear Amplifiers". *Phys. Rev. D* **26**, 1817–1839 (1982),

Cited on pages 2, 7–8, 23, 35, 37, 91.

[*Cirac97*] J. I. Cirac et al. "Quantum State Transfer and Entanglement Distribution among Distant Nodes in a Quantum Network". *Physical Review Letters* **78**, 3221–3224 (1997), arXiv: quant-ph/9611017

Cited on page 2.

[*Clarke08*] John Clarke and Frank K. Wilhelm. "Superconducting Quantum Bits". *Nature* **453**, 1031–1042 (2008),

Cited on page 1.

[*Clerk10*] Aashish A. Clerk et al. "Introduction to Quantum Noise, Measurement, and Amplification". *Rev. Mod. Phys.* **82**, 1155–1208 (2010),

Cited on pages 7, 23, 35.

[*Dambach15*] Simon Dambach et al. "Time-Resolved Statistics of Nonclassical Light in Josephson Photonics". *Phys. Rev. B* **92**, 054508 (2015),

Cited on pages 2, 6.

[*daSilva10*] Marcus P. daSilva et al. "Schemes for the Observation of Photon Correlation Functions in Circuit QED with Linear Detectors". *Phys. Rev. A* **82**, 043804 (2010),

Cited on pages 6–7, 41, 44.

[*Delsing89*] Per Delsing et al. "Effect of High-Frequency Electrodynamic Environment on the Single-Electron Tunneling in Ultrasmall Junctions". *Phys. Rev. Lett.* **63**, 1180–1183 (1989),

Cited on page 3.

[*Devoret04*] Michel H. Devoret, Andreas Wallraff, and John M. Martinis. "Superconducting Qubits: A Short Review" (2004). arXiv: cond-mat/0411174

Cited on page 1.

[*Eichler11*] Christopher Eichler et al. "Experimental State Tomography of Itinerant Single Microwave Photons". *Phys. Rev. Lett.* **106**, 220503 (2011),

Cited on page 1.

[*Ekert91*] Artur K. Ekert. "Quantum Cryptography Based on Bell's Theorem". *Phys. Rev. Lett.* **67**, 661–663 (1991),

Cited on page 2.

[*Fulton87*] T. A. Fulton and G. J. Dolan. "Observation of Single-Electron Charging Effects in Small Tunnel Junctions". *Phys. Rev. Lett.* **59**, 109–112 (1987),

Cited on page 3.

[*Geerligs89*] L. J. Geerligs et al. "Influence of Dissipation on the Coulomb Blockade in Small Tunnel Junctions". *EPL* **10**, 79 (1989),

Cited on page 3.

[*Girvin90*] S. M. Girvin et al. "Quantum Fluctuations and the Single-Junction Coulomb Blockade". *Phys. Rev. Lett.* **64**, 3183–3186 (1990),

Cited on page 3.

[*Glauber63*] Roy J. Glauber. "The Quantum Theory of Optical Coherence". *Phys. Rev.* **130**, 2529–2539 (1963),

Cited on pages 5, 87.

[*Glauber06*] Roy J. Glauber. "Nobel Lecture: One Hundred Years of Light Quanta". *Rev. Mod. Phys.* **78**, 1267–1278 (2006),

Cited on pages 6, 88.

[*Gramich13*] Vera Gramich et al. "From Coulomb-Blockade to Nonlinear Quantum Dynamics in a Superconducting Circuit with a Resonator". *Phys. Rev. Lett.* **111**, 247002 (2013),

Cited on page 3.

[*Grimm15*] Alexander Grimm. *Josephson Photonics: Statistics of Photons Emitted by Inelastic Cooper Pair Tunneling*. PhD thesis. Grenoble University, 2015

Cited on pages 1, 5, 32, 62–63, 65, 71.

[*Heffner62*] H. Heffner. "The Fundamental Noise Limit of Linear Amplifiers". *Proceedings of the IRE* **50**, 1604–1608 (1962),

Cited on page 2.

[*Hofheinz11*] Max Hofheinz et al. "Bright Side of the Coulomb Blockade". *Phys. Rev. Lett.* **106**, 217005 (2011),

Cited on pages 3–5, 62, 72, 91.

[*Hoi13*] Io-Chun Hoi et al. "Microwave Quantum Optics with an Artificial Atom in One-Dimensional Open Space". *New J. Phys.* **15**, 025011 (2013),

Cited on page 2.

[*Holst94*] T. Holst et al. "Effect of a Transmission Line Resonator on a Small Capacitance Tunnel Junction". *Phys. Rev. Lett.* **73**, 3455–3458 (1994),

Cited on pages 3–4.

[*Houck07*] Andrew A. Houck et al. "Generating Single Microwave Photons in a Circuit". *Nature* **449**, 328–331 (2007),

Cited on pages 1–2.

[*Houle17*] Samuel Houle et al. "Photon-Assisted Dynamical Coulomb Blockade in a Tunnel Junction" (2017). arXiv: 1706.09337 `[cond-mat]`

Cited on page 3.

[*Hover12*] D. Hover et al. "Superconducting Low-Inductance Undulatory Galvanometer Microwave Amplifier". *Appl. Phys. Lett.* **100**, 063503 (2012),

Cited on page 2.

[*Ingold91*] Gert-Ludwig Ingold and Hermann Grabert. "Finite-Temperature Current-Voltage Characteristics of Ultrasmall Tunnel Junctions". *EPL* **14**, 371 (1991),

Cited on pages 3, 7, 23, 31.

[*Ingold92*] Gert-Ludwig Ingold and Yuli V. Nazarov. “Charge Tunneling Rates in Ultrasmall Junctions”. In: *Single Charge Tunneling*. NATO ASI Series. Springer, Boston, MA, 1992, pp. 21–107

Cited on pages 3, 24, 28, 32.

[*Jebari17*] Salha Jebari. *The Inelastic Cooper Pair Tunneling Amplifier (ICTA)*. PhD thesis. Université Grenoble Alpes, 2017

Cited on pages 1–2, 35, 62–63, 91, 96.

[*Knill01*] E. Knill, R. Laflamme, and G. J. Milburn. "A Scheme for Efficient Quantum Computation with Linear Optics". *Nature* **409**, 46–52 (2001),
Cited on page 2.

[*Lee82*] G. S. Lee. "Superconductor-insulator-superconductor Reflection Parametric Amplifier". *Appl. Phys. Lett.* **41**, 291–293 (1982),
Cited on page 2.

[*Leppäkangas14*b] Juha Leppäkangas et al. "Input–Output Description of Microwave Radiation in the Dynamical Coulomb Blockade". *New J. Phys.* **16**, 015015 (2014),
Cited on page 4.

[*Leppäkangas15*] Juha Leppäkangas et al. "Antibunched Photons from Inelastic Cooper-Pair Tunneling". *Phys. Rev. Lett.* **115**, 027004 (2015),
Cited on pages 2, 6.

[*Leppäkangas18*] Juha Leppäkangas et al. "Multiplying and Detecting Propagating Microwave Photons Using Inelastic Cooper-Pair Tunneling". *Phys. Rev. A* **97**, 013855 (2018),
Cited on pages 4, 104.

[*Likharev88*] K. K. Likharev. "Correlated Discrete Transfer of Single Electrons in Ultrasmall Tunnel Junctions". *IBM Journal of Research and Development* **32**, 144–158 (1988),
Cited on page 3.

[*Likharev85*] K. K. Likharev and A. B. Zorin. "Theory of the Bloch-Wave Oscillations in Small Josephson Junctions". *J Low Temp Phys* **59**, 347–382 (1985),
Cited on page 3.

[*Macklin15*] Chris Macklin et al. "A near–Quantum-Limited Josephson Traveling-Wave Parametric Amplifier". *Science* **350**, 307–310 (2015), pmid: 26338795
Cited on page 2.

[*Mollow67*a] B. R. Mollow and Roy J. Glauber. "Quantum Theory of Parametric Amplification. I". *Phys. Rev.* **160**, 1076–1096 (1967),
Cited on page 6.

[*Mollow67*b] B. R. Mollow and Roy J. Glauber. "Quantum Theory of Parametric Amplification. II". *Phys. Rev.* **160**, 1097–1108 (1967),
Cited on page 6.

[*Mora17*] Christophe Mora et al. "Quantum Properties of the Radiation Emitted by a Conductor in the Coulomb Blockade Regime". *Phys. Rev. B* **95**, 125311 (2017),
Cited on pages 4, 28–29.

[*Nazarov13*] Yuli V. Nazarov and Jeroen Danon. *Advanced Quantum Mechanics: A Practical Guide*. Cambridge University Press, 2013
Cited on pages 7, 23–24, 32.

[*Neugebauer62*] C. A. Neugebauer and M. B. Webb. "Electrical Conduction Mechanism in Ultrathin, Evaporated Metal Films". *Journal of Applied Physics* **33**, 74–82 (1962),
Cited on page 3.

[*Pashkin11*] Yuri A. Pashkin et al. "Charge Transport through Ultrasmall Single and Double Josephson Junctions Coupled to Resonant Modes of the Electromagnetic Environment". *Phys. Rev. B* **83**, 020502 (2011),
Cited on page 3.

[*Pechal14*] Marek Pechal et al. "Microwave-Controlled Generation of Shaped Single Photons in Circuit Quantum Electrodynamics". *Phys. Rev. X* **4**, 041010 (2014),
Cited on page 2.

[*Pothier91*] H. Pothier. *Coulomb Blockade and Transfer of Electrons One by One*. PhD thesis. Université Pierre et Marie Curie - Paris VI, 1991
Cited on page 3.

[*Ribeill11*] G. J. Ribeill et al. "Superconducting Low-Inductance Undulatory Galvanometer Microwave Amplifier: Theory". *Journal of Applied Physics* **110**, 103901 (2011),
Cited on page 2.

[*Rolland16*] Chloé Rolland. *Strong Coupling Quantum Electrodynamics of a Voltage Biased Josephson Junction*. thesis. Lille 1, 2016
Cited on pages 2, 99.

[*Rolland18*] Chloé Rolland et al. "Antibunched Photons Emitted by a Dc Biased Josephson Junction" (2018). arXiv: 1810.06217 [cond-mat, physics:quant-ph]
Cited on pages 2, 6, 99.

[*Sathyamoorthy16*] Sankar Raman Sathyamoorthy et al. "Simple, Robust, and on-Demand Generation of Single and Correlated Photons". *Phys. Rev. A* **93**, 063823 (2016),
Cited on page 2.

[*Souquet14*] J.-R. Souquet et al. "Photon-Assisted Tunnelling with Nonclassical Light". *Nature Communications* **5**, 5562 (2014),
Cited on pages 2, 6.

[*Wallraff04*] Andreas Wallraff et al. "Strong Coupling of a Single Photon to a Superconducting Qubit Using Circuit Quantum Electrodynamics". *Nature* **431**, 162–167 (2004),
Cited on page 1.

[*Yin13*] Yi Yin et al. "Catch and Release of Microwave Photon States". *Phys. Rev. Lett.* **110**, 107001 (2013),
Cited on page 1.

[*Zeller69*] H. R. Zeller and I. Giaever. "Tunneling, Zero-Bias Anomalies, and Small Superconductors". *Phys. Rev.* **181**, 789–799 (1969),
Cited on page 3.

Table of contents – *Josephson photonics: Microwave generation & amplification in the quantum regime*

List of symbols & abreviations

Other Symbols

$|f|$ Absolute value of f

$Y_\nu,\ Y_t,\ Y_\omega$ Admittance, $i \equiv Y_t * u$ and $Y_\nu \equiv \mathcal{F}_\nu[Y_t]$ & $Y_\omega \equiv \mathcal{F}_\omega[Y_t]$

adv, , ret Advanced & retarded solution abbreviations

$a,\ a^\dagger$ Annihilation & creation operators

$\{f_0, f1\}$ Anti-commutator of f_0 & f_1, i.e. $\{f_0, f_1\} \equiv f_0 f_1 + f_1 f_0$

$\langle f \rangle$ Average over the configuration space: $\langle f \rangle \equiv \mathrm{Tr}(f)$

$_n$ n^{th}-order Bessel function defined as $_n(z) \equiv \sum_m \frac{(-1)^m}{m!(m+n)!}\left(\frac{z}{2}\right)^{2m+n}$

$\beta,\ T$ Temperature, $\beta \equiv 1/k_B T$

$C,\ L,\ R$ Capacitance, inductance & resistance

$q,\ \phi$ Charge & flux at a circuit node or branch, $[\phi, q] \equiv \pm i\hbar$

$[f_0, f1]$ Commutator of f_0 & f_1, i.e. $[f_0, f_1] \equiv f_0 f_1 - f_1 f_0$

$*$ Convolution product $[f_0 * f_1](t) \equiv \int_{\mathbb{R}} f_0(\tau) f_1(t-\tau)\,\mathrm{d}\tau$

$G^{(1)}_{t,f},\ G^{(2)}_{t,f}$ First and second order correlation functions of field operator f: $G^{(1)}_{t,f}(t) \equiv \Gamma_{t,ff}(t)$ & $G^{(2)}_{t,f}(\tau) \equiv \left\langle f^\dagger(t) f^\dagger(t+\tau) f(t+\tau) f(t)\right\rangle$

$\Gamma_{t,f_0f_1},\ S_{\nu,f_0f_1},\ S_{\omega,f_0f_1}$ f_0-f_1 correlation t-function, i.e. $\Gamma_{t,f_0f_1}(\tau) \equiv \left\langle f_0^\dagger(t+\tau) f_1(t)\right\rangle$ for real stationary ergodic processes, see also equation C.2

$\kappa_\nu,\ \kappa_z,\ \kappa_t,\ \kappa_\omega$ Coupling function

$i,\ u$ Current & voltage through a circuit branch

δ Dirac distribution, $\langle \delta_t, f \rangle \equiv f(t)$, or Kronecker symbol

e $\equiv \exp 1$

$\mathcal{F}_\nu[f],\ \mathcal{F}_\omega[f]$ Ordinary & angular frequency Fourier transform $\mathcal{F}_\nu[f](\nu) \equiv \int_{\mathbb{R}} f(t)\ e^{i2\pi\nu t}\,\mathrm{d}t$ and $\mathcal{F}_\omega[f](\omega) \equiv \int_{\mathbb{R}} f(t)\ e^{i\omega t}\,\mathrm{d}t$

$\bar{\phi}_0\ R_Q$ Reduced magnetic flux quantum $\bar{\phi}_0 \equiv \hbar/2e$ and quantum of resistance $R_Q \equiv h/4e^2 = 2\pi\bar{\phi}_0^2/\hbar \simeq 6.453\,\mathrm{k\Omega}$ where e is the elementary charge

$\nu,\ \omega$ Ordinary (Hz) and angular ($\mathrm{rad\,s^{-1}}$) frequency

$\rightarrow,\ \leftarrow$ Forward & backward notation

$\mathcal{H}$ Hamiltonian notation

$\mathfrak{h.c.}$ Hermitian (or complexe) conjugate of the previous term

Θ Heaviside distribution $\partial_t \Theta \equiv \delta$

Z_ν, Z_t, Z_ω Impedance, $u \equiv Z_t * i$ and $Z_\nu \equiv \mathcal{F}_\nu [Z_t]$ & $Z_\omega \equiv \mathcal{F}_\omega [Z_t]$

in, out Input & output abbreviations

i Imaginary unit, i.e. $i^2 \equiv -1$

$J_{t,f}$, P_f Defined for an hermitian operator f as $J_{t,f}(t) \equiv \Gamma_{t,ff}(t) - \Gamma_{t,ff}(0)$ and $P_f(h\nu) \equiv \frac{1}{h} \mathcal{F}_\nu \left[e^{J_{t,f}} \right] (\nu)$

m^* Effective mass

$\mathbb{N}$ Set of natural numbers

n, φ Cooper pairs number & phase through a weak link branch, $[\varphi, n] \equiv i$

Im Image of a function, i.e. $\forall f : A \to B, \mathrm{Im}(f) \equiv \{f(x), \forall x \in A\}$

v_ϕ Phase velocity

$\mathcal{V}_\phi$ An arbitrary potential

Q Quality factor

$\mathbb{R}$ Set of real numbers

$\chi_{\nu,}$, $\chi_{t,}$, χ_ω, Response function, e.g. $\chi_{\nu,f_0 f_1}$ response on f_0 due to f_1

Re, Im Real and imaginary part

sgn Sign distribution

Tr Trace of an operator

$\mathcal{T}[f]$, $\mathcal{S}[f]$ Reversal operator, i.e. $\mathcal{T}[f](t) \equiv f(-t)$, symmetric and antisymmetric operator, i.e. $\mathcal{S}[f] \equiv f + \mathcal{T}[f]$

V_J, ν_J, ω_J, I_c Voltage bias, in V and Hz – $2eV_J \equiv h\nu_J \equiv \hbar\omega_J$ – and effective critical current

R_T Tunnelling resistance

$R_\square$ Square resistance

RRR Residual Resistivity Ratio

Acronyms / Abbreviations

zpf Zero point fluctuation abbreviation

AC Alternative Current

AWG Arbitrary Wave Generator

CB Coulomb blockade

CCR Canonical Commutation Relations

CPW Coplanar Waveguide

cQED	circuit Quantum Electrodynamic
CVD	Chemical Vapour Deposition
DC	Direct Current
EBL	Electron Beam Lithography
FDT	Fluctuation-Dissipation Theorem
GUI	Graphical User Interface
HDF5	Hierarchical Data Format 5
ICPT	Inelastic Cooper Pair Tunnelling
IO	Input Output
IOT	Input Output Theory
IQ	In-phase & quadrature
JPA	Josephson Parametric Amplifier
OL	Optical Lithography
PCB	Printed Circuit Board
PPMS	Physical Property Measurement System
PSD	Power Spectral Density
QLE	Quantum Langevin Equation
RF	Radio Frequency
RIE	Reactive Ion Etching
RWA	Rotating Wave Approximation
SFDR	Spurious-Free Dynamic Range
SIS	Superconductor Insulator Superconductor
SMA	SubMiniature version A
SNR	Signal to Noise Ratio
SPD	Single Photon Detector
SQUID	Superconducting Quantum Interference Device
TL	Transmission Line
VNA	Vector Network Analyser

Part A

Theoretical & experimental contexts

Chapter I

Inelastic Cooper Pair Tunnelling

French resume

Ce chapitre introduit deux théories complémentaires décrivant l'ICPT, c'est à dire la façon dont les paires de Cooper traversent par effet tunnel une jonction Josephson en fonction de l'environnement électromagnétique l'entourant :

- La théorie *P*[*Ingold91*; *Nazarov13*] qui est une généralisation de la règle d'or de Fermi;
- L'IOT qui apporte plus d'information sur la manière dont l'énergie est dissipée dans l'environnement.

Ces deux théories ont aussi des limitations que nous verrons.

Ensuite notre attention se portera sur la PSD et l'amplification paramétrique [*Clerk10*] (à travers l'expression du gain et du bruit [*Caves82*]) dans le cas de l'ICPT. Une approche classique sera présentée avant l'utilisation du modèle quantique.

Un mémento sur le modèle Caldeira-Leggett [*Caldeira83*] est inclus en fin de chapitre, c'est un outil puissant qui permet de traiter des environnement électromagnétique arbitrairement complexe. De plus, il permet d'étudier certaines propriétés – sous la forme de la fonction P – d'un environnement complexe fait d'un ensemble d'environnements simples et bien connus.

Contents

In this chapter, a generic model of ICPT is introduced, it will be useful to afterwards describe our experiments. This model encompasses two parts:

- A Josephson junction through which a Cooper pair current flows;
- A linear dissipative environment that can absorb or emit some energy.

This dissipative environment can itself be described by some resonators coupled to a *Transmission Line* (TL) through which outgoing and incoming energies flow.

Note here that this model is an application of many theoretical works developed previously [*Ingold92*; *Nazarov13*] and is pictured as simple as possible[1]. As a consequence, advanced models of dissipative systems are not discussed[2] [*König95*; *Weiss12*].

1 Current trough Josephson junctions

1.a Classical description by noise sources

First of all, a fully classical physics can be derived. While it does not capture all features of the full quantum description it provides some quantitative insights. There are three elements involved in all our samples (figure I.1 left panel) that can be described classically (figure I.1 right panel):

A non-zero voltage DC bias Described by a voltage source u_{source} (constant);

A dissipative electromagnetic environment Described by a linear impedance Z_ω in series with a noise voltage source u_N (Johnson-Nyquist noise);

A Josephson junction Described by a junction linear admittance $Y_{\omega,J}$ in parallel with a current source i_ω. Its critical current is I_c.

The indices t, ν, ω denote, respectively, time, ordinary frequency and angular frequency quantities; the two last one are Fourier transforms of the first one.

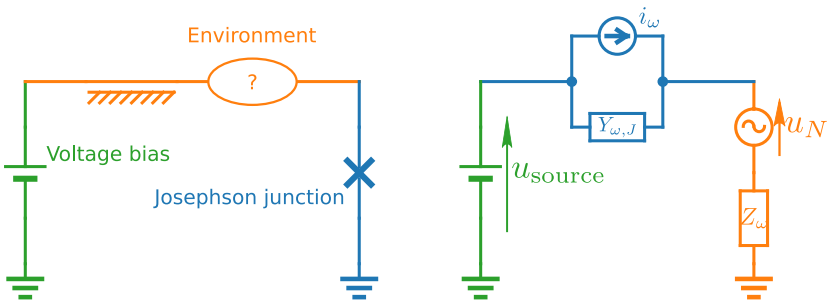

Figure I.1: **General description of our samples and classical model.** ***Left panel:*** General desciption of our samples, a Josephson junction (blue) in series with an arbitrary electromagnetic environment (orange), bias by a DC voltage source (green). ***Right panel:*** The corresponding classical electrical model, the Josephson junction is a current source i_ω in parallel with a linear admittance $Y_{\omega,J}$ (blue). The electromagnetic environment is described by a linear impedance Z_ω in series with a noise voltage source u_N (orange).

Current harmonics generation

First, let's neglect the noise source u_N and assume a low junction admittance ($Y_{\omega,J} Z_\omega \ll 1$). The AC Josephson effect [*Josephson62*; *Tinkham04*], with $\bar{\phi}_0 \equiv \hbar/2e$ the reduced magnetic flux quantum, gives

[1] Only a simple system & bath model at thermal equilibrium is used.
[2] A more complete approach is to use a path integral formalism.

(together with Kirchhoff's laws):

$$i_t(t) = I_c \sin\left(\frac{1}{\bar{\phi}_0}\int_{-\infty}^{t} u_{\text{source}} - \frac{1}{\bar{\phi}_0}\underbrace{\int_{-\infty}^{t} Z_t * i_t}_{\delta\phi}\right) \tag{I.1}$$

As u_{source} is constant, $\int_{-\infty}^{t} u_{\text{source}}$ can be rewritten as $\bar{\phi}_0\omega_J t + \alpha$ where $\omega_J \equiv u_{\text{source}}/2e$ is the Josephson frequency and α an arbitrary phase offset[3]. We perform Taylor expansion up to first-order in $|\delta\phi| = \left|\int_{-\infty}^{t} Z_t * i_t\right| \ll 2\pi\,\bar{\phi}_0$. As this condition cannot be fulfilled for a DC current, those components are treated apart. The n^{th}-order (in sense of iteration with equation I.1) current is $i_t^{(n)}(t) + i_0^{(n)}$ where $i_0^{(n)}$ is its DC component.

$$\begin{aligned}
i_t^{(0)}(t) &= I_c \sin(\omega_J t + \alpha) \\
i_t^{(0)}(t) + i_t^{(1)}(t) + i_0^{(1)} &= I_c \sin(\omega_J t + \alpha) \\
&\quad -\tfrac{I_c}{\bar{\phi}_0}\cos(\omega_J t + \alpha)\int_{-\infty}^{t} Z_t * i_t^{(0)} \\
&\dots \\
\sum_n^{N+1} i_t^{(n)}(t) + i_0^{(n)} &= I_c \sin\left({\omega_J}^{(n)} t + \alpha\right) \\
&\quad -\tfrac{I_c}{\bar{\phi}_0}\cos\left({\omega_J}^{(n)} t + \alpha\right)\int_{-\infty}^{t} Z_t * \sum_n^N i_t^{(n)}
\end{aligned} \tag{I.2}$$

Where ${\omega_J}^{(n)} \equiv \omega_J - \frac{Z_\omega(0)}{\bar{\phi}_0}\sum_n^N i_0^{(n)}$. Combining the two first equations:

$$\begin{aligned}
i_t^{(1)}(t) + i_0^{(1)} &= -\tfrac{{I_c}^2}{\bar{\phi}_0}\int_{-\infty}^{t} \mathrm{d}\tau \int_{\mathbb{R}} \mathrm{d}\tau' Z_t(\tau')\sin(\omega_J(\tau-\tau')+\alpha)\cos(\omega_J t+\alpha) \\
&= \tfrac{{I_c}^2}{\bar{\phi}_0}\,\mathrm{Im}\left[Z_\omega(\omega_J)\int_{-\infty}^{t} e^{-i\omega_J\tau - i\alpha}\cos(\omega_J t+\alpha)\,\mathrm{d}\tau\right] \\
i_t^{(1)}(t) + i_0^{(1)} &= \tfrac{{I_c}^2}{\bar{\phi}_0}\,\tfrac{1}{2\omega_J}\,\mathrm{Re}\left[Z_\omega(\omega_J)\;e^{-i2\omega_J t - i2\alpha}\right] \\
&\quad + \tfrac{{I_c}^2}{\bar{\phi}_0}\,\tfrac{1}{2\omega_J}\,\mathrm{Re}\left[Z_\omega(\omega_J)\right]
\end{aligned} \tag{I.3}$$

Before pushing this expansion further, note that this equation already highlights the non-linear effect of the Josephson junction: There is a generation of a DC signal and a second harmonic from a ω_J-oscillating superconducting phase.

[3] If a time at which the u_N is settled is introduced, u_N becomes proportional to an Heaviside distribution and α is the summation of vacuum quantum fluctuations before this time, and consequently is fully arbitrary.

Now, using the third equation, $i_t^{(n+1)}$ is expressed similarly using $i_t^{(n)}$ and adding the hypothesis $Z_\omega(0)\, i_\omega(0) \ll \bar{\phi}_0 \omega_J$:

$$\begin{aligned} i_t^{(n+1)}(t) + i_0^{(n+1)} &= -\frac{I_c}{\bar{\phi}_0} \int_{-\infty}^{t} \mathrm{d}\tau \int_{\mathbb{R}} \mathrm{d}\tau' Z_t(\tau-\tau')\, i_t^{(n)}(\tau') \cos(\omega_J t + \alpha) \\ &= -\frac{I_c}{\bar{\phi}_0} \frac{1}{2\pi} \int_{\mathbb{R}} \mathrm{d}\omega \; Z_\omega(\omega)\, i_\omega^{(n)}(\omega) \int_{-\infty}^{t} \mathrm{d}\tau \; e^{-i\omega\tau} \cos(\omega_J t + \alpha) \\ i_t^{(n+1)}(t) + i_0^{(n+1)} &= \frac{I_c}{\bar{\phi}_0} \frac{1}{2\pi} \int_{\mathbb{R}} \frac{\mathrm{d}\omega}{2\omega} \; \mathrm{Im}\left[Z_\omega(\omega)\, i_\omega^{(n)}(\omega) \; e^{-i(\omega-\omega_J)t + i\alpha} \right] \\ &\quad + \mathrm{Im}\left[Z_\omega(\omega)\, i_\omega^{(n)}(\omega) \; e^{-i(\omega+\omega_J)t - i\alpha} \right] \end{aligned} \tag{I.4}$$

The interpretation of this relation is straightforward: A first current oscillating at Josephson frequency ω_J generates a DC current and a current at frequency $2\omega_J$, each of them generates two currents, one at a frequency increased by ω_J and one at a frequency decreased by ω_J, and so on. Figure I.2 shows a diagrammatic picture of those successive current generations.

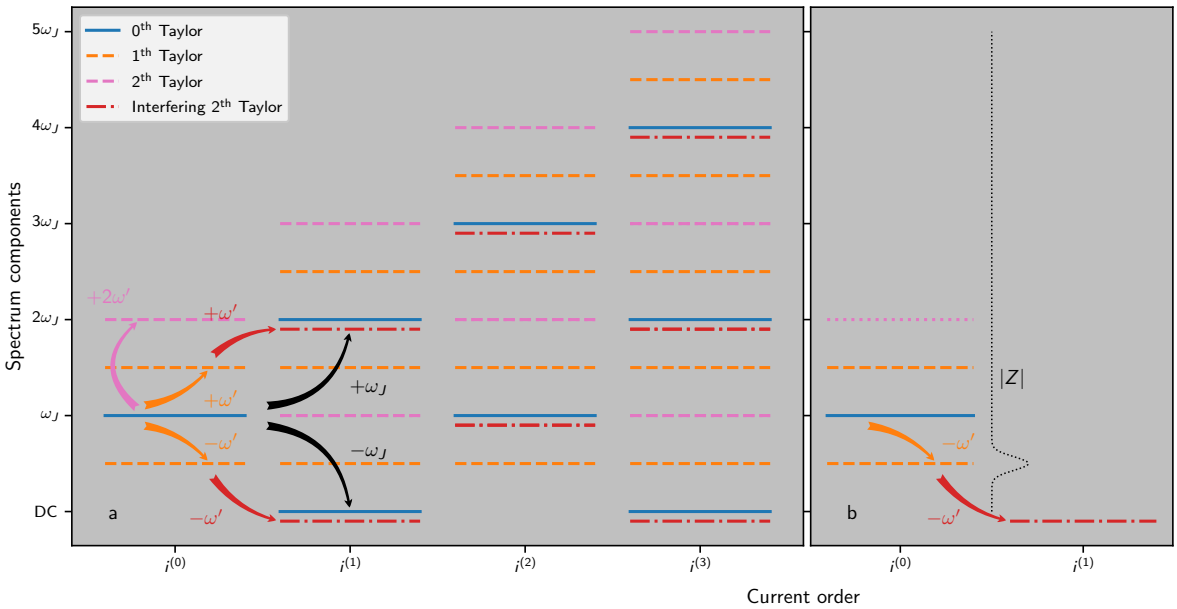

Figure I.2: **Diagrammatic representation of current harmonics** each line is a component of the spectrum as a function of the frequency in ordinate, the abscissa corresponds to successive iterations obtained with equation I.1. The full current is the sum of all currents $\sum_n i_\omega^{(n)}$. ***Panel a,*** solid blue lines and black arrows correspond to the single photon generation according to equation I.4, in particular $i_\omega^{(0)}$ oscillates at ω_J (most left solid blue line) and generates (downwards black arrow) a DC current (bottom left solid blue line). Dotted lines correspond to higher (Taylor) orders of $\sum_n i_\omega^{(n)}$ with a noise source at $\omega_J/2$ and explain multi-photon generation according to equation I.5. In particular, with this noise, first order Taylor expansion of $i_\omega^{(0)}$ oscillates at $\omega_J - \omega_J/2 = \omega_J/2$ (bottom left dotted orange line) and $i_\omega^{(1)}$ includes a term resulting from interference between $i_\omega^{(0)}$ and the noise at $\omega_J/2$, at second order Taylor expansion it gives a DC component: $[\omega_J/2]_{\text{noise}} + [\omega_J/2]_{i_\omega^{(0)}} - [\omega_J]_{\text{source}} = 0$. ***Panel b,*** shows which processes are preserved for a particular shape of Z where impedance is high at frequency $\omega_J/2$. In equation I.5, $i_\omega^{(0)}$ is non-negligible in $i_\omega^{(1)}$ only at frequencies where Z is high.

From an energetic point of view, at first order there are two components:

A flow of Cooper pairs: This flow gives rise to a DC current $i_0^{(1)}$ and is generated by a potential $\approx \bar{\phi}_0 \omega_J$. The instantaneous power is then $\frac{{I_c}^2}{2} \mathrm{Re}\left[Z_\omega(\omega_J)\right]$;

Energy dissipated by the electromagnetic environment: At first order, it results from the current $i_t^{(0)}$ oscillating at frequency ω_J, the resulting instantaneous power has two terms, a constant one $\frac{{I_c}^2}{2} \mathrm{Re}\left[Z_\omega(\omega_J)\right]$ and an oscillating one $-\frac{{I_c}^2}{2} \left|Z_\omega(\omega_J)\right| \cos(2\omega_J t + 2\alpha - \mathrm{Arg}\left[Z_\omega(\omega_J)\right])$.

Finally these balanced powers can be interpreted as particles from a flow of Cooper pairs giving their energies to an oscillating field at ω_J, i.e. photons. Moreover, as the energy of Cooper pairs tunnelling

through a Josephson junction biased at $\bar{\phi}_0\omega_J$ is $\hbar\omega_J$ and the energy of photons at ω_J is also $\hbar\omega_J$, this process can be seen as each Cooper pair producing one photon[4]. Note that as there are also fields oscillating at higher harmonics (see figure I.2) there are also processes where n Cooper pairs give one photon at frequency $n\omega_J$, but there are no processes where one Cooper pair gives several photons.

Multi-photon generation

Now, the noise source u_N is added back in. To highlight its influence, let's consider the simple case where $u_N \equiv u_0\, e^{i\omega' t} + \text{h.c.}$. The Kirchhoff's laws with this added source imply:

$$i_t(t) = I_c \sin\left(\omega_J t + \alpha - \frac{1}{\bar{\phi}_0}\underbrace{\left(\int_{-\infty}^{t} Z_t * i_t - \frac{1}{\omega'}\left[i u_0\, e^{i\omega' t} + \text{h.c.}\right]\right)}_{\delta\phi}\right) \tag{I.5}$$

Using complex notation, the Taylor expansion can be rewritten as:

$$i_t(t) = \frac{I_c}{2}\left[-e^{i\omega_J t + i\alpha}\sum_n \frac{(-i)^n}{n!}\left(\frac{\delta\phi}{\bar{\phi}_0}\right)^n + \text{h.c.}\right] \tag{I.6}$$

In the expression of $i_t^{(0)}(t)$, $\delta\phi$ has only one component at frequency ω' of amplitude $\propto u_0$. The $(n-1)^{\text{th}}$ order – n will be the number of photons involved – of the Taylor expansion in $\delta\phi$ gives rise to oscillating fields[5] at frequencies $\omega_J \pm (n-1)\omega'$. Their complex amplitudes are respectively $\propto u_0^{n-1}/(n-1)!$ and $\propto u_0^{*,n-1}/(n-1)!$.

If one of them oscillates at ω', i.e. $\omega_J = n\omega'$[6], in the expression of $i_t^{(1)}(t) + i_0^{(1)}$, the component at frequency ω' of $\delta\phi$ is a sum of two amplitudes $\propto u_0$ and $\propto u_0^{*,n-1}/(n-1)!$. And so the n^{th} order of the Taylor expansion results now in a DC component $\propto \left|u_0^{n-1}/(n-1)!\right|^2$.

For $n = 1$ the previous analysis is recovered: A process where one Cooper pair gives its energy to one photon. When $\omega_J = n\omega'$, as before there is an equality between DC and RF powers:

- **A flow of Cooper pairs:** This flow has an intensity $i_0^{(1)} \propto \left|\frac{u_0^{n-1}}{(n-1)!}\right|^2$ and is generated by a potential $\approx \bar{\phi}_0\omega_J$, each Cooper pair energy is $h\omega_J$;
- **Energy dissipated by the electromagnetic environment:** It results from the current $i_t^{(0)}(t) \propto \frac{u_0^{*,n-1}}{(n-1)!}\, e^{i\omega' t} + \text{h.c.}$ oscillating at frequency ω', each photon energy is $h\omega'$.

Energy conservation, as $\omega_J = n\omega'$, corresponds to a process where one Cooper pair gives n photons at frequency ω'.

Note that voltage fluctuations at ω' create current fluctuations at the same frequency, i.e. the junction behaves, at first order, as a linear admittance Y_{ω,J^*}. Moreover, as the junction is a source of energy, the real part of this admittance can be negative.

Dissipated power

The first noise source u_N is a direct consequence of the *Fluctuation-Dissipation Theorem* (FDT) [*Kubo66*]: a linear dissipative impedance is ultimately noisy (described by a voltage source in series), moreover the spectrum of this source is fully determined by the dissipative part of the electromagnetic linear environment $\text{Re}[Z_\omega]$.

[4] It can also be n Cooper pairs giving n photons, however n can be reduced to 1 because processes involving fewer particles are more probable.

[5] $i_t^{(0)}(t)$ also encompasses DC components, however they are $\propto u^n$ or $\propto u^{*,n}$ and if u_N is a noise the mean values are 0.

[6] This condition is also the one of Shapiro steps, which are recovered if $Z_t \equiv 0$ in equation I.5, see [*Shapiro63*; *Tinkham04*].

The second noise source i_ω is not the fluctuation over the junction admittance is a consequence of the AC Josephson effect giving rise to a DC current and an additional noise. Note also that, as shown below, this noise encompasses the usual shot noise [*Frey17*].

Applying Kirchhoff's laws, the current flowing through Z_ω is:

$$\frac{i_\omega + Y_{\omega,J}\left(u_N - u_{\text{source}}\right)}{1 - Y_{\omega,J} Z_\omega} \tag{I.7}$$

In the low junction admittance limit, $Y_{\omega,J} Z_\omega \ll 1$, the power dissipated in the electromagnetic environment is :

$$\gamma_\omega \equiv \text{Re}\left[Z_\omega\right] S_{\omega,i_t i_t} \tag{I.8}$$

where $S_{\omega,i_t i_t} \equiv |i_\omega|^2$ is the current PSD. This formula does not give insights about the nature of the dissipation: It can be in the form of phonons or photons for example.

As shown, this dissipated power is strongly related to the noise over the dissipative linear environment. At first sight this noise is purely thermal noise; however at low temperature quantum fluctuations become important [*Kubo66*]. To address then, a quantum model of the ICPT has to be introduced.

1.b ICPT Hamiltonian description

To go further, the noise voltage source u_N is characterised by the FDT ([*Kubo66*] & equation A.13), via the following relation between the flux auto-correlation function $\Gamma_{t,\phi\phi}$, and the dissipative part of the electromagnetic environment $\text{Re}\left[Z_\omega\right]$:

$$\mathcal{S}\left[\Gamma^\beta_{t,\phi\phi}\right](t) = \frac{1}{2\pi} \int_{\mathbb{R}} \underbrace{\frac{2\hbar\,\text{Re}\left[Z_\omega(\omega)\right]}{\omega} \coth\left(\frac{\beta\hbar\omega}{2}\right)}_{\mathcal{S}[S_{\omega,\phi\phi}](\omega)\ \text{Symmetrised PSD}} e^{-i\omega t}\,\mathrm{d}\omega \tag{I.9}$$

With:

- β**:** The thermodynamic temperature, when used as superscript means that the superscripted quantity is taken at thermal equilibrium;
- $\Gamma_{t,\phi\phi}$**:** The flux auto-correlation function defined as $\Gamma_{t,\phi\phi}(t,\tau) \equiv \left\langle \phi^\dagger(t+\tau)\,\phi(t)\right\rangle = \left\langle \phi(t+\tau)\,\phi(t)\right\rangle$, the t-dependence vanishes if the process is stationary and ergodic[7];
- $\mathcal{S}\left[\Gamma^\beta_{t,\phi\phi}\right]$**:** The symmetrised auto-correlation function, i.e. $\mathcal{S}\left[\Gamma^\beta_{t,\phi\phi}\right] \equiv \Gamma^\beta_{t,\phi\phi} + \mathcal{T}\left[\Gamma^\beta_{t,\phi\phi}\right]$ where $\mathcal{T}[f](t) \equiv f(-t)$ is the time reversal operator.

This noise includes thermal noise as well as quantum fluctuations.

System & drive model

First, let's consider the following Hamiltonian [*Ingold92*; *Leppäkangas14*a; *Mora17*]:

$$\mathcal{H}_{\text{tot}} \equiv \mathcal{H}_{\text{env}} + \underbrace{\left\{\kappa_t(t)\,\mathcal{H}_\kappa(\phi) + \mathfrak{h.c.}\right\}}_{\mathcal{H}_{\text{drive}}} \tag{I.10}$$

Here, $\mathcal{H}_{\text{env}}$ contains all the reservoirs: both electrodes of the Josephson junction and the electromagnetic environment bath. ϕ is the overall branch flux across the environment, it is the only degree of freedom of interest for that description. The remaining $\mathcal{H}_{\text{drive}}$ is the energy of interaction and depends only on ϕ and t. It is a generalisation of the previous model:

- $\kappa_t(t)$**:** The time dependence is used to model the evolution of the junction phase created by u_{source}. As this source is DC, a classical description is sufficient;

[7] This hypothesis is assumed further on.

$\mathcal{H}_\kappa(\phi)$**:** This term models how the Josephson junction affects the electromagnetic environment through the degree of freedom ϕ. For example the explicit form, $\mathcal{H}_\kappa(\phi) \equiv -\hbar\phi_0 I_c\, e^{-i\frac{\phi}{\hbar\phi_0}}$ used afterwards, corresponds to the usual Josephson junction Hamiltonian.

Figure I.3 shows how this Hamiltonian maps on to the general description shown in figure I.1

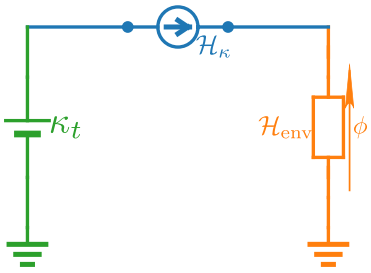

Figure I.3: **General description of our samples and semi-classical model.** The Josephson junction (in blue) and its bias (in green) are modelled by $\mathcal{H}_{\text{drive}} \equiv \kappa_t(t)\,\mathcal{H}_\kappa(\phi) + \text{h.c.}$, time-dependence is the source of energy, electromagnetic environment (in orange) is modelled by $\mathcal{H}_{\text{env}}$ and coupled though the degree of freedom ϕ.

The instantaneous energy of the system is $\mathcal{H}_{\text{env}}$ and consequently the instantaneous power received by the system is [*Leppäkangas14*a; *Mora17*]:

$$\begin{aligned}
\partial_t \mathcal{H}_{\text{env}} &\underbrace{=}_{\text{Heisenberg eq. } \mathcal{H}_{\text{env}}} \frac{1}{i\hbar}\overbrace{[\mathcal{H}_{\text{env}}, \mathcal{H}_{\text{tot}}]}^{[\mathcal{H}_{\text{tot}}-\mathcal{H}_{\text{drive}},\mathcal{H}_{\text{tot}}]} \\
&\underbrace{=}_{[\mathcal{H}_{\text{tot}},\mathcal{H}_{\text{tot}}]\,=\,0} \frac{1}{i\hbar}[-\mathcal{H}_{\text{drive}}, \mathcal{H}_{\text{tot}}] \\
&\underbrace{=}_{\text{Heisenberg eq. } -\mathcal{H}_{\text{drive}}} -\partial_t \mathcal{H}_{\text{drive}} + \{[\partial_t \kappa_t]\,\mathcal{H}_\kappa + \text{h.c.}\} \\
&= -\overbrace{\{\kappa_t \partial_t \mathcal{H}_\kappa + \text{h.c.}\}}^{\{\kappa_t \frac{1}{2}\{\partial_\phi \mathcal{H}_\kappa, \partial_t\phi\}+\text{h.c.}\}} - \{[\partial_t \kappa_t]\,\mathcal{H}_\kappa + \text{h.c.}\} \\
&\quad + \{[\partial_t \kappa_t]\,\mathcal{H}_\kappa + \text{h.c.}\} \\
\partial_t \mathcal{H}_{\text{env}} &= \frac{1}{2}\{-\partial_\phi \mathcal{H}_{\text{drive}}, \partial_t \phi\}
\end{aligned} \tag{I.11}$$

We can interpret this relation using a mechanical analogy given in table I.1 (see also table A.1 and [*Vool17*]). The RHS is the power associated to the force corresponding to the current defined as the conjugated quantity of the flux, i.e. $i_t \equiv -\partial_\phi \mathcal{H}_{\text{drive}}$.

Table I.1: Mechanical and cQED analogy

Mechanical picture	**cQED picture**
Position x	Flux ϕ
Velocity $\partial_t x$	$\partial_t \phi$
Additional potential energy $\mathcal{V}_x$	$\mathcal{H}_{\text{drive}}$
Driving force $-\partial_x \mathcal{V}_x$	Driving current $i_t \equiv -\partial_\phi \mathcal{H}_{\text{drive}}$
Resulting power $\frac{1}{2}\{-\partial_x \mathcal{V}_x, \partial_t x\}$	Power dissipated $\frac{1}{2}\{-\partial_\phi \mathcal{H}_{\text{drive}}, \partial_t \phi\}$

$G^{(1)}$ & PSD

So far, our model describes how energy is pumped from Cooper pairs tunnelling through a Josephson junction to an arbitrary linear electromagnetic environment. However, as described below (see also [*Roy18*]), such an environment can be described with IOT by a closed system coupled to a semi-infinite TL, see figure I.4. Following the conservation of energy, powers coming from the junction and going through the TL should be characterised in the same way as before.

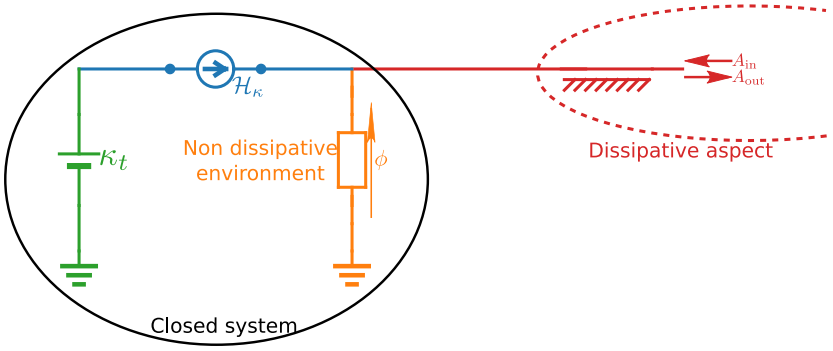

Figure I.4: **Previous quantum model with TL.** Now the electromagnetic environment is split in two, a non-dissipative part with the degree of freedom ϕ and the dissipation through a TL (in red).

Such a TL is defined by incoming and outgoing propagating wave amplitude operators $A_{\text{in/out}}$ and so the outgoing power is $A^\dagger_{\text{out}} A_{\text{out}}$. It corresponds to the value at $\tau = 0$ of the following correlation function:

$$G^{(1)}_{t,A_{\text{out}}}(\tau) \equiv \Gamma_{t,A_{\text{out}}A_{\text{out}}}(\tau) \equiv \left\langle A^\dagger_{\text{out}}(t+\tau)\, A_{\text{out}}(t) \right\rangle \tag{I.12}$$

This correlation function is hermitian symmetric, i.e. $G^{(1),*}_{t,A_{\text{out}}}(\tau) = G^{(1)}_{t,A_{\text{out}}}(-\tau)$ and consequently the PSD ($\gamma^{\text{out}}_\omega \equiv S_{\omega,A_{\text{out}}A_{\text{out}}}$) defined as the Fourier transform of $\mathcal{T}\left[\Gamma_{t,A_{\text{out}}A_{\text{out}}}\right]$ is purely real.

Following equation I.11, the power coming from the junction is also the i_t-$\partial_t\phi$ correlation, i.e. the force-velocity correlation (see table I.1) at $\tau = 0$. To have the same properties and be consistent with $G^{(1)}_{t,A_{\text{out}}}$, let's take its hermitian symmetrised form:

$$\begin{aligned} \tfrac{1}{2}\left\{\Gamma_{t,i_t\partial_t\phi} + \mathcal{T}\left[\Gamma_{t,i_t\partial_t\phi}\right]^*\right\} &= \tfrac{1}{2}\left\{\Gamma_{t,i_t\partial_t\phi} + \Gamma_{t,\partial_t\phi i_t}\right\} \\ &= \text{Re}\left[\chi_{t,\partial_t\phi i_t}\right] * \Gamma_{t,i_t i_t} \end{aligned} \tag{I.13}$$

Going to the frequency domain using the Fourier transform, the PSD is expressed as:

$$\begin{aligned} \gamma_\omega &= \tfrac{1}{2}\left\{S_{\omega,i_t\partial_t\phi} + S_{\omega,\partial_t\phi i_t}\right\} \\ &= \text{Re}\left[Z_\omega\right]\ S_{\omega,i_t i_t} \end{aligned} \tag{I.14}$$

Note that it assumes that the flux variation due to the driving current is negligible which is equivalent to $\chi_{\omega,\partial_t\phi i_t} = Z_\omega$ where $\chi_{\omega,\partial_t\phi i_t}$ is the response function.

Before going further and see how current and flux auto-correlation functions are linked, let's note that this PSD is consistent with equation I.8 presented in the simple classical model.

Josephson junction drive

We now focus on the case of an environment driven by a voltage biased Josephson junction. $\mathcal{H}_{\text{drive}}(t)$ is then $-\bar{\phi}_0 I_c \cos\left(\omega_J t + \alpha - \frac{\phi(t)}{\bar{\phi}_0}\right)$ [*Josephson62*; *Tinkham04*], i.e. $\kappa_t(t) \equiv e^{i\omega_J t + i\alpha}/2$ and $\mathcal{H}_\kappa(\phi) \equiv -\bar{\phi}_0 I_c\ e^{-i\frac{\phi}{\bar{\phi}_0}}$, and so:

$$i_t \equiv -\partial_\phi \mathcal{H}_{\text{drive}} = I_c \sin\left(\omega_J t + \alpha - \frac{\phi(t)}{\bar{\phi}_0}\right) \tag{I.15}$$

In view of equation I.14, let's focus on the i_t auto-correlation function at thermal equilibrium (β is the thermodynamic temperature):

$$\begin{aligned}
\Gamma^{\beta}_{t,i_t i_t}(\tau) &\equiv && \left\langle \dot{i}_t(t+\tau)\, i_t(t)\right\rangle_\beta \\
&= \frac{{I_c}^2}{4} e^{i\omega_J\tau} && \left\{ -\, e^{i2\omega_J t}\left\langle\, e^{i2\alpha}\right\rangle \left\langle\, e^{-i\frac{\phi(t+\tau)}{\bar\phi_0}}\; e^{-i\frac{\phi(t)}{\bar\phi_0}}\right\rangle_\beta + \left\langle\, e^{-i\frac{\phi(t+\tau)}{\bar\phi_0}}\; e^{i\frac{\phi(t)}{\bar\phi_0}}\right\rangle_\beta \right\} \\
&\quad + \frac{{I_c}^2}{4} e^{-i\omega_J\tau} && \left\{ +\left\langle\, e^{i\frac{\phi(t+\tau)}{\bar\phi_0}}\; e^{-i\frac{\phi(t)}{\bar\phi_0}}\right\rangle_\beta - \, e^{-i2\omega_J t}\left\langle\, e^{i2\alpha}\right\rangle \left\langle\, e^{i\frac{\phi(t+\tau)}{\bar\phi_0}}\; e^{i\frac{\phi(t)}{\bar\phi_0}}\right\rangle_\beta \right\} \\
\text{(equation C.6)} \quad &= \frac{{I_c}^2}{2} e^{J^\beta_{t,\phi/\bar\phi_0}(\tau)} && \cos(\omega_J\tau) \\
&\quad - \frac{{I_c}^2}{2} e^{-J^\beta_{t,\phi/\bar\phi_0}(\tau)} && \underbrace{\left\langle\cos\left(\omega_J(\tau+2t)+2\alpha\right)\right\rangle}_{0} \\
\Gamma^{\beta}_{t,i_t i_t}(\tau) &= \frac{{I_c}^2}{2}\cos(\omega_J\tau) && e^{J^\beta_{t,\phi/\bar\phi_0}(\tau)}
\end{aligned} \tag{I.16}$$

Where $J^\beta_{t,\phi/\bar\phi_0}(\tau) \equiv \Gamma^\beta_{t,\phi/\bar\phi_0\phi/\bar\phi_0}(\tau) - \Gamma^\beta_{t,\phi/\bar\phi_0\phi/\bar\phi_0}(0) = \left\langle[\phi(t+\tau)-\phi(t)]\,\phi(t)\right\rangle_\beta/\bar\phi_0^2$. In order to simplify notation, $\phi/\bar\phi_0$ subscripts and β superscripts will now be omitted.

This relation is the fundamental link between the current and flux auto-correlation functions. However, this expression is cumbersome to use because J is challenging to compute[8], moreover the FDT (see equation I.9) expresses the flux auto-correlation in frequency domain as the dissipative part of the electromagnetic environment. The next step, therefore, is to look at the PSD to reach a more pleasant relation.

Probability function P

In frequency domain, $S_{\omega,i_t i_t} \equiv \mathcal{F}_\omega\left[\mathcal{T}\left[\Gamma^\beta_{t,i_t i_t}\right]\right]$, equations I.14 and I.16 become (in ordinary frequency):

$$\begin{aligned}
\gamma_\nu(\nu_J,\nu) &= \overbrace{\frac{h{I_c}^2}{4}\mathrm{Re}\left[Z_\nu(\nu)\right]P(h\nu_J - h\nu)}^{\gamma_{\nu,\rightarrow}(\nu_J,\nu)} \\
&\quad + \underbrace{\frac{h{I_c}^2}{4}\mathrm{Re}\left[Z_\nu(\nu)\right]P(-h\nu_J - h\nu)}_{\gamma_{\nu,\leftarrow}(\nu_J,\nu)\,=\,\gamma_{\nu,\rightarrow}(-\nu_J,\nu)}
\end{aligned} \tag{I.17}$$

Where $hP(h\nu_J) \equiv \mathcal{F}_\nu\left[\, e^J\right](\nu_J)$.

An important property of P is the *Minnhagen equation* (see equation C.10 for derivation):

$$\nu_J P(h\nu_J) = \int_{\mathbb{R}} P(h\nu_J - h\nu)\;\frac{\mathrm{Re}\left[Z_\nu(\nu)\right]}{R_Q/2}\;\frac{1}{1-\, e^{-\beta h\nu}}\;\mathrm{d}\nu \tag{I.18}$$

This relation is a direct consequence of the FDT, it states the same result: Flux auto-correlation properties are fully determined by the electromagnetic environment $\mathrm{Re}\left[Z_\nu(\nu)\right]$ and the temperature. Moreover, this expression is easier to compute with iterative methods [*Ingold91*].

A brief interpretation of P can be made by recalling that there are only two sources of energy in our system:

Dissipative part of the environment: energy is added or removed in the form of photons of energy $h\nu$ entering or leaving the system via a TL;

DC biased Josephson junction: energy $\pm h\nu_J$ is added or removed when a Cooper pair tunnels from one electrode to the other.

[8] Divergence appears in analytic expressions.

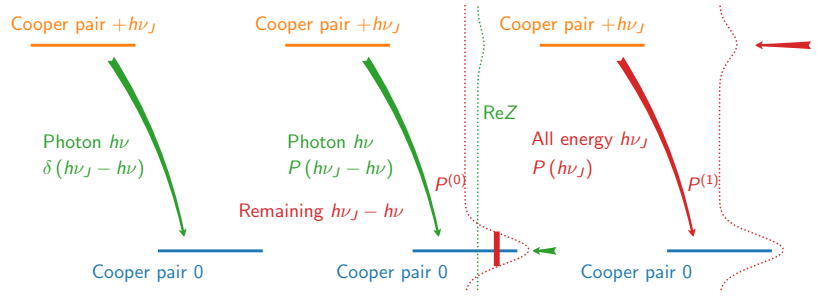

Figure I.5: P **for inelastic processes.** ***Left scheme:*** The usual Fermi golden rule. The Cooper pair can go from the high energy state $(+h\nu_J)$ to the low energy state (0) if interacting with a field oscillating at $\nu = \nu_J$. ***Centre scheme:*** Shows how the Fermi golden rule is update to include the mode width (green dotted line): $P^{(0)}$-function (dotted red line) substitutes δ, allowing the process to happen even if $\nu_J - \nu$ is non-zero. (0/1) are iterations of the Minnhagen equation. ***Right scheme*** shows that P-function can also be applied directly to the full energy $h\nu_J$: If this energy can be dissipated in the electromagnetic environment, $P(h\nu_J)$ is significant.

Therefore the argument of P is either the difference between a Cooper pair forward tunnelling through the junction and a photon leaving via a TL; or the sum of a Cooper pair backward tunnelling through the junction and a photon leaving via a TL. P can also be interpreted as a generalisation of the Fermi golden rule [*Ingold92*; *Grimm15*] (figure I.5 left panel), P being the inelastic counterpart of δ: A process involving unbalanced energy $h\nu_J - h\nu$ can still happen if the remaining energy can be balanced somehow (figure I.5 centre & right panel). This what P captures [*Nazarov13*]. Moreover, the process corresponding to the backward tunnelling is negligible compared to the forward tunnelling: $\gamma_{\nu,\leftarrow} \ll \gamma_{\nu,\rightarrow}$ (for ν, $\nu_J > 0$). Figure I.6 shows the resulting expression of $\gamma_\nu(\nu_J, \nu)$ depending on $\nu_J - \nu$ domain.

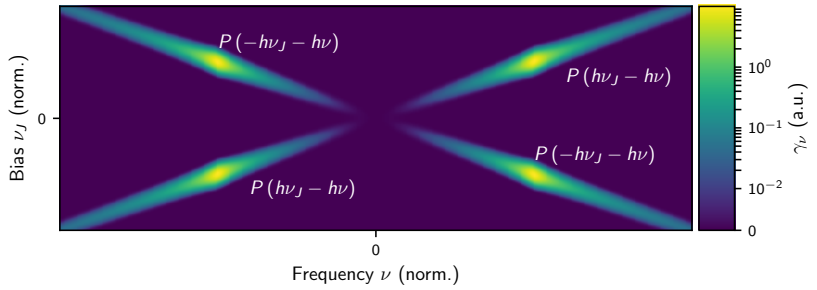

Figure I.6: **PSD quadrants** of a single mode resonator γ_ν, each quadrant is dominated by $P(h\nu_J - h\nu)$ or $P(-h\nu_J - h\nu)$ (in white). Vertical symmetry corresponds to reversing the bias, horizontal symmetry depends on the temperature: Negative frequencies correspond to absorption from the electromagnetic environments. At low temperature it is empty and subsequently no absorption can happen.

2 Relaxation through the environment

The P-theory developed so far cannot be applied when the system is far from thermal equilibrium. In particular an input electromagnetic field breaks the equilibrium. To deal with non-equilibrium case, IOT is now applied.

2.a Single mode resonator

First, let's deal with a single mode resonator in IOT. To do so, $\mathcal{H}_{\text{env}}$ is split in $\mathcal{H}_{\text{reso}}$ and $\mathcal{H}_{\text{damp}}$, the full Hamiltonian is:

$$\mathcal{H}_{\text{tot}} \equiv \underbrace{\mathcal{H}_{\text{reso}} + \mathcal{H}_{\text{damp}}}_{\mathcal{H}_{\text{env}}} + \mathcal{H}_{\text{drive}} \tag{I.19}$$

$\mathcal{H}_{\text{reso}}$: For a single mode, $\mathcal{H}_{\text{reso}} \equiv \hbar\omega_{\text{sys}} b^\dagger b$ with a mode impedance Z_{sys}, where b if the annihilation operator of the resonator[9];

[9] $\mathcal{H}_{\text{reso}}$ also includes an half photon, however it does not matter for equations of motion.

$\mathcal{H}_{\text{damp}}$**:** Figure I.7 shows how the model is updated for a single mode resonator; the term $\mathcal{H}_{\text{damp}}$ includes all dissipative elements.

Input output relation & impedance

The *Input Output* (IO) relations – under *Rotating Wave Approximation* (RWA) and Markov approximation – are then (see equations A.8 and B.12 and [*Walls08*; *Leppäkangas14*a; *Roy18*]):

$$\begin{aligned} i\hbar\partial_t b &= [b, \mathcal{H}^*] - i\hbar\tfrac{\kappa}{2} b - i\hbar\sqrt{\kappa} a_{\text{out}} \\ i\hbar\partial_t b &= [b, \mathcal{H}^*] + i\hbar\tfrac{\kappa}{2} b - i\hbar\sqrt{\kappa} a_{\text{in}} \end{aligned} \tag{I.20}$$

Where $a_{\text{in/out}}$ are the input and output annihilation operators of the TL. With:

κ**:** The coupling strength between the system and the TL, for a single mode resonator $\kappa \equiv \omega_{\text{sys}}/Q$ where Q is the usual quality factor[10];

$\mathcal{H}^* \equiv \mathcal{H}_{\text{reso}} + \mathcal{H}_{\text{drive}}$**:** The effective Hamiltonian. The influence of $\mathcal{H}_{\text{damp}}$ is taken into account by κ.

Note also that $A_{\text{in/out}} \simeq \sqrt{\hbar\omega_{\text{sys}}}\, a_{\text{in/out}}$ thanks to the RWA.

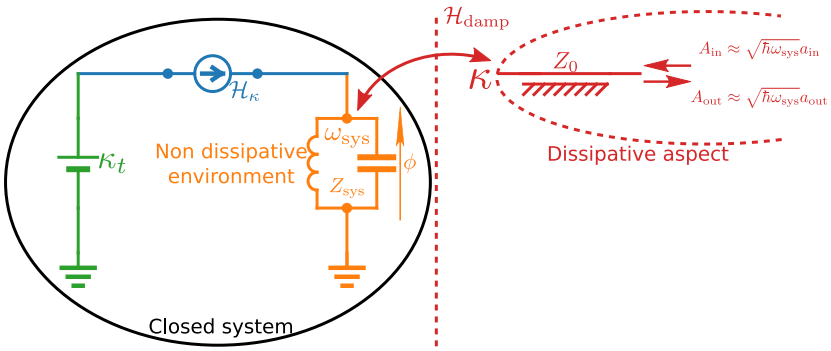

Figure I.7: **Single mode resonator model.** A special cas of the model figure I.4 where the non-dissipative part is restricted to a single mode resonator (LC circuit in orange) and the dissipative part is a TL coupled to the resonator with strength κ (in red).

In frequency domain equation I.20 are:

$$\begin{aligned} \hbar\omega_{\text{sys}} b \quad &+\chi_\omega^* \left\{ \hbar\omega_{\text{sys}} a_{\text{out}} + i\sqrt{Q\omega_{\text{sys}}}\, \mathcal{F}_\omega \left[[b, \mathcal{H}_{\text{drive}}] \right] \right\} = 0 \\ \hbar\omega_{\text{sys}} b \quad &-\chi_\omega \left\{ \hbar\omega_{\text{sys}} a_{\text{in}} + i\sqrt{Q\omega_{\text{sys}}}\, \mathcal{F}_\omega \left[[b, \mathcal{H}_{\text{drive}}] \right] \right\} = 0 \end{aligned} \tag{I.21}$$

Where $\chi_\omega^{-1}(\omega) \equiv i\sqrt{\frac{Q}{\omega_{\text{sys}}}} \left[\omega - \omega_{\text{sys}} - i\frac{\omega_{\text{sys}}}{2Q} \right]$ is the raw response function, describing how b is linearly governed by a_{in} neglecting the driving term. In particular the following relation holds:

$$a_{\text{out}} = a_{\text{in}} - \sqrt{\frac{\omega_{\text{sys}}}{Q}}\, b \tag{I.22}$$

It describes the evolution of IO operators knowing the evolution of the cavity field b, the first step of the scattering approach.

[10] $Q = 1/2$ discriminates the different regimes of damping; under-damped, critically damped and over-damped.

PSD

Before pushing futher the scattering approach, let's focus on the PSD. To do so, in view of equation I.21, the driving Hamiltonian gives:

$$\begin{array}{lll} [b, \mathcal{H}_{\text{drive}}] & \underbrace{=}_{b \equiv \sqrt{\frac{1}{2\hbar Z_{\text{sys}}}}(\phi + i Z_{\text{sys}} q)} & \sqrt{\frac{1}{2\hbar Z_{\text{sys}}}}\overbrace{[\phi, \mathcal{H}_{\text{drive}}]}^{0} + i\sqrt{\frac{Z_{\text{sys}}}{2\hbar}}\overbrace{[q, \mathcal{H}_{\text{drive}}]}^{-i\hbar\partial_\phi \mathcal{H}_{\text{drive}}} \\ [b, \mathcal{H}_{\text{drive}}] & \underbrace{=}_{i_t \equiv -\partial_\phi \mathcal{H}_{\text{drive}}} & -\sqrt{\frac{\hbar Z_{\text{sys}}}{2}}\, i_t \end{array} \tag{I.23}$$

The link between the photonic dynamics and the driving current shown with the classical picture is recovered here. Together with equation I.22:

$$a_{\text{out}} \;=\; -\frac{\chi_\omega}{\chi_\omega^*}\, a_{\text{in}} + i\sqrt{\frac{Z_{\text{sys}}}{2\hbar}}\, \chi_\omega\, i_\omega \tag{I.24}$$

Now, let's take a look at the hypothesis of an input field smaller than the driving term. The condition[11] is $|a_{\text{in}}| \;\ll\; 2\sqrt{Q/\omega_{\text{sys}}}\sqrt{Z_{\text{sys}}/2\hbar}\,|i_\omega|$. Under that assumption, implying $a_{\text{out}} \;=\; i\sqrt{Z_{\text{sys}}/2\hbar}\chi_\omega i_\omega$, the output PSD is:

$$\begin{array}{lllll} \gamma_\omega^{\text{out}}(\omega_J, \omega) & = & & & S_{\omega, A_{\text{out}} A_{\text{out}}}(\omega) \\ & \underbrace{\simeq}_{a_{\text{out}} \simeq \sqrt{\hbar\omega_{\text{sys}}} A_{\text{out}}} & & \hbar\omega_{\text{sys}} & S_{\omega, a_{\text{out}} a_{\text{out}}}(\omega) \\ & \underbrace{\simeq}_{a_{\text{out}} = \sqrt{\frac{Z_{\text{sys}}}{2\hbar}}\chi_\omega i_\omega} & 2 & \frac{\omega_{\text{sys}} Z_{\text{sys}}}{4}\left|\chi_\omega(\omega)\right|^2 & S_{\omega, i_t i_t}(\omega) \\ & \simeq & 2 & \frac{Q Z_{\text{sys}}}{4(Q/\omega_{\text{sys}})^2}\left|\frac{1}{\omega - \omega_{\text{sys}} - i\omega_{\text{sys}}/2Q}\right|^2 & S_{\omega, i_t i_t}(\omega) \\ \gamma_\omega^{\text{out}}(\omega_J, \omega) & \simeq & 2 & \text{Re}\left[Z_\omega(\omega)\right] & S_{\omega, i_t i_t}(\omega) \end{array} \tag{I.25}$$

Using the P function introduced above (see equation I.17), in ordinary frequency:

$$\gamma_\nu^{\text{out}}(\nu_J, \nu) \;\simeq\; \overbrace{\frac{h I_c{}^2}{2}\,\text{Re}\left[Z_\nu(\nu)\right] P(h\nu_J - h\nu)}^{\gamma_{\nu,\to}^{\text{out}}(\nu_J,\nu)} \tag{I.26}$$

2.b Scattering matrix

Classical description

As seen previously from the noise due to the electromagnetic environment, the circuit is seen – at first order – as a linear admittance Y_{ω, J^*}. Figure I.8 shows how the circuit is reduced to this single linear admittance.

This picture is very simple; together with the linear admittance introduced earlier, there is a TL of impedance $Z_0 \;>\; 0$ from which sends Johnson-Nyquist noise as well as microwave signals to the circuit. With $i_{\omega,\text{in/out}}$, $u_{\omega,\text{in/out}}$ the incoming and outgoing currents and voltages in frequency domain in the TL, Kirchhoff's and Ohm's laws give:

- $u_{\omega,\text{in}} \;=\; Z_0 i_{\omega,\text{in}}$

[11] It requires a norm, however as this condition is not pushed further, giving an explicit norm is not useful. $|O| \;\equiv\; \sqrt{\langle O^\dagger O\rangle}$ is a candidate.

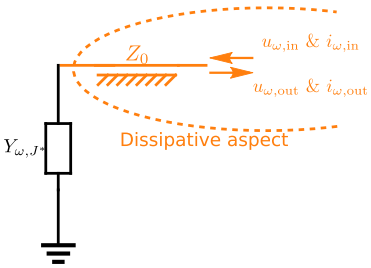

Figure I.8: **Reduced model** where Josephson junction, bias and non-dissipative part are reduced to a linear admittance which can have negative values. The input field is then reflected by this admittance and can even be amplified when it is negative.

- $u_{\omega,\text{out}} = Z_0 i_{\omega,\text{out}}$
- $i_{\omega,\text{in}} - i_{\omega,\text{out}} = Y_{\omega,J^*}\left(u_{\omega,\text{in}} + u_{\omega,\text{out}}\right)$

Then, the reflection coefficient is:

$$r \equiv \frac{u_{\omega,\text{out}}}{u_{\omega,\text{in}}} = \frac{1 - Z_0\, Y_{\omega,J^*}}{1 + Z_0\, Y_{\omega,J^*}} \tag{I.27}$$

Looking at this coefficient in power, it results in a gain:

$$G \equiv |r|^2 = 1 - \frac{4 Z_0\, \text{Re}\left[Y_{\omega,J^*}\right]}{\left|1 + Z_0\, Y_{\omega,J^*}\right|^2} \tag{I.28}$$

$\text{Re}\left[Y_{\omega,J^*}\right] < 0$ gives rise to amplification.

Quantum description

We now give the quantum description of such a reflection amplifier. A key aspect of the linear scattering theory is that a (bosonic) field can be amplified only if at least one supplementary mode is involved [*Caves82*][12]. To push our development further, a second single mode resonator is introduced, the flux through the environment is then:

$$\phi \equiv \underbrace{\sqrt{\frac{\hbar Z_{\text{sys}}^{(0)}}{2}}\left(b^{(0)\dagger} + \text{h.c.}\right)}_{\phi^{(0)}} + \underbrace{\sqrt{\frac{\hbar Z_{\text{sys}}^{(1)}}{2}}\left(b^{(1)\dagger} + \text{h.c.}\right)}_{\phi^{(1)}} \tag{I.29}$$

We give here only a brief overview[13] of the derivation of the quantum IO relation. For a general derivation see [*Clerk10*], derivations applied to superconducting circuits are shown [*Devoret16*; *Jebari17*]. To describe amplification we focus on the quadratic part of the form $b^{(0)} b^{(1)}$ (or h.c.) of $\mathcal{H}_{\text{drive}}$:

$$\begin{aligned}
\mathcal{H}_{\text{drive}}(t) &\equiv -\bar{\phi}_0 I_c \cos\left(\omega_J t - \tfrac{\phi(t)}{\bar{\phi}_0}\right) \\
&= -\tfrac{\bar{\phi}_0 I_c}{2}\left\{ e^{i\omega_J t}\, e^{-i\phi^{(0)}(t)/\bar{\phi}_0}\, e^{-i\phi^{(1)}(t)/\bar{\phi}_0} + \text{h.c.}\right\} \\
\mathcal{H}_{\text{drive}}(t) &\simeq \underbrace{\hbar \frac{I_c}{4\bar{\phi}_0}\sqrt{Z_{\text{sys}}^{(0)} Z_{\text{sys}}^{(1)}}}_{Q^*\sqrt{\frac{\omega_{\text{sys}}^{(0)}}{Q^{(0)}}\frac{\omega_{\text{sys}}^{(0)}}{Q^{(0)}}}}\left\{ e^{i\omega_J t} b^{(0)}(t) b^{(1)}(t) + \text{h.c.}\right\}
\end{aligned} \tag{I.30}$$

Where $Q^*\sqrt{\frac{\omega_{\text{sys}}^{(0)}}{Q^{(0)}}\frac{\omega_{\text{sys}}^{(0)}}{Q^{(0)}}} \in \mathbb{R}$ is called the pump power, expressed in ordinary frequency.

[12] The key argument is preservation of CCR when $b_{\text{out}}^{(n)} = \sum_m t_m^n b_{\text{in}}^{(m)}$.

[13] Only the amplification case is derived, conversion is recovered with $b^{(0)} b^{(1)\dagger}$ (or h.c.).

The input relation of equation I.21 becomes:

$$\begin{Bmatrix} b^{(0)}(\omega) & -\chi_\omega^{(0)}(\omega) & \left\{ a_{\text{in}}(\omega) + iQ^* \sqrt{\frac{\omega_{\text{sys}}^{(1)}}{Q^{(1)}}}\, b^{(1)}(\omega_J-\omega)^\dagger \right\} &= 0 \\ b^{(1)}(\omega_J-\omega)^\dagger & -\chi_\omega^{(1)}(\omega_J-\omega)^* & \left\{ a_{\text{in}}(\omega_J-\omega)^\dagger - iQ^* \sqrt{\frac{\omega_{\text{sys}}^{(0)}}{Q^{(0)}}}\, b^{(0)}(\omega) \right\} &= 0 \end{Bmatrix}$$

$$b^{(0)}(\omega) = \chi_\omega^{(0)}(\omega) \frac{a_{\text{in}}(\omega) + iQ^* \overbrace{\sqrt{\omega_{\text{sys}}^{(1)}/Q^{(1)}}\chi_\omega^{(1)}(\omega_J-\omega)^*}^{\widehat{\chi_\omega}^{(1)}(\omega_J-\omega)^*} a_{\text{in}}(\omega_J-\omega)^\dagger}{1 - Q^* \underbrace{\sqrt{\omega_{\text{sys}}^{(0)}/Q^{(0)}}\chi_\omega^{(0)}(\omega)}_{\widehat{\chi_\omega}^{(0)}(\omega)} \; Q^* \underbrace{\sqrt{\omega_{\text{sys}}^{(1)}/Q^{(1)}}\chi_\omega^{(1)}(\omega_J-\omega)^*}_{\widehat{\chi_\omega}^{(1)}(\omega_J-\omega)^*}} \tag{I.31}$$

Where $\widehat{\chi_\omega}$ is a normalised[14] form of χ_ω. Together with equation I.22, it results in:

$$a_{\text{out}}(\omega_J;\omega) = \underbrace{\overbrace{\frac{\widehat{\chi_\omega}^{(0)}(\omega)/\widehat{\chi_\omega}^{(0)}(\omega)^* + Q^*\widehat{\chi_\omega}^{(0)}(\omega)\; Q^*\widehat{\chi_\omega}^{(1)}(\omega_J-\omega)^*}{Q^*\widehat{\chi_\omega}^{(0)}(\omega)\; Q^*\widehat{\chi_\omega}^{(1)}(\omega_J-\omega)^* - 1}}^{r(\omega_J,\omega)} a_{\text{in}}(\omega)}_{t(\omega_J,\omega)} \\ i\, Q^*\widehat{\chi_\omega}^{(1)}(\omega_J-\omega)^* \frac{1 + \widehat{\chi_\omega}^{(0)}(\omega)/\widehat{\chi_\omega}^{(0)}(\omega)^*}{Q^*\widehat{\chi_\omega}^{(0)}(\omega)\; Q^*\widehat{\chi_\omega}^{(1)}(\omega_J-\omega)^* - 1} a_{\text{in}}(\omega_J-\omega)^\dagger \tag{I.32}$$

Where $r(\omega_J,\omega)$ is the gain and $t(\omega_J,\omega)$ the trans gain between frequencies ω and $\omega_J-\omega$ responsible for the input added noise ($N(\omega_J,\omega)$) of the amplification process. From that relation, it is straightforward that this amplification process affects equally both quadratures[15], i.e. it is a phase preserving amplifier. Figure I.9 shows the *lollipop* representation used to picture the operation of an amplifier. The left panel shows the input field, the centre of the ellipsis is $\langle a_{\text{in}}\rangle$ and its radii are $\sqrt{\left\langle \left|\text{Re}\left[a_{\text{in}}\right] - \langle \text{Re}\left[a_{\text{in}}\right]\rangle\right|^2 \right\rangle}$ and $\sqrt{\left\langle \left|\text{Im}\left[a_{\text{in}}\right] - \langle \text{Im}\left[a_{\text{in}}\right]\rangle\right|^2 \right\rangle}$ along both axes representing the quadratures of the signal, the outer ellipsis on the right panel describes a_{out} after amplification.

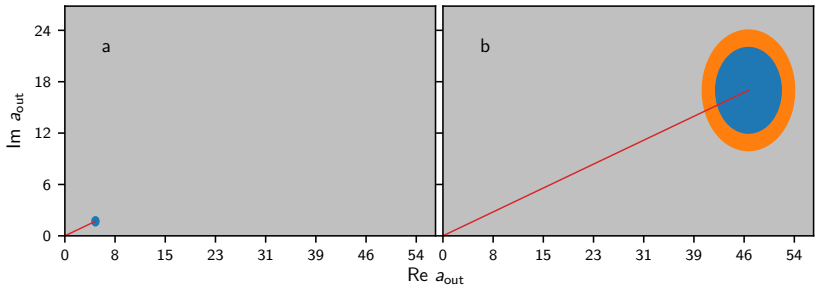

Figure I.9: **Lollipop picture** describing the behaviour of an amplifier. ***Panel a*** representing the field before amplification, centre of the lollipop is the complex amplitude of the field while its radii are variances. ***Panel b*** represents the field after amplification, the orange crown corresponds to the noise added by amplification.

Now, let $\omega \simeq \omega_{\text{sys}}^{(0)}$ and $\omega_J - \omega \simeq \omega_{\text{sys}}^{(1)}$, so that $\gamma_\omega^{\text{in}}(\omega) \simeq \hbar\omega_{\text{sys}}^{(0)} S_{\omega,a_{\text{in}}a_{\text{in}}}(\omega)$ and $\gamma_\omega^{\text{in}}(\omega_J-\omega) \simeq \hbar\omega_{\text{sys}}^{(1)} S_{\omega,a_{\text{in}}a_{\text{in}}}(\omega_J-\omega)$. In terms of power, amplification can then be described as:

$$\gamma_\omega^{\text{out}}(\omega_J,\omega) = \underbrace{G(\omega_J,\omega)}_{|r(\omega_J,\omega)|^2} \left[\gamma_\omega^{\text{in}}(\omega) + \underbrace{N(\omega_J,\omega)}_{\hbar\omega_{\text{sys}}^{(0)}\left(1+\gamma_\omega^{\text{in}}(\omega_J-\omega)/\hbar\omega_{\text{sys}}^{(1)}\right)|t(\omega_J,\omega)/r(\omega_J,\omega)|^2} \right] \tag{I.33}$$

This second term is responsible of the noise added by amplification, however does a minimal amount of noise exist?

[14] Maximum value is 2 and consequently $Q^* = 1/2$ is a particular value.
[15] For a phase-sensitive amplifier, both $a_{\text{in}}(\omega)$ and h.c. have to be implied.

Quantum-limited amplification

To answer this question we have to remember that IO fields are bosonic, i.e. they follow the usual *Canonical Commutation Relations* (CCR), and consequently: $|t(\omega_J,\omega)|^2 = |r(\omega_J,\omega)|^2 - 1 = G(\omega_J,\omega) - 1$. To simplify notation we define $\sqrt{G(\omega_J,\omega)-1}\, n(\omega_J,\omega)^\dagger \equiv t(\omega_J,\omega)\, a_{\text{in}}(\omega_J-\omega)^\dagger$. The CCR $\left[n, n^\dagger\right] \equiv 1$ is preserved, and allows us to derive[16] a bound value of the PSD [*Caves82*]:

$$\begin{aligned} S_{\omega,n^\dagger n^\dagger} &= \tfrac{1}{2}\langle\{\mathrm{Re}\, n, \mathrm{Re}\, n\}\rangle + \tfrac{1}{2}\langle\{\mathrm{Im}\, n, \mathrm{Im}\, n\}\rangle \qquad \underbrace{-i\langle[\mathrm{Re}\, n, \mathrm{Im}\, n]\rangle}_{\langle[n,n^\dagger]\rangle/2\,=\,1/2} \\ &= \tfrac{1}{2}\left(\sqrt{\langle\{\mathrm{Re}\, n, \mathrm{Re}\, n\}\rangle} - \sqrt{\langle\{\mathrm{Im}\, n, \mathrm{Im}\, n\}\rangle}\right)^2 + \underbrace{\sqrt{\langle\{\mathrm{Re}\, n, \mathrm{Re}\, n\}\rangle\langle\{\mathrm{Im}\, n, \mathrm{Im}\, n\}\rangle}}_{(\text{Uncertainty}) \,\geq\, |\langle[\mathrm{Re}\, n, \mathrm{Im}\, n]\rangle| \,=\, 1/2} + \tfrac{1}{2} \\ S_{\omega,n^\dagger n^\dagger} &\geq \tfrac{1}{2}\left(\sqrt{\langle\{\mathrm{Re}\, n, \mathrm{Re}\, n\}\rangle} - \sqrt{\langle\{\mathrm{Im}\, n, \mathrm{Im}\, n\}\rangle}\right)^2 \qquad +1 \end{aligned} \tag{I.34}$$

Straightforwardly, the equality holds only if n is a single mode, note also the equality implies that the two quadrature variances are equal, i.e. that the amplifier adds the same amount of noise on both quadratures. Figure I.9 shows which noise comes from this second mode (area between inner and outer ellipsis).

Finally, together with equation I.33 this fundamental limit becomes $N \geq \left|1 - G^{-1}\right| \hbar\omega_{\text{sys}}^{(0)}$, a more meaningful relation is the excess noise relative to the quantum limit $\epsilon \equiv N / \left|1 - G^{-1}\right| \hbar\omega_{\text{sys}}^{(0)}$. With the expression of N of equation I.33 where the idler input field (the one at $\omega_J - \omega$) is at thermal equilibrium $\gamma_\omega^{\text{in}}(\omega_J - \omega) \equiv \hbar\omega_{\text{sys}}^{(1)}(\coth(\beta\hbar(\omega_J-\omega)/2) - 1)/2$:

$$\epsilon = \frac{1}{2}\left[1 + \coth\left(\frac{\beta\hbar(\omega_J-\omega)}{2}\right)\right] \tag{I.35}$$

As $\omega_J - \omega \simeq \omega_{\text{sys}}^{(1)}$, the input added noise can be reduced by lowering the temperature or increasing the idler frequency. Figure I.10 shows how the noise evolves with temperature and the idler frequency.

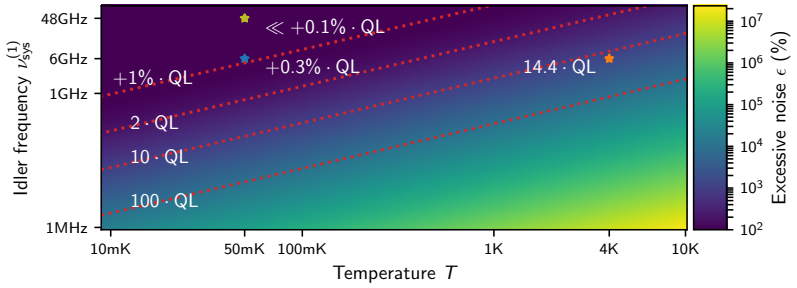

Figure I.10: **Excessive noise** expressed relatively to the quantum limit, as a function of the temperature and the idler frequency. Dotted lines identify remarkable values, coloured stars show working points of our devices (blue and yellow) and 4 K device (orange).

Moreover, using equation I.26, an explicit expression of the gain in quantum-limited amplification regime can be straightforwardly derived (in ordinary frequency):

$$G(\nu_J,\nu) \simeq 1 + \frac{1}{1+\coth(\beta(h\nu_J - h\nu)/2)} \frac{{I_c}^2}{\nu_{\text{sys}}^{(0)}} \mathrm{Re}\left[Z_\nu(\nu)\right] P(h\nu_J - h\nu) \tag{I.36}$$

Note however that equation I.26 and therefore this expression assume all modes are near thermal equilibrium, which implies a low gain.

Notes on the Caldeira-Leggett model

Let's discuss the Caldeira-Leggett model useful to going from our discrete modes to an arbitrary environment. Let's decompose the environment in many environments in series, see figure I.11, i.e. $Z_\omega = \sum_n Z_\omega^{(n)}$.

[16] The proof assumes $\langle n\rangle \equiv 0$ for sake of simplicity, the general case is recovered with $\Delta n \equiv n - \langle n\rangle$.

Straightforwardly the PSD due to the n^{th} environment is:

$$\gamma_\omega^{(n)} \;=\; \mathrm{Re}\left[Z_\omega^{(n)}\right]\; S_{\omega,i_t i_t} \tag{I.37}$$

Moreover, if all those environments are independent, i.e. $\left[\phi^{(n)},\phi^{(m)}\right] \;=\; 0$ where $\phi^{(n)}$ is the flux through the n^{th} environment (see figure I.11), then a couple $J^{(n)},\; P^{(n)}$ can be defined for each environment and thanks to theirs definitions:

$$\begin{aligned} J \;&=\; \sum_n J^{(n)} \\ P \;&=\; P^{(0)} * P^{(1)} * \dots \end{aligned} \tag{I.38}$$

The first equation is a direct consequence of Kirchhoff's laws for correlation functions when cross-correlations are negligible. The second one is consistent with our previous interpretation of P: The full P describes how the remaining energy can be dissipated through all the environments. With δ the remaining energy to dissipate as $\delta \;=\; \sum_n \delta^{(n)}$ where $\delta^{(n)}$ is dissipated through the n^{th} environment, all different remaining energy decomposition are captured as:

$$\begin{array}{cccccc} & & P^{(0)}\left(\delta_0^{(0)}\right) & & P^{(1)}\left(\delta_0^{(1)}\right) & \dots \\ & + & P^{(0)}\left(\delta_1^{(0)}\right) & & P^{(1)}\left(\delta_1^{(1)}\right) & \dots \\ & \dots & \text{Sum over all different decomposition} & & & \\ \hline P & = & P^{(0)} & & * P^{(1)} & * \dots \end{array} \tag{I.39}$$

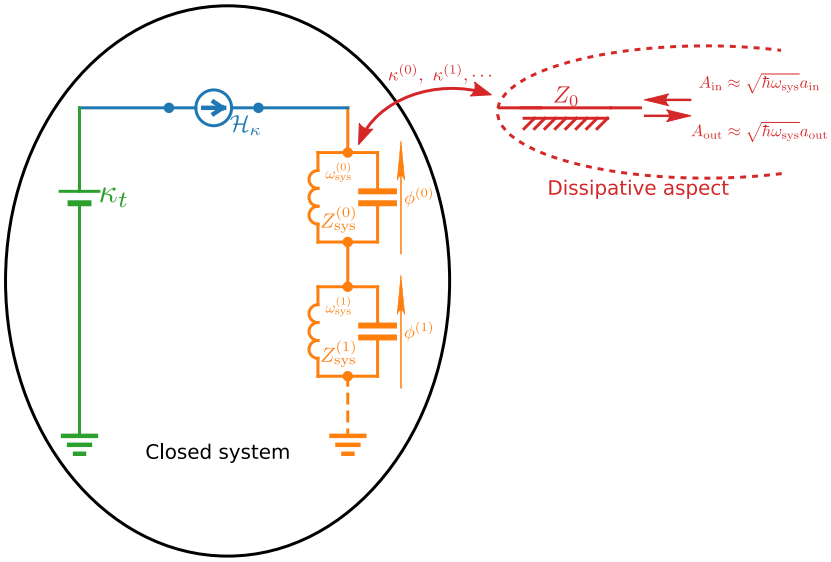

Figure I.11: **Many weak interacting environments model** extends the previous model figure I.7, now the single mode resonator is substituted with many resonators in series. Each of them has its frequency $\omega_{\text{sys}}^{(n)}$, impedance $Z_\omega^{(n)}$, flux $\phi^{(n)}$, couple $J^{(n)},\; P^{(n)}$ and coupling strength $\kappa^{(n)}$.

Now, the Caldeira-Leggett model [*Caldeira83*] states that an arbitrary electromagnetic environment can be decomposed into a set of single modes. The idea is that by reducing the dissipative element of such a single mode, $\mathrm{Re}\left[Z_\omega\right] \;\to\; \delta_{\omega\text{sys}}$. An arbitrary electromagnetic environment can be approximated by a set of Dirac peaks. They can subsequently be slightly enlarged to give a set of single modes (see figure I.12). Moreover, even if the electromagnetic environment is made of a set of single modes (for exemple with some LC circuits or quarter wave resonators), the Caldeira-Leggett decomposition does not necessary recover those modes: The decomposition is not unique.

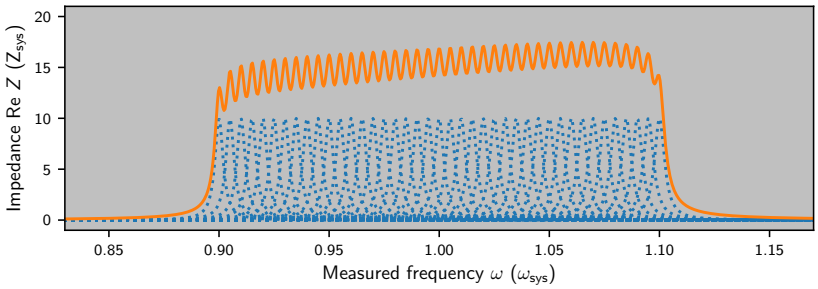

Figure I.12: **Example of Caldeira-Leggett decomposition** where many single mode resonators (in blue) results to a wideband mode with some ripples.

Conclusion

Apart from the classical picture used as a first simple approach, we have considered Josephson junctions using two descriptions:

P-theory: Where a P function describes how energies carried by tunnelling Cooper pairs can be dissipated by the electromagnetic environment;

IOT: Where the electromagnetic environment was reduced to one or a few some modes. It relates input and output field of the DC biased Josephson junction.

Moreover, those two descriptions are linked by a power balance.

However the two models cannot necessary be applied, P-theory requires an electromagnetic environment at thermal equilibrium and low critical current and cannot be applied with an input field. Conversely, IOT easily deals with IO fields and larger critical current, but can only be derived for simple models – like single mode resonators.

Chapter II

Experimental setup

French resume

Ce chapitre couvre l'ensemble des systèmes expérimentaux utilisés pour mesurer nos dispositifs : systèmes 4 K pour sélectionner les dispositifs les plus prometteurs; réfrigérateur à dilution He, son électronique; et aussi le support informatique développé pour mesurer et analyser les résultats.

4 K est une température aisé à atteindre en utilisant un bain He, de plus elle est assez basse pour estimer les propriétés des matériaux et structures – jonctions Josephson & résonateurs – de nos échantillons. Lorsqu'un échantillon est convenable, il est ensuite refroidit à 12 mK avec notre réfrigérateur à dilution He.

L'instrument de mesure principal utilisé à 12 mK est un numériseur ultrarapide (AlazarTech ATS9373) qui nous permet d'extraire les corrélations du champs microonde émis par l'échantillon [*daSilva10*]. Cette partie donnera des précisions théoriques et techniques sur cette méthode de mesure.

Une dernière partie décrira comment les mesures sont réalisées et analysées. Pour ce faire une architecture flexible a été développée en mintinlinepythonpython :

- Une structure de donnée compatible avec nos mesures actuelles et futures;
- Une structure de contrôle et des pilotes associés décrivant comment les mesures sont faites;
- Une GUI pour afficher nos données de manière compréhensible grâce à divers filtres.

Contents

1 Sample characterisation

Each wafer contains several hundred devices; in order to efficiently use the dilution fridge, electrical properties, that can be accessed without cooling down to 12 mK, are measured and compared with the expected values.

These measurements compromise:

- Room temperature measurements, to characterise the normal state properties;
- 4 K measurements with a He dipstick and 4 K to 300 K with a *Physical Property Measurement System* (PPMS), to characterise the NbN superconducting state properties.

1.a Room temperature measurements

For all room temperature measurements, we use a four point probe scheme. There are two ways for the current to flow in the trilayer, see figure II.1:

- Parallel to the trilayer, giving access to the sheet resistance, $R_\square$, of NbN;
- Perpendicular to the trilayer, giving access to the tunnelling resistance, R_T, through the MgO barrier.

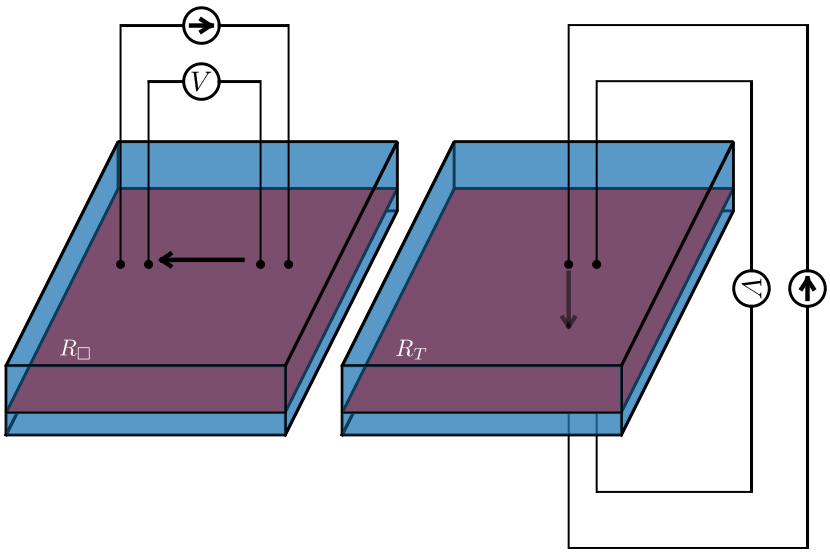

Figure II.1: **Currents flowing in a trilayer.** ***Left panel*** shows how current parallel to the trilayer is measured, the dark sheet is the barrier of the trialyer, the four wires show how current source and bias probe are setup to measure $R_\square$. ***Right panel*** shows how current though the barrier is measured and how R_T is measured.

The first one is measured a first time just after the trilayer is sputtered and before it is patterned at the centre of the wafer. For subsequent measurements, the fabrication process includes two useful features:

- Some technology dies including several structures used to monitor and check the fabrication process. Especially Hall bars and meanders that can be used to measure $R_\square$ of each layer after the fabrication process;

- Some structures are repeated on each die. They are designed to be used with a four point station, see figure II.2. At first there were only junctions with different sizes measured with those structures, giving R_T. In subsequent designs, other elements were added, giving also $R_\square$ for several layers.

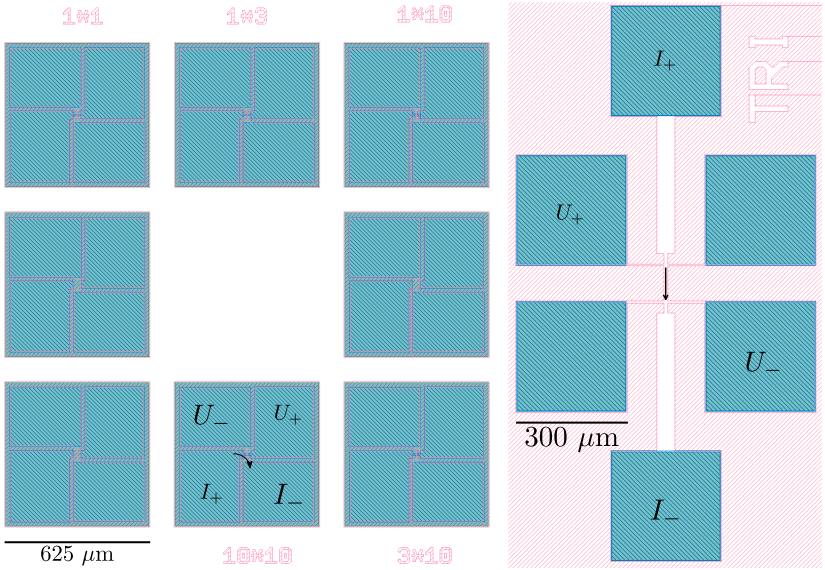

Figure II.2: **Four point probe scheme** for two test structures. ***Left panel*** are test structures at the centre of each chip. Josephson junctions of different sizes are connected between four pads to measure their characteristics, wiring is shown on the $10\times10\mu m^2$ junction. In future designs, similar structures will host other lumped elements to test – e.g. resistors. ***Righ panel*** is a structure of a chip dedicated to measuring quality of the process, it is a Hall bar, in particular it can be used to measure $R_\square$ with the wiring shown here.

Moreover, the junctions and test structures on each die show the homogeneity of the full process (see figure II.3). As expected, trilayer quality decreases from the centre to the edge due to the sputtering process over the wafer.

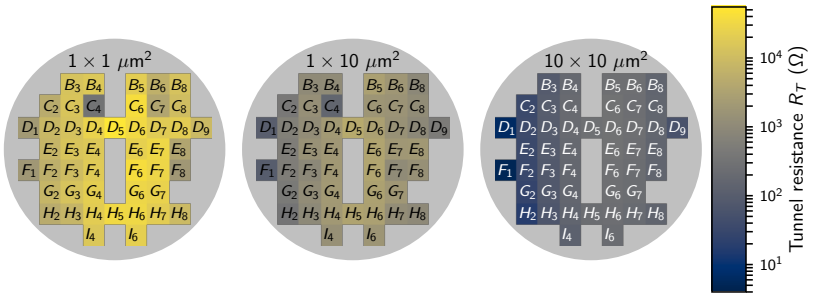

Figure II.3: **Homogeneity of junctions** is measured on each chip with a probe station. Here each plot show R_T for different junction sizes: $1\times1\mu m^2$, $1\times10\mu m^2$ & $10\times10\mu m^2$. Colour scale is the same for the three schemes. First there is a factor 10 between each plot corresponding to a factor 10 between areas. Moreover, an inhomogeneity is also observed towards the border of the wafer.

1.b He dipstick & PPMS

Even through the studied processes require a temperature well below 1 K, the critical temperature of NbN of around 16 K allows us to use a He bath at 4 K to access the superconducting properties of our samples. Two experimental setups are used:

- A simple dipstick to plunge the sample in a He bath. The sample is connected through RF coaxial cables;
- A PPMS, which measures only DC properties but does it with accurate temperature control from room temperature to 4 K.

The PPMS is used to measure the square resistance as a function of temperature, see figure II.4. From those data the *RRR* can be extracted.

Thanks to the He bath, current voltage characteristics of junctions are measured with an USB-1608GX-2AO analogue IO card. To do so, a slow triangular voltage bias is applied through a large resistor, i.e. the junction is current biased; and the voltage through the junction is measured after amplification, see figure II.5.

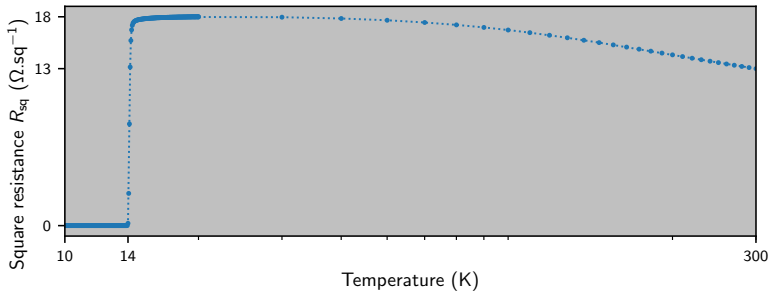

Figure II.4: **Square resistance as a function of the temperature** measured with the Hall bar. First the square resistance becomes 0 when the temperature is below the critical temperature of NbN, 14 mK. Second, ratio between resistance just above the critical temperature and at room temperature give $RRR = 13\,\Omega\text{sq}^{-1}/17\,\Omega\text{sq}^{-1} = 0.7$.

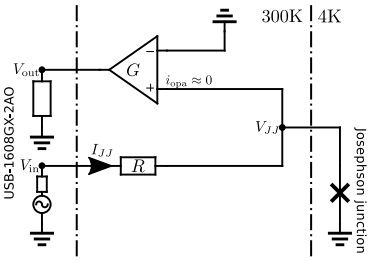

Figure II.5: **He bath and USB-1608GX-2AO setup** used to measure IV characteristics of Josephson junctions plunged in a He bath. The sample is current biased by a voltage source V_{in} over a large resistor R, and the effective voltage V_{JJ} over the junction is measured with an amplifier of gain G. USB-1608GX-2AO acquisition board is used to apply a triangular wave V_{in} and measure V_{out}.

Following the notation in figure II.5, voltage and current through the junction can be expressed as follows: $V_{JJ} = \frac{V_{out}}{G}$ and $I_{JJ} = \frac{V_{in} - V_{JJ}}{R}$. Moreover to compare the data from junctions with different sizes, junction currents are divided by junction areas resulting in current densities. Those results are shown in figure II.6.

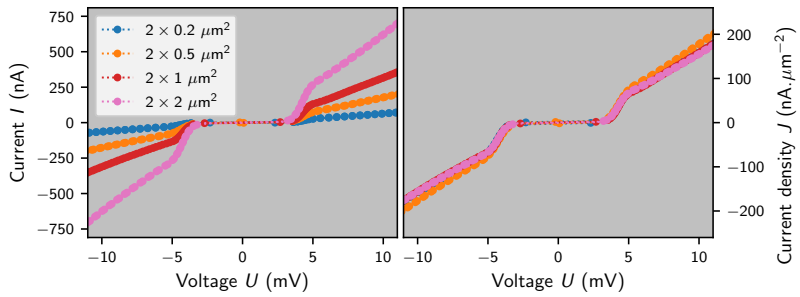

Figure II.6: **Current (densities) as functions of the voltage bias** for different junction size. Both panels show the same data. ***Left panel*** shows the current as a function of the voltage bias while ***right panel*** is the current density as a function of the voltage bias. First, the current scales properly with the expected junction size. Moreover, the current is close to zero below $|U| < 5$ mV, which corresponds to the excepted gap value of NbN Josephson junctions.

2 Low temperature setup

2.a General setup model

The most important goal of our setup is to determine fluctuations of the output field a_{out} at base temperature (generally $\simeq 12$ mK) thanks to a voltage measurement $u \equiv \sqrt{h\nu_0 \cdot 50\,\Omega/2}\left[ib^\dagger + \text{h.c.}\right]$ (where $\nu_0 > 0$ is the carrier frequency) through a 50 Ω matched acquisition channel at room temperature. A first order, such a channel can be modelled the same way as an amplifier, see figure II.7, in time domain:

$$b = r * [a_{\text{out}} + n] \tag{II.1}$$

First of all, our acquisition method has to give access to γ_ν^{out} and $G^{(1),\text{out}}$. Even through these two quantities are equivalent, a method to extract $G^{(1),\text{out}}$ can then be extended to measure photon correlations $G^{(2),\text{out}}(\tau) \equiv \left\langle a_{\text{out}}^\dagger(t)\, a_{\text{out}}^\dagger(t+\tau)\, a_{\text{out}}(t+\tau)\, a_{\text{out}}(t)\right\rangle$.

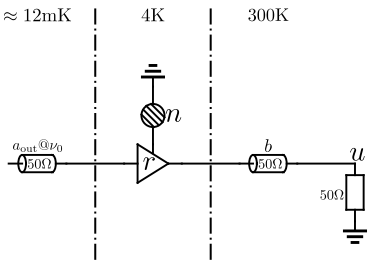

Figure II.7: **Acquisition channel – amplifier model.** There are three stages at 12 mK, 4 K & 300 K. The field to measured is generated at the 12 mK stage. It is amplified at the 4 K stage which adds noise n. Finally, the voltage is measured at the 300 K stage.

In-phase & quadrature (IQ) demodulation

A central aspect of our method is IQ demodulation [*daSilva10*]. Our technical realisation is described later, we focus here on its theoretical consequences.

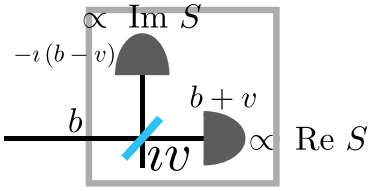

Figure II.8: **IQ demodulation – beam-splitter model.** The transmitted field is not dephased while the reflected field is dephased by $-\pi/2$. The second input field is written iv. On each arm, the voltage, i.e. the imaginary part of the field, is measured. In total both quadratures of a virtual field $S \equiv -i\left[b - v^\dagger\right]/\sqrt{2}$ (see text). The original figure comes from [*daSilva10*].

Figure II.8 shows how IQ demodulation is modelled: The output field is mixed with another field v thanks to a balanced beam-splitter and subsequently in-phase and quadrature components are measured (see technical details for how they are measured):

In-phase

$$I \equiv \frac{\sqrt{h\nu_0 \cdot 50\,\Omega}}{2}\left[i\,(v+b)^\dagger + \mathfrak{h.c.}\right] = \sqrt{\frac{h\nu_0 \cdot 50\,\Omega}{2}}\left[S^\dagger + \mathfrak{h.c.}\right] \tag{II.2}$$

Quadrature

$$Q \equiv \frac{\sqrt{h\nu_0 \cdot 50\,\Omega}}{2}\left[(v-b)^\dagger + \mathfrak{h.c.}\right] = \sqrt{\frac{h\nu_0 \cdot 50\,\Omega}{2}}\left[iS^\dagger + \mathfrak{h.c.}\right] \tag{II.3}$$

Where $S \equiv -i\left[b - v^\dagger\right]/\sqrt{2}$ is a self-commutating ($\left[S^\dagger, S\right] = 0$) virtual field. This property allows to write products without taking care of ordering, consistent with classical quantities.

Assuming v can be rewritten as $v \equiv r^* * v'$, putting it all together, the equation II.1 becomes:

$$S = \frac{-ir}{\sqrt{2}} * \left[a_{\text{out}} + \underbrace{n - v'^{,\dagger}}_{n'}\right] = \frac{I + iQ}{\sqrt{2h\nu_0 \cdot 50\,\Omega}} \tag{II.4}$$

As n contains the noise from the 4 K amplifier, it is the main source of noise and $n' \simeq n$.

PSD

The PSD is measured as follows $S_{\text{PSD}} \equiv \left\langle \left|\mathcal{F}_\nu\left[I + iQ\right]\right|^2 \right\rangle = 2h\nu_0 \cdot 50\,\Omega \left\langle \left|\mathcal{F}_\nu\left[S\right]\right|^2 \right\rangle$ (absolute value is unambiguous as S is self-commutating), consequently (derivation is straightforward):

$$S_{\text{PSD}} = \underbrace{2 \cdot 50\,\Omega \cdot \underbrace{\frac{|r|^2}{2}}_{G}}_{\chi_\nu}\left\{\gamma_\nu^{\text{out}} + h\nu_0 \underbrace{S_{\nu,n'n'}}_{N}\right\} \tag{II.5}$$

χ_ν is the full channel susceptibility in V^2/W; N the input added noise of the full channel as $\gamma_\nu^{\text{out}}/Nh\nu_0$ is the *Signal to Noise Ratio* (SNR).

Calibrating our setup requires determining both χ_ν & N. This linear problem with two unknown quantities is easily solved with two calibration points with well-known γ_ν^{out}. Experimentally, a 50 Ω load

thermalised at β is a well-known source[1]. For calibration we use so two loads at temperature β_{cold} & β_{hot}:

$$\begin{aligned} h\nu_0\chi_\nu &= 2\frac{S_{\text{PSD,hot}}-S_{\text{PSD,cold}}}{\coth(\beta_{\text{hot}}h\nu_0/2)-\coth(\beta_{\text{cold}}h\nu_0/2)} \\ N-\tfrac{1}{2} &= \frac{1}{h\nu_0\chi_\nu}\frac{\coth(\beta_{\text{hot}}h\nu_0/2)S_{\text{PSD,cold}}-\coth(\beta_{\text{cold}}h\nu_0/2)S_{\text{PSD,hot}}}{\coth(\beta_{\text{hot}}h\nu_0/2)-\coth(\beta_{\text{cold}}h\nu_0/2)} \end{aligned} \tag{II.6}$$

Moreover, if our sample can be turned off (i.e tuned to $\gamma_\nu^{\text{out}} \simeq 0$): $S_{\text{PSD,off}} \simeq h\nu_0\chi_\nu N$ and consequently:

$$\frac{\gamma_\nu^{\text{out}}}{h\nu_0} = \frac{S_{\text{PSD}}-S_{\text{PSD,off}}}{h\nu_0\chi_\nu} \tag{II.7}$$

If the two measurements are done in close succession, G & N do not vary and even if the gain subsequently varies, this calibration gives a quantity proportional to the PSD without any offset.

Cross PSD & $G^{(1)}$

An other way to handle the noise offset is to reduce it at its origin. This term comes from $S_{\nu,nn}$ that arises because of the amplifier noise of our channel and our measurement that correlates it with itself. Thus, to avoid it, it is sufficient to not perform this correlation: We measure the field S two times with two independent channels: $S_{\text{PSD,X}} \equiv 2h\nu_0 \cdot 50\,\Omega \left\langle \mathcal{F}_\nu\left[S_0\right]^\dagger \mathcal{F}_\nu\left[S_1\right]\right\rangle$. Figure II.9 shows this model and notation.

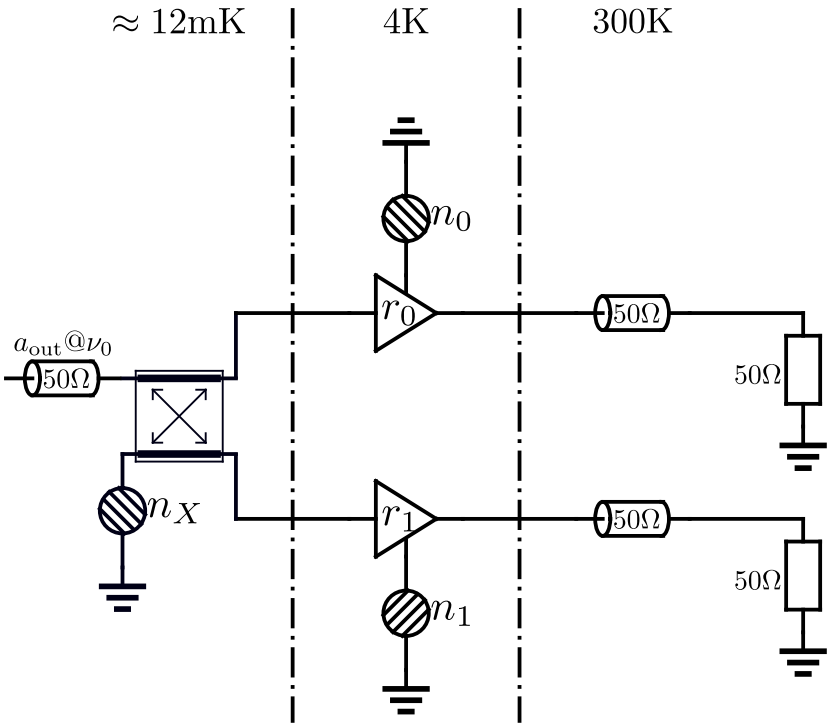

Figure II.9: **Acquisition dual channels – amplifiers model** includes two times the previous model thanks to a balanced beam-splitter placed just after the field to characterise. Compared to the previous model, correlations between amplifier noise $n_{0/1}$ vanish and only n_{X} remains.

Some algebra gives:

$$S_{\text{PSD,X}} = \underbrace{2\cdot 50\,\Omega\cdot \underbrace{\frac{r_0^* r_1}{2\cdot 2}}_{|G_{\text{X}}| = \sqrt{G_0 G_1}/2}}_{|\chi_{\nu,\text{X}}| = \sqrt{\chi_{\nu,0}\chi_{\nu,1}}/2} \left\{ \gamma_\nu^{\text{out}} + h\nu_0 \underbrace{\left[2S_{\nu,n_0' n_1'} - S_{\nu,n_{\text{X}} n_{\text{X}}}\right]}_{N_{\text{X}}} \right\} \tag{II.8}$$

[1] $\gamma_\nu^{\text{out}} = h\nu_0\left(\coth\left(\beta h\nu_0/2\right)-1\right)/2$

Experimentally, both channels are physically different, consequently their noise should be independent[2]. The coupler noise $N_{\mathrm{X}} \simeq S_{\nu,n_{\mathrm{X}}n_{\mathrm{X}}} \simeq (\coth(\beta h\nu_0/2)-1)/2$ can be very low because the idler mode of a coupler can easily be cooled to the ground state.

In summary our full calibration procedure is:

1. Calibrate G_0 & G_1 (and so $\chi_{\nu,0}$ & $\chi_{\nu,1}$) using $50\,\Omega$ loads at β_{cold} & β_{hot};
2. (Optional) Also calibrate N_0 & N_1, to verify the noise performance of our channels;
3. Measure $S_{\mathrm{PSD,X}}$ & $S_{\mathrm{PSD,X,off}}$;
4. Use calibration to reach PSD:
$$\frac{\gamma_\nu^{\mathrm{out}}}{h\nu_0} = 2\frac{|S_{\mathrm{PSD,X}} - S_{\mathrm{PSD,X,off}}|}{h\nu_0\sqrt{\chi_{\nu,0}\chi_{\nu,1}}} \tag{II.9}$$
5. (Optional) Also extract the argument of $S_{\mathrm{PSD,X}} - S_{\mathrm{PSD,X,off}}$. It shows variations of the phase difference between both channels;
6. (Optional) Also calibrate $N_{\mathrm{X}} \simeq 2S_{\mathrm{PSD,X,off}}/h\nu_0\sqrt{\chi_{\nu,0}\chi_{\nu,1}}$, to verify that the coupler is cold. Note that N_{X} also includes crosstalk between channels (mostly on the acquisition board).

$G^{(1)}$ is the time domain counterpart of equation II.8

$$\begin{aligned} \Gamma^{\mathrm{X}}(t,\tau) &\equiv 2h\nu_0\cdot 50\,\Omega\left\langle S_0^\dagger(t+\tau)\,S_1(t)\right\rangle \\ &= \underbrace{2h\nu_0\cdot 50\,\Omega\cdot G_{\mathrm{X}}(\nu_0)}_{\chi_{\nu,\mathrm{X}}(\nu_0)}\left\{ G^{(1),\mathrm{out}}(t,\tau) + \underbrace{\left[2\Gamma_{t,n_0'n_1'}(\tau) - G^{(1)}_{t,n_{\mathrm{X}}}(\tau)\right]}_{2\Gamma_{t,n_0''n_1''}(\tau)\,=\,\Gamma^{\mathrm{X,off}}(\tau)/\chi_{\nu,\mathrm{X}}(\nu_0)}\right\} \end{aligned} \tag{II.10}$$

where the overall gain is supposed to be constant over the signal bandwidth. This gain can be calibrated directly through $G^{(1)}$ measurement using $G^{(1)}(0)$ of $50\,\Omega$ loads as described previously with PSD measurements[3]. Note also that correlations of noise fields are t-independent because they are stationary and ergodic processes, in particular *off* quantities are t-independent. Finally:

$$G^{(1),\mathrm{out}}(t,\tau) = \frac{\Gamma^{\mathrm{X}}(t,\tau) - \Gamma^{\mathrm{X,off}}(\tau)}{\chi_{\nu,\mathrm{X}}(\nu_0)} \tag{II.11}$$

Moreover, using cross correlations instead of direct ones does not only reduce the linear noise of our model, but also make it less sensitive to non-linearities in the measurement chain that would reduce the *Spurious-Free Dynamic Range* (SFDR), which becomes crucial for higher order correlation functions.

Results First of all, a rough sum of amplifications and attenuations along our acquisition channel (see technical details chapter II section 2.b) gives a total gain of 101 dB, however this sum does not include neither losses of circulators ($\simeq$ 0.5 dB per components) or mixers ($\simeq$ 7 dB per components), nor cables $\simeq$ 0.9 dB/m. Consequently, this value is only an upper bound.

After measuring $50\,\Omega$ reference loads and extracting gains, figure II.10 is plotted. As expected, the gains are well below the upper bound of 101 dB. A first observation is that gains are different for different local oscillators; e.g. at 5.1 there is a jump of $\simeq$ 1 dB. This results is due to the mixing. Actually if the gain can be decomposed in two parts: $G_{\mathrm{before}}(\nu)$ before the mixer depending only on the signal frequency, and $G_{\mathrm{after}}(|\nu-\nu_{LO}|)$ after the mixer depending on the down-mixed signal frequency.

[2] They are coupling only through grounds of active components and noise leaking from one channel to the other thanks to backward reflections.

[3] It allows to calibrate $G^{(1)}$ exactly like measurements of $G^{(1)}$ will be taken, numerical filter encompassed.

The full gain is then $G_{\text{before}}(\nu)\, G_{\text{after}}(|\nu - \nu_{LO}|)$, and consequently the order of magnitude of the jump is $G_{\text{before}}(\nu)\,|G_{\text{after}}(1\,\text{GHz}) - G_{\text{after}}(2\,\text{GHz})|$ if the jump occurs with two local oscillators working with the same Nyquist band (i.e. local oscillators both below or upper 6 GHz). In the other case, e.g. between green and red lines, there is no jump.

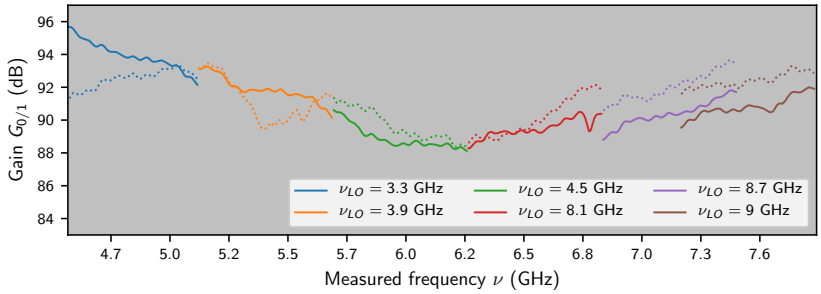

Figure II.10: **Channel gains** as functions of the measured frequency and the local oscillator frequency, solid lines correspond to one channel, dotted lines to the other. There are some jumps between different local oscillator due to the fact that gain depends on both input signal frequency and local oscillator frequency, see text. Moreover, the gain amplitude is compatible with the upper limit obtained by summed theoretical amplifications and attenuations along all the setup of 101 dB.

Together with the gains, full channel noises are also extracted, these noises mainly come from the 4 K amplifiers. Figure II.11 shows them on the left axis. Except for the first oscillator, all curves overlap, which is excepted because the noises arise mostly before mixing. The curve close to 0 is plotted on the right axis and is measured using a short circuit instead of a sample. As a consequence, the PSD measured is the sum of backward noises coming from the amplifiers after isolation through circulators.

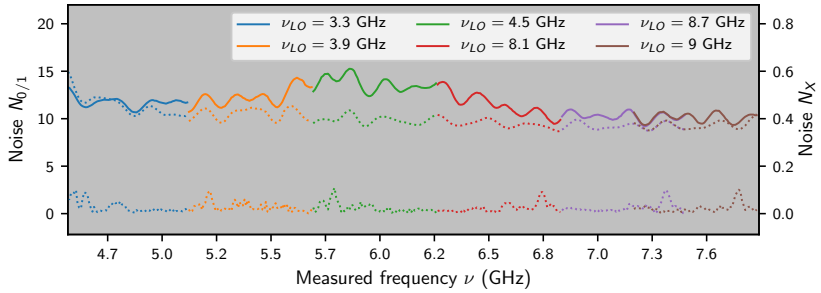

Figure II.11: **Channel noises** in photons as functions of the measured frequency. Note that there are no more jumps because most part of the noise comes from the 4 K stage before the down conversion. The unique jump is between the first two local oscillators due to aliasing.

As excepted this backward noise is close to 0 – many orders of magnitude below amplifier noise. A last observation is the jump between the two first local oscillators, this jump is explained by mixer aliasing due to spurious conversion terms with $3\nu_{LO}$ for $\nu_{LO} = 3.3\,\text{GHz}$ which let noise from 7.9 GHz to 8 GHz appears at the frequency as 5.2 GHz to 5.3 GHz down-converted with 3.3 GHz

$G^{(2)}$

The way $G^{(1)}$ is measured can be extended to higher order correlation functions. However, SNR dramatically decreases with order, consequently our method can be experimentally extended to $G^{(2)}$ but no more. To go further, SNR should have to be increased, the element to improve is the amplification, for example the use quantum-limited amplifiers would increase the SNR and allow measurements of higher order correlation functions.

To measure $G^{(2)}$ we compute $\Gamma^{(2)}(t,\tau) \equiv [2h\nu_0 \cdot 50\,\Omega]^2 \left\langle S_0^\dagger(t)\, S_0^\dagger(t+\tau)\, S_1(t+\tau)\, S_1(t) \right\rangle$. Let's develop this expression using Wick's theorem:

$$
\begin{aligned}
\Gamma^{(2)}(t,\tau) &= [2h\nu_0 \cdot 50\,\Omega \cdot G_{\mathrm{X}}(\nu_0)]^2 \Big\langle \quad \left[a_{\mathrm{out}} + \sqrt{2}n_0''\right]^\dagger (t) \left[a_{\mathrm{out}} + \sqrt{2}n_0''\right]^\dagger (t+\tau) \\
&\qquad\qquad \left[a_{\mathrm{out}} + \sqrt{2}n_1''\right](t+\tau) \left[a_{\mathrm{out}} + \sqrt{2}n_1''\right](t) \quad \Big\rangle \\
&\underbrace{=}_{\text{Wick}} \chi_{\nu,\mathrm{X}}(\nu_0)^2 \Big[\quad \left\langle a_{\mathrm{out}}^\dagger(t)\, a_{\mathrm{out}}^\dagger(t+\tau)\, a_{\mathrm{out}}(t+\tau)\, a_{\mathrm{out}}(t) \right\rangle \\
&\qquad\qquad + \underbrace{4 \left\langle n_0''^\dagger(t)\, n_0''^\dagger(t+\tau)\, n_1''(t+\tau)\, n_1''(t) \right\rangle}_{\Gamma^{(2),\mathrm{off}}(\tau)/\chi_{\nu,\mathrm{X}}(\nu_0)^2} \\
&\qquad\qquad + 2 \left\langle a_{\mathrm{out}}^\dagger(t)\, a_{\mathrm{out}}(t+\tau) \right\rangle \left\langle n_0''^\dagger(t+\tau)\, n_1''(t) \right\rangle \\
&\qquad\qquad + 2 \left\langle a_{\mathrm{out}}^\dagger(t)\, a_{\mathrm{out}}(t) \right\rangle \left\langle n_0''^\dagger(t+\tau)\, n_1''(t+\tau) \right\rangle \\
&\qquad\qquad + 2 \left\langle n_0''^\dagger(t)\, n_1''(t+\tau) \right\rangle \left\langle a_{\mathrm{out}}^\dagger(t+\tau)\, a_{\mathrm{out}}(t) \right\rangle \\
&\qquad\qquad + 2 \left\langle n_0''^\dagger(t)\, n_1''(t) \right\rangle \left\langle a_{\mathrm{out}}^\dagger(t+\tau)\, a_{\mathrm{out}}(t+\tau) \right\rangle \quad \Big] \\
\Gamma^{(2)}(t,\tau) &= \chi_{\nu,\mathrm{X}}(\nu_0)^2 \quad G^{(2),\mathrm{out}}(t,\tau) \\
&\qquad\qquad + \Gamma^{(2),\mathrm{off}}(\tau) \\
&\qquad + \chi_{\nu,\mathrm{X}}(\nu_0) \quad G^{(1),\mathrm{out}}(t,-\tau)\, \Gamma^{\mathrm{X,off}}(\tau) \\
&\qquad + \chi_{\nu,\mathrm{X}}(\nu_0) \quad G^{(1),\mathrm{out}}(t,0)\, \Gamma^{\mathrm{X,off}}(0) \\
&\qquad + \chi_{\nu,\mathrm{X}}(\nu_0) \quad \Gamma^{\mathrm{X,off}}(-\tau)\, G^{(1),\mathrm{out}}(t,\tau) \\
&\qquad + \chi_{\nu,\mathrm{X}}(\nu_0) \quad \Gamma^{\mathrm{X,off}}(0)\, G^{(1),\mathrm{out}}(t+\tau,0)
\end{aligned}
\tag{II.12}
$$

Inverting this equation, $G^{(2)}$ can be extracted. Note also this expression is simplified if the field a_{out} is also stationary and ergodic. Experimentally, we can measure both, depending if a trigger can be used or not (see below):

$$
\begin{aligned}
G^{(2),\mathrm{out}}(t,\tau) &= \frac{\Gamma^{(2)}(t,\tau) - \Gamma^{(2),\mathrm{off}}(\tau)}{\chi_{\nu,\mathrm{X}}(\nu_0)^2} \quad - \frac{\Gamma^{\mathrm{X,off}}(0)\left[G^{(1),\mathrm{out}}(t,0) + G^{(1),\mathrm{out}}(t+\tau,0)\right]}{\chi_{\nu,\mathrm{X}}(\nu_0)} \\
&\qquad\qquad - \frac{\Gamma^{\mathrm{X,off}}(\tau)\, G^{(1),\mathrm{out}}(t,-\tau) + \Gamma^{\mathrm{X,off}}(-\tau)\, G^{(1),\mathrm{out}}(t,\tau)}{\chi_{\nu,\mathrm{X}}(\nu_0)}
\end{aligned}
\tag{II.13}
$$

Scattering parameter

Determining the scattering parameter of a sample only means comparing the power (or amplitude) coming from the sample to the power (or amplitude) sent to it. Two methods are used in our fridge:

- A *Vector Network Analyser* (VNA) designed for this measurement. However, the calibration method introduced earlier cannot be used because the signal paths differ;
- The PSD & cross PSD together with an external microwave source can be used to extract the scattering parameters. Roughly, measuring a short circuit reference – that fully reflects the signal – with an external source, gives then the effective power sent to the sample. Then measuring the sample instead of the short circuit with the same external source gives the power after amplification by the sample. The gain is then the ratio between these two powers.

VNA sends a microwave signal at ν_0 to the device and directly measures the ratio between this field $S_{\text{out}}(\nu_0)$ and the received one $S_{\text{in}}(\nu_0)$. When an ICTA sample is measured $a_{\text{out}} \equiv r_G * [a_{\text{in}} + n_G]$, however the signal coming from the VNA is attenuated before reaching the sample and amplified after, consequently $r_{\text{out}} r_G r_{\text{in}}$ is measured.

To calibrate this measurement, we use two methods:

- If a mainly fully reflecting sample is assumed – i.e. for most parameters the sample fully reflects the signal – a statistical analysis can be used to determine $r_{\text{out}} r_{\text{in}}$;
- Using a short instead of the sample fully reflects the signal, it results to a measurement of $r_{\text{out}} r_{\text{in}}$.

Both methods have drawbacks, the first one requires a strong hypothesis that cannot be fulfilled for all samples. The second one has a systematic error because the path used to measure the short reference and the one for the sample are sightly different: The second one includes a coaxial cable and for some devices a bias-tee.

Moreover, the power at the input of our sample also has to be determined, i.e. r_{in}. To do so, an external source is used to send a signal at ν_0 on the short reference, afterwards the previous PSD method is used to determine the power (by integration of PSD). The ratio of sent and measured powers gives $|r_{\text{in}}|^2$.

2.b Technical details

Here we give technical details on our measurement chain from the sample holder to the high speed digitiser.

Sample holder

Our sample is made of a 1 cm × 1 cm chip including eight NbN 234 µm × 249 µm CPW landers. Figure II.12 shows the sample holder used to connect each pad to a *SubMiniature version A* (SMA) connector. The square hole in the centre surrounded by a gold-plated *Printed Circuit Board* (PCB) holds the chip. Sample and PCB are linked through Al wire bonds, whereas connector centre pins are Sn soldered.

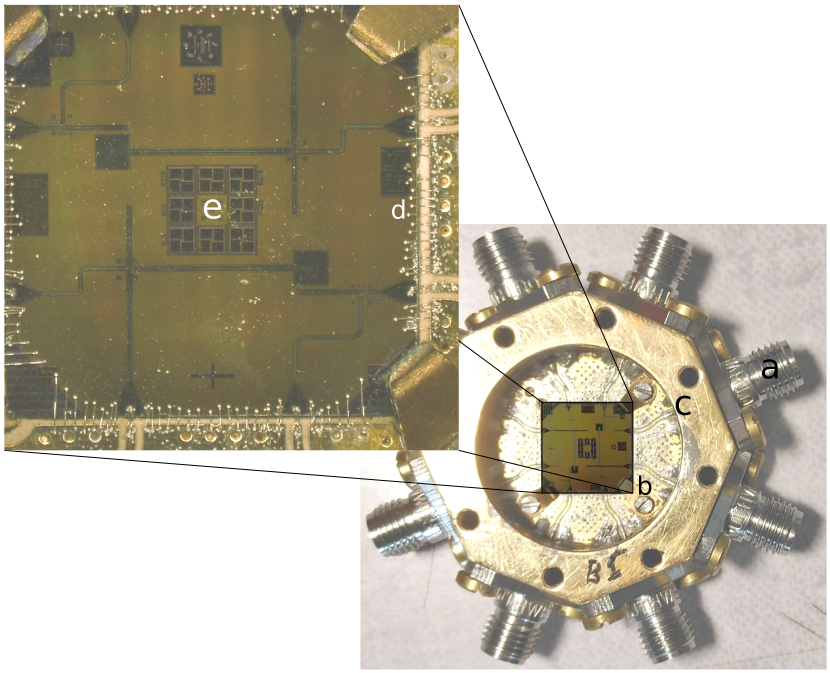

Figure II.12: **Sample holder** and zoom on a mounted sample. ***a*** is a SMA connector, its pin goes through the holder and is soldered on the PCB at ***b***. ***c*** are clamps used to fix the sample. ***d*** are bonding between the PCB and the sample. ***e*** are test structures.

Bias circuit

DC voltage and flux biases are independent for each sample. DC voltage biases are applied through home-made 25 Ω or 50 Ω bias boxes made of three RLC stages (see figure II.13 for details).

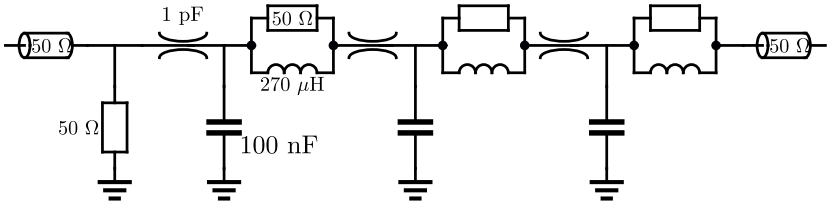

Figure II.13: **Bias box scheme** made of three RLC filters in series, each of them is inside a Copper cavity.

The flux biases are applied through home-made dissipative filters (Eccosorb CRS 124), which are Gaussian filters with cut-off at $\simeq$ 300 MHz (see figure II.14).

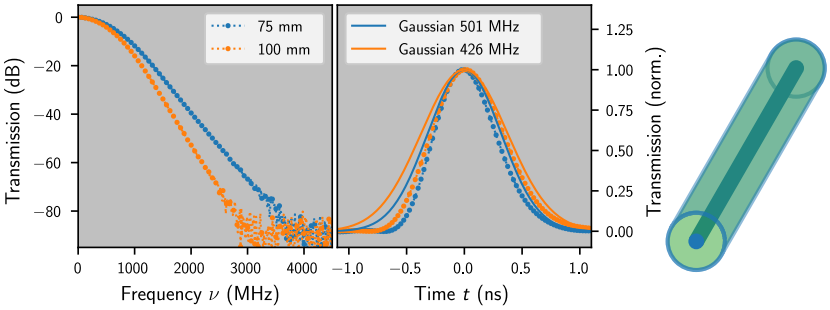

Figure II.14: **Eccorsorb filter.** ***Left panel:*** Frequency response. ***Middle panel:*** Impulse response in time domain. The expected Gaussian behaviour depending on the filter length is observed. ***Right scheme:*** Elements of an eccorsorb filter. Eccosorb CRS 124 (in green) is poured in a copper coaxial cable (RG-402) where dielectric has been removed (copper shield and core in blue). The centre conductor comes from a RG-405 cable in order to get correct impedance.

RF circuit

Two kinds of samples are studied in this thesis:

- One port samples where DC & RF signals are on the same 50 Ω port. This kind of samples is intended to be measured without using cross PSD or $G^{(1)}$ methods;
- Three port samples with on-chip beam-splitters and bias-tee. There are two RF ports corresponding to the split output fields, and one DC port. This kind of samples is intended to be characterised with PSD, $G^{(1)}$ or $G^{(2)}$ methods.

For one port samples, DC and RF components of our setup are added through a 50 MHz bias-tee (Marki DPXN-M50). The first kind of samples is used to study amplification, second one photon source. Moreover, to connect the amplifiers to different calibration standards (see above) and samples, two six-ports switches (Radial R591763600) are used.

The rest of the setup is the same for both types of samples. The first amplification stage is at the 4 K stage using HEMT low noise cryogenic amplifiers (LNF-LNC4-8 A) working between 4 GHz to 8 GHz. Some elements along the channel at base temperature protect the sample from amplifier noise:

- A bandpass between 4 GHz to 8 GHz (Microtronics BP50403) protects our devices from and out-of-band noise;
- Three circulators (Raditek RADC-4.0-8.0-Cryo-523-1WR-M2-b) reduce in-band noise coming from amplifiers.

Figure II.15 shows a block diagram of the amplification stage.

For some measurements, a signal must be sent to the sample. This can be done easily though one of the circulators already used to isolate the sample from backward noises. Note also some attenuators, 3 dB to 6 dB are used to reduce stationary waves by improving 50 Ω matching – especially with amplifiers and mixers – 20 dB are used to block the black-body radiation on input lines.

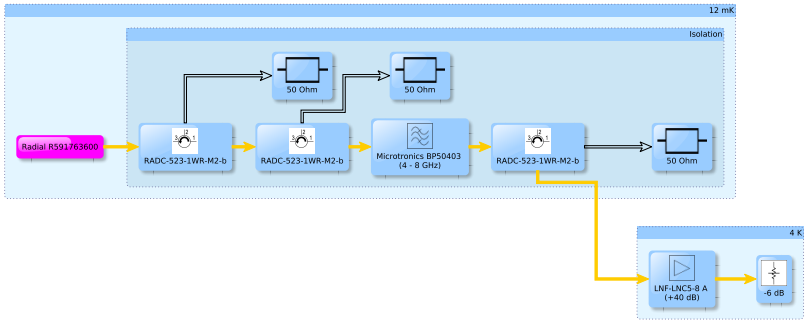

Figure II.15: **Amplifiers wiring.** Samples and calibration references are connected to the six-ports switch (the left most block). The signal goes from left to right, the right most block is the 4 K amplifier, between these two blocks others are here for isolation and filtering. Moreover, substituting the left most 50 Ω block by an input line allows to send microwaves to the sample.

IQ demodulation

The IQ demodulation is done with two mixers (Marki MM1-0312SS) that mix the signal with a local oscillator generated by an RF source (Rohde & Schwarz SMF 100A) between 3 GHz to 9 GHz. At the end our signal is digitised at 2 GS s^{-1} on a two channel high speed digitiser (AlazarTech ATS9373). As a consequence only one Nyquist band may be preserved after mixing and all other have to be filtered out. Figure II.16 shows aliasing depending on the Nyquist band.

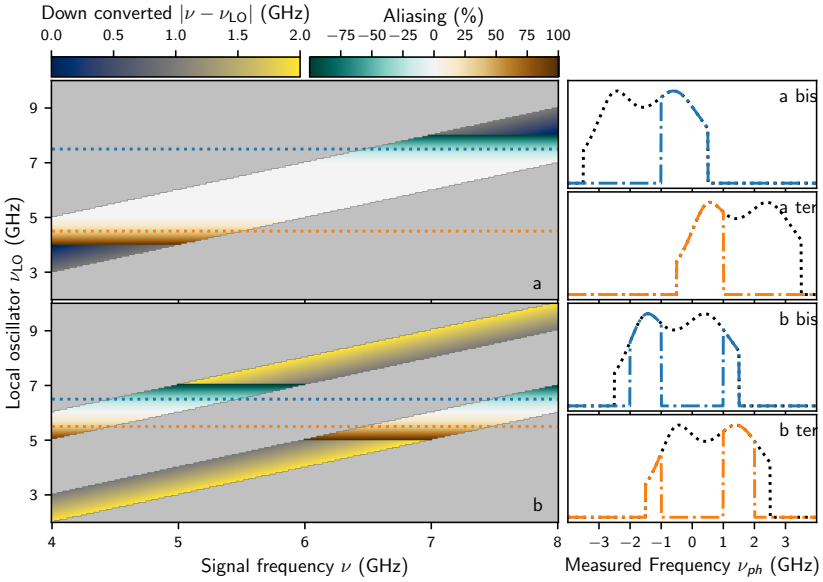

Figure II.16: **Mixer aliasing** depending on the Nyquist band. ***Panel a, a bis & a ter*** correspond to the first band. When the signal upper band is down converted only to positive or negative frequencies, a down converted frequency is well-defined (top left colour bar). In other case there is aliasing between negative and positive frequencies after down conversion. The top right colour bar varies between −100 % to 100 %. ±100 % corresponds to the situation where the upper signal band is fully down converted to positive/negative frequencies, 0 % is maximal aliasing with the signal upper band covering the full range −1 GHz to 1 GHz. ***a bis & a ter*** shows spectrum after down conversion in situation of aliasing. The dotted line is the full spectrum, the dash-dotted line is the spectrum inside the first Nyquist band. ***Panel b, b bis & b ter*** correspond to the second Nyquist band. While the first band cannot give access to frequencies around 6 GHz, the second band allows to measure frequencies between 4 GHz to 8 GHz. This is why this solution is chosen. Note that this analysis does not include aliasing due to higher order mixing terms.

Our setup uses the second Nyquist band thanks to a bandpass between 1 GHz to 2 GHz (Microtronics BPM18939). Additional amplifiers (Miteq AMF-5F-04000800-07-10p, Minicircuits ZRL-2150+ & Minicircuits ZX60-V62+) and bandpass filters between 4 GHz to 8 GHz (Microtronics BPI17597) are used to filter unwanted noise before mixing and adapt powers for mixing and digitising. Figure II.17 shows the block diagram of the IQ stage.

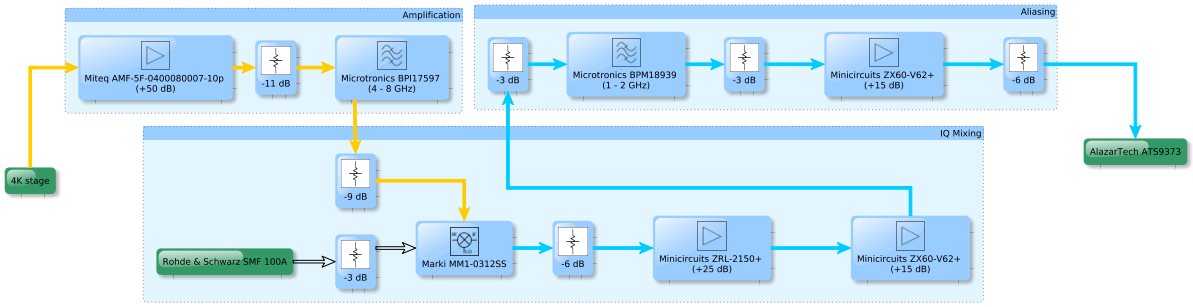

Figure II.17: **IQ wiring.** The block diagram shows the wiring starting from 4 K (the most left block, see also figure II.15), orange arrows are the signal between 4 GHz to 8 GHz before down conversion and blue arrows are the signal between 1 GHz to 2 GHz after down conversion. There are three groups, the first one is the room temperature amplification stage, the second one is the mixing, and the last one is the filtering stage between 1 GHz to 2 GHz to avoid aliasing between the two Nyquist bands. The last block is the high speed digitiser.

Digitising

We describe here how the complex envelope is extracted from the digitised signal. Let's describe the output field by its envelope: $b(t) \equiv \widetilde{b}(t)\ e^{-i\omega_0 t}$; subsequently the voltage is:

$$\begin{aligned} u(t) &= \sqrt{\tfrac{\hbar\omega_0 \cdot 50\,\Omega}{2}}\ \left[i\widetilde{b}(t)^\dagger\ e^{i\omega_0 t} + \mathfrak{h.c.}\right] \\ &= \sqrt{2\hbar\omega_0 \cdot 50\,\Omega}\ \left[\mathrm{Im}\left[\widetilde{b}(t)\right]\cos(\omega_0 t) - \mathrm{Re}\left[\widetilde{b}(t)\right]\sin(\omega_0 t)\right] \end{aligned} \tag{II.14}$$

After mixing with a reference signal at ω_{LO}, cos and sin arguments are shifted by $-\omega_{\mathrm{LO}}$. This reference can be chosen such that the resulting signal is at $\omega_s[1+2n]/4$ where n is the used Nyquist band[4]. Moreover, we need to take into account a noise term $\widetilde{v}(t)\ e^{-i\omega' t}$ at $\omega' = \omega_{\mathrm{LO}} - \omega_s[1+2n]/4$ because its resulting frequency is $-\omega_s[1+2n]/4$, indistinguishable from the signal frequency. The voltage is then[5]:

$$u(t) \propto \underbrace{\begin{array}{ll} \overbrace{\widetilde{I}(t) = \sqrt{\frac{\hbar\omega_0\cdot 50\,\Omega}{2}}\left[\widetilde{S}(t)^\dagger + \mathfrak{h.c.}\right]}^{} & \\ \sqrt{\hbar\omega_0 \cdot 50\,\Omega}\,\mathrm{Im}\left[\widetilde{b}(t) + \widetilde{v}(t)\right] & \cos\left(\frac{\omega_{\mathrm{sys}}}{4}[1+2n]\,t\right) \\ -\sqrt{\hbar\omega_0 \cdot 50\,\Omega}\,\mathrm{Re}\left[\widetilde{b}(t) - \widetilde{v}(t)\right] & \sin\left(\frac{\omega_{\mathrm{sys}}}{4}[1+2n]\,t\right) \\ \underbrace{\qquad\qquad}_{\widetilde{Q}(t) = \sqrt{\frac{\hbar\omega_0\cdot 50\,\Omega}{2}}\left[i\widetilde{S}(t)^\dagger + \mathfrak{h.c.}\right]} & \end{array}} \tag{II.15}$$

Where $\widetilde{S} \equiv -i\left[\widetilde{b} - \widetilde{v}^\dagger\right]/\sqrt{2}$ is recovered as previously.

Afterwards, the voltage is sampled at $\nu_s = 2\,\mathrm{GHz}$, i.e. samples are $x_m \equiv 2u(m/\nu_s)/u_{\mathrm{pp}}$ where $u_{\mathrm{pp}} = 800\,\mathrm{mV}$ is the peak-to-peak voltage of the full scale, allowing to extract both quadratures:

$$\begin{aligned} I\left(\tfrac{m}{\nu_s}\right) &\propto (-1)^{m/2} \quad \tfrac{u_{\mathrm{pp}}x_m}{2}, \ m \text{ even} \\ Q\left(\tfrac{m}{\nu_s}\right) &\propto (-1)^{n+(m-1)/2} \quad \tfrac{u_{\mathrm{pp}}x_m}{2}, \ m \text{ odd} \end{aligned} \tag{II.16}$$

Figure II.18 shows the two quadratures and the virtual field S with extracted samples highlighted. To go from quadratures to S, both quadratures have to be taken at the same time. This is done by convolving $(x_{2m})_{m\in\mathbb{N}} / (x_{2m+1})_{m\in\mathbb{N}}$ with $\mathcal{F}_\nu^{-1}\left[\nu \mapsto e^{\mp i\pi\nu/\nu_s}\right] \equiv \left(k_m^{I/Q}\right)_{m\in\mathbb{N}}$, i.e. samples corresponding to I are advanced by $1/2\nu_s$ and samples corresponding to Q are retarded by $1/2\nu_s$, they are noted $\widetilde{x}$ (see also

[4] Indexing starts at 0.

[5] There is also an overall factor depending on reference power, however this factor is included in the overall gain of our model.

figure II.18):

$$\begin{aligned}\left(\widetilde{x}_{2m}\right)_{m\in\mathbb{N}} &= \left((-1)^m \tfrac{u_{\mathrm{pp}} x_{2m}}{2}\right)_{m\in\mathbb{N}} * \left(k^I_m\right)_{m\in\mathbb{N}} \\ \left(\widetilde{x}_{2m+1}\right)_{m\in\mathbb{N}} &= \left((-1)^{n+m} \tfrac{u_{\mathrm{pp}} x_{2m+1}}{2}\right)_{m\in\mathbb{N}} * \left(k^Q_m\right)_{m\in\mathbb{N}}\end{aligned} \tag{II.17}$$

And finally samples are summed one-to-one:

$$S\left(\frac{1+4m}{2\nu_s}\right) \propto \frac{\widetilde{x}_{2m} + i\widetilde{x}_{2m+1}}{\sqrt{2h\nu_0 \cdot 50\,\Omega}} \tag{II.18}$$

The kernels $k^{I/Q}$ also include numerical filters that adapt the measurement bandwidth to the signal bandwidth to reduce the noise, especially to measure correlation functions.

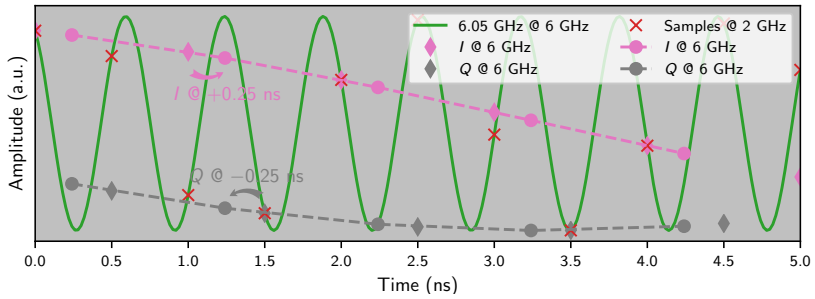

Figure II.18: **Quadrature extraction.** The input signal at 6.05 GHz is down converted with a local oscillator at 4.5 GHz (solid green line), Then the signal is sampled at 2 GS s^{-1} (red crosses), even samples give I quadrature (pink diamonds) and odd ones Q quadrature (brown diamonds). Finally, a numerical filter is used to advance I by 0.25 ns (pink dots) and to retarded Q by 0.25 ns (brown dots). As the input signal is not at the centre of the measured band, IQ components are not constant in time.

Now that S fields are extracted, correlations can be computed numerically, either in frequency domain when possible (PSD and $G^{(1)}$ of stationary processes) or directly in time domain doing correlations with smaller blocks[6], see figure II.19.

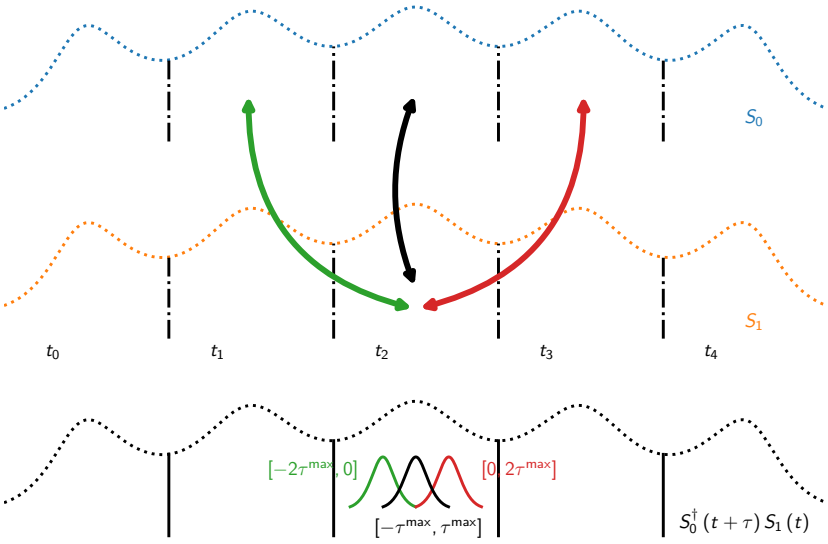

Figure II.19: **Correlation method** using blocks to compute correlations when there is not long-time correlation. Blue & green dotted line represent the two signals to correlate. First they are cut in small blocks (vertical lines) as correlation of non-adjacent blocks are negligible. Then by summing correlations (green, black and red lines) of aligned blocks (black arrow) and adjacent blocks (green and red arrows). If block are long enough, green and red correlations can also be neglected.

3 Instrumentation framework

At the beginning of my Ph.D., for each type of data acquisition a `python` script was written to vary the needed parameters, acquire data and store them; figure II.20 pictures one of those scripts. This task was repetitive, error-prone, and resulted in many scripts doing almost the same thing. The goal of the new

[6] As only short time correlations are useful, doing computations with a wide buffer is useless and resources consuming.

instrumentation framework I wrote during my Ph.D. is to remove those issues by providing a flexible software framework.

```
fluxBias = agilent_power_source.Channel(1)
fluxBias.setCurrent(0)
fluxBias.switchOn()
#Idem for voltage and uWaveSource

sv = DataSaver(
        title,
        [('Vbias','V'),('Coil current','A'),...],
        [('ch0 PSD Von', 'V^2/Hz'),...,
         ('ch0 PSD Voff','V^2/Hz'),... ])
sv.text("FFT points: %d" % (1<<log2nfft))
#Idem others metadata

digitizer = ats.AnalyzerBoard()
digitizer.setupCSD(averages, order=log2nfft)

for C in numpy.linspace(0, 1e-3, 11):
        fluxBias.setCurrent(C)
        for V in numpy.linspace(0, 10, 101):
                voltage.setVoltage(V)
                result = numpy.zeros((1<<(log2nfft-1)+1,12))

                result[:,0] = V
                #...

                digitizer.start()
                digitizer.waitEndMeasurement()
                voltage.setVoltage(0.0)
                af, apsd0, apsd1, acsd = digitizer.getData()

                result[:,3] = af
                result[:,4] = apsd0
                #...

                \\Idem lines 26 to 33 for Off values

                sv.data(result)

fluxBias.setCurrent(0)
fluxBias.switchOff()
#Idem voltage and uWaveSource
```

Figure II.20: **Typical old measurement script** where each loop (`for C in` & `for V in`) and all initialisations (`fluxBias`, `voltage`, `uWaveSource`, `digitizer` & `sv`) were hand written.

Moreover, the task of storing data is crucial: How data is stored fixes how they have to be read! One of the simplest ways is to store data in a human-readable format as matrices. However, when the development of the new instrumentation framework started, our measurements became heavier and heavier – mainly due to gain measurements with high frequency and voltage resolutions – and the need of a new format became apparent. A binary format *Hierarchical Data Format 5* (HDF5) was chosen. This key-point duality is kept orthogonal in the new instrumentation framework:

- A way to write data in various formats, useful to make measurements with our setups;
- A way to read data in various formats, useful to analyse data taken from different platforms in the same way.

Another need is to quickly observe the data, as required by any experimental design – in order to verify the measurement and plan the next one – optionally calibrated. However, as our setup is used with different measurements, there are as many ways to observe the data as there are schemes. To do so, the new instrumentation framework embeds a GUI based on a more fundamental and simple `python` core interface.

3.a Parameter space exploration

First of all, let's describe four use cases of measurements:

- Hypercube scan (see figure II.20):

  1. All instruments are settled – N (real) values – and some measurements are performed;
  2. One of the instruments is successfully settled to new values and measurements are performed;
  3. The instrument of step 2 is settled to its value at step 1, another one of the instruments is successfully settled to new values and step 2 is performed for each;
  4. Optionally the same as step 3 with another instrument;
  5. ...
  6. $N_{walk} \leq N$ instruments.

  Formally, those N instruments are described by an Hilbert space on $\mathbb{R}^N = \mathbb{R}^{N-N_{walk}} \times \mathbb{R}^{N_{walk}}$, and with a proper scalar product, all settled values make a regular mesh on $S \times H$ where:

  – S is a singleton in $\mathbb{R}^{N-N_{walk}}$;

  – H is an unit hypercube in $\mathbb{R}^{N_{walk}}$ – thanks to the proper scalar product.

  And so, interpolating from the mesh, a measurement is a function $S \times H \to M$, where M is an arbitrary metric space – needed to have notion of continuity and interpolation, e.g. $\mathbb{R}$ for a single real value measurement;

- Hyper-surface scan; e.g. when vector magnets are used, the three components have often to be settled simultaneously. Contrary to the first case, it corresponds to settle simultaneously $n \geq 1$ (real) values in step 2 or 3 etc. Formally, in the first case, it would be a regular mesh on a hypercube in $\mathbb{R}^n$, in the second one it is a mesh on $\mathrm{Im}\,(\gamma \in \mathbb{R} \supset I \to \mathbb{R}^n)$ – with I a closed interval of $\mathbb{R}$ – i.e. a mesh on the image of a parametric curve on $\mathbb{R}^n$;

- Adaptive scan, e.g. a Ramsey experiment on a transmon qubit with tunable external parameters controlling the resonance frequency depends on those external parameters. To do the Ramsey sequence for different parameters, a preliminary measurement of the resonance frequency has to be done. In view of the first case, each *measurement* task is replaced by two subsequent tasks:

  – Measure the resonance frequency;

  – Perform the Ramsey pulse sequence.

- The fourth one is the monitoring use case, for example the monitoring of temperature and pressure in a cryogenic fridge. Contrary to the first case, there is only one step: Perform the measurements, that is repeated indefinitely until the end of the experiment.

Iterative measurement

The core design of the new instrumentation framework is built on this iterative aspect present in each use case. The following code snippet, figure II.21, shows this aspect:

Let's comment line by line:

4 Perform an infinite loop, i.e. it will repeat the measurements indefinitely;

5 A `for` statement over an association (`zip`) between each measurement and its result, returned by `generator.next()`;

```
1  savers    =
2  generator = process_sampling(parameters, measurements)
3
4  while True:
5      for measurement, data_set in zip(measurements, generator.next()):
6          for saver in savers:
7              saver(measurement, data_set)
```

Figure II.21: **Iterative measurement core code** where all the loops are hidden behind the `generator`, `generator.next()` sets all the next parameters and runs measurements, therefore only saving in a file remains.

2 The `generator` is responsible for the iterative aspect. At each `generator.next()` the parameters are updated and the measurements performed;

7 Thanks to an object `saver`, the results of measurements are pushed to a storage space (see below).

To go further, the second use case can be transformed to correspond to the first one. Actually, by using a parametrisation of a parametric curve γ, the n parameters can be transformed to n measurements and the chosen parametrisation become a parameter. Moreover, a regular mesh on a hypercube can be stored as a dense matrix, which is simpler to store than a sparse one. And so, a way to perform a hypercube exploration has to be developed.

Hypercube exploration

In accordance to figure II.21, a `generator` function should do the following:

- Settle each parameter;
- Perform all measurements.

Moreover, to save time, settling a parameter should be avoided if it is already settled. A trace is also an useful feature to monitor the script. Let's consider the following code snippet: figure II.22.

```
1  def process_sampling(parameters, measurements):
2      for sample in hypercube_sampling(parameters):
3          settle_ = 0
4          print 'Set instruments at'
5
6          for parameter, value in to_treat(parameters, sample):
7              parameter(value)
8              settle_ = max(settle_, parameter.settle)
9              print '\t%s %.4g %s' % (
10                     parameter.name, value, parameter.unit)
11
12         time.sleep(settle_)
13
14         yield tuple(measurement() for measurement in measurements)
```

Figure II.22: **Process sampling core code** embeds hypercube walk with two loops. The first one gives the new parameters set to measure, the second one goes through this set and updates each instrument if required. Finally, all measurements are performed and returned at each iteration (`yield` instruction).

The regular mesh is returned by `hypercube_sampling(parameters)`, so at each step `sample` contains the next values for each parameter. Next, `to_treat(parameters, sample)` select only the parameters that effectively have to be updated. Lines 8 and 11 introduce a time delay to allow instruments to effectively settle. Finally, the `yield` statement performs all the measurements.

Moreover, as the results of measurements are pushed to the saver proxy, it also has to be setup with the mesh to push the results in the same order as they are measured. On figure II.23, lines 5-7, 19 and 20-21 show how the HDF saver keeps the order defined by the mesh.

An example

Now, an example from end user point of view can be build, see figure II.24. Each parameter, here `VB` and `FB`, can be called with a value, e.g. `VB(0)`, which update the bound instrument. Moreover, they embed

```python
class HDF5Saver(h5py.File):
    def __init__(self, file_, parameters, measurements):
        super(HDF5Saver, self).__init__(file_)

        self.shape = [len(parameter.data) for parameter in parameters]
        self.generator = itertools.product(
            *(range(0, size) for size in self.shape))

        for parameter in parameters:
            parameter_data_set = self.create_dataset(
                parameter.name, data=parameter.data)

        for measurement in measurements:
            measurement_group = self.create_group(
                measurement.name)

    def __call__(self, measurement, data_set):
        if measurement is self.firstMeasurement:
            self.currentIndex = self.generator.next()

        self[measurement.name][measurement_.name][self.currentIndex]
            = measurement_.data
```

Figure II.23: **HDF saver code.** The constructor (`__init__`) determines number and shapes of arrays in the HDF5 file. Such a saver has to be callable (`__call__`). When called it saves data in the corresponding HDF5 file.

the values to explore. The measurement `PSD` can be called to perform the measurement, i.e. `PSD()` return a dataset corresponding to the PSD.

```python
VB = parameters.VoltageBias(numpy.linspace(0, 10    , 101))
FB = parameters.FluxBias    (numpy.linspace(0,  1e-3,  11))

PSD = measurements.DigitizerPSD()
HDF = HDF5Saver('file.hdf5', [FB,VB], (PSD,))

hypercube_sampling.enumerate_and_save([FB, VB], (PSD,), HDF)
```

Figure II.24: **Example code** corresponding to the same measurement as the old code seen above, a PSD with voltage and flux sweeps. The code is more concise than the old one: Two lines define parameters to sweep (`VB` & `FB`), one line define what is measured (`PSD`), one how data will be saved (`HDF`). The last line explicit sweep order and starts the measurement, initialises required instruments (some are also initialised when parameters are defined), asks where the file will be saved and then performs all loops.

3.b Visualisation pipeline

A way to visualise the measured data quickly is essential in order to quickly interpret the physics and refine what has to be measured. There are two main key points:

- First, when more than two parameters are explored, some of them have to be fixed while the measurement is plotted as a function of one or two parameters;
- Second, as seen in section 2.a, our measurements require highly demanding calibrations. Moreover, a new measurement setup can require a new calibration scheme, and so our visualisation tool has to be extensible.

Both of them can be addressed if underlying data can be accessed and transformed, until the data can be pictured by a one or two-dimensional array, which is easy to plot.

Those successive transformations act on the data step by step: The data flows through a pipeline of filters (see figure II.25) with the raw data at the source and the plotted figure at the sink.

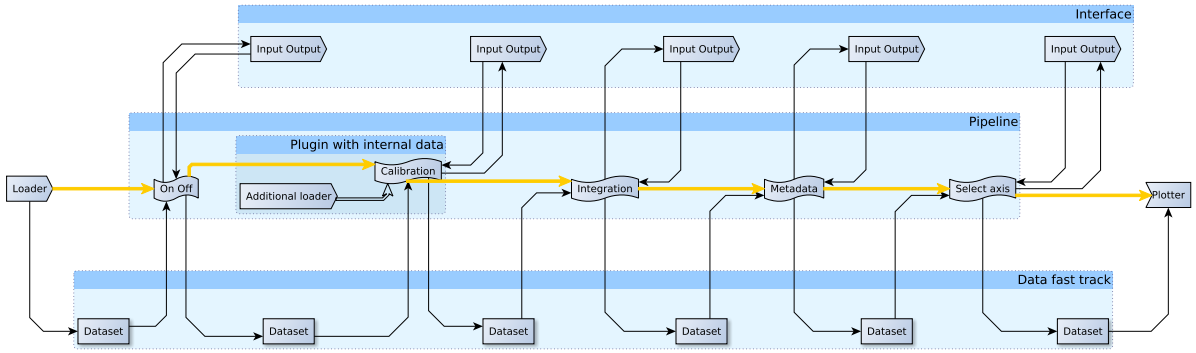

Figure II.25: **Pipeline model** in which data flow. Orange arrows show the path followed by a dataset. Each block connected by an orange arrow is a plugin that performs a required treatment on the dataset. If a plugin needs some additional data it can also use IO (in the group *Interface*). Moreover, at each step the resulting dataset is saved and will be used if IO changes to not reapply all plugins but only the one following the changed IO.

Dataset model

First of all, to ensure the consistency of the data all along the pipeline, the arrays inside our data structures are immutable, so the data can be accessed but not altered, to do a transformation the arrays are copied and put inside a new data structure. Moreover, at cost of memory, it speeds up the update of the pipeline that happens when a filter is added, removed or altered. Actually the data structure just before the modification is reusable and only the downstream elements have to be subsequently updated, as pictured in figure II.25.

Our data structures have two responsibilities:

- Hierarchically organise the data: Each axis of arrays of data is associated to a parameter, arrays of data are grouped together to form a dataset;
- Add semantics to each array of data: A name, unit and some metadata – e.g. how instruments are setup and synchronised.

This hierarchical organisation is summarised in figure II.26, a `Dataset` contains two dictionaries, one associating a name to each `Parameter` and one associating a name to each `Measurement`. It also contains a third dictionary which structures all the metadata.

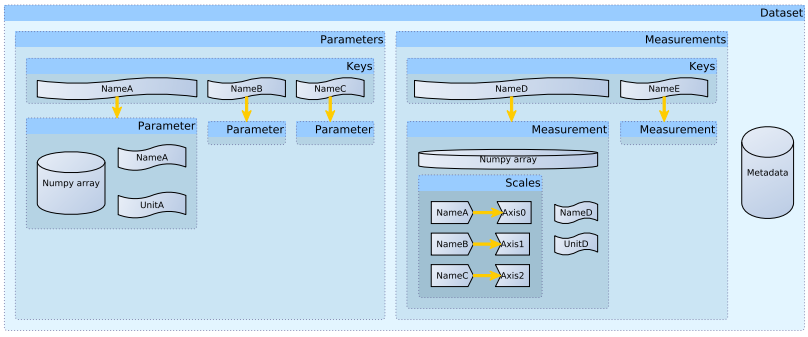

Figure II.26: **Dataset model hierarchy** includes three subgroups, one for the parameters, one for the measurements and finally a dictionary (the right most cylinder) for the metadata. The two first subgroups are dictionaries associating names to `Parameter` or `Measurement` objects. Those objects are also similar, they include `str` objects to store a name and an unit and a `numpy.array` to store the data. `Measurement` also includes a dictionary that associates parameter names to axis indices.

`Parameter` and `Measurement` share some properties, both have an immutable array, a name and an unit, i.e. the semantic due to the physics is associated to the data array, and so at each time the physical meaning of the data can be retrieved. Moreover, each `Measurement` includes a dictionary associating a parameter name to each axis of the data array.

Operations

The dataset model offers all elements to perform all needed analysis. Actually, measured data can be opened with the framework and an usual `numpy` array can be retrieved and used as any other `numpy` array, and thanks to the last dictionary (see above) and the `Parameter` objects the correspondence between axis and `Parameter` is known. Figure II.27 shows an example of framework usage for analysis.

```
1  from meavis import core
2  from meavis import load
3
4  data = load.load(filename)
5  data = core.reduce_dim(data)
6
7  print data.measurements.keys()
8  #Display: ['/VNA/s12']
9  print data.measurements['/VNA/s12'].scales
10 #Display: {u'/Flux Bias': 0, u'/VNA/Frequency': 1, u'/Voltage Bias': 2}
11
12 data_vna = data.measurements['/VNA/s12'].data
13
14 data_fb = data.parameters[  '/Flux Bias'    ].data
15 data_freq = data.parameters['/VNA/Frequency'].data
16 data_vb = data.parameters[  '/Voltage Bias' ].data
17
18 print data.parameters['/Flux Bias'    ].unit #Display: A
19 print data.parameters['/VNA/Frequency'].unit #Display: Hz
20 print data.parameters['/Voltage Bias' ].unit #Display: V
21
22 #Here data_vna[2,12,5] is the S parameter when:
23 #    - The flux bias is data_fb[2] A
24 #    - The voltage bias is data_vb[5] V
25 #At data_freq[12] Hz
26 #Now all data_xxx can be used as any other numpy array
```

Figure II.27: **Snippet of analysis code.** This is an example of `python` code that loads the data from a filename, prints information about the dataset structure and retrieves useful data. Afterwards they can be plotted for example.

Moreover, as previously explained, this dataset model is useful for building a visualisation tool following the idea presented in figure II.25. Screenshot figure II.28 shows how this principle is implemented with a GUI: The tabs at the bottom configure filters which the dataset goes through, that can be added, removed and reorganised. The current tab displays the interface used to choose:

- Which data is plotted, on the left panel;
- Along which parameters, labelled *abscissa* and *ordinate*;
- To pin some parameters at chosen values, with a slider for each parameter.

The code resulting of those filters looks like line 4-5 in figure II.27: A `data` object is given to a function – with other arguments to configure the filter, like *abscissa* and *ordinate* names – and the function output become the new `data` object. Moreover, this resulting code can be copied to the clipboard to be pasted and enhanced for further analysis.

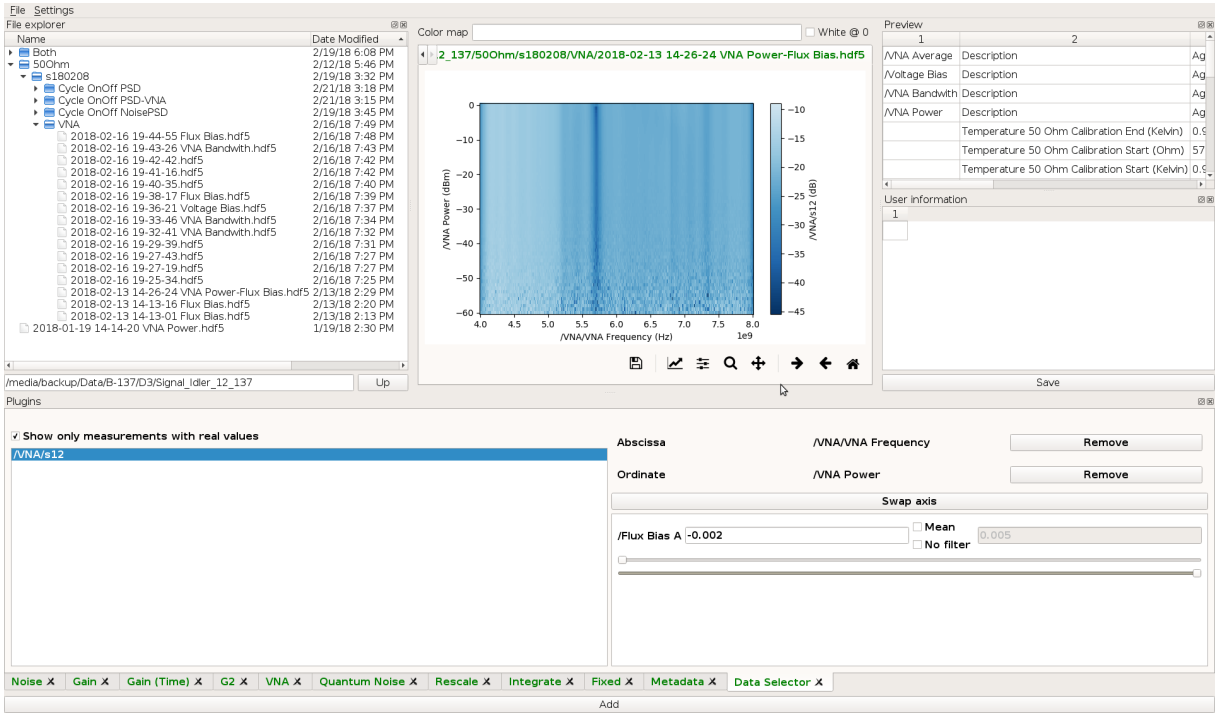

Figure II.28: **Screenshot of the data explorer GUI** where five areas are visible. First left panel is the file explorer, it allows to navigate through the arborescence of files. When a file is selected the two right panels update, top one shows metadata, bottom one allows to add some user information. When opened, the centre area shows a plot of the data, while the bottom panel has as many tabs as plugins. Here the last plugin, *Data Selector* is shown, the left list is used to select which data to plot while the right part selects abscissa, ordinate and pins other parameters (or averages them over a range).

Chapter III

Sample design and fabrication

French resume

Ce court chapitre est dédié à la fabrication de nos échantillons. Une première partie explique la déposition et la gravure d'une tri-couche de NbN/MgO/NbN pour former des jonctions Josephson, des lignes de transmission et d'autres structures. Une seconde partie étudie les environnements électromagnétiques élémentaires que l'on peut réaliser et assembler pour former des circuits plus complexes.

Contents

1 Fabrication

Preamble As I did not develop new aspects for the fabrication process, the description will be succinct; for details and problems encountered during the development, see [*Grimm15*; *Grimm17*; *Jebari17*].

First, the fabrication process will be described to explain how it SQUIDs are patterned and how CPWs are obtained with the same steps.

1.a Trilayer deposition

First of all a thin buffer (20 nm) of MgO is sputtered on a 4 in Si(500 µm)/SiO_2(500 nm) wafer, this buffer increases the trilayer critical temperature and acts as etch stop [*Grimm15*; *Jebari18*]. After, the trilayer NbN/MgO/NbN is sputtered.

Thicknesses of the different layers depend on the device because our fabrication process is continuously evolving, table III.1 shows the thicknesses for four devices:

ICTA Saclay: Is the sample used [*Hofheinz11*] to begin the exploration of the photonic side of inelastic Cooper pair tunnelling. The fabrication process is not the one described here (*standard* Al–junctions & Nb for large structures);

SPS: Is the sample presented in chapter IV and one of the first built with this NbN fabrication process;

ICTA low noise: Is presented in chapter V and has been designed by S. Jebari [*Jebari17*] also with this NbN fabrication process;

Future designs: A new process for Nb/Al/Al_2O_3/Nb junctions has been developed by R. Albert and will be used for future designs.

Table III.1: Thicknesses of layers

Device	Species	Thickness
ICTA Saclay	Structure Nb	50 nm
	Bottom Al	30 nm
	Al_2O_3	Oxidation
	Top Al	30 nm
SPS	Bottom NbN	80 nm
	MgO	4 nm
	Top NbN	200 nm
	Dielectric Si_3N_4	500 nm
	Top-wiring NbN	300 nm
ICTA low noise	Bottom NbN	30 nm
	MgO	5 nm
	Top NbN	170 nm
	Dielectric Si_3N_4	300 nm
	Top-wiring NbN	350 nm
Future designs	Bottom Nb	50 nm
	Al	10 nm
	Al_2O_3	Oxidation
	Top Nb	50 nm
	Dielectric Si_3N_4	200 nm
	Top-wiring Nb	200 nm

RF & DC magnetron sputtering is done with an Alcatel SCM 600 with two targets:

- Nb which is nitrided with N_2 gas and sputtered with a DC field and a static (for top layer of the trilayer and top-wiring) or rotating (for bottom layer of the trilayer) substrate;
- MgO is sputtered with an RF field and a rotating substrate.

Note that the Alcatel SCM 600 also allows back-sputtering to clean the substrate. Back-sputtering is performed each time the wafer is introduced in the machine, i.e. before the first MgO sputtering on the substrate and before the top-wiring is sputtered.

1.b Etching of structures

***Superconducting Quantum Interference Device* (SQUID)**

A SQUID is made of two Josephson junctions. To make each of them, two conducting fingers have to cross:

- Bottom fingers are defined by etching all the trilayer. Figure III.1 top left shows the wafer after etching. The MgO buffer is red, the blue structure is the trilayer defining the two fingers,
- Si_3N_4 dielectric is deposited by CVD and anisotropically mechanically. Subsequently, Si_3N_4 only remains clung to vertical trilayer walls. Figure III.1 bottom left shows the structure after Si_3N_4 deposition and etching, Si_3N_4 is orange and some of it clings to the trilayer fingers (in blue);
- Top fingers are defined by sputtering and etching top-wiring (NbN). The etch step also removes the top NbN of the trilayer. Figure III.1 right shows the final structure, as the top NbN has been removed on the bottom finger, they are made only of bottom NbN and MgO barrier (red fingers); moreover as vertical walls have been protected with Si_3N_4 bottom (blue) and top (red) fingers cross and the interface is the MgO barrier.

Techniques used for each step are summed up in table III.2.

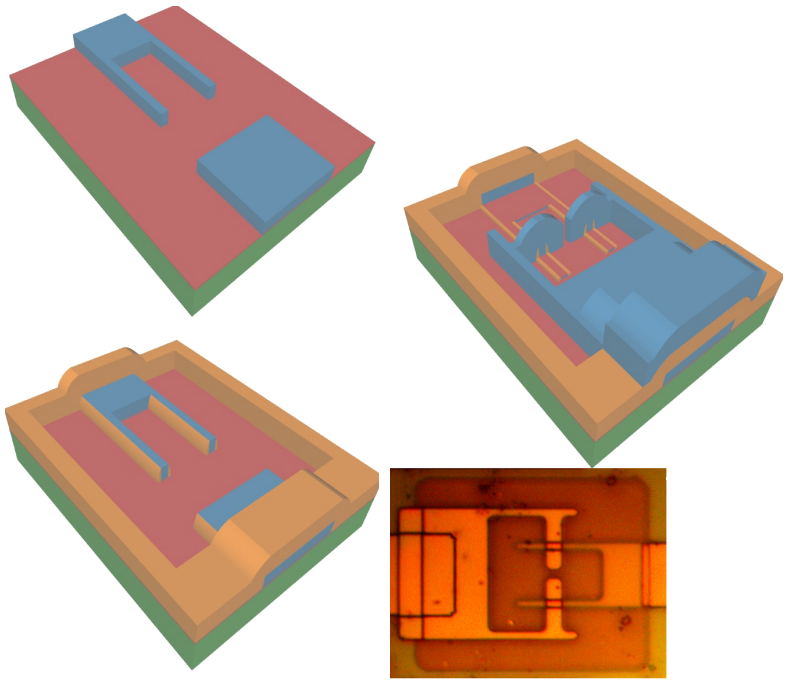

Figure III.1: **SQUID fabrication.** ***Top left:*** Green is the SiO_2 of the wafer, red is the MgO buffer, blue is the trilayer NbN/MgO/NbN. The first step defines the two fingers of the SQUID and is done by etching the trilayer (see text). ***Bottom left:*** In the second fabrication step, a layer of Si_3N_4 is deposited and etched anisotropically so that spacers remain clinging to the trilayer edge (orange). ***Centre right:*** In the last step, the top-wiring (NbN in blue) closes the SQUID loop. Note that the top part of the trilayer is etched together with the top-wiring, so the junctions are defined between the bottom part of the trilayer (below the two red fingers) and the top-wiring. The current has to go through the barrier because the spacers avoid that the top-wiring shunts the trilayer. ***Bottom right*** is a optical micrograph of such a SQUID, borders of each structure are visible, the two junctions are the two rectangles (in the centre) defined by the crossing of fingers.

RIE is done with an Oxford ICP Plasmalab 100 RIE using a plasma of three gases:

- Ar mechanically etches MgO when strongly biased, or makes chemical etches more directional (see CH_2F_2));
- SF_6 chemically etches NbN or Si_3N_4 in all directions;
- CH_2F_2 polymerises the surface to protect it from SF_6, however this polymer is etched by Ar consequently only vertical edges are protected and the SF_6 chemical etching becomes directional.

When possible, interfaces between layers are used for end point detection, especially the MgO buffer or barrier. Details about masks and resists used for EBL or OL are given [*Grimm15*; *Jebari17*].

Table III.2: Sum up of coating & etching steps

Step	Coating	Lithography	Etching
Trilayer	DC & RF magnetron sputtering NbN/MgO/NbN	EBL & OL	RIE $Ar/SF_6/CH_2F_2$
Spacer	CVD Si_3N_4	OL	RIE $Ar/SF_6/CH_2F_2$
Top-wiring	DC magnetron sputtering NbN	EBL & OL	RIE $Ar/SF_6/CH_2F_2$

Electron Beam Lithography (EBL)
Optical Lithography (OL)
Reactive Ion Etching (RIE)
Chemical Vapour Deposition (CVD)

Coplanar Waveguide (CPW)

A CPW is made of three conductors, a centre conductor and two ground planes (see figure III.2):

- Conductors are made by only etching the top-wiring, both trilayer and spacer remain;
- Gaps between conductors are made by etching both trilayer and top-wiring, only the dielectric remains.

Figure III.2 top shows the three conductors in blue (red is the MgO buffer), figure III.2 middle shows how the structure is covered by Si_3N_4 dielectric. Moreover, to balance the two ground planes, they have to be linked. This can be achieved by going over the central conductor from one ground plane to the other, simply by not etching the top-wiring. This strap is connected to the ground planes thanks to vias through the dielectric made by etching it (blue on top of orange in figure III.2). Moreover, regularly spaced holes are made in the top-wiring part of the ground plane to pin vortices.

Other structures

Using the same fabrication process, two other structures can be patterned:

Spiral inductors are easy included by etching the spiral pattern in the trilayer and using vias and top-wiring straps (as those used to link lateral ground planes) to escape from the spiral centre;

Capacitor are simply formed by using the dielectric sandwiched between the trilayer and the top-wiring.

Adding a supplementary coating step, a resistive material – Cr – can be deposited, either between the trilayer and the dielectric, or after the top-wiring. See [*Grimm15*] for details about pattern and geometry of cooling pads.

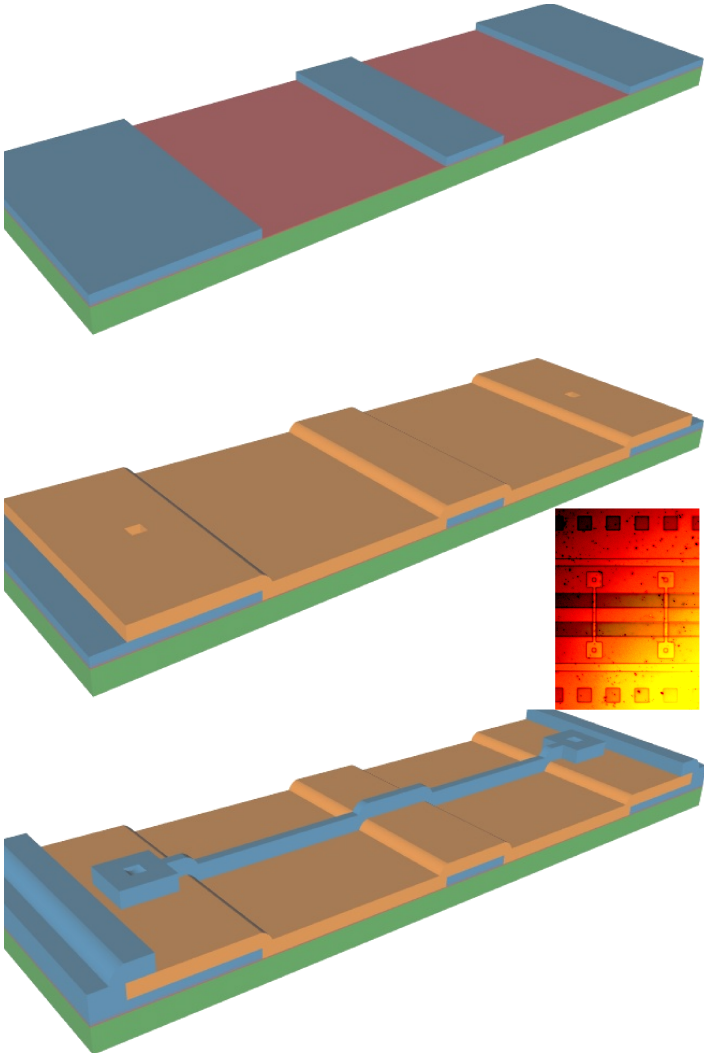

Figure III.2: **CPW fabrication.** ***Top*** is the first fabrication step. After this step the CPW is already defined: There are two lateral ground planes and a central conductor (in blue). ***Centre:*** In the second step, the CPW is recovered by the dielectric Si_3N_4, eventually some holes can be made to from vias between the CPW conductors and the future top-wiring. Here there are two holes on top of the ground planes. ***Bottom:*** As the last step, NbN is deposited as top-wiring. Here the top-wiring connects both ground planes to avoid charge imbalances. ***Right*** is a micrograph of a section of CPW. The conductors are visible, two bridges between ground planes are also visible.

2 Environment tailoring

As seen in chapter I, an electromagnetic environment can be decomposed in several independent environments in series. Knowing the behaviour of each one of them in terms of P-function ($P^{(n)}$), gives the behaviour of the full environment $P = P^{(0)} * P^{(1)} * \cdots$.

Two simple examples of such decompositions (see also figure III.3):

- The P-function of a resonator is made of peaks at integer multiples of the energy of a photon inside this resonator $nh\nu_0$. This means Cooper pairs can tunnel at zero bias (supercurrent) or if their energy corresponds to an integer number of photons inside the resonator. And consequently, if the environment is made of two resonators, Cooper pairs can tunnel if $\nu_J = n\nu_0 + m\nu_1$ while creating n photons in the first resonator and m in the second one;

- If an environment has a high impedance at $\nu_J \simeq 0$, tunnelling Cooper pairs have to pay a charging energy E_C to tunnel. The maximum of the corresponding P-function is slightly shifted from 0 to E_C. In the same way, if the environment is made of a resonator and such an impedance, Cooper pairs can tunnel if $h\nu_J = E_C + nh\nu_0$ while creating n photons in the resonator and providing the charging energy.

2.a Single mode resonator: $\lambda/4$ versus LC

All our device are based on resonators, two designs have been investigated:

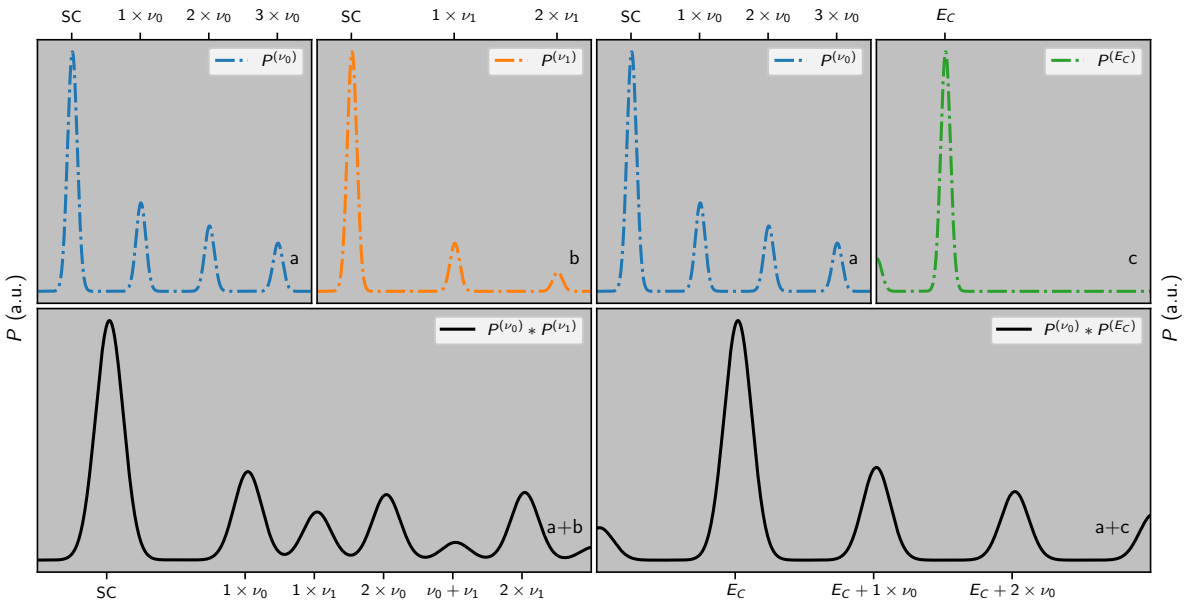

Figure III.3: ***P*-function decomposition.** ***Panel a and b*** correspond to the P-function when the electromagnetic environment is a single mode resonator at $\nu_{0/1}$. There is a peak at zero corresponding to supercurrent: No mandatory energy is required to tunnel. Other peaks correspond to a Cooper pair tunnelling while dissipating its energy in the form of photons at $\nu_{0/1}$. ***Panel c*** corresponds to the P-function when the electromagnetic environment requires an energy to tunnel: There is a single peak at E_C, to tunnel though this environment a Cooper pair energy E_C is required. This feature is typical of an RC circuit (with $R > R_Q$) for example, $E_C \equiv (2e)^2/2C$. ***Panel a+b*** corresponds to the combination in series of the environments a and b. Now Cooper pairs can tunnel and give theirs energy to photons in the environment a, or b, or both! Abscissa labels these different processes. ***Panel a+c*** corresponds to the combination in series of the environments a and c, now Cooper pairs have to pay the mandatory energy required by the environment c and can emit their remaining energy to photons in the environment a. Abscissa labels these different processes.

- Two cascaded quarter-wave TLs;
- LC resonators made of lumped elements together with a quarter-wave transformer.

Both are shown in figure III.4. Those are two of the simplest designs as they have the minimal number of parameters to tune frequency, effective impedance and quality factor.

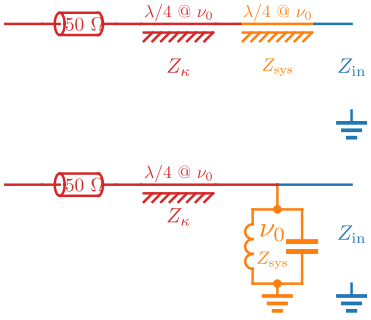

Figure III.4: **Designs of resonators.** ***Top design*** is two cascaded quarter-wave TL, the first TL seen (starting from Z_{in}) defines the effective impedance of the resonator $4Z_{\text{sys}}/\pi$, while the second one transforms (a quarter-wave TL transform high-impedance to low-impedance, relatively to this TL impedance Z_κ and reciprocally) the load impedance and so tune the quality factor. ***Bottom design*** is a LC resonator with a quarter-wave TL, as for the previous design, the first part defines the effective impedance $\sqrt{L/C}$ while the quarter-wave tune the quality factor. See text and table III.3 for details.

Before going further, let's remind some definitions for characteristic quantities of a resonator. There, definitions are based on the current i_{in} and the voltage u_{in} at input of the resonator which follow[1] the equation:

$$\partial_t^2 u_{\text{in}} + \frac{\omega_{\text{sys}}}{Q}\partial_t u_{\text{in}} + \omega_{\text{sys}}^2 u_{\text{in}} = \omega_{\text{sys}} Z_{\text{eff}} \partial_t i_{\text{in}} \tag{III.1}$$

ω_{sys} is the resonance frequency, Z_{eff} the effective impedance and Q the quality factor. Moreover, a load impedance is then defined as QZ_{eff}. All these definitions are exactly recovered for a parallel RLC. When $Q \to \infty$, the equation degenerates and physically corresponds to a resonator where no photon can escape, i.e. unloaded resonator. The corresponding degenerate effective impedance is the internal impedance $Z_{\text{sys}}^{(0)}$.

[1] For quantities oscillating close to ω_{sys}

With $Z_{\text{in}} \equiv u_{\omega,\text{in}}/i_{\omega,\text{in}}$ and $Z_{\text{in}}^{(0)} \equiv u_{\omega,\text{in}}/i_{\omega,\text{in}}$ for normal and degenerate cases, it follows:

$$Z_{\text{sys}}^{(0)} \equiv \left|\partial_\omega \left[\frac{\omega_{\text{sys}}}{2Z_{\text{in}}^{(0)}}\right](\omega_{\text{sys}})\right|^{-1}, \quad Z_{\text{eff}} \equiv \sqrt{\frac{-8Z_{\text{in}}(\omega_{\text{sys}})^3}{\omega_{\text{sys}}^2[\partial_\omega^2 Z_{\text{in}}](\omega_{\text{sys}})}}, \quad Q \equiv \sqrt{\frac{-\omega_{\text{sys}}^2[\partial_\omega^2 Z_{\text{in}}](\omega_{\text{sys}})}{8Z_{\text{in}}(\omega_{\text{sys}})}} \tag{III.2}$$

In both cases a resonator is formed:

- A piece of TL of characteristic impedance Z_{sys} allows for a stationary wave if its length is a multiple n of the quarter-wave[2]. It forms a resonance with characteristic impedance $4Z_{\text{sys}}/n\pi$;
- A capacitor C and an inductor L in parallel, as a textbook derivation shows, form a resonator at $1/\sqrt{LC}$ with characteristic impedance $\sqrt{L/C}$.

Table III.3: Characteristics of resonators

Design	$Z_{\text{sys}}^{(0)}$	Z_{damp}	Z_{eff}	Q
Cascaded $\lambda/4$	$Z_{\text{sys}}\frac{4}{\pi}$	$50\,\Omega\frac{Z_{\text{sys}}^2}{Z_\kappa^2}$	$\underbrace{Z_{\text{sys}}\frac{4}{\pi}}_{Z_{\text{sys}}^{(0)}}\sqrt{\frac{Z_{\text{sys}}}{Z_{\text{sys}}+2Z_\kappa}}$	$\underbrace{50\,\Omega\frac{Z_{\text{sys}}}{Z_\kappa^2}}_{Z_{\text{damp}}/Z_{\text{sys}}}\frac{\pi}{4}\sqrt{\frac{Z_{\text{sys}}+2Z_\kappa}{Z_{\text{sys}}}}$
LC & $\lambda/4$ transformer	$Z_{\text{sys}} \equiv \sqrt{\frac{L}{C}}$	$\frac{Z_\kappa^2}{50\,\Omega}$	$Z_{\text{sys}}\sqrt{\frac{2Z_\kappa}{2Z_\kappa+\pi Z_{\text{sys}}}}$	$\underbrace{\frac{Z_\kappa^2}{50\,\Omega\cdot Z_{\text{sys}}}}_{Z_{\text{damp}}/Z_{\text{sys}}}\sqrt{\frac{2Z_\kappa+\pi Z_{\text{sys}}}{2Z_\kappa}}$

$Z_{\text{sys}}^{(0)}$ Internal impedance
Z_{damp} Load impedance
Z_{eff} Effective impedance
Q Quality factor

In both cases, the resonator needs to be coupled to a TL in order to extract photons, the coupling to the TL can be adjusting by adding a quarter-wave transformer to transform the $50\,\Omega$ to the needed load. In the cascaded quarter-wave case, the $50\,\Omega$ is transformed two times. The second column of table III.3 shows the resulting Z_{damp}. Figure III.5 shows the impedance line shape of these two resonators, the main difference is the DC impedance, zero for an LC–circuit and $50\,\Omega$ for cascaded quarter-wave resonators.

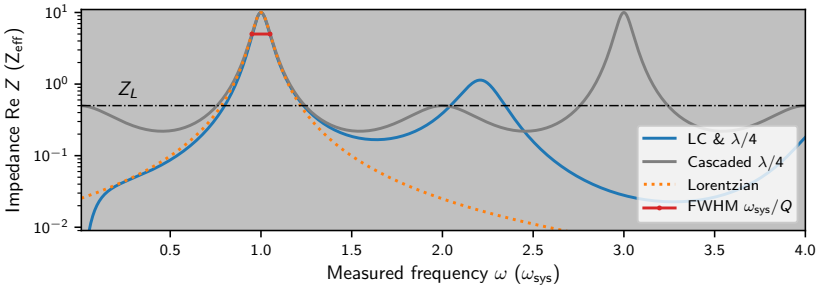

Figure III.5: **Resonator shapes.** The dotted line is the Lorentzian shape $QZ_{\text{eff}}/\left[1+4\,(Q/\omega_{\text{sys}})^2\,(\omega-\omega_{\text{sys}})^2\right]$. Blue and grey lines are the real part of the impedance of respectively an LC circuit coupled to a quarter-wave TL and two cascaded quarter-wave TL where characteristic values are chosen to give the same effective impedance and quality factor, see table III.3. A first difference is the behaviour at low-frequencies, LC & $\lambda/4$ goes to zero while cascaded $\lambda/4$ to the load impedance $Z_L \equiv 50\,\Omega$. The second difference is the existence of higher modes. The cascaded $\lambda/4$ has resonances at $(2n+1)\,\omega_{\text{sys}}$ while LC & $\lambda/4$ higher modes are lower in characteristic impedance.

[2] If there is a node a one end, there is an anti-note at the other. However, it is only a necessary condition, not sufficient.

In order to apply equation III.2 to our models, `sympy` is used. First, it is used to solve Z_{in} for each model. Then it finds the resonance frequency ω_{sys} and performs a second order Taylor expansion of Re Z_{sys} around ω_{sys}, where only the two first dominant terms are kept. Table III.3 shows the final expressions.

2.b Fabrication capabilities

Now let's see how flexible our designs are. From numerical simulations (done with *Sonnet* & home-made software), feasible parameters ranges for each element are determined – see table III.4. And finally figure III.6 shows which resonator parameters can be designed.

Table III.4: Order of magnitude

Quantity	Minimum	Maximum
Spiral inductor	0.1 nH	100 nH
Face to face capacitor	10 fF	200 pF
Frequency LC	35 MHz	160 GHz
CPW $\lambda/4$	20 Ω	180 Ω
Microstrip $\lambda/4$	0.1 Ω	50 Ω
Frequency $\lambda/4$	20 MHz (2.5 m)	1.2 THz (NbN gap)

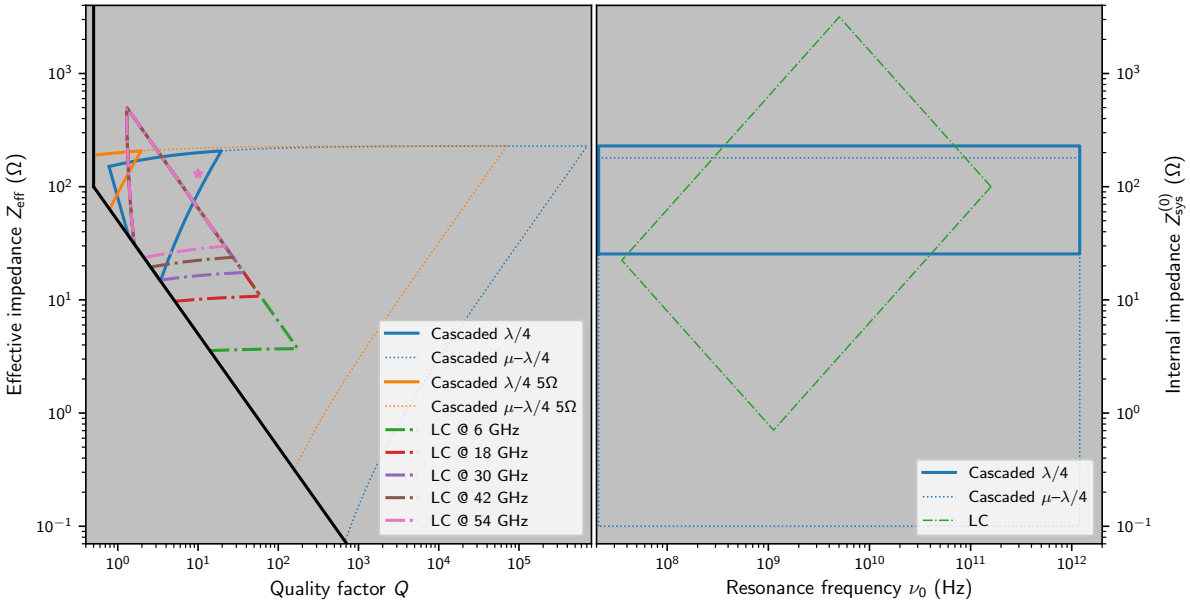

Figure III.6: **Characteristics of our resonators.** ***Left panel:*** Black border delimits the region where $Q \geq 1/2$ and $QZ_{\text{eff}} \geq 50\,\Omega$ which are requirements to be under-damped and have an impedance at resonance frequency above $Z_L \equiv 50\,\Omega$. Each triangle delimits the $Q - Z_{\text{eff}}$ space accessible with each design. Note that higher Q can be reached with additional $\lambda/4$ transformers. For LC & $\lambda/4$ the different triangles show how the space shrinks with the frequency. The star indicates the typical resonator used in our device, see chapters IV and V. ***Right panel:*** Each parallelogram delimits the $\nu_0 - Z_{\text{sys}}^{(0)}$ space accessible with each design ($\nu_0 \equiv 2\pi\omega_{\text{sys}}$).

Part B

Experimental results

Chapter IV

Non-classical radiation

French resume

Ce chapitre s'intéresse à la réalisation d'une source de photons non-classique en utilisant l'ICPT. Une première partie décrit le dispositif expérimental et la manière dont il utilise l'ICPT pour produire des photons dans un régime quantique. La mesure expérimentale de la PSD permet alors de caractériser l'échantillon grâce à la théorie P :

- Le courant critique;
- La température thermodynamique;
- L'impédance vue par la jonction Josephson.

On peut ensuite étudier deux modes de fonctionnement : un mode libre et un à la demande. Le premier est celui pour lequel l'échantillon a été conçu. Le second tire profit d'un comportement inattendu : un courant critique important permet d'échapper au régime décrit par l'ICPT et d'atteindre un comportement non-radiatif où l'échantillon est essentiellement résistif. Pour les deux modes, la PSD et la $g^{(2)}$ sont mesurées pour caractériser notre échantillon.

Contents

Preamble The results of this chapter have been submitted for publication [*Grimm18*]. The device includes an on-chip resistor that has to be very cold (see below), and has to be designed properly to provide sufficient cooling. This aspect has been studied in previous work [*Grimm15*; *Grimm18*], and will not be detailed here.

1 Design

Here, the design used to achieve a source of single photons is presented. First the working principle of the sample studied previously by M. Hofheinz [*Hofheinz11*] is recalled, then an update to turn from coherent to single photon operating mode is developed.

1.a Coherent source

[*Hofheinz11*] studied a source made of two quarter-wave TL. Figure IV.1 shows this design. The peak at 6 GHz of the P-function corresponds to a Cooper pair tunnelling and dissipating its energy in the form of a photon inside the resonator. From now, we will focus on this process. As there is a peak at zero energy, no charging energy is required for tunnelling. Consequently, the Cooper pairs tunnel freely and independently, and each Cooper pair that tunnels creates a photon inside the resonator. Photons coming from the resonator are, therefore, also independent, which corresponds to a coherent state.

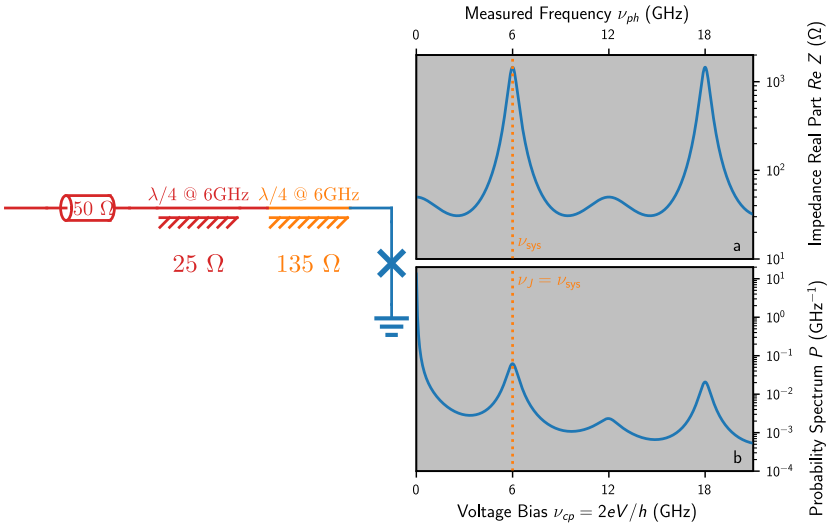

Figure IV.1: **Coherent source.** ***Left scheme*** shows the two cascaded quarter-wave TL, the orange one mainly defines the resonator impedance while the red one together with the 50 Ω port defines the Q factor. The Josephson junction is in blue. ***Panel a*** shows the real part of the impedance as a function of the frequency, there are modes at $(2n+1)\,\nu_{\rm sys}$, 6 GHz and 18 GHz peaks are visible. ***Panel b*** shows the corresponding P-function as a function of the voltage bias expressed in GHz. The peaks correspond to biases where Cooper pair tunnelling can happen. The zero bias peak is the supercurrent, the second and last correspond to first order processes with photons at respectively 6 GHz and 18 GHz, the third one is a second order process where a Cooper pair gives two photons at 6 GHz. ***Orange dotted lines*** indicate the process used as photon source.

The coherent state is also recovered by applying the interaction Hamiltonian[1] $e^{-i\sqrt{Z_{\rm sys}/(R_Q/\pi)}b^\dagger}$ to the vacuum state $|0\rangle$, then it displaces the vacuum[2] by $-i\sqrt{Z_{\rm sys}/(R_Q/\pi)}$, i.e. a coherent state by definition.

[1] Chapter V will give more details about it.
[2] The previous expression includes only one term of the displacement operator for brevity.

1.b Working principle

To turn this source in to a SPS, an RC circuit is added. The goal is to require an excess charging energy together with the photon energy for Cooper pairs to tunnel. Moreover, if the charging energy is higher for a second Cooper pair, the bias voltage is not sufficient to provide the increased charging energy and the photon energy, therefore photon emission is prevented. Consequently, an RC circuit with a large enough relaxation time – larger than resonator relaxation time – fits the requirements. The energy to charge the capacitor with a first Cooper pair is $(2e)^2/2C$ while it becomes $(2\cdot 2e)^2/2C - (2e)^2/2C = 3\cdot(2e)^2/2C$ for a second Cooper pair (see figure IV.2). Moreover, the resistor tunes the relaxation time $\simeq RC$. Note here that to avoid thermal charging of the capacitor, the capacitor has to be small:

$$C \ll \frac{(2e)^2}{2k_B \cdot 20\,\mathrm{mK}} \simeq 186\,\mathrm{fF} \tag{IV.1}$$

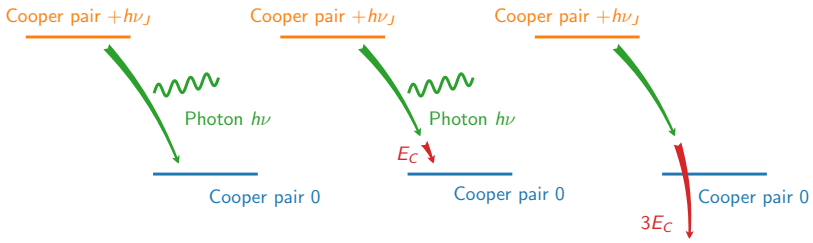

Figure IV.2: **Blocking mechanism.** ***Left diagram*** Coherent source. Tunnelling happens when the Cooper pair energy $h\nu_J$ and photon energy $h\nu$ are equal. Then each tunnelling Cooper pair gives a photon. ***Centre diagram:*** The same process in presence of a high impedance RC circuit where a charging energy E_C is required for a Cooper pair to tunnel and charge the capacitor, while dissipating the remaining energy as a photon. ***Right diagram:*** When the capacitor is already charged, the charging energy to pay is now $3E_C$, consequently energies are not balanced any more blocking further tunnelling and photon emission.

Figure IV.3 shows this design and corresponding P-function displaying a shift by E_C with the characteristics due to the charging mechanism. There is also a broadening of all processes, a consequence is that two different processes are more likely to happen at the same voltage bias. For example, if the process shown by the vertical orange dotted line is driven at a slightly lower bias, the process can still be driven but tunnelling whitout photon emission is also possible. We therefore expect emission along wide ranges of bias.

1.c Implementation

To experimentally implement this new design, a capacitor has to be designed. The way chosen was to take advantage of the flux bias which has to be close to the SQUID. This line has been designed to cross the line of the SQUID, and so it forms a capacitor, see figure IV.4.

However, this way to realise the capacitor designed for DC flux has a drawback, it introduces unwanted coupling between the flux line and the voltage bias. Modulation of the flux bias also modulates the voltage bias through an inductive and capacitive coupling (see figure IV.4).

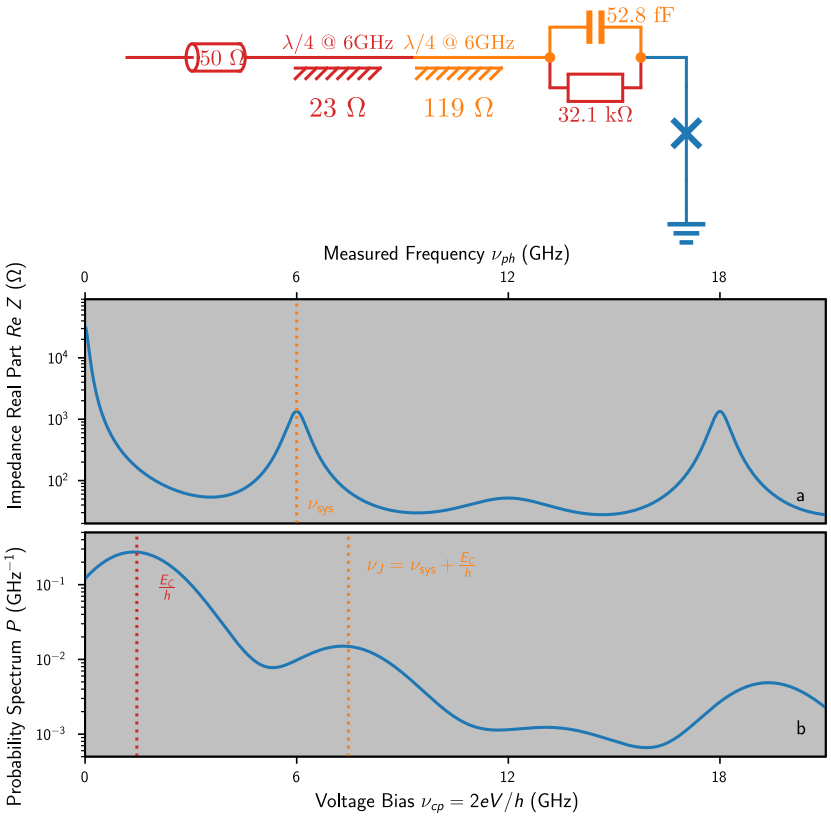

Figure IV.3: **SPS design.** ***Top scheme*** shows how the coherent source is modified to include a blocking mechanism: An RC circuit is added. In orange the capacitor that will be charged by tunnelling Cooper pairs, in red the resistor that dissipates those charges. ***Panel a*** shows the real part of the impedance as a function of the frequency. Compared to the previous scheme, the impedance at low-frequencies is high. ***Panel b*** shows the corresponding P-function as a function of the voltage bias expressed in GHz. Now the peaks are shifted by E_C/h, a signature of the charging mechanism: Cooper pairs have to charge the capacitor while tunnelling. ***Orange dotted lines*** indicate the process used as SPS: A Cooper pair biased at $\nu_J \equiv \nu_{\rm sys} + E_C/h$ tunnels while charging the capacitor $E_C \equiv (2e)^2/2C$ and creating a photon at $\nu_{\rm sys}$ in the resonator.

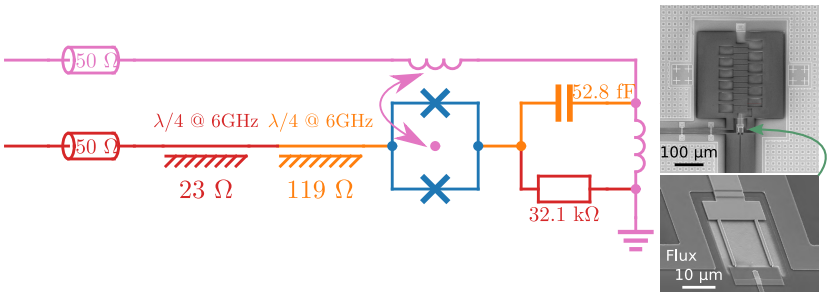

Figure IV.4: **SQUID and RC.** ***Right micrographs*** show how the capacitor is made. The flux line – used to tune the effective critical current of the SQUID – crosses the line between the SQUID and the resistor. Moreover, the short wire to ground after the crossing is equivalent to an inductance. ***Left scheme*** updates the previous scheme (figure IV.3) taking into account this coupling. In pink the elements added for the flux control.

2 PSD measurements & characterisation

This second section is dedicated to show how PSD is used to extract P-function and impedance seen by the junction, following the theory recalled in chapter I section 1.b.

2.a Characterisation in the P-theory regime

All this section is based on equation I.26:

$$\gamma_\nu^{\rm out}(\nu_J,\nu) \simeq \frac{h{I_c}^2}{2}\,{\rm Re}\left[Z_\nu(\nu)\right]P(h\nu_J - h\nu) \tag{IV.2}$$

First of all, this equation requires the Josephson junction to be a small perturbation, i.e. $\bar{\phi}_0 I_c \ll \hbar\nu_0$. At 6 GHz this corresponds to $I_c \ll 1.9\,$nA. We reach this limit by almost completely frustrating the SQUID. Figure IV.5 shows the corresponding PSD.

First, integrating along ν_J gives $h{I_c}^2\,{\rm Re}\left[Z_\nu(\nu)\right]/2$ thanks to the normalisation property of the P-function. Subsequently, dividing the PSD by this quantity gives $P(h\nu_J - h\nu)$ for many ν_J, ν. Finally, a

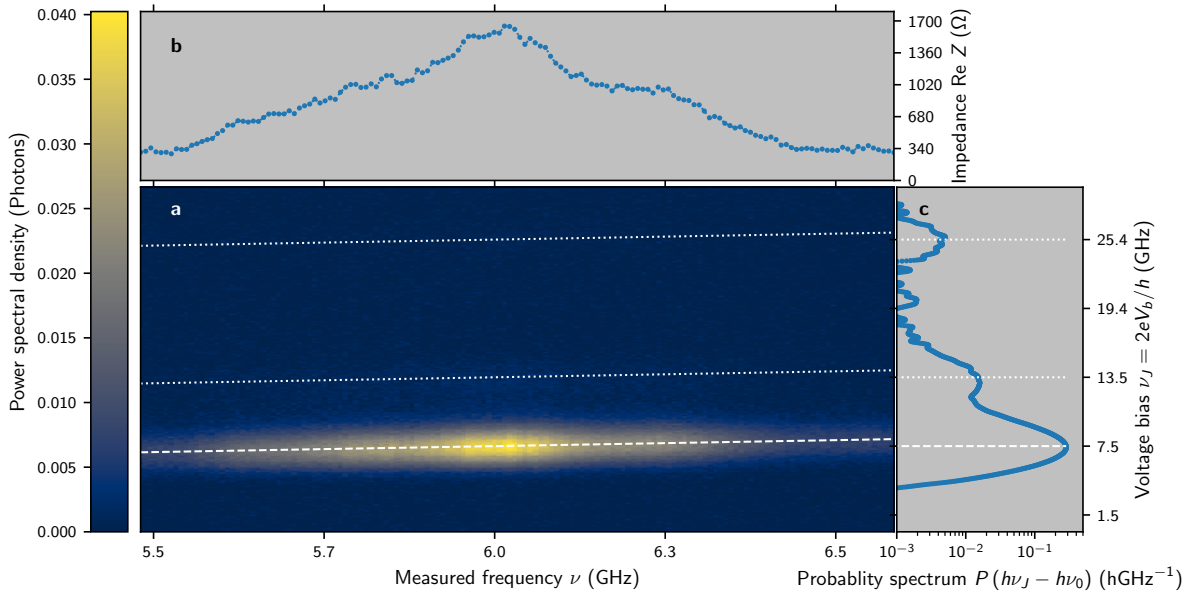

Figure IV.5: **Low current PSD & P-function.** ***Panel a*** is the PSD as a function of the frequency and the voltage bias expressed in frequency. The dashed white line is the first order process $\mathrm{CP}_{\nu_J} \underset{E_C}{\to} \mathrm{Ph}_\nu$, the dotted while lines are second order processes, respectively $\mathrm{CP}_{\nu_J} \underset{E_C}{\to} \mathrm{Ph}_\nu + \mathrm{Ph}_{\nu_0}$ and $\mathrm{CP}_{\nu_J} \underset{E_C}{\to} \mathrm{Ph}_\nu + \mathrm{Ph}_{\nu_1}$ where $\nu_n \equiv (2n+1)\,\nu_{\mathrm{sys}}$ are the resonance frequencies of the different modes. ***Panel b*** is the real part of the impedance as a function the frequency extracted from the PSD (see panel a). Up to a prefactor, it is the integration over bias of the PSD (see text). ***Panel c*** is the P-function as a function of the bias. Up to a prefactor, the PSD is the integration along the dotted and dashed while lines of the PSD (see text).

normalised window function $w(\nu_J, \nu, \nu') \propto e^{-\left(\nu_J-\nu-\nu'\right)^2/2\sigma^2}\gamma_\nu^{\mathrm{out}}(\nu_J, \nu)$ is used to extract $P(h\nu')$:

$$P(h\nu') \simeq \int\int P(h\nu_J - h\nu)\, w(\nu_J, \nu, \nu')\, \mathrm{d}\nu_J\, \mathrm{d}\nu \tag{IV.3}$$

Integration is performed over the measurement space. This corresponds to integration parallel to the dashed and dotted lines in figure IV.5. Figure IV.5 shows the P-function on the right panel.

Moreover, white lines show the three different processes:

- A first order process where one Cooper pair gives one photon at ν_0 and charging the capacitor with one Cooper pair;
- Two second order processes where one Cooper pair gives two photons (two at ν_0 or one at ν_0 and one at $3\nu_0$).

Electronic temperature extraction

From the P-function, the thermodynamic temperature can be extracted (see equation C.7 for derivation):

$$P(-h\nu_J) = e^{-\beta h\nu_J} P(h\nu_J) \tag{IV.4}$$

Inverting this relation, β can be expressed as a function of the frequency ν_J:

$$\beta(\nu_J) = \frac{\ln P(h\nu_J) - \ln P(-h\nu_J)}{h\nu_J} \tag{IV.5}$$

Figure IV.6 shows this relation, even through it should be constant, numerical errors and algebraic properties induces variations.

Differential form associated to equation IV.5 is:

$$\delta\beta\left(\nu_J\right) \;=\; \frac{\delta P\left(h\nu_J\right)}{h\nu_J}\left(\frac{1}{P\left(h\nu_J\right)}+\frac{1}{P\left(-h\nu_J\right)}\right) \tag{IV.6}$$

Therefore we use a normalised weight function $\propto \nu_J/P\left(h\nu_J\right)^{-1}+P\left(-h\nu_J\right)^{-1}$ (orange line on figure IV.6) get an averaged the thermodynamic temperature of 20.9 mK.

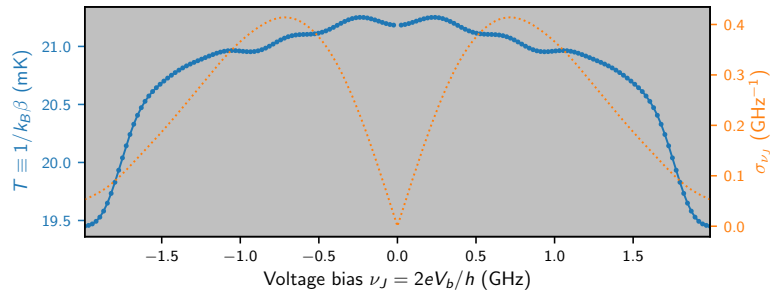

Figure IV.6: **Temperature extraction.** ***Left axis*** is the temperature as a function of the bias following equation IV.5, when far from zero, P is small and then the value extracted with equation IV.5 can diverge. ***Right axis*** is the window function used to mean the temperature taking into account where equation IV.5 is the less noisy, see equation IV.6.

Critical current extraction

In order to extract the critical current of the SQUID, let's recall the *Minnhagen relation*:

$$\nu_J P\left(h\nu_J\right) \;=\; \int_{\mathbb{R}} P\left(h\nu_J - h\nu\right)\,\frac{\mathrm{Re}\left[Z_\nu\left(\nu\right)\right]}{R_Q/2}\,\frac{1}{1-\;e^{-\beta h\nu}}\;\mathrm{d}\nu \tag{IV.7}$$

Together with equation IV.2 and P normalisation, it can be rewritten:

$$\frac{h{I_c}^2}{4}\int \mathrm{d}\nu_J\;\nu_J P\left(h\nu_J\right)\sigma_{\nu_J}\left(\nu_J\right) \;=\; \int \mathrm{d}\nu\;\frac{1}{R_Q}\frac{1}{1-\;e^{-\beta h\nu}}\;\underbrace{\sigma_\nu\left(\nu\right)}_{\int \mathrm{d}\nu_J\;\sigma_{\nu_J}(\nu_J)P(h\nu_J-h\nu)}\;\underbrace{\int \mathrm{d}\nu_J\;\gamma_\nu^{\mathrm{out}}\left(\nu_J,\nu\right)}_{\frac{h{I_c}^2}{2}\,\mathrm{Re}[Z_\nu(\nu)]} \tag{IV.8}$$

All terms excepted I_c and σ_{ν_J} are known, now a well adapted choice for σ_{ν_J} can limit integration to measurement ranges.

The two black lines on figure IV.7 show that a sharp integration of P around 7.4 GHz corresponds to an integration in frequency space around 6 GHz. However even through this integration is done with a sharp Gaussian shape, the corresponding integration is too wide. A way to reduce the integration range is to include negative values in σ_{ν_J}. The orange lines show this behaviour.

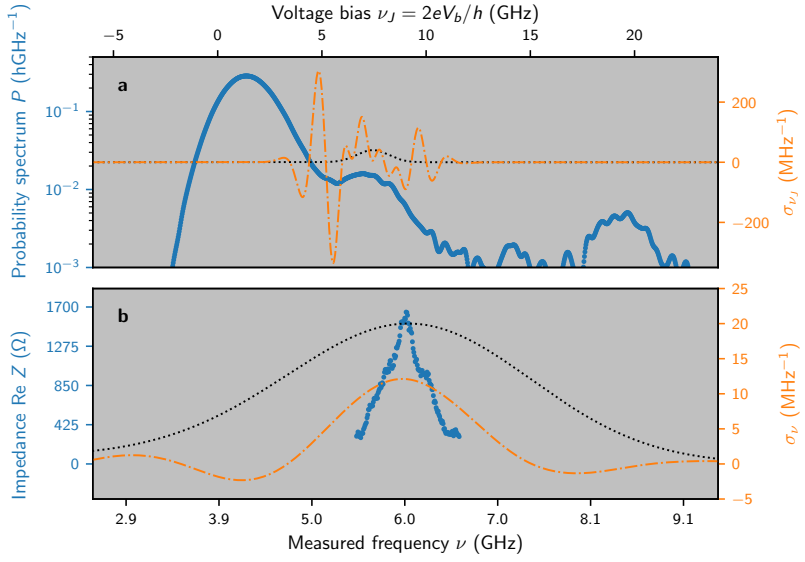

Figure IV.7: P**-function extraction.** ***Panel a*** is the P-function (in blue) as a function of the bias, it is the same data as figure IV.5. ***Panel b*** is the real part of the impedance as a function of the frequency, it is the same data as figure IV.5. ***The dotted black line on both panels*** is the window function used to extract the critical current (see equation IV.8): On panel a the window function is chosen as a Gaussian, while on panel b the window function is the convolution of the first window function and $P\left(arg1\right)$-function (see equation IV.8 & text). ***Dashed orange line on both panels*** are different weight functions, see panel a. A wise choice of the initial window function can give a final window function with most of the weight where the data have been measured.

For now, the construction of σ_{ν_J} is empirical. I choose an orthonormal basis made of Hermite functions and maximise the weight of σ_ν inside the measurement range. However, this method has drawbacks:

- The oscillation of σ_{ν_J} can lead to a numerical value close to 0, and consequently a diverging result due to numerical errors;
- If the impedance outside the measurement range is high, even a small amount of σ_ν outside the measurement range can lead to an important error.

To confirm our method, I also apply it to a measurement covering a wider frequency range. Figure IV.8 shows this comparison; the left panel and blue line are the previous measurement, the right one and orange line is the second measurement done after with a slightly different critical current.

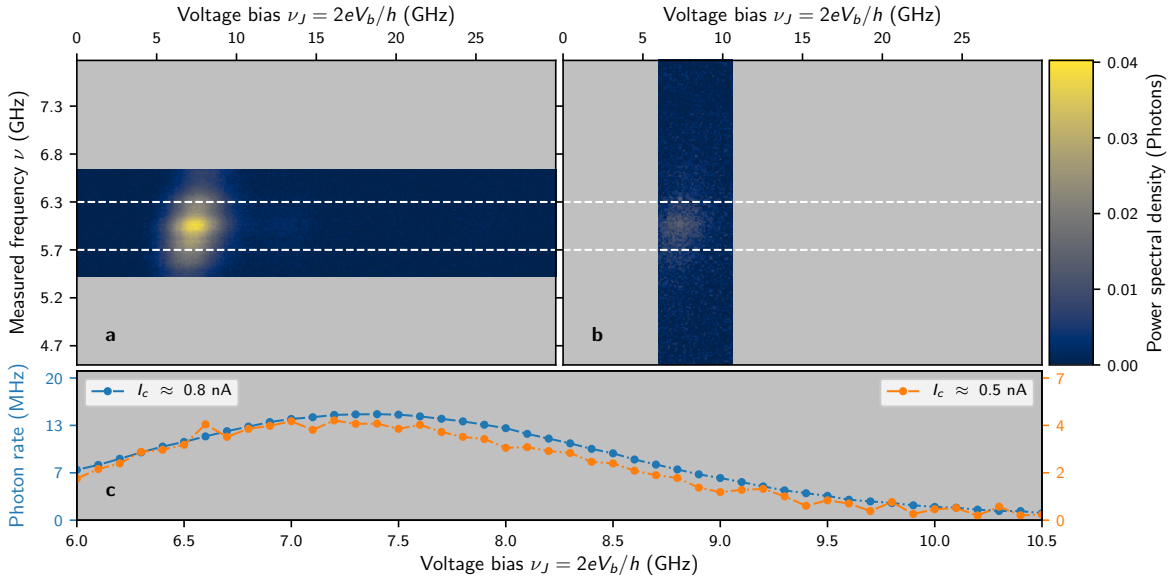

Figure IV.8: **Critical current extraction for different measurement ranges.** ***Panel a*** is the PSD as a function of the bias and the frequency. Dotted white lines delimits the FWHM of the resonator. Here the data are the same as previously. ***Panel b*** is the PSD as a function of the bias and the frequency. Here the data are taken at a lower critical current and measured over a different range. ***Panel c*** is the photon rate – integration of the PSD over the FWHM – as a function of the bias. Left axis corresponds to panel a and right one to panel b, the two critical current are determined with equation IV.8 (see also text). Right scale is the left one multiplied by $(0.5\,\mathrm{nA}/0.8\,\mathrm{nA})^2$. The curves should superpose if the sample is operated in the P-regime and the extracted critical currents are correct. The difference between the two critical current extraction is that the second one is done over a wider frequency range, and so the window functions for integration are easier to choose (see text and figure IV.7).

On the bottom panel, left and right are scaled according to the critical current as blue and orange lines should superpose.

2.b Blocking mechanism

When the critical current is increased – thanks to the flux bias – another working regime can become dominant. Indeed, the resistor results in a high-impedance environment at low-frequencies, and so when the current flowing though the system is too high, a non negligible voltage drops over the resistor. And finally the voltage can even be fully dropped over on the resistor as a Josephson junction locks to the zero-voltage state when the critical current is large enough.

This mechanism is very different from the previous P-theory, there is no more photonic aspect and all the energy is dissipated in the resistor. Therefore, the following measurements will exhibit different regions where photon emission happens or is blocked. The last section of this chapter actually uses this mechanism for on-demand emission.

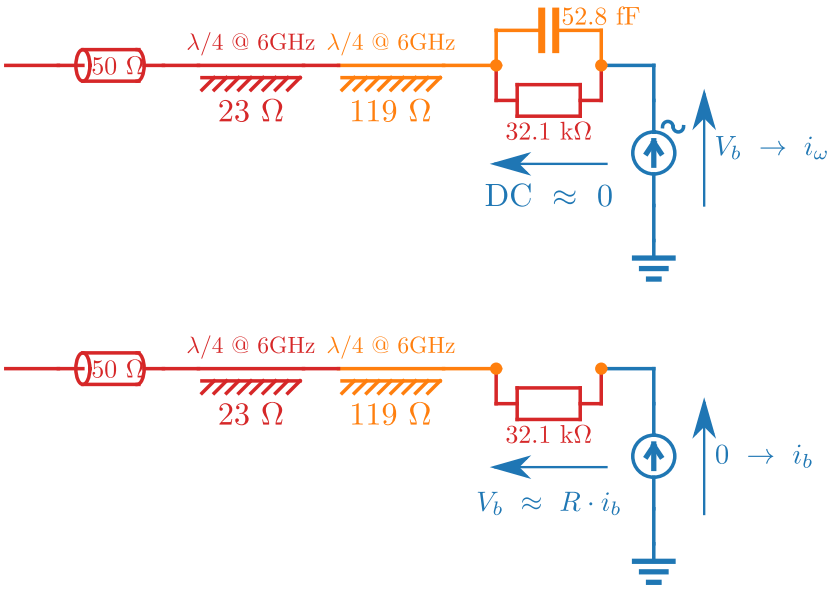

Figure IV.9: **Dark state of the device.** ***Top scheme*** is the standard operating mode, the Josephson junction is DC biased and results to an oscillating current[a]. ***Bottom scheme*** is the blocking operating mode, the Josephson junction is in zero-voltage bias state and admits a DC current while the applied bias drops over the resistor. However, this state is possible only if the critical current is high enough: $I_c \geq V_b/R$.

[a] There is also a DC component, see chapter I.

DC current

In order to better investigate this blocking mechanism, a DC current measurement is very helpful: When the device is in the dark state, the current flows as if only the load was there. Figure IV.10 shows this measurement. As excepted the current follows the resistance load-line (dark line on right panel) at 32.1 kΩ.

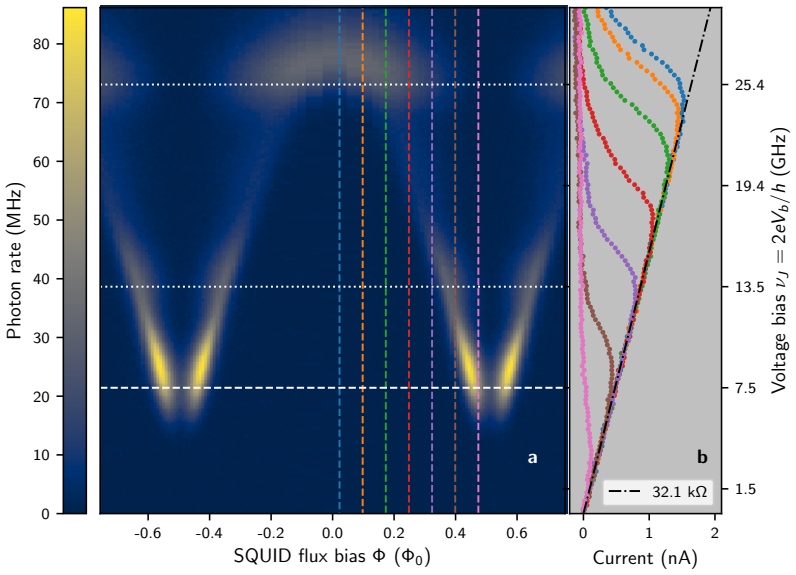

Figure IV.10: **Cross PSD & DC current.** ***Panel a*** is the photon rate – integration of the PSD over the measured frequencies – as a function of the SQUID flux bias – i.e. the effective critical current – and the voltage bias. ***Panel b*** is the DC current as a function of the voltage bias at different flux biases (vertical dotted lines of panel a). There is a correlation between a resistive behaviour – equivalent to 32.1 kΩ – and the region where there is no emission. It is explained by an effective critical current high enough to lock the SQUID to the zero-voltage state, so that the bias voltage drops over the resistor, see figure IV.9. Then the load-line at 32.1 kΩ corresponds to the resistor of the RC circuit. Note that the two measurements have been performed in different cool-downs. There may be a slight difference in the effective critical currents.

Another way to confirm that interpretation is to look at the resonator frequency. Actually when the device is in the dark state the SQUID is in its zero-voltage state and consequently behaves as an inductance following the rule:

$$L_J(\phi) \equiv \frac{\bar{\phi}_0}{I_c^{\max} |\cos(\phi/2\,\bar{\phi}_0)|} \tag{IV.9}$$

This inductance subsequently shifts upward the resonator frequency in the region where the mechanism is blocked. Figure IV.11 shows a measurement of the resonator frequency done with a VNA. It confirms our interpretation and a closer look at the border between the regions shows the blocking is continuous.

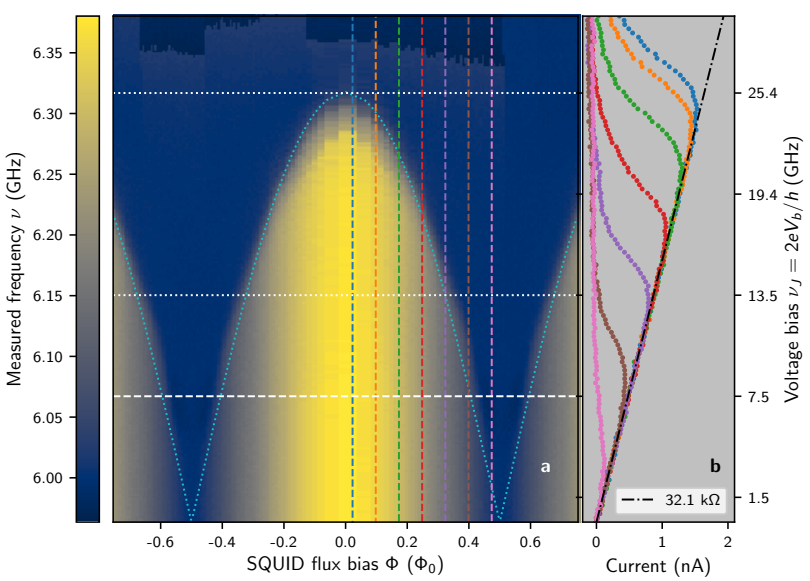

Figure IV.11: **Resonator frequency.** ***Panel a*** is the resonator frequency – measured with a VNA – as a function of the SQUID flux bias – i.e. the effective critical current – and the voltage bias. ***Panel b*** is the DC current as a function of the voltage bias at different flux bias (vertical dotted lines of panel a). There is a correlation between a resistive behaviour – equivalent to 32.1 kΩ – and the region where the frequency is higher. Both are explained by an effective critical current being high enough to lock to the zero-voltage state, see figure IV.9. Indeed, in that case the SQUID behaves as an inductance which effectively shifts the resonator frequency. Note that the two measurements have been performed in different cool-downs. There may be a slight difference in the effective critical currents.

Numerical calculations

In order to verify that our model (see figure IV.9) accurately captures the device behaviour we numerically calculate Z and P and compare it to the measured quantities. Before going further in numerical calculations, let's recall the values extracted from the actual measurements: Even through all those parameters can be

Table IV.1: Parameters extracted from measurements

ν_0	C	$1/k_B\beta$	I_c	Q	Z_0	R	RC
5.98 GHz	56.7 fF $\frac{2e^2}{hC} \equiv 1.37\,\text{GHz}$	20.9 mK	0.86 nA	10.9 $\frac{\nu_0}{\Delta\nu}$ FWHM	106 Ω $\text{Re}\,Z(\nu_0) \equiv QZ_0$	32.1 kΩ	1.82 ns

roughly estimated, the ones corresponding to the resonators have been extracted by a fit with a Lorentzian shape.

To go further, PSD have been calculated numerically and fitted with the measurement with a least squares algorithm starting with the extracted values. Finally, the impedance seen by the junction and

Table IV.2: Parameters fitted from measurements

ν_0	C	$1/k_B\beta$	I_c	Q	Z_0	R	RC
5.99 GHz	52.8 fF $\frac{2e^2}{hC} \equiv 1.47\,\text{GHz}$	21.4 mK	0.85 nA	10.39 $\frac{\nu_0}{\Delta\nu}$ FWHM	129 Ω $\text{Re}\,Z(\nu_0) \equiv QZ_0$	32.1 kΩ not fitted	1.69 ns

P-function can be calculated numerically with those values.

First, the impedance shown on figure IV.12 (green line). The simulation is consistent with the measurement, except a small modulation of the order of 200 MHz, which can be attributed to stationary waves at base temperature – 200 MHz corresponds to 20 cm which is the coaxial cable length at base temperature. Second, the P-function is seen on figure IV.13 (solid green line). Again the simulation is consistent with the measurement. Empirically the difference between both (around 5 GHz) can be compensated by a small capacitance in parallel with the junction, however even if such a capacitance exists its value is too small (compared to the main capacitance) to be properly fitted.

On figure IV.13, the theoretical curve without the RC circuit (i.e. without the blocking mechanism) is shown. The differences between both curves highlights the influence of the RC circuit:

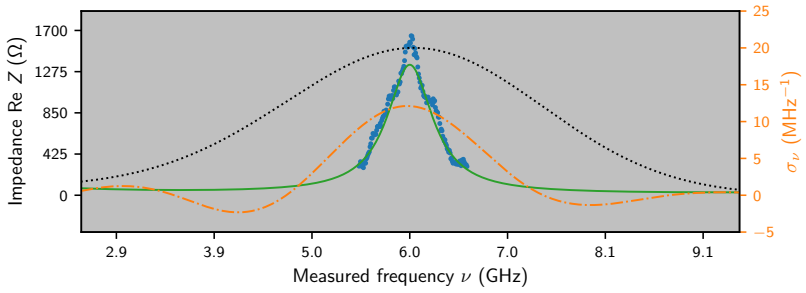

Figure IV.12: **Impedance simulated** as a function of the frequency (solid green). For comparison, data (and window functions) extracted before are recalled (see figure IV.7). The simulation is done with numerical values, see table IV.2, obtained by fitting the full PSD with our numerical simulation.

- Each peak is thermally and lifetime broaden by the resistance of the RC;
- Each peak is shifted by the charging energy.

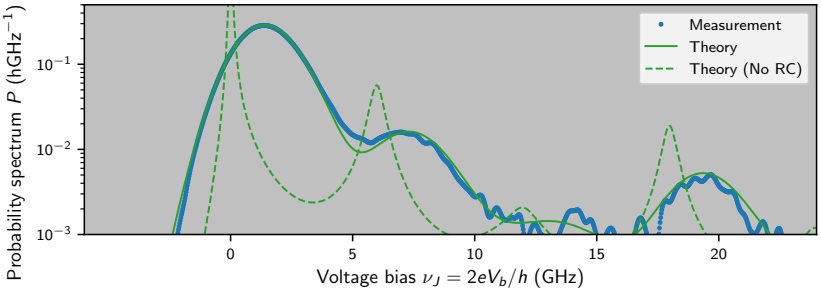

Figure IV.13: ***P*-function simulated** as a function of the frequency (solid green). For comparison, data extracted before are recalled. The simulation is done with numerical values, see table IV.2, obtained by fitting the full PSD with our numerical simulation. Dashed green is the simulation without the RC circuit – i.e. no charging mechanism – the shifting due to the charge energy is recovered as excepted.

3 Free-running mode

Two kinds of experiments have been conducted:

Free-running: where the flux bias is fixed and photons continuously flow from our source;

Pulse-mode: where the flux bias is pulsed, with the goal of emitting a single photon per cycle.

This section is dedicated to the first one. We start with a description of calibration methods necessary to accurately measure photon correlations.

3.a Calibration

Calibration drifts

Whereas PSD measurements are quick to conduct, $G^{(2)}$ have to be repeated many times up to several 100 h to beat the low SNR. Consequently, the channel gains and noises may drift. As we measure repeatedly our device one time switched *on* $G_n^{(1),\mathrm{on}}$ and one switched *off* $G_n^{(1),\mathrm{on}}$, if only the channel noises vary it will be compensated by our method, however a variation is still observed, meaning the channel gains vary and can be quantified if no variation on noises are assumed. This assumption is supported by the distribution of gains and noises over each channel: As the channel noise mainly comes from the 4 K stage – which its temperature does not vary a lot due to the monitoring of the fridge automaton – while the gain is distributed over many stages (including a part at room temperature).

Blue dots on figure IV.14 panel c show the result when the calibration is done with a single value, blue dots spreads somewhat meaning the calibration drifts over time. The initial calibration gives the $G^{(1),\mathrm{ref}}$ of the input added noise, subsequently the instantaneous gain is $G_n = G^{(1),\mathrm{off}}/G^{(1),\mathrm{ref}}$ assuming constant amplifier noise, G_n are averaged to remove short time variations due to statistical errors in the $G^{(1)}$ measurement. Blue and orange lines on figure IV.14 panel a show those new calibrations and orange dots on figure IV.14 panel c shows the result with those new calibrations.

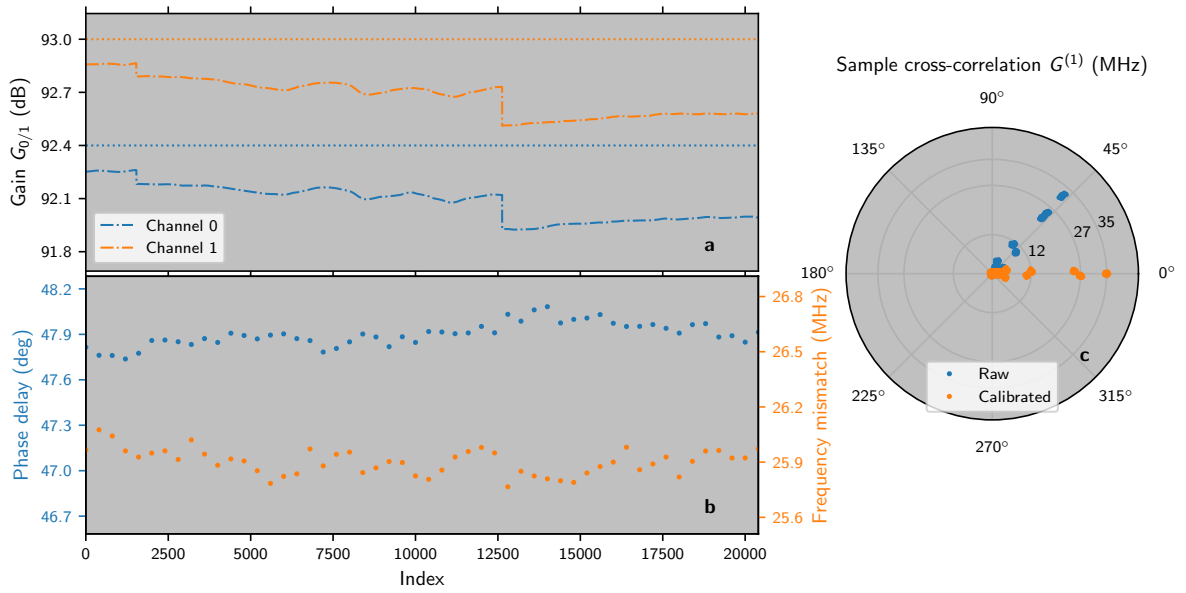

Figure IV.14: $G^{(1)}$ **&** $G^{(2)}$ **calibration.** ***Panel a*** shows the different gains as a function of the index of the measurement which is repeated many times. Blue lines correspond to the first channel, orange ones to the second channel. Dotted lines are the gain determined by a calibration measurement done before (see chapter II), dashed ones are the instantaneous gains determined by using $G_n^{(1),\text{off}}$ and $G^{(1),\text{ref}}$ – also determined by the calibration measurement – which affected by gain fluctuations (see text). ***Panel b left axis*** is the phase delay between the two channels as a function of the index, it depends mainly on the length difference between the two channels and so is almost constant. ***Panel b right axis*** is the frequency mismatch between the centre frequency and the centre of the measurement range as a function of the index. This mismatch is responsible for the phase variation of $G^{(1)}$ with τ. Here, the mismatch of 25.9 MHz is negligible compared to the FWHM of the resonator. ***Panel c*** are all the samples on the same complex space, each group of dots corresponds to one value of τ, centre groups correspond to long τ, the group with maximal amplitude corresponds to $\tau = 0$. Blue dots are $G^{(1)}$ calibrated with the initial gains (dotted lines of panel a) and orange dots with the instantaneous gain (dashed lines of panel a) and corrected for phase delay and frequency mismatch (panel c): Each group of dots is smaller (due to the instantaneous gain), and there is no more overall phase shift (due to phase delay correction) and variation of phase between each group (i.e. variation with τ) is reduced.

Moreover, if the signal after down-conversion is not centred at 1.5 GHz, $G^{(1)}$ can be rewritten $G^{(1)}(2n/2\,\text{GHz}) \propto e^{i2\pi|\nu_0-\nu_{LO}|2n/2\,\text{GHz}}(-1)^n$. The orange line on figure IV.14 panel b shows this mismatch $||\nu_0 - \nu_{LO}| - 1.5\,\text{GHz}|$. The blue line is the overall delay between both channels.

Kernel influence

As explained in chapter II section 2.a a numerical filter is used to increase the SNR when measuring $G^{(2)}$, figure IV.15 panel a shows the kernel filter together with the impedance seen by the junction. First our kernel is very selective: It focuses on the region extending over the FWHM of the impedance. However, it also means that $G^{(1)}$ encompasses only a part of the full emitted power.

To quantify this efficiency, the parameters determined previously are very useful. Actually the efficiency is given by the ratio between the power inside the kernel and the power over a wide range that can be simulated. Figure IV.15 panel b shows this ratio in orange, in blue it corresponds to a flat kernel as used by the PSD. The order of magnitude is consistent with a Lorentzian shape which slow roll off and extending over a wide range.

We now verify the consistency of our two methods. Figure IV.16 shows the photon rate emitted by our sample and cuts in three orientation (blue lines). Superimposed dots are $G^{(1)}(0)$ measured for different parameters. For both PSD and $G^{(1)}$ they are renormalised with the efficiency determined before, and now dots are along respective lines. The good agreement between photon rate extracted from PSD and $G^{(2)}$ validates our analysis.

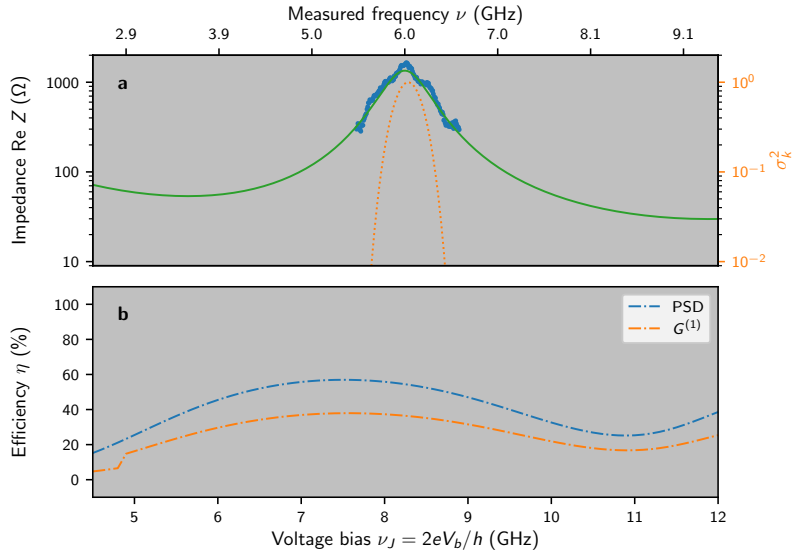

Figure IV.15: **Power in the kernel.** ***Panel a left axis*** is the real part of the impedance as a function of the frequency, blue dots are the measurement while the green line is the simulation. ***Panel a right axis*** is the numerical kernel used to measure $G^{(1)}$ as a function of the frequency. It rolls off faster than the resonator, i.e. $G^{(1)}$ does not include all the power. ***Panel b*** is the efficiency – defined as the power inside the kernel relative to the full power – as a function of the voltage bias. The blue line corresponds to the kernel used for the PSD which is flat over all the measurement range, the orange line corresponds to the kernel used for the $G^{(1)}$.

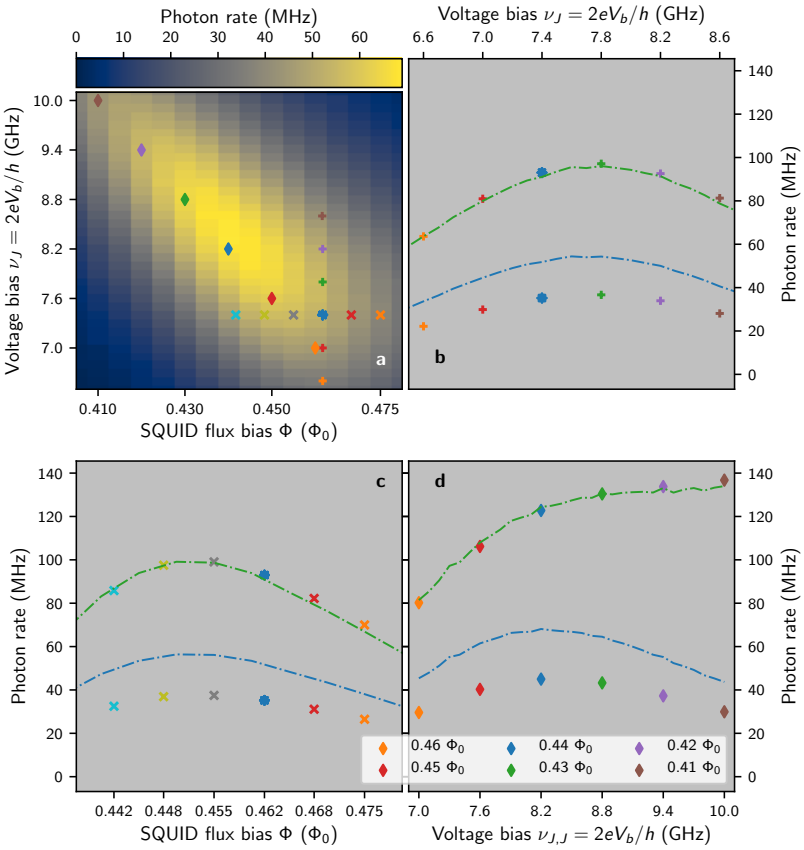

Figure IV.16: **Kernel consistency.** ***Panel a*** is the photon rate obtained via integration of the PSD over the measured frequencies as a function of the SQUID flux bias and the voltage bias. Plus, cross and diamonds indicate parameters where $G^{(1)}$ are measured. ***Panel b, c & d*** are the photon rates as functions of the voltage bias and show the photon rate, respectively along the vertical, horizontal and diagonal lines of markers in panel a. Blue line is the data of panel a, bottom symbols are the measured $G^{(1)}$. Green line and top symbols are the same data corrected with the corresponding efficiency, see figure IV.15.

3.b Parameter space exploration

Finally, $G^{(2)}$ is extracted from the data for each parameter identified before, and then normalised with:

$$g^{(2)}(\tau) \equiv \frac{G^{(2)}(\tau)}{G^{(1)}(0) \cdot G^{(1)}(0)} \tag{IV.10}$$

First, figure IV.17 shows the evolution of $g^{(2)}$ with flux bias. The lowest value measured is $g^{(2)}(0) = 0.57$ for a flux close to the frustration $\phi \simeq 0.5\,\bar{\phi}_0$. As we approach lower flux biases – in order to increase the critical current – the dip remains, but a broad bunching peak develops around it. We attribute this broad peak to random jumps between the bright voltage state of the junction and the dark zero-voltage

state discussed above. This is consistent with the reduction in emission rate observed. Moreover, the dip remains and the blocking mechanism is still active.

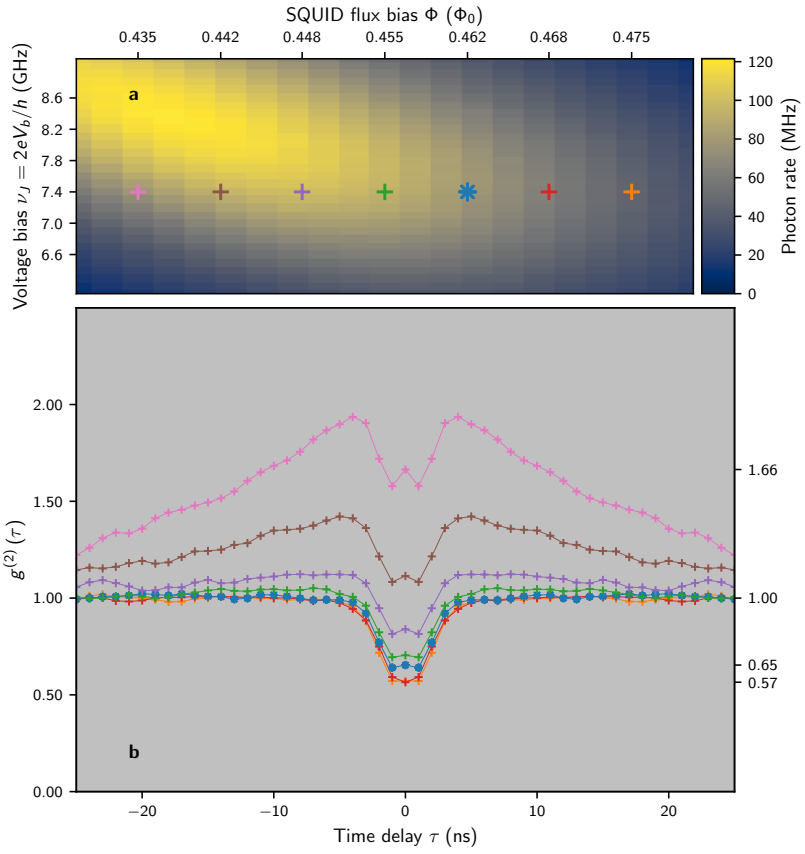

Figure IV.17: $g^{(2)}$ **for different flux biases.** ***Panel a*** is the photon rate as a function of the voltage bias and the flux bias, plus symbols indicate where $g^{(2)}$ are measured. ***Panel b*** is the $g^{(2)}$ function at the points indicated in panel a as functions of the time delay. The different curves show the evolution of $g^{(2)}$ with the flux bias, i.e. when the critical current is changed.

In order to study the influence of the voltage bias, we fix the flux bias to $\phi \simeq 0.462$. At this bias the jumps between the bright and dark regions are negligible, i.e. except the dip $g^{(2)}$ is flat. Figure IV.18 shows the evolution of $g^{(2)}$ with the voltage bias. When the voltage is reduced, both $g^{(2)}$ and photon rate decrease. This is consistent with our mechanism when thermal fluctuations are included: At a lower bias, the tunnelling of a first Cooper pair $\mathrm{CP}_{\nu_J} \underset{E_C}{\rightarrow} \mathrm{Ph}_{\nu}$ is less probable – i.e. the photon rate is lower, but also the process $\mathrm{CP}_{\nu_J+\delta} \underset{3\cdot E_C}{\rightarrow} \mathrm{Ph}_{\nu}$ where δ comes from thermal fluctuations, which is responsible for the dip closure. When the bias is increased, the process $\mathrm{CP}_{\nu_J+\delta} \underset{3\cdot E_C}{\rightarrow} \mathrm{Ph}_{\nu}$ becomes more and more likely and then the dip closes.

Moreover, J. Leppäkangas did numerical simulation (solid line) extending P-theory to fourth order in critical current. The agreement is good at low biases, however the agreement gets worse when the bias increases, likely because correlations between more than two Cooper pairs play a role, i.e. calculations have to be pushed beyond fourth order.

Super-bunching mechanism

Third, figure IV.19 shows the evolution of $g^{(2)}$ following the maximum photon rate, i.e. the diagonal cut seen previously. The observation is the same as before, but as the photon rate is higher, a higher voltage bias can be measured until reaching $g^{(2)}(0) \simeq 2$.

Moreover, going to higher biases, super-bunching ($g^{(2)}(0) \gg 2$) is observed, see figure IV.20. This mechanism is explained by the additional second order process where one Cooper pair gives two photons. In addition, now there are two processes that can emit photons, when the second order process happens and charges the capacitor $\mathrm{CP}_{\nu_J} \underset{E_C}{\rightarrow} \mathrm{Ph}_{\approx\nu_0} + \mathrm{Ph}_{\nu_0}$, the first order process is then approximately on resonance $\mathrm{CP}_{\nu_J} \underset{3\cdot E_C}{\rightarrow} \mathrm{Ph}_{\approx\nu_0}$, it increases the probability of the first order process i.e. emission of two photons calls for the emission of another one.

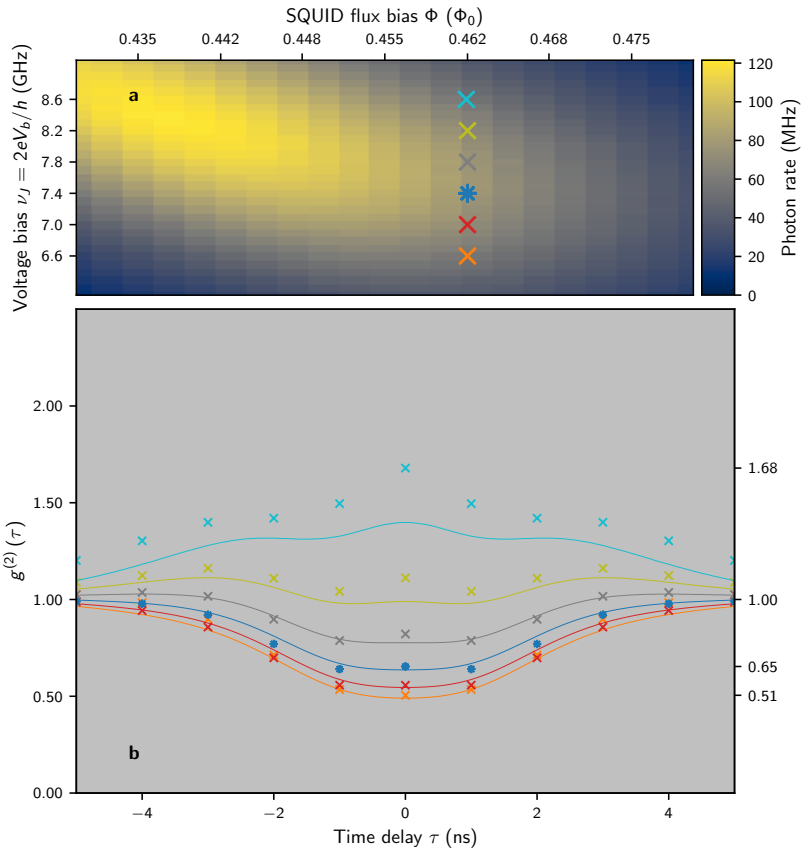

Figure IV.18: $g^{(2)}$ **for different voltage biases.** ***Panel a*** is the photon rate as a function of the voltage bias and the flux bias, cross symbols indicate where $g^{(2)}$ are measured. ***Panel b*** is the $g^{(2)}$ function at the points indicated in panel a as functions of the time delay. The different curves show the $g^{(2)}$ evolution with the voltage bias, i.e. when more energy has to be dissipated when a Cooper pair tunnels. Solid lines are theoretical results of J. Leppäkangas.

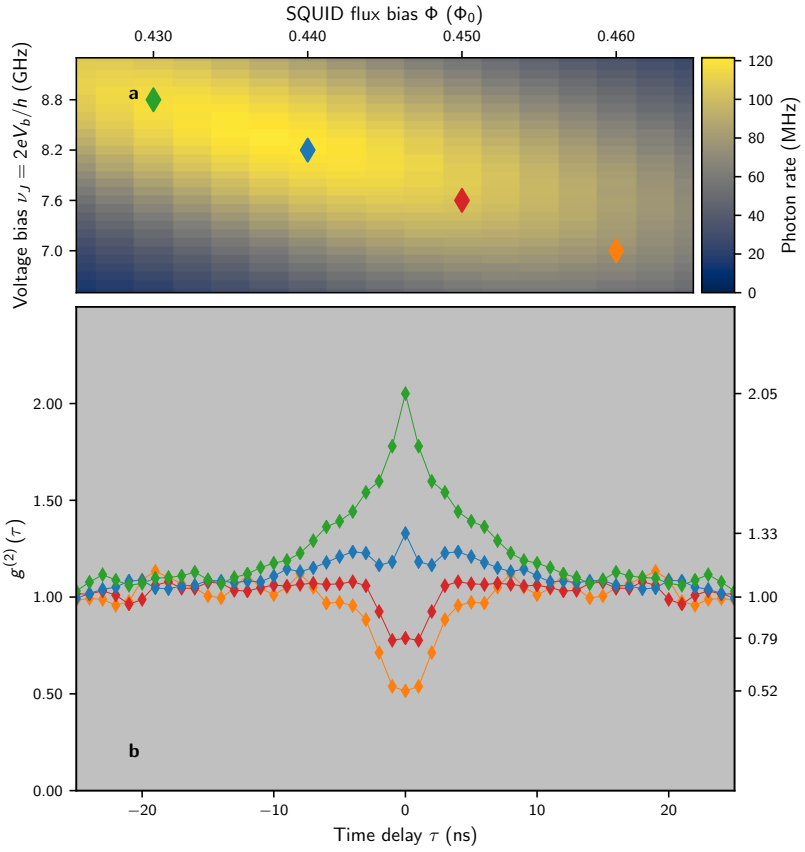

Figure IV.19: $g^{(2)}$ **for different bias points along a line of maximal photon rate.** ***Panel a*** is the photon rate as a function of the voltage bias and the flux bias, diamond symbols indicate where $g^{(2)}$ are measured. ***Panel b*** is the $g^{(2)}$ function at the points indicated in panel a as functions of the time delay. The different curves show the $g^{(2)}$ when the flux bias is tuned to maximal. The value $g^{(2)}(0) = 2$ is reached, i.e. photon as bunched as much as a thermal source.

Experimental precision

To conclude this section, as the measurement is repeated many times, statistical properties of $g^{(2)}(0)$ can be derived, the statistical uncertainty. Figure IV.21 shows the uncertainty at $\pm 3\sigma$ for $g^{(2)}(0)$ along each

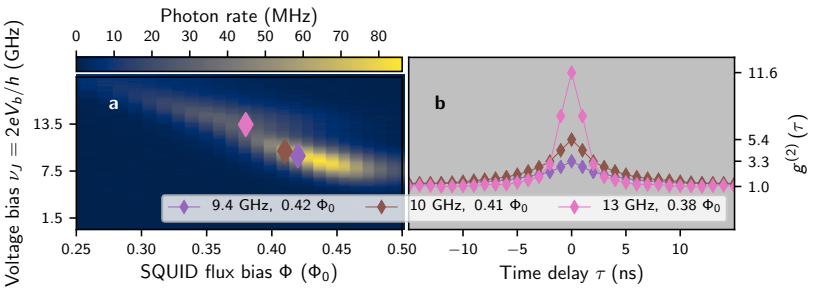

Figure IV.20: **Super-bunching.** ***Panel a*** is the photon rate as a function of the voltage bias and the flux bias. Diamond symbols indicate where $g^{(2)}$ are measured. ***Panel b*** shows the $g^{(2)}$ of panel a as functions of the time delay. The different curves show the $g^{(2)}$ evolution when the photon rate is maximum at high voltage biases. Now $g^{(2)}(0) \gg 2$, i.e. photons are super-bunched.

cut. Together with the uncertainties, we claim and proof our source is non-classical. However, as $g^{(2)}(0)$ is slightly above 0.5, so we cannot proof that our source is a SPS [*Grünwald17*].

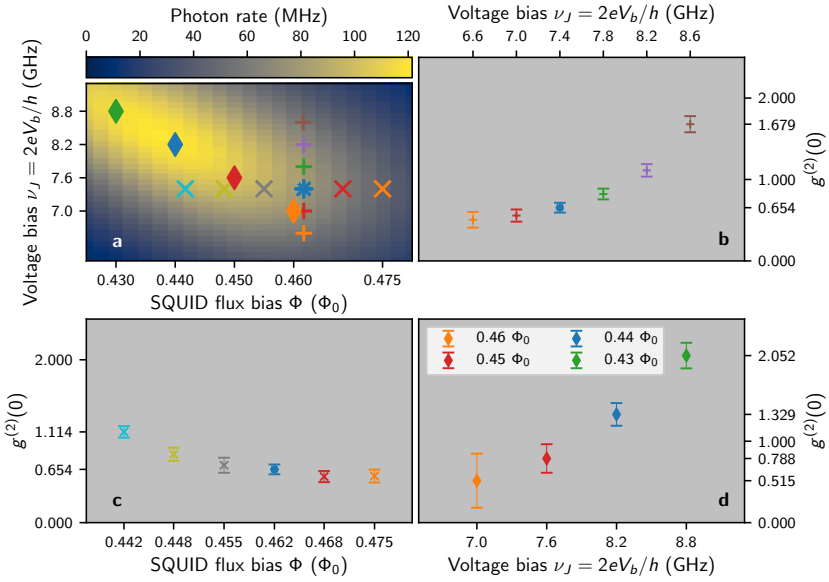

Figure IV.21: $g^{(2)}$ **statistical power.** ***Panel a*** reminds all the $g^{(2)}$ measured in figures IV.17 to IV.19. ***Panel b*** are the $g^{(2)}(0)$ as a function of the voltage bias with error bars at $\pm 3\sigma$ along the vertical cut. ***Panel c*** are the $g^{(2)}(0)$ as a function of the flux bias with error bars at $\pm 3\sigma$ along the horizontal cut. ***Panel d*** are the $g^{(2)}(0)$ as a function of the voltage bias with error bars at $\pm 3\sigma$ along the diagonal cut.

4 On-demand mode

This last section describes experiments using a pulse. The idea is built on the observation of a large area without photon emission. A cycle going back and forth between emission and non-emission area is used to, ultimately, emit one photon per cycle: the source is triggered on-demand.

4.a Pulse description

The pulse is applied using an *Arbitrary Wave Generator* (AWG) on the flux line. Figure IV.22 panel a shows the intended pulse shape. This signal is added to a DC component through a bias-tee. Figure IV.22 panel b shows how the flux evolves according to this bias (orange line). The expected amplitude is $0.3\phi_0$.

Moreover, as described earlier, the flux line crosses the TL close to the SQUID to form a capacitor. This coupling also induces a fluctuation of the bias voltage (red line on figure IV.22 panel b). Consequently, the pulse trajectory in parameter space is not a straight line but follows the white dotted line.

Before going further, figure IV.23 panel b & c show the first and second order correlation measurements. The time localisation of the emission process is visible with these two measurements: $G^{(1)}$ has only one peak, $G^{(2)}$ has equally spaced peaks along one line.

4.b Parameter space exploration

As before, second order correlation measurements are time consuming. Therefore the parameter space cannot be fully explored.

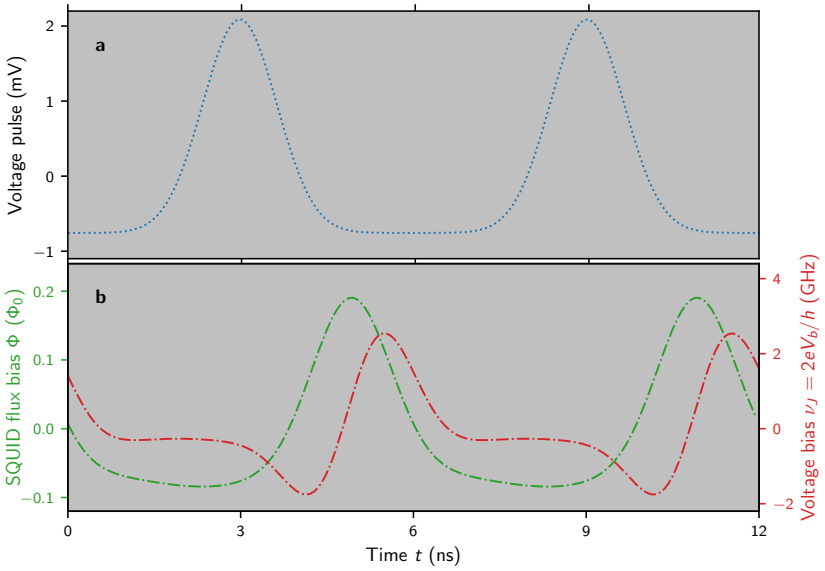

Figure IV.22: **Pulse trajectory.** ***Panel a*** voltage pulse – voltage as a function of the time – send by the AWG to pulse the flux line (target signal, not measured). ***Panel b*** expected flux and voltage bias shifts (simulations with an home-made software) due to the pulse. The orange line is the flux shift to go back and forth between the dark and bright regime. The red line is the voltage shift due to the inducto-capacitive coupling figure IV.4.

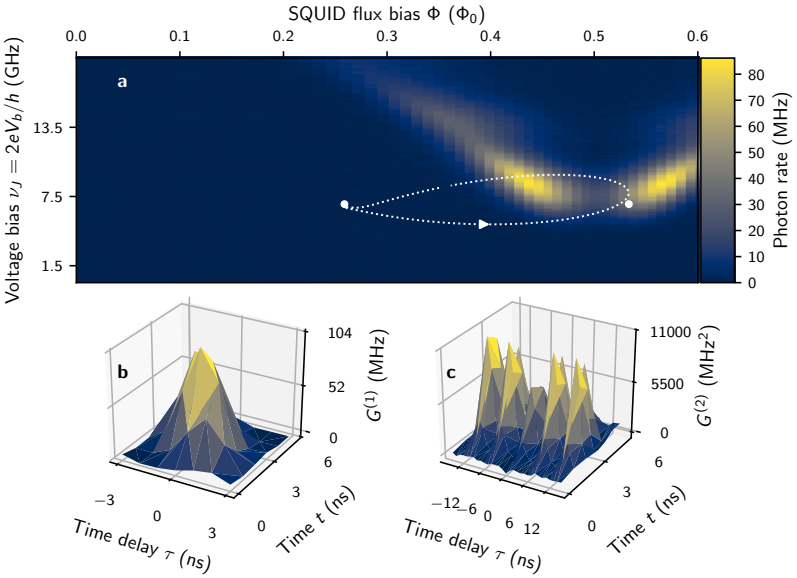

Figure IV.23: **Correlation functions with reference flux.** ***Panel a*** is the photon rate as a function of the SQUID flux bias and the voltage bias, dotted white line is the pulse applied, this shape is a simulation. ***Panel b*** is $G^{(1)}$ as a function of t and τ. The time runs over a pulse cycle, i.e. 6 ns. ***Panel b*** is $g^{(2)}$ as a function of t and τ. Both $G^{(1)}$ and $g^{(2)}$ confirm the radiation is time localised.

Photon rate

We therefore start by only measuring $G^{(1)}(t,0)$ on the full parameter space – it is equivalent to measure the integrated PSD. Figure IV.24 shows the result. The pulse period is 6 ns and our acquisition interval 1 ns, therefore there are six different $G^{(1)}(t,0)$. The choice of $t = 0$ is arbitrary.

We recover the V shape seen in free-running mode, however it is slightly deformed. The asymmetry can be explained qualitative:

- The two bright regions correspond to the V shape, they are shifted by $0.1\phi_0$ accordingly to the pulse shape;
- The left arm is thicker than right one, due to the pulse shape. Indeed, when starting in the left dark region slightly below the V shape, the pulse can reach the left arm of the V shape due to the voltage shift, whereas it is less probable to reach the right arm when starting slightly below the V shape;

$g^{(2)}$ normalisation

Before discussing $g^{(2)}$ measurements, let's discuss the normalisation of $g^{(2)}$, which is not as straightforward in the free-running case [*Glauber63*]. Figure IV.25 recalls the Hanbury Brown-Twiss setup useful to

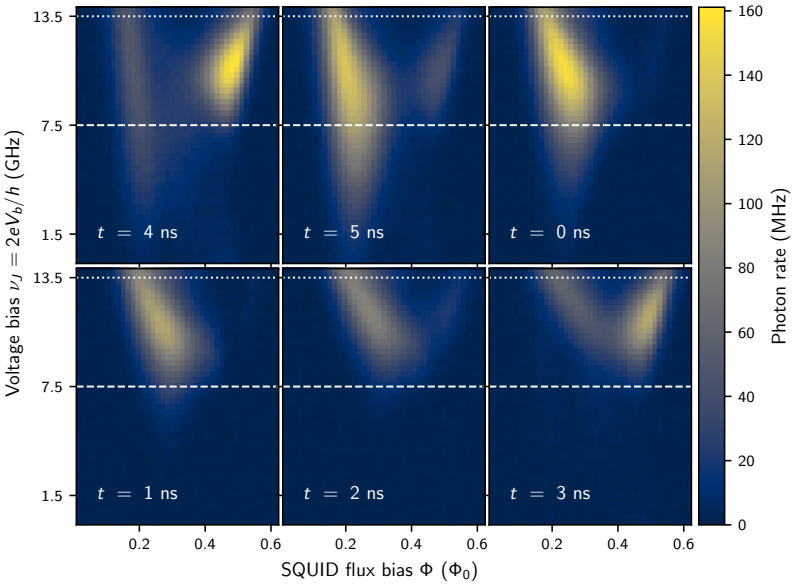

Figure IV.24: **PSD time-dependence.** Each panel shows $G^{(1)}(t,0)$ as a function of the flux bias and the voltage bias. The six panels correspond to the pulse period. The V shape observed in the free-running mode is recovered. The horizontal white lines correspond to the first and second order processes identified previously.

interpret the $g^{(2)}$ in terms of probabilities. It is the probability to measure a photon on D_1 when a photon is measured on D_2 compared to the probability to measure a photon on D_1:

$$g^{(2)} \equiv \frac{p(D_1|D_2)}{p(D_1)} = \frac{p(D_1 \cap D_2)}{p(D_1) \cdot p(D_2)} \tag{IV.11}$$

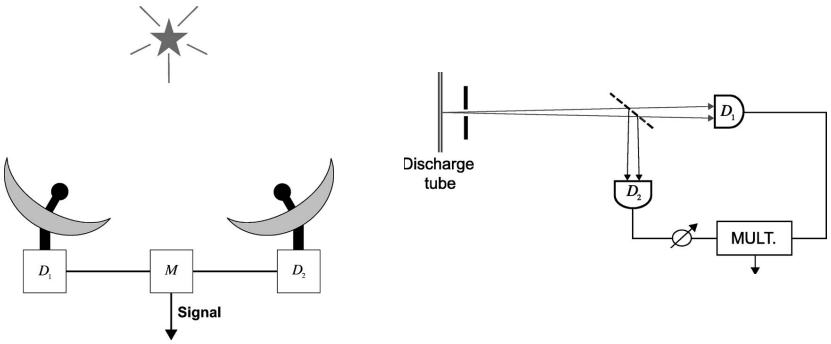

Figure IV.25: **Photon correlation measurement using Hanbury Brown-Twiss setup** (image [*Glauber06*]). ***Left scheme*** is used in astronomy, the radiation coming from a celestial object is detected at two different points and coincidences are then computed. ***Right scheme*** is used in optics, a light source is split in two and counters are used on each path to measure coincidences (see text).

In terms of correlation functions (for now expressed with two times and not the delay), $p(D_{1/2})$ is equivalent to $G^{(1)}(t_{1/2}, t_{1/2})$ while the intersection probability is $G^{(2)}(t_0, t_1)$. Rewritten with time delay:

$$g^{(2)}(t,\tau) \equiv \frac{G^{(2)}(t,\tau)}{G^{(1)}(t,0) \cdot G^{(1)}(t+\tau,0)} \tag{IV.12}$$

Note that when the process is stationary and there is no t variable, equation IV.10 is recovered.

Results

First, time-resolved $G^{(2)}$ measurements are tested against the stationary ones used for the free-running regime. To do so, a working point is measured two times, one time with the stationary mode and one with the time-resolved mode. When the time-resolved measurement is $G^{(1)}_{\text{resolved}}(t,\tau)$, the stationary one ignores the information about t, only the mean value is kept:

$$G^{(1)}_{\text{stationary}}(\tau) \equiv \frac{1}{6\,\text{ns}} \int_{0\,\text{ns}}^{6\,\text{ns}} G^{(1)}_{\text{resolved}}(t,\tau)\,\mathrm{d}t \tag{IV.13}$$

Figure IV.26 shows the comparison of measured $G^{(1)}_{\text{stationary}}$ with the one computed from $G^{(1)}_{\text{resolved}}$ according to equation IV.13 and confirm our two methods are in agreement.

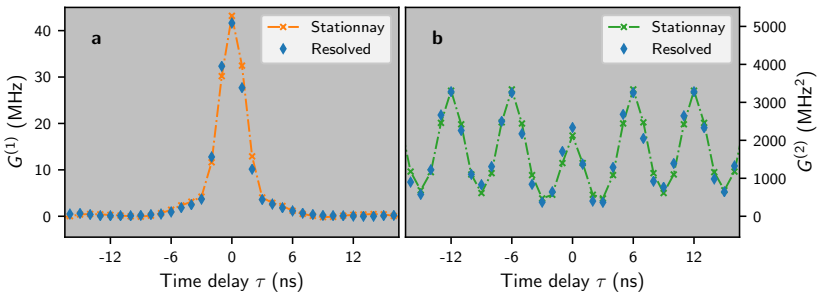

Figure IV.26: **Stationary and time-resolved methods comparison.** ***Panel a*** is the first order correlation function as a function of the time delay. ***Panel b*** is the second order correlation function as a function of the time delay. Solid orange lines are measurements obtained with the stationary method. Blue diamond symbols are measurements obtained with the time-resolved method after integration, see equation IV.13.

Finally, following figure IV.18 the voltage bias is chosen as low as possible to get minimal $g^{(2)}(0) - \simeq 0.5$ – while keeping $G^{(1)}(0)$ sufficient to be able to measure in a reasonable time. The flux is chosen such as the pulse reaches the frustration[3]. The pulse is shown on figure IV.23 as the white dotted line. Figure IV.27 presents the final results. First the temporal width along t-axis and τ-axis are roughly identical and equal to 2 ns, indicating that there is no jitter in the emission process, otherwise width along t-axis would be larger. Moreover, our cycle cannot be much faster, otherwise the single photon would not escape from the resonator between two cycles.

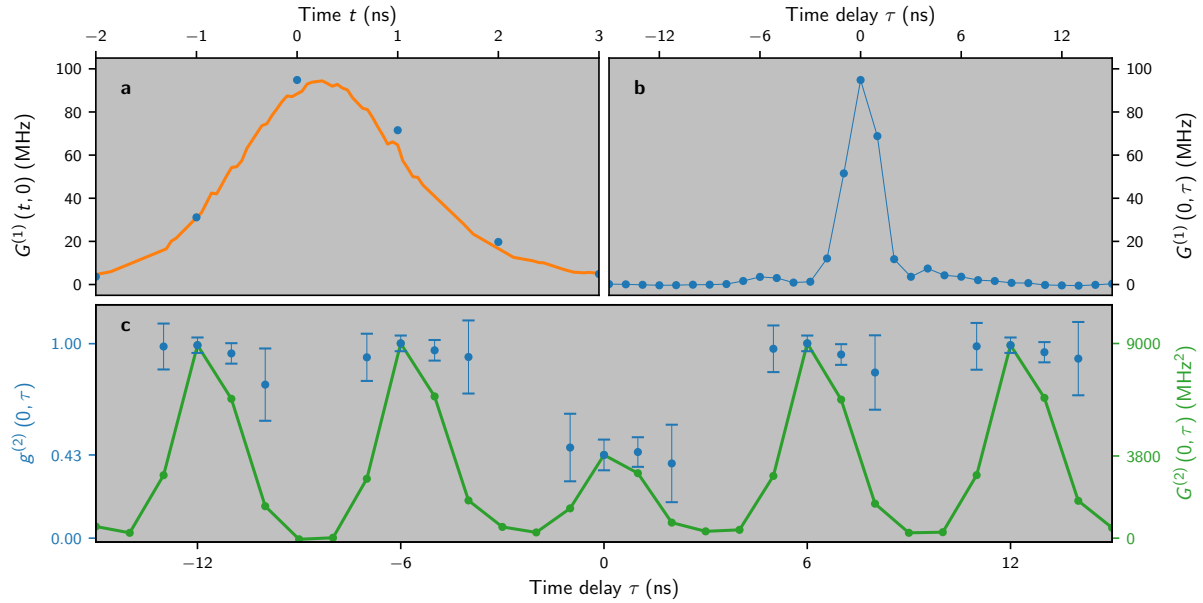

Figure IV.27: $G^{(2)}$ **time-dependence.** ***Panel a & b*** is $G^{(1)}$ as a function of the time and the time delay. $= 0$ is chosen as it is the maximum time emission. Orange solid line is obtained by repeating the measurement many times with a slightly different time delay between the pulse and the acquisition board trigger. Blue dots are the data taken at the same time of $g^{(2)}$. ***Panel c*** is $g^{(2)}$ as a function of the time delay at the maximum time emission. Left axis (solid green line) is the normalised form as the right one (blue dots) is the raw form. Normalisation is done with equation IV.12 when $G^{(1)}$ is high enough.

Here we achieve a stronger anti-bunching than in the free-running case, likely due to the additional blocking effect given by the latching to the zero-voltage state in the dark region. At the same time, the pulsing scheme allows us to maintain very good quantum efficiency and photon flux (0.2 photons per pulse), because of the high emission rates at low flux bias. This makes it likely for a tunnel event to happen during each cycle even for very short flux pulses. The residual $g^{(2)}(0)$ is mainly attributed to the low charging energy of our RC circuit and its relatively low time constant, only slightly larger than the decay time of the resonator.

[3]Flux where the effective critical current of the SQUID is minimal.

Conclusion

First, a general method based on the P-theory has been derived and used to fully characterise our device in the P-regime. Then the statistics of our device have been measured in two operating modes: Free-running & on-demand.

It demonstrates that a Josephson photonics device – based on ICPT – can produce anti-bunched microwave radiation. Moreover, by modulating the effective critical current of the SQUID, using fast flux pulses and locking to a dark state after photon emission, the anti-bunched photons can be produced on-demand at very high rates.

Increasing the charging energy and the RC time, or replacing the RC circuit by a high impedance resonant mode, should allow for significant improvements of anti-bunching and quantum efficiency. Ultimately, we expect that it can be optimised to be an on-demand single photon source with near unity quantum efficiency and negligible $g^{(2)}(0)$.

Chapter V

Quantum-limited amplification

French resume

Ce dernier chapitre se concentre sur les processus d'amplification proche de la limite quantique rendus possibles avec l'ICPT. Une première partie détaille comment les processus de l'ICPT peuvent être mis à contribution pour permettre l'amplification, et les avantages et inconvénients qu'ils apportent.

Les expressions des grandeurs caractéristiques de tels amplificateurs, comme la bande-passante et le point de compression, seront démontrées et comparées aux résultats expérimentaux. Pour réaliser cette caractérisation, les gains et PSD sont mesurés et utilisés pour quantifier la proximité du bruit ajouté avec la limite quantique ([*Caves82*]). Nos résultats montrent que l'ICPT permet d'approcher une amplification proche de cette limite à condition que le bruit en tension soit contrôlé.

Contents

Preamble Some results of this chapter are direct continuation of [*Jebari18*] and will be recalled so that we can build on them. Moreover, I will focus three designs of amplifiers, even thought many others have been developed, see [*Jebari17*] for details.

1 Amplification based on ICPT

Different designs used to achieve amplification will be presented in this chapter. Here the working principle of the sample studied previously by M. Hofheinz [*Hofheinz11*; *Jebari18*] is recalled, then some drawbacks and solutions are highlighted.

1.a Working principle & implementation

First of all, let's recall the main idea of inelastic Cooper pair tunnelling (see chapter I). A Cooper pair can tunnel through a DC biased Josephson junction by dissipating its energy $h\nu_J$ in the form of photons inside the electromagnetic environment. Instead of the first order process $\mathrm{CP}_{\nu_J} \to \mathrm{Ph}_{\nu}$ explored in chapter IV, here our device is based on the second order process $\mathrm{CP}_{\nu_J} \to \mathrm{Ph} \simeq \nu_0 + \mathrm{Ph}_{\nu_1}$, see figure V.1.

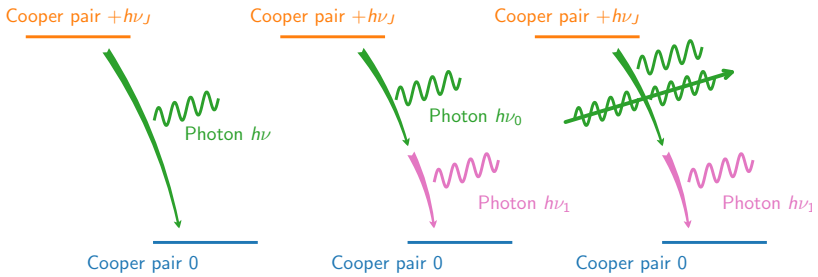

Figure V.1: **Amplification process.** ***Left diagram:*** Initial situation. Tunnelling happens when the Cooper pair energy $h\nu_J$ and photon energy $h\nu$ are equal. Then each tunnelling Cooper pair gives a photon. ***Centre diagram:*** Situation where a Cooper pair tunnels and creates two photons, one at ν_0 and one at ν_1. ***Right diagram:*** Same process with an additional input photon at ν_0, resulting in stimulated emission and amplification.

Then, an input photon – at one of the two modes involved – sent on such a device will stimulate the process, the photon at the same mode will be identical to the input photon, i.e. it will have the same frequency and phase – while the second photon has a frequency complementary to match energy balance $\nu_J = \nu_{\mathrm{in}} + \nu_1$ and a complementary phase.

The design shown in figure V.2 can actually operate as amplifier. Indeed, the peak at 12 GHz corresponds to the dissipation in the form of two photons at 6 GHz.

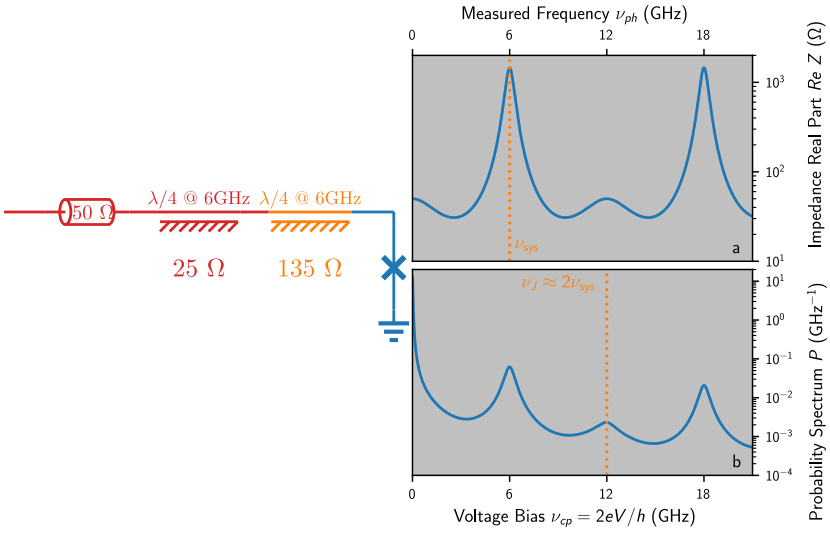

Figure V.2: **Degenerate amplifier.** ***Left scheme*** shows the two cascaded quarter-wave TL, the orange one mainly defines the resonator impedance while the red one together with the 50 Ω port defines the Q factor. The Josephson junction is in blue. ***Panel a*** shows the real part of the impedance as a function of the frequency, there are modes at $(2n+1)\,\nu_{\mathrm{sys}}$, 6 GHz and 18 GHz peaks are visible. ***Panel b*** shows the corresponding P-function as a function of the voltage bias expressed in GHz. The peaks correspond to biases where Cooper pair tunnelling can happen. The zero bias peak is the supercurrent, the second and last correspond to first order processes with photons at respectively 6 GHz and 18 GHz, the third one at 12 GHz is a second order process where a Cooper pair gives two photons at 6 GHz. ***Orange dotted lines*** indicate the process used as amplifier.

1.b Experimental results

Figure V.3 shows the measured gain and input added noise of this device. Along the lowest dash dotted line, the amplification process of interest is observed. First, as the slope is 1, resonance relation is $\nu_J = \nu + \nu_{\mathrm{sys}}$ where ν_{sys} is the resonator mode.

Note there is also an amplification process at higher bias along the highest dash dotted line. However, the gain is significantly lower. To understand why, let's recall the effective gain (at resonance) – see

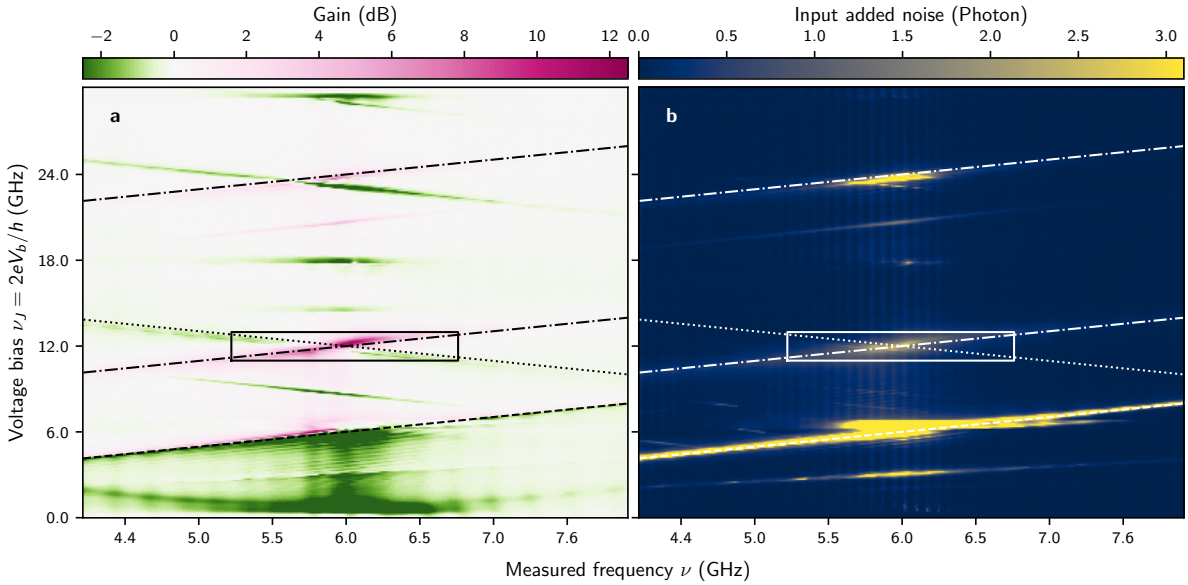

Figure V.3: **Gain and input added noise.** ***Panel a*** is the gain as a function of the measured frequency and the voltage bias. Pink lines are amplification processes while green ones are absorption processes. ***Panel b*** is the input added noise, i.e. the noise emitted when there is no input signal, divided by the gain, as a function of the measured frequency and the voltage bias. Amplification processes have significant input added noise. Dash dotted lines correspond to the discussed amplification processes (see text), respectively with two photons around 6 GHz or one photon at 6 GHz and one at 18 GHz. The dotted line is an unwanted conversion process (see text). The dashed line corresponds to the first order process which produces both gain and conversion with low frequency photons. Therefore, the noise is significantly higher. The square corresponds to the zoom used for figure V.6.

chapter I:

$$G^* \simeq \left|\frac{1+4Q^{*2}}{1-4Q^{*2}}\right|^2 \text{ white } Q^* \equiv \frac{\bar{\phi}_0 I_c}{2\hbar}\sqrt{\frac{Q^{(0)}Q^{(1)}}{\omega_{\text{sys}}^{(0)}\omega_{\text{sys}}^{(1)}}\frac{Z_{\text{sys}}^{(0)}Z_{\text{sys}}^{(1)}}{(R_Q/\pi)^2}} \tag{V.1}$$

Where $\cdot^{(0)}$ corresponds to the mode at ν_{sys} and $\cdot^{(1)}$ to the mode at ν_{sys} and $3\nu_{\text{sys}}$ depending on the process considered. The two gains can be expressed using a common Q^* as:

- The effective gain of the lowest amplification process $G^*_{\nu_{\text{sys}}} \simeq \left|\frac{1+4Q^{*2}}{1-4Q^{*2}}\right|^2$
- The effective gain of the highest amplification process $G^*_{3\nu_{\text{sys}}} \simeq \left|\frac{1+4Q^{*2}/3}{1-4Q^{*2}/3}\right|^2$

For $G^*_{\nu_{\text{sys}}} \simeq 12\,\text{dB}$ it gives $G^*_{3\nu_{\text{sys}}} \simeq 3.5\,\text{dB}$.

Conversion process

Moreover, figure V.3 shows also absorption processes (in green). To understand these processes, figure V.4 shows, energetically, how a photon can be absorbed and converted to a photon at higher frequencies. The energy of a Cooper pair $h\nu_J \simeq h \cdot 12\,\text{GHz}$ together with the energy of a photon $h\nu_0 \simeq h \cdot 6\,\text{GHz}$ gives a photon of energy $h\nu_2 = h \cdot 18\,\text{GHz}$: $\text{CP}_{\nu_J} + \text{Ph}_{\simeq \nu_0} \rightarrow \text{Ph}_{\nu_2}$. Consequently this process appears only when there are input photons. Note that these conversion processes provide energy gain but appear as loss in our gain measurement because it considers only photons at the same frequency as the input signal.

As seen on figure V.3 the two processes, amplification and conversion, can cross and be efficient at the same bias and frequency, which reduces the effective gain. Both happen when $\nu_{\text{in}} + \nu_1 = \nu_2 - \nu_{\text{in}}$, i.e. $\nu_2 = 2\nu_{\text{in}} + \nu_1$. Which is true with this design as $\nu_{\text{in}} \simeq \nu_1 \simeq 6\,\text{GHz}$ i.e. $\nu_2 \simeq 3\nu_1 \simeq 18\,\text{GHz}$ (see figure V.5 panel a). Note that this is also visible on the P-function: Instead of looking at $P(h\nu_J)$ which describes if an inelastic process is possible for a Cooper pair of energy $h\nu_J \simeq 12\,\text{GHz}$, $P(h\nu_J + h\nu_{\text{sys}})$ describes if an inelastic process is possible for a Cooper pair of energy $h\nu_J \simeq 12\,\text{GHz}$ assisted by a photon of energy $h\nu_{\text{sys}} \simeq 6\,\text{GHz}$.

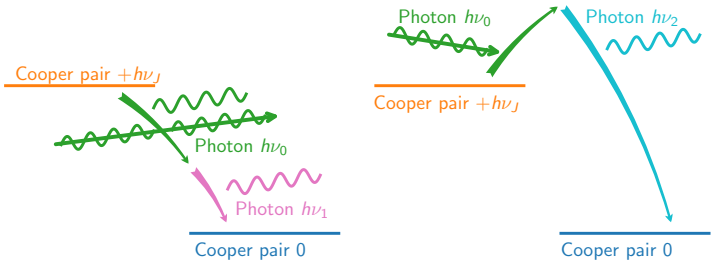

Figure V.4: **Conversion process.** ***Left diagram:*** Amplification process described in figure V.1. ***Right diagram:*** Situation where a Cooper pair tunnels assisted by a photon at ν_0 and creates a photon at ν_2. This process is observed as loss at frequency ν_0.

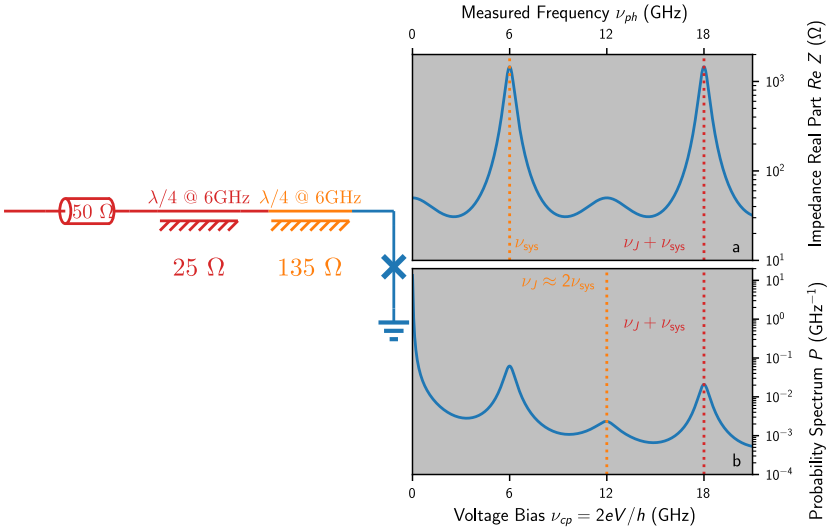

Figure V.5: **Conversion process & P-function.** ***Left scheme*** shows the two cascaded quarter-wave TL, the orange one mainly defines the resonator impedance while the red one together with the 50 Ω port defines the Q factor. The Josephson junction is in blue. ***Panel a*** shows the real part of the impedance seen by the junction as a function of the frequency. There are modes at $(2n+1)\,\nu_{\rm sys}$, 6 GHz and 18 GHz peaks are visible. ***Panel b*** shows the corresponding P-function as a function of the voltage bias expressed in GHz. The peaks correspond to biases where Cooper pair tunnelling can happen. The zero bias peak corresponds to supercurrent, the second and last correspond to first order processes with photons at respectively 6 GHz and 18 GHz, the third one at 12 GHz is a second order process where a Cooper pair gives two photons at 6 GHz. ***Orange dotted lines*** indicate the process used as amplifier. ***Red dotted lines*** indicate the unwanted conversion process.

2 Noise performance

We first analyse the noise performance of the previous design: How close is the first simple design to the quantum limit? Then a second design is presented, intending to overcome the identified drawbacks, i.e. conversion process and imperfect noise.

2.a Noise of initial design

First, figure V.6 is the zoom indicated on figure V.3. The dash dotted line and the dotted line correspond to the resonance condition for amplification and conversion. They cross at $\nu_J \simeq 12\,\text{GHz}$ and $\nu \simeq 6\,\text{GHz}$, resulting in reduced gain at this point. In order to check how close to the quantum limit this device operates, cuts along the dashed lines are shown on panel c & d. Although this device adds very low noise, it is still far from the quantum limit. It operates at 11 dB with 3 photons input added noise while the quantum limit is 0.9 photons.

We attribute the excess photon noise to low frequency voltage noise, i.e. phase noise of the pump frequency ν_J. If the width of the fluctuations $\Delta\nu_J$ is large enough to bring the amplifier out of its optimal working condition, it will modulate the gain in phase and amplitude. In the phase-sensitive VNA measurement both effects reduce the average gain. The phase insensitive PSD on the other hand is only affected by amplitude fluctuations, so that the input noise, i.e. the ratio of photon noise over gain, is degraded. In our setup we achieve bias fluctuations[1] $\Delta\nu_J \simeq 120\,\text{MHz}$, only slightly lower than the

[1] This value is the width of the PSD peak at the first order process around $\nu_J \simeq 6\,\text{GHz}$ when the SQUID is almost completely frustrated.

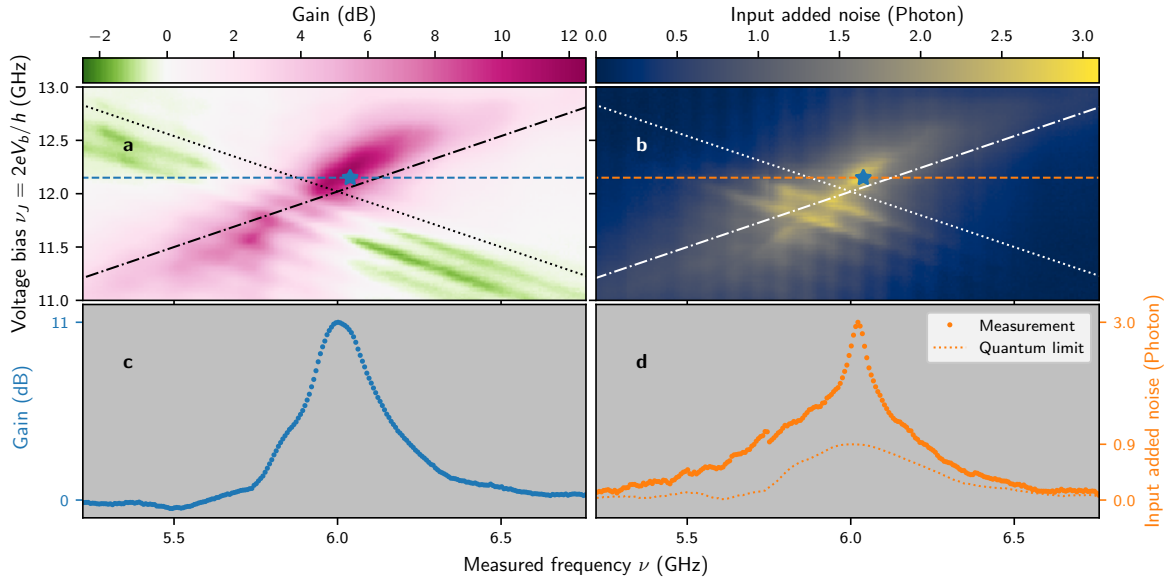

Figure V.6: **Amplifier near optimal working point.** ***Panel a & b*** are zooms of figure V.3 ***Panel c*** is the cut along the blue dashed line on panel a. The maximum gain is 11 dB. ***Panel d*** is the cut along the orange dashed line on panel b, the orange dotted line is the quantum limit corresponding on the gain of panel a.

bandwidth of the amplifier. When the ICTA bandwidth can be made much larger than $\Delta\nu_J$, this noise source should become negligible and the ICTA approach quantum limited noise.

2.b Improved design

To overcome these issues – unwanted conversion process and bias fluctuations – a first step is to alter the design on figure V.5. An open quarter-wave stub is added to suppress impedance at the target frequency 18 GHz. Figure V.7 panels a & b shows which influence this stub has on the impedance and P-function. Both are significantly reduced at 18 GHz, and the conversion peak is shifted to $\simeq$ 15 GHz. Amplification and conversion do not cross any more at $\nu_{\text{in}} \simeq 6$ GHz because now the conversion process is on resonance at $\nu_J \simeq 15\,\text{GHz} - 6\,\text{GHz} \simeq 9$ GHz while the amplification process is still on resonance at 12 GHz.

Moreover, in order to limit this influence of bias fluctuations a capacitively shunted half-wave stub is added. Figure V.5 panels c & d shows the result: This structure suppresses the impedance at low-frequency and at 12 GHz and thereby reduces voltage noise $P(\simeq 0\,\text{GHz})$.

Finally, to compensate the drift of the resonator frequency due to the quarter-wave transformer (brown solid line) at 18 GHz, the frequency of the quarter-wave resonator is shifted upwards (dash dotted green line).

2.c Noise of improved design

Figure V.8 presents the amplification process of a sample based on this second design with increased bandwidth and circuitry to suppress bias fluctuations. A first remark concerns the resonance frequency at $\simeq$ 4.3 GHz, shifted from the designed value due to fabrication issues, mainly the capacitance of the junction which is higher than expected, see [*Jebari17*] for details. However, amplification and conversion do not cross, just as designed. Moreover, from the bias at which the conversion process appears, we deduce that $\nu_2 \simeq 12.2$ GHz.

As expected the device operates very close to the quantum limit (panel d), however as the resonance frequency is close to the minimal frequency our setup can measure, it is impossible to characterise the amplifier over a wide bandwidth. For a gain of 10 dB, there is 1 photon input added noise while the quantum limit is 0.9.

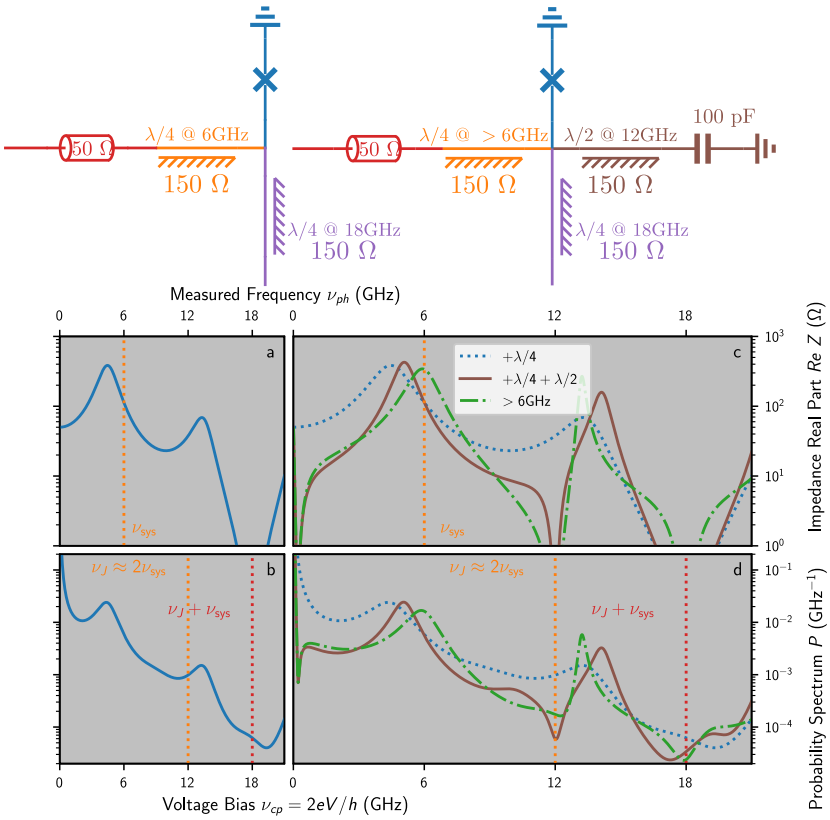

Figure V.7: **Low noise ICTA design.** ***Left part*** shows how the design of figure V.5 is updated with an open quarter-wave stub at the second frequency involved for the conversion process. The impedance at the frequency is then close to zero, however it also shifts the resonator frequency slightly below 6 GHz (blue lines). ***Right part*** shows how an additional capacitively shunted half-wave stub at the bias frequency (red lines) lowers the impedance at the bias frequency 12 GHz and close to 0 GHz, limiting the fluctuations of the bias which is responsible for excessive input added noise. To compensate the frequency shift, the resonator frequency is pushed upwards (green lines).

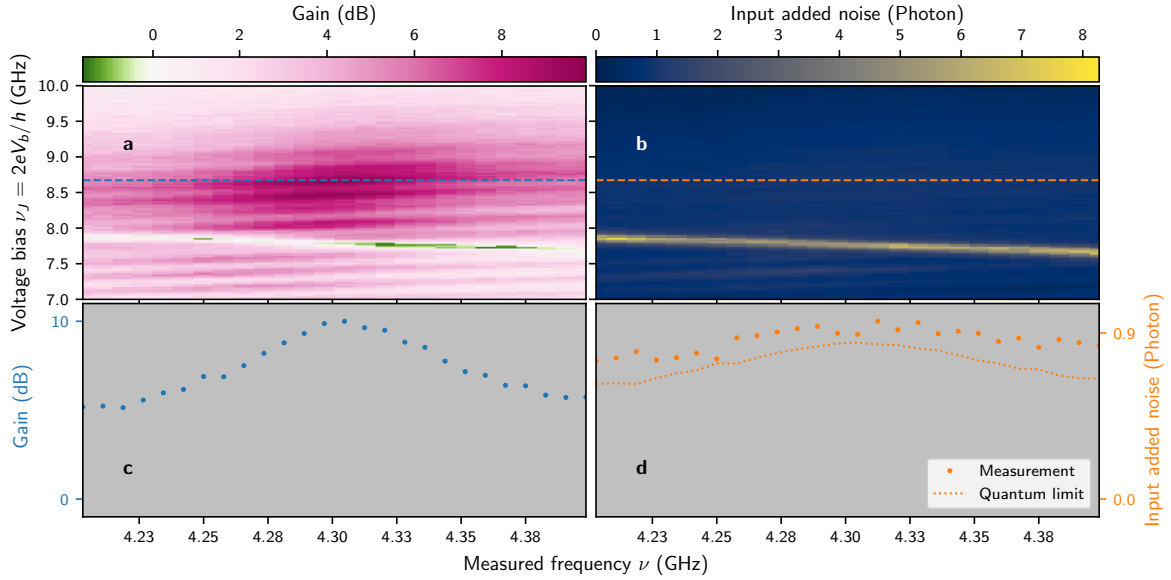

Figure V.8: **Low noise amplifier working point.** ***Panel a & b*** are zoom around the amplification process (in the same way as figure V.6). Now amplification and conversion do not cross at the resonance frequency.***Panel c*** is the cut along the blue dashed line on panel a. The maximum gain is 10 dB. ***Panel d*** is the cut along the orange dashed line on panel b, the orange dotted line is the quantum limit corresponding on the gain of panel a. Now, amplification is near quantum-limited.

Remarks about calibration

Figure V.8 is calibrated as explained in chapter II section 2.a, however calibration reference points are subtle:

Gain & quantum limit: The reference point is the sample itself, working points where the sample is assumed to be fully reflected are used as a reference where $G \equiv 0$ dB, i.e. we measure G on figure V.9;

Input added noise: The reference point of PSD measurements are the six-port switch, i.e. we measure γ_ν^{out} on figure V.9. Note that $\gamma_\nu^{\text{out}} = GAN_G + \cdots$. Therefore in order to obtain an upper limit of the input added noise, the gain referred to this second reference point is also measured using a short as reference, i.e. we measure GA^2 on figure V.9 to compute $\gamma_\nu^{\text{out}}/GA^2 = N_G/A + \cdots \geq N_G + \cdots$. The data plotted in figure V.8 is the system noise of amplifier and cable. With $A \simeq 0.5\,\text{dB}$, we except the actual amplifier noise to be at the quantum limit within measurement accuracy.

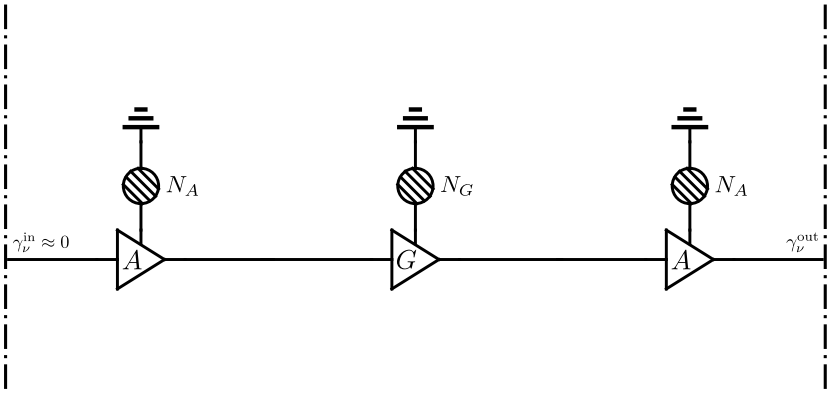

Figure V.9: **Calibration reference points.** From left to right, attenuation between the six-port switch and the sample, ICTA sample and attenuation between the sample and the six-port switch.

3 Bandwidth & dynamic range

3.a Gain bandwidth product

In order to calculate the bandwidth, we have a closer look at the expression of the gain derived in chapter I:

$$G\left(\omega_J,\omega\right) = \left|\frac{1 + Q^*\widehat{\chi_\omega}^{(0)}\left(\omega\right)^* Q^*\widehat{\chi_\omega}^{(1)}\left(\omega_J-\omega\right)^*}{1 - Q^*\widehat{\chi_\omega}^{(0)}\left(\omega\right) Q^*\widehat{\chi_\omega}^{(1)}\left(\omega_J-\omega\right)^*}\right|^2 \tag{V.2}$$

By solving $\left[\partial_\omega G\right]\left(\omega_J,\omega^*\right) = 0$ & $\left[\partial_{\omega_J} G\right]\left(\omega_J,\omega^*\right) = 0$, the main terms gives the resonance condition $\omega^* \equiv \omega_J - \omega^{(1)}$. Now, to determine effective gain and bandwidth, the approximation $\omega_J \simeq \omega^{(0)} + \omega^{(1)}$ is made, yielding:

- Gain: $G^* \simeq G\left(\omega^{(0)}+\omega^{(1)},\omega^*\right) = \left|\frac{1+4Q^{*2}}{1-4Q^{*2}}\right|^2$
- Bandwidth ($-3\,\text{dB}$): $\Gamma_{\text{BW}} \simeq \sqrt{\frac{-8G^*}{\left[\partial_\omega^2 G\right]\left(\omega^{(0)}+\omega^{(1)},\omega^*\right)}} \underbrace{=}_{\text{Taylor } 1/\sqrt{G^*}} \frac{1}{\sqrt{G^*}}\frac{2}{Q^{(0)}/\omega^{(0)}+Q^{(1)}/\omega^{(1)}}$

Table V.1 sums up the second relation, moreover this relation also implies that the effective bandwidth of the amplifier is limited by the bandwidths of the two modes. The relation between gain and bandwidth

Table V.1: ICTA characteristics

	Bandwidth
Characteristic product	$\Gamma_{\text{GBW}} \equiv \frac{2}{Q^{(0)}/\omega^{(0)}+Q^{(1)}/\omega^{(1)}}$
Constitutive equation	$\sqrt{G^*}\Gamma_{\text{BW}} = \Gamma_{\text{GBW}}$

has been measured with the first design for different critical currents. Figure V.10 shows the result and a good agreement between measurement and theoretical curve.

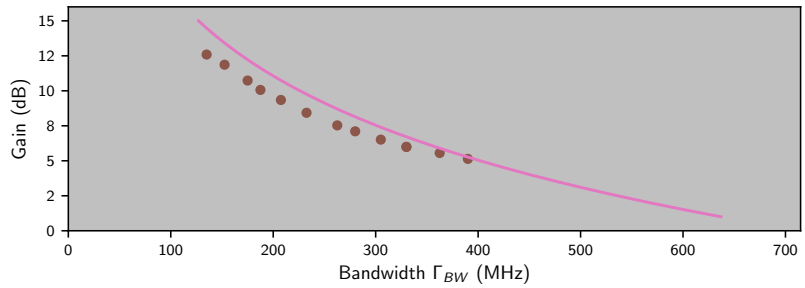

Figure V.10: **Gain-bandwidth relation.** The effective gain is shown as a function of the effective bandwidth. Brown dots are experimental data taken with the first design. Purple line is the theoretical curve, see table V.1.

3.b Compression point

The compression point is the input power at which the effective gain decreases – usually by 1 dB. In *Josephson Parametric Amplifier* (JPA), the physical orig [*Abdo11*; *Roy18*] is that the input field is so strong that it depletes the pump and so reduces the process efficiency. From a theoretical point of view, it corresponds to any reason that decreases Q^* in the interaction Hamiltonian $\propto Q^*\left\{e^{i\omega_J t}b^{(0)}(t)b^{(1)}(t)+\text{h.c.}\right\}$. In analogy to JPA and laser theories, we also call pump depletion the gain compression phenomena in the ICTA although the physical origin is different here.

Pump depletion

To study the pump depletion, $\mathcal{H}_{\text{drive}}$ has to be expanded at higher order in photon operators:

$$\begin{aligned} e^{-i\phi^{(0)}/\bar{\phi}_0} &\underbrace{=}_{\text{Glauber}} e^{-i\sqrt{Z^{(0)}_{\text{sys}}/(R_Q/\pi)}b^{(0)\dagger}}\, e^{-i\sqrt{Z^{(0)}_{\text{sys}}/(R_Q/\pi)}b^{(0)}}\, e^{-Z^{(0)}_{\text{sys}}/2(R_Q/\pi)} \\ &= e^{-Z^{(0)}_{\text{sys}}/2(R_Q/\pi)}\sum_n :\underbrace{\sum_m \frac{\left(-i\sqrt{Z^{(0)}_{\text{sys}}/(R_Q/\pi)}\right)^{2m+n}}{m!\,(m+n)!}\left(b^{(0)\dagger}b^{(0)}\right)^m}_{\mathrm{J}_n\left(2\sqrt{\frac{Z^{(0)}_{\text{sys}}}{R_Q/\pi}}\sqrt{b^{(0)\dagger}b^{(0)}}\right)\left(\frac{-i}{\sqrt{b^{(0)\dagger}b^{(0)}}}\right)^n}\left[b^{(0)\dagger,n}+\text{h.c.}\right]: \end{aligned} \tag{V.3}$$

Where :: is the normal ordering operator and J_n is the n^{th}-order Bessel function. Now, a mean-field approximation is done on the Bessel function so that only $b^{(0)\dagger,n}$ (or h.c.) remains, i.e. $e^{-i\phi^{(0)}/\bar{\phi}_0} \simeq \sum_n c_n\left[b^{(0)\dagger,n}+\text{h.c.}\right]$ with c_n complex scalars. Let's assume[2] $\left\langle :\left(b^{(0)\dagger}b^{(0)}\right)^n: \right\rangle \equiv \beta^{2n}$ consistently with the result for a coherent state $|\beta\rangle$.

Propagating to our original derivation, Q^* becomes $Q^*\eta(\beta)$ where:

- $Q^* \equiv \frac{\bar{\phi}_0 I_c}{2\hbar}\sqrt{\frac{Q^{(0)}}{\omega^{(0)}_{\text{sys}}}\frac{Q^{(1)}}{\omega^{(1)}_{\text{sys}}}\frac{Z^{(0)}_{\text{sys}}Z^{(1)}_{\text{sys}}}{(R_Q/\pi)^2}}\, e^{-\left(Z^{(0)}_{\text{sys}}+Z^{(1)}_{\text{sys}}\right)/2(R_Q/\pi)}$
- $\eta(\beta) \equiv \mathrm{J}_1\left(2\beta\sqrt{\frac{Z^{(0)}_{\text{sys}}}{R_Q/\pi}}\right)\frac{1}{\beta}\sqrt{\frac{R_Q/\pi}{Z^{(0)}_{\text{sys}}}}$

First, Q^* is renormalised by a factor depending on the mode impedances. However, in the limit $Z^{(0)}_{\text{sys}}, Z^{(1)}_{\text{sys}} \ll R_Q/\pi$ this factor is negligible as assumed before. Second, the efficiency $\eta(\beta)$ goes to unity when $\beta \ll \sqrt{1/2\cdot(R_Q/\pi)/Z^{(0)}_{\text{sys}}}$ (see figure V.11), moreover this condition is easier to fulfil when $Z^{(0)}_{\text{sys}} \ll R_Q/\pi$. This means the characteristic impedance of the mode has to be as low as possible to get the best dynamic range.

[2] $\beta \in \mathbb{R}_+$ without loss of generality.

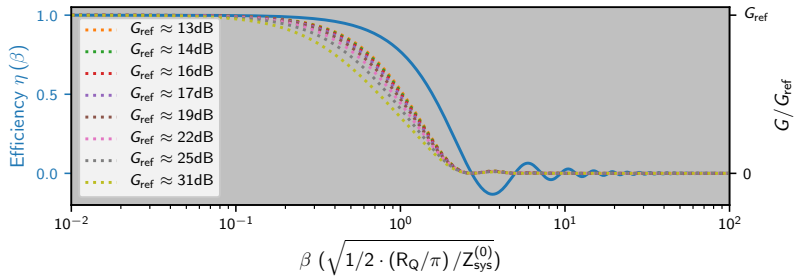

Figure V.11: **Gain compression.** ***Solid line on the left axis*** the efficiency η as a function of β. ***Dashed lines on the right axis*** are the effective gain, normalised to their value when efficiency is unity, as a function of β for different values of gain.

Finally to estimate β with the input power $\gamma^{\rm in}$, a self-consistent method is applied. We start with $\eta \equiv 1$, and coherent states $|\beta\rangle$ (for the field $b^{(0)}$) and $|\sqrt{\gamma^{\rm in}/\hbar\omega}\rangle$ (for the field $a_{\rm in}$) are assumed. IO relations give then:

$$\beta = \sqrt{\frac{\gamma^{\rm in}}{\hbar\omega}}\left|\frac{\chi^{(0)}_\omega(\omega)}{1-4Q^{*2}}\right| \tag{V.4}$$

Then the efficiency expressed as a function of $\gamma^{\rm in}$ becomes:

$$\eta\left(\gamma^{\rm in}\right) \equiv \mathrm{J}_1\left(2\sqrt{\frac{Z^{(0)}_{\rm sys}}{R_Q/\pi}\frac{\gamma^{\rm in}}{\hbar\omega}}\left|\frac{\chi^{(0)}_\omega(\omega)}{1-4Q^{*2}}\right|\right)\sqrt{\frac{R_Q/\pi}{Z^{(0)}_{\rm sys}}\frac{\hbar\omega}{\gamma^{\rm in}}}\left|\frac{1-4Q^{*2}}{\chi^{(0)}_\omega(\omega)}\right| \tag{V.5}$$

As previously, a nominal value of η is defined when on resonance:

$$\eta^*\left(\gamma^{\rm in}\right) \equiv \mathrm{J}_1\left(2\frac{2}{|1-4Q^{*2}|}\sqrt{\frac{Z^{(0)}_{\rm sys}}{R_Q/\pi}\frac{Q^{(0)}}{\omega^{(0)}}\frac{\gamma^{\rm in}}{\hbar\omega^{(0)}}}\right)\frac{|1-4Q^{*2}|}{2}\sqrt{\frac{R_Q/\pi}{Z^{(0)}_{\rm sys}}\frac{\omega^{(0)}}{Q^{(0)}}\frac{\hbar\omega^{(0)}}{\gamma^{\rm in}}} \tag{V.6}$$

Remarks about Q^* re-normalisation

Note here, that the mean-field approximation can be done because the input field is assumed to be coherent. Even through the general case is difficult to deal with, equation V.3 (together with RWA approximation) can also be used to derive transition coefficients, between number states:

$$\begin{aligned}\langle 0|\ e^{-i\phi^{(0)}/\bar{\phi}_0}\,|1\rangle &\simeq -i\ e^{-Z^{(0)}_{\rm sys}/2(R_Q/\pi)}\sqrt{\frac{Z^{(0)}_{\rm sys}}{R_Q/\pi}}\\ \langle 1|\ e^{-i\phi^{(0)}/\bar{\phi}_0}\,|2\rangle &\simeq -i\ e^{-Z^{(0)}_{\rm sys}/2(R_Q/\pi)}\sqrt{\frac{Z^{(0)}_{\rm sys}}{R_Q/\pi}}\left[1-\frac{Z^{(0)}_{\rm sys}}{2\cdot R_Q/\pi}\right]\end{aligned} \tag{V.7}$$

These coefficients imply that a mode with a characteristic impedance of $Z^{(0)}_{\rm sys} \simeq 2\cdot R_Q/\pi$ driven by ICPT[3] contains zero or one photon because $\langle 1|\ e^{-i\phi^{(0)}/\bar{\phi}_0}\,|2\rangle \simeq 0$. This mechanism is the second mechanism used to build a SPS with ICPT and has been implemented by C. Rolland [*Rolland16*; *Rolland18*].

Characteristic product

Finally, a relation similar to the gain-bandwidth product can be derived for the compression point. First, the equation defining the compression point, $10\log G^*\left(\eta^*\left(\gamma^{\rm in}_{-1\,\rm dB}\right)\right) = 10\log G^* - 1\,\rm dB$ is analytically solved to obtain the relation between the nominal efficiency at the compression point $\eta^*\left(\gamma^{\rm in}_{-1\,\rm dB}\right)$ as a function of the gain – when $G^* \gg 1$:

$$\eta^*\left(\gamma^{\rm in}_{-1\,\rm dB}\right) \underbrace{\simeq}_{\text{Taylor } 1/\sqrt{G^*}} 1-\frac{10^{1\,\rm dB/20}-1}{\sqrt{G^*}} \tag{V.8}$$

[3] If the thermodynamic temperature is small enough such as the ground state is the vacuum.

Next, the expression of $\eta^*\left(\gamma^{\text{in}}\right)$ is developed to second order in γ^{in} and Q^* is substituted with the gain when $G^* \gg 1$:

$$\begin{aligned}\eta^*\left(\gamma^{\text{in}}\right) &\underbrace{\simeq}_{\text{Taylor } \gamma^{\text{in}}} 1- \frac{Z_{\text{sys}}^{(0)}}{R_Q/\pi}\frac{\gamma^{\text{in}}}{\hbar\omega^{(0)}}\frac{2Q^{(0)}}{\omega^{(0)}|1-4{Q^*}^2|^2} \\ &\underbrace{\simeq}_{G^* \gg 1} 1- G^*\frac{Z_{\text{sys}}^{(0)}}{R_Q/\pi}\frac{\gamma^{\text{in}}}{\hbar\omega^{(0)}}\frac{Q^{(0)}}{2\omega^{(0)}}\end{aligned} \tag{V.9}$$

Asymptotic solution of the compression point is then:

$$\gamma^{\text{in}}_{-1\,\text{dB}} \simeq \frac{1}{\sqrt{G^*}^3}\hbar\omega^{(0)}\frac{R_Q/\pi}{Z_{\text{sys}}^{(0)}}\frac{2\omega^{(0)}}{Q^{(0)}}\left(10^{1\,\text{dB}/20}-1\right) \tag{V.10}$$

Table V.2 summarises the two characteristic products derived here. The relation between gain and compression point has been measured with the first design. Figure V.10 shows the experimental result and a good agreement between measurement and theoretical curve.

Table V.2: ICTA characteristics

	Bandwidth	**Compression point**
Characteristic product	$\Gamma_{\text{GBW}} \equiv \frac{2}{Q^{(0)}/\omega^{(0)}+Q^{(1)}/\omega^{(1)}}$	$\gamma^{\text{in}}_{\text{GCP}} \equiv \hbar\omega^{(0)}\frac{R_Q/\pi}{Z_{\text{sys}}^{(0)}}\frac{2\omega^{(0)}}{Q^{(0)}}$
Constitutive equation	$\sqrt{G^*}\Gamma_{\text{BW}} = \Gamma_{\text{GBW}}$	$\sqrt{G^*}^3\gamma^{\text{in}}_{-1\,\text{dB}} = \gamma^{\text{in}}_{\text{GCP}}\left(10^{1\,\text{dB}/20}-1\right)$

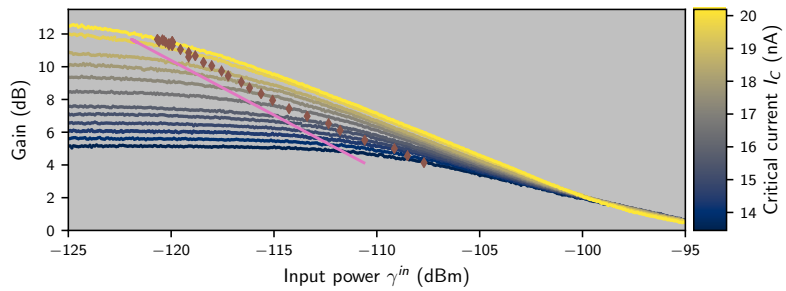

Figure V.12: **Gain-compression point relation.** The gain is shown as a function of the input power for different critical currents. Brown dots correspond to 1 dB compression points of each curve. Purple line of slope 2/3 is the theoretical curve, see table V.2.

Conclusion & outlooks

In conclusion our results experimentally show that ICPT can lead to quantum-limited amplification despite imperfections of the bias voltage. Limits of these noise, bandwidth and compression point have been derived and experimentally observed. Moreover, those limits can be engineered with an appropriate impedance seen by the junction; the amplification scheme can be optimised for:

Lower noise: It is quantum limited if the bias fluctuations are mastered, which can be done by lowering the bias fluctuation themself with a low-impedance environment at bias frequency and zero-frequency, or by increasing the effective bandwidth.

Higher bandwidth: By designing low quality factor resonators (see chapter III).

Dynamic range: It is limited by the quality factor and the characteristic impedance of the mode of the amplified frequency. Both have to be low and can be engineered (see chapter III).

The remaining limit is the critical current of the Josephson junction, low quality factors and characteristic impedances imply a high critical current to reach amplification regime.

A way to overcome issues observed above – conversion process and excessive noise – is to use an LC resonator instead of a cascaded quarter-wave resonator. Figure V.13 shows this design. Moreover, it allows reaching higher idler frequency allowing to stay closer to the quantum limit up to higher temperature (chapter I). Indeed, any resonance between signal and idler is susceptible to interfere with the amplification process. An LC resonator avoids these interferences, however an high frequency idler cannot be dissipated off chip (frequency is too high for coaxial cables) and an on-chip resistor has to be included.

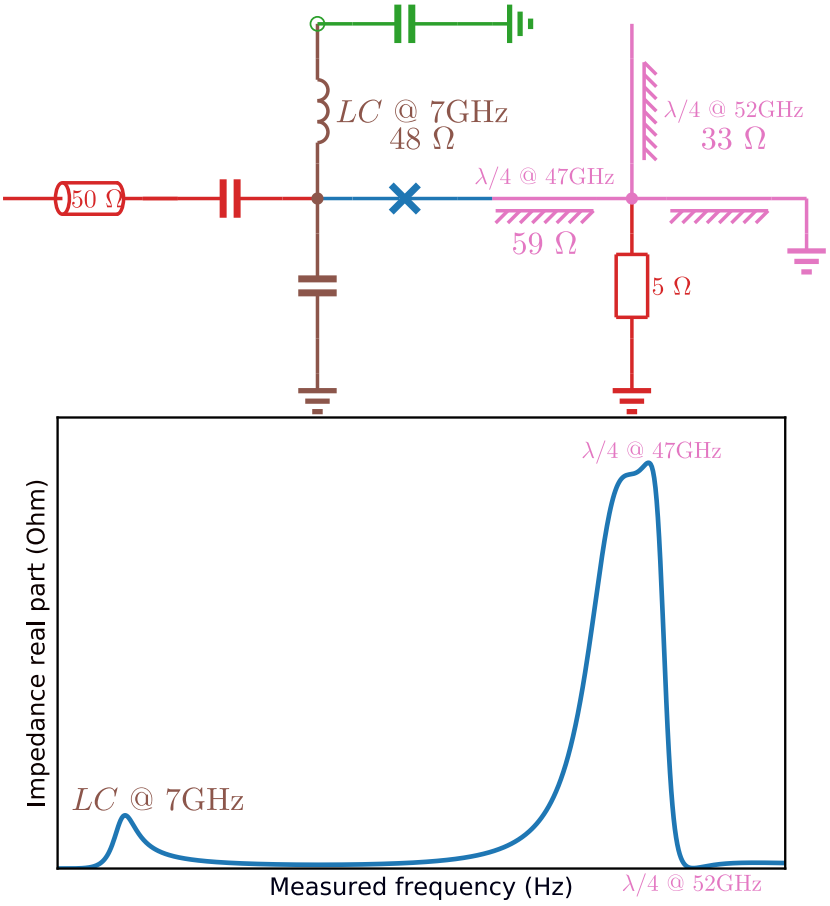

Figure V.13: **High frequency ICTA.** ***Upper panel*** shows the schematic of this design. Now low (brown) and high (pink) frequency modes are physically separated – DC bias also has its own port (green circle). The low frequency mode is made of a LC circuit coupled through a capacitance (defining the quality factor). The high frequency mode is a quarter-wave TL slightly flattened thanks to a quarter-wave TL at the bias frequency and a small piece of TL (acting as an inductance), this mode is dissipated on-chip by a 5 Ω resistor. ***Panel bottom*** shows the real part of the impedance seen by the junction, annotations show which components are responsible for the shape.

Finally, such an amplifier, powered by simple DC voltages could then make measuring microwave signals at the single photon level much easier and allow deploying many amplifiers on a chip. It could, therefore, be an important ingredient for qubit readout in large-scale quantum processors.

Conclusion & outlooks

In this manuscript, I sum up the work I did on Josephson photonics. First I presented two different theoretical approaches to explain this physics: *P-theory* and *Input-Output Theory*. Then I presented, theoretical and experimental, results about two different devices based on that physics:

Single Photon Source: A source of microwave photons that are highly non-classical, with $g^{(2)}(0) < 1$ with the goal to ultimately produce single photons with $g^{(2)}(0) \ll 1$;

Inelastic Cooper pair Tunnelling Amplifier: A microwave amplifier working close to the quantum limit.

Both devices are designed to be very simple to operate: They are powered by a DC voltage.

The two theoretical approaches of the first part have been used to derive characteristic quantities for both devices:

Single Photon Source is characterised by its *Power Spectral Density* which we numerically compute thanks to the *P-theory*. However, the statistics cannot be derived without more sophisticate theory, provided by J. Leppäkangas;

Inelastic Cooper pair Tunnelling Amplifier is characterised by its gain, bandwidth and compression point, derived via *Input-Output Theory*. Moreover, fundamental relations on one hand between gain and bandwidth ($\sqrt{G^*}\Gamma_{\mathrm{BW}}$ is constant), and on other hand between gain and compression point ($\sqrt{G^*}^3\gamma^{\mathrm{in}}_{-1\,\mathrm{dB}}$ is constant) are derived.

A sample implementing a *Single Photon Source* has been measured and fully characterised. *Power Spectral Density*, first $G^{(1)}$ and second $G^{(2)}$ order correlation functions have been measured and properly calibrated. The P-function has been used to propose a method to characterise such a sample. We demonstrate a non-classical source of photons with $g^{(2)}(0) \simeq 0.43$, operating at 6 GHz with a rate of 100 MHz in free-running or on-demand mode.

A sample implementing an *Inelastic Cooper pair Tunnelling Amplifier* has been measured. A gain of 10 dB over 200 MHz up to -115 dBm is observed. Moreover, both relations between gain and bandwidth ($\sqrt{G^*}\Gamma_{\mathrm{BW}}$ is constant) and between gain and compression point ($\sqrt{G^*}^3\gamma^{\mathrm{in}}_{-1\,\mathrm{dB}}$ is constant) are experimentally verified. However, this sample was not quantum-limited. A second sample mastering the bias fluctuations has then been measured and is effectively within 10 % of the quantum limit.

We, therefore, have demonstrated that both non-classical sources and near quantum-limited amplifiers can be designed from *Inelastic Cooper Pair Tunnelling* where the electromagnetic environment is designed at will. Moreover, these Josephson photonic devices are very easy to operate as they are powered by a simple DC bias.

In parallel to exploration of *Inelastic Cooper Pair Tunnelling* physics, I also developed an instrumentation framework that we used to measure our samples and which has been designed to be a versatile tool that can be applied to various kind of experiments: It monitors many instruments, performs loops and records data in a flexible way.

Perspectives

Limitations of the measured *Single Photon Source* sample have been identified: First the characteristic time of the RC circuit is not long enough compared to the resonator relaxation time. In addition, when operated on-demand, there is an unwanted coupling between the flux line and the DC line. Most importantly the charging energy of the RC circuit is too low, making it impossible to reach $k_B T \ll E_C$ necessary for single photon generation.

Limitations of the measured *Inelastic Cooper pair Tunnelling Amplifier* sample have also been observed: First an unwanted conversion process that reduces the effective gain. A second sample overcoming this issue has been measured and shows a noise very close to the quantum limit. Second, a high sensitivity to fluctuations of the bias. A future design overcoming this second issue is proposed and will be measured in the future.

In this thesis, we have already demonstrated that Josephson photonics be used to build a non-classical source of photons and a near quantum-limited amplifier. Next, optimised versions of these devices can be designed to, respectively, reach the single photon level and higher bandwidth and dynamic range while maintaining quantum limited noise for the amplifier. Moreover, other devices such as *Single Photon Detectors* [*Leppäkangas18*] can be build. To do so, the conversion process we saw when we measured the amplifier, can be used to convert a photon at one frequency to several photons at another frequency that are subsequently detected.

Josephson photonics therefore appears as a promising field to build photonic devices on a frequency range up to few 100 GHz and gives tools for further experiments on quantum information and quantum electrodynamics. These devices can improve correlation function measurements and help to manipulate and read qubits, a crucial element for the development of quantum information.

References

[*Abdo11*] Baleegh Abdo et al. "Josephson Amplifier for Qubit Readout". *Appl. Phys. Lett.* **99**, 162506 (2011),
Cited on page 97.

[*Altimiras14*] Carles Altimiras et al. "Dynamical Coulomb Blockade of Shot Noise". *Phys. Rev. Lett.* **112**, 236803 (2014),
Cited on page 3.

[*Armour15*] A. D. Armour, Björn Kubala, and Joachim Ankerhold. "Josephson Photonics with a Two-Mode Superconducting Circuit". *Phys. Rev. B* **91**, 184508 (2015),
Cited on page 3.

[*Armour13*] A. D. Armour et al. "Universal Quantum Fluctuations of a Cavity Mode Driven by a Josephson Junction". *Phys. Rev. Lett.* **111**, 247001 (2013),
Cited on page 3.

[*Aspect82*a] Alain Aspect, Jean Dalibard, and Gérard Roger. "Experimental Test of Bell's Inequalities Using Time-Varying Analyzers". *Phys. Rev. Lett.* **49**, 1804–1807 (1982),
Cited on page 1.

[*Aspect82*b] Alain Aspect, Philippe Grangier, and Gérard Roger. "Experimental Realization of Einstein-Podolsky-Rosen-Bohm Gedankenexperiment: A New Violation of Bell's Inequalities". *Phys. Rev. Lett.* **49**, 91–94 (1982),
Cited on page 1.

[*Astafiev10*] Oleg V. Astafiev et al. "Resonance Fluorescence of a Single Artificial Atom". *Science* **327**, 840–843 (2010), pmid: 20150495
Cited on page 2.

[*Averin90*] D. V. Averin, Yuli V. Nazarov, and A. A. Odintsov. "Incoherent Tunneling of the Cooper Pairs and Magnetic Flux Quanta in Ultrasmall Josephson Junctions". *Physica B: Condensed Matter*. LT-19 **165-166**, 945–946 (1990),
Cited on page 3.

[*Averin85*] D. V. Averin, A. B. Zorin, and K. K. Likharev. "Bloch Oscillations in Small Josephson Junctions". *Sov. Phys. JETP* **61**, 407–413 (1985),
Cited on page 3.

[*Basset10*] J. Basset, Hélène Bouchiat, and R. Deblock. "Emission and Absorption Quantum Noise Measurement with an On-Chip Resonant Circuit". *Phys. Rev. Lett.* **105**, 166801 (2010),
Cited on page 3.

[*Bennett14*] Charles H. Bennett and Gilles Brassard. "Quantum Cryptography: Public Key Distribution and Coin Tossing". *Theoretical Computer Science*. Theoretical Aspects of Quantum Cryptography – celebrating 30 years of BB84 **560**, 7–11 (2014),
Cited on page 2.

[*Bergeal10*a] Nicolas Bergeal et al. "Analog Information Processing at the Quantum Limit with a Josephson Ring Modulator". *Nature Physics* **6**, 296–302 (2010),
Cited on page 2.

[*Bergeal10*b] Nicolas Bergeal et al. "Phase-Preserving Amplification near the Quantum Limit with a Josephson Ring Modulator". *Nature* **465**, 64–68 (2010),
Cited on page 2.

[*Blais04*] Alexandre Blais et al. "Cavity Quantum Electrodynamics for Superconducting Electrical Circuits: An Architecture for Quantum Computation". *Phys. Rev. A* **69**, 062320 (2004),
Cited on page 1.

[*Blais07*] Alexandre Blais et al. "Quantum-Information Processing with Circuit Quantum Electrodynamics". *Phys. Rev. A* **75**, 032329 (2007),
Cited on page 1.

[*Bozyigit11*] Deniz Bozyigit et al. "Antibunching of Microwave-Frequency Photons Observed in Correlation Measurements Using Linear Detectors". *Nature Physics* **7**, 154–158 (2011),
Cited on page 1.

[*Caldeira83*] A. O Caldeira and A. J Leggett. "Quantum Tunnelling in a Dissipative System". *Annals of Physics* **149**, 374–456 (1983),
Cited on pages 7, 23, 38.

[*Cassidy17*] M. C. Cassidy et al. "Demonstration of an Ac Josephson Junction Laser". *Science* **355**, 939–942 (2017), pmid: 28254938
Cited on page 5.

[*CastellanosBeltran09*] M. A. Castellanos-Beltran et al. "Bandwidth and Dynamic Range of a Widely Tunable Josephson Parametric Amplifier". *IEEE Transactions on Applied Superconductivity* **19**, 944–947 (2009),
Cited on page 2.

[*Caves82*] Carlton M. Caves. "Quantum Limits on Noise in Linear Amplifiers". *Phys. Rev. D* **26**, 1817–1839 (1982),
Cited on pages 2, 7–8, 23, 35, 37, 91.

[*Cirac97*] J. I. Cirac et al. "Quantum State Transfer and Entanglement Distribution among Distant Nodes in a Quantum Network". *Physical Review Letters* **78**, 3221–3224 (1997), arXiv: quant-ph/9611017
Cited on page 2.

[*Clarke08*] John Clarke and Frank K. Wilhelm. "Superconducting Quantum Bits". *Nature* **453**, 1031–1042 (2008),
Cited on page 1.

[*Clerk10*] Aashish A. Clerk et al. "Introduction to Quantum Noise, Measurement, and Amplification". *Rev. Mod. Phys.* **82**, 1155–1208 (2010),
Cited on pages 7, 23, 35.

[*Dambach15*] Simon Dambach et al. "Time-Resolved Statistics of Nonclassical Light in Josephson Photonics". *Phys. Rev. B* **92**, 054508 (2015),
Cited on pages 2, 6.

[*daSilva10*] Marcus P. daSilva et al. "Schemes for the Observation of Photon Correlation Functions in Circuit QED with Linear Detectors". *Phys. Rev. A* **82**, 043804 (2010),
Cited on pages 6–7, 41, 44.

[*Delsing89*] Per Delsing et al. "Effect of High-Frequency Electrodynamic Environment on the Single-Electron Tunneling in Ultrasmall Junctions". *Phys. Rev. Lett.* **63**, 1180–1183 (1989),
Cited on page 3.

[*Devoret16*] Michel H. Devoret and Ananda Roy. "Introduction to Quantum-Limited Parametric Amplification of Quantum Signals with Josephson Circuits". *Comptes Rendus Physique* **17**, 740–755 (2016), arXiv: 1605.00539
Cited on page 35.

[*Devoret04*] Michel H. Devoret, Andreas Wallraff, and John M. Martinis. "Superconducting Qubits: A Short Review" (2004). arXiv: cond-mat/0411174
Cited on page 1.

[*Eichler11*] Christopher Eichler et al. "Experimental State Tomography of Itinerant Single Microwave Photons". *Phys. Rev. Lett.* **106**, 220503 (2011),
Cited on page 1.

[*Ekert91*] Artur K. Ekert. "Quantum Cryptography Based on Bell's Theorem". *Phys. Rev. Lett.* **67**, 661–663 (1991),
Cited on page 2.

[*Ford88*] G. W. Ford, J. T. Lewis, and R. F. O'Connell. "Quantum Langevin Equation". *Phys. Rev. A* **37**, 4419–4428 (1988),
Cited on page vi.

[*Frey17*] Moritz Frey and Hermann Grabert. "Current Noise in Tunnel Junctions". *Fortschr. Phys.* **65** (2017)
Cited on page 28.

[*Fulton87*] T. A. Fulton and G. J. Dolan. "Observation of Single-Electron Charging Effects in Small Tunnel Junctions". *Phys. Rev. Lett.* **59**, 109–112 (1987),
Cited on page 3.

[*Geerligs89*] L. J. Geerligs et al. "Influence of Dissipation on the Coulomb Blockade in Small Tunnel Junctions". *EPL* **10**, 79 (1989),
Cited on page 3.

[*Girvin90*] S. M. Girvin et al. "Quantum Fluctuations and the Single-Junction Coulomb Blockade". *Phys. Rev. Lett.* **64**, 3183–3186 (1990),
Cited on page 3.

[*Glauber63*] Roy J. Glauber. "The Quantum Theory of Optical Coherence". *Phys. Rev.* **130**, 2529–2539 (1963),
Cited on pages 5, 87.

[*Glauber06*] Roy J. Glauber. "Nobel Lecture: One Hundred Years of Light Quanta". *Rev. Mod. Phys.* **78**, 1267–1278 (2006),
Cited on pages 6, 88.

[*Gramich13*] Vera Gramich et al. "From Coulomb-Blockade to Nonlinear Quantum Dynamics in a Superconducting Circuit with a Resonator". *Phys. Rev. Lett.* **111**, 247002 (2013),
Cited on page 3.

[*Grimm15*] Alexander Grimm. *Josephson Photonics: Statistics of Photons Emitted by Inelastic Cooper Pair Tunneling*. PhD thesis. Grenoble University, 2015
Cited on pages 1, 5, 32, 62–63, 65, 71.

[*Grimm17*] Alexander Grimm et al. "A Self-Aligned Nano-Fabrication Process for Vertical NbN–MgO–NbN Josephson Junctions". *Supercond. Sci. Technol.* **30**, 105002 (2017),
Cited on page 62.

[*Grimm18*] Alexander Grimm et al. "A Bright On-Demand Source of Anti-Bunched Microwave Photons Based on Inelastic Cooper Pair Tunneling" (2018). arXiv: 1804.10596 `[cond-mat, physics:physics, physics:quant-ph]`
Cited on page 71.

[*Grünwald17*] Peter Grünwald. "What $g\hat{}(2)(0)<1/2$ Tells You - and What It Does Not" (2017). arXiv: 1711.05897 `[cond-mat, physics:quant-ph]`
Cited on page 84.

[*Heffner62*] H. Heffner. "The Fundamental Noise Limit of Linear Amplifiers". *Proceedings of the IRE* **50**, 1604–1608 (1962),
Cited on page 2.

[*Hofheinz11*] Max Hofheinz et al. "Bright Side of the Coulomb Blockade". *Phys. Rev. Lett.* **106**, 217005 (2011),
Cited on pages 3–5, 62, 72, 91.

[*Hoi13*] Io-Chun Hoi et al. "Microwave Quantum Optics with an Artificial Atom in One-Dimensional Open Space". *New J. Phys.* **15**, 025011 (2013),
Cited on page 2.

[*Holst94*] T. Holst et al. "Effect of a Transmission Line Resonator on a Small Capacitance Tunnel Junction". *Phys. Rev. Lett.* **73**, 3455–3458 (1994),
Cited on pages 3–4.

[*Houck07*] Andrew A. Houck et al. "Generating Single Microwave Photons in a Circuit". *Nature* **449**, 328–331 (2007),
Cited on pages 1–2.

[*Houle17*] Samuel Houle et al. "Photon-Assisted Dynamical Coulomb Blockade in a Tunnel Junction" (2017). arXiv: 1706.09337 [cond-mat]
Cited on page 3.

[*Hover12*] D. Hover et al. "Superconducting Low-Inductance Undulatory Galvanometer Microwave Amplifier". *Appl. Phys. Lett.* **100**, 063503 (2012),
Cited on page 2.

[*Ingold91*] Gert-Ludwig Ingold and Hermann Grabert. "Finite-Temperature Current-Voltage Characteristics of Ultrasmall Tunnel Junctions". *EPL* **14**, 371 (1991),
Cited on pages 3, 7, 23, 31.

[*Ingold92*] Gert-Ludwig Ingold and Yuli V. Nazarov. "Charge Tunneling Rates in Ultrasmall Junctions". In: *Single Charge Tunneling*. NATO ASI Series. Springer, Boston, MA, 1992, pp. 21–107
Cited on pages 3, 24, 28, 32.

[*Jebari17*] Salha Jebari. *The Inelastic Cooper Pair Tunneling Amplifier (ICTA)*. PhD thesis. Université Grenoble Alpes, 2017
Cited on pages 1–2, 35, 62–63, 91, 96.

[*Jebari18*] Salha Jebari et al. "Near-Quantum-Limited Amplification from Inelastic Cooper-Pair Tunnelling". *Nature Electronics* **1**, 223–227 (2018),
Cited on pages 62, 91.

[*Josephson62*] B. D. Josephson. "Possible New Effects in Superconductive Tunnelling". *Physics Letters* **1**, 251–253 (1962),
Cited on pages 25, 30.

[*Knill01*] E. Knill, R. Laflamme, and G. J. Milburn. "A Scheme for Efficient Quantum Computation with Linear Optics". *Nature* **409**, 46–52 (2001),
Cited on page 2.

[*König95*] Jürgen König, Herbert Schoeller, and Gerd Schön. "Resonant Tunneling and Coulomb Oscillations". *EPL* **31**, 31 (1995),
Cited on page 24.

[*Kubo66*] Ryogo Kubo. "The Fluctuation-Dissipation Theorem". *Rep. Prog. Phys.* **29**, 255 (1966),
Cited on pages 27–28, iii.

[*Lee82*] G. S. Lee. "Superconductor-insulator-superconductor Reflection Parametric Amplifier". *Appl. Phys. Lett.* **41**, 291–293 (1982),
Cited on page 2.

[*Leppäkangas14*a] Juha Leppäkangas et al. "Fully Superconducting Bloch-Oscillating Transistor: Amplification and Bifurcation Based on Bloch Oscillations and Counterflowing Cooper Pairs" (2014). arXiv: 1412.7431 [cond-mat]
Cited on pages 28–29, 33.

[*Leppäkangas14*b] Juha Leppäkangas et al. "Input–Output Description of Microwave Radiation in the Dynamical Coulomb Blockade". *New J. Phys.* **16**, 015015 (2014),
Cited on page 4.

[*Leppäkangas15*] Juha Leppäkangas et al. "Antibunched Photons from Inelastic Cooper-Pair Tunneling". *Phys. Rev. Lett.* **115**, 027004 (2015),
Cited on pages 2, 6.

[*Leppäkangas18*] Juha Leppäkangas et al. "Multiplying and Detecting Propagating Microwave Photons Using Inelastic Cooper-Pair Tunneling". *Phys. Rev. A* **97**, 013855 (2018),
Cited on pages 4, 104.

[*Likharev88*] K. K. Likharev. "Correlated Discrete Transfer of Single Electrons in Ultrasmall Tunnel Junctions". *IBM Journal of Research and Development* **32**, 144–158 (1988),
Cited on page 3.

[*Likharev85*] K. K. Likharev and A. B. Zorin. "Theory of the Bloch-Wave Oscillations in Small Josephson Junctions". *J Low Temp Phys* **59**, 347–382 (1985),
Cited on page 3.

[*Macklin15*] Chris Macklin et al. "A near–Quantum-Limited Josephson Traveling-Wave Parametric Amplifier". *Science* **350**, 307–310 (2015), pmid: 26338795
Cited on page 2.

[*Mollow67*a] B. R. Mollow and Roy J. Glauber. "Quantum Theory of Parametric Amplification. I". *Phys. Rev.* **160**, 1076–1096 (1967),
Cited on page 6.

[*Mollow67*b] B. R. Mollow and Roy J. Glauber. "Quantum Theory of Parametric Amplification. II". *Phys. Rev.* **160**, 1097–1108 (1967),
Cited on page 6.

[*Mora17*] Christophe Mora et al. "Quantum Properties of the Radiation Emitted by a Conductor in the Coulomb Blockade Regime". *Phys. Rev. B* **95**, 125311 (2017),
Cited on pages 4, 28–29.

[*Nazarov13*] Yuli V. Nazarov and Jeroen Danon. *Advanced Quantum Mechanics: A Practical Guide*. Cambridge University Press, 2013
Cited on pages 7, 23–24, 32.

[*Neugebauer62*] C. A. Neugebauer and M. B. Webb. "Electrical Conduction Mechanism in Ultrathin, Evaporated Metal Films". *Journal of Applied Physics* **33**, 74–82 (1962),
Cited on page 3.

[*Pashkin11*] Yuri A. Pashkin et al. "Charge Transport through Ultrasmall Single and Double Josephson Junctions Coupled to Resonant Modes of the Electromagnetic Environment". *Phys. Rev. B* **83**, 020502 (2011),
Cited on page 3.

[*Pechal14*] Marek Pechal et al. "Microwave-Controlled Generation of Shaped Single Photons in Circuit Quantum Electrodynamics". *Phys. Rev. X* **4**, 041010 (2014),
Cited on page 2.

[*Pothier91*] H. Pothier. *Coulomb Blockade and Transfer of Electrons One by One*. PhD thesis. Université Pierre et Marie Curie - Paris VI, 1991
Cited on page 3.

[*Ribeill11*] G. J. Ribeill et al. "Superconducting Low-Inductance Undulatory Galvanometer Microwave Amplifier: Theory". *Journal of Applied Physics* **110**, 103901 (2011),
Cited on page 2.

[*Rolland16*] Chloé Rolland. *Strong Coupling Quantum Electrodynamics of a Voltage Biased Josephson Junction*. thesis. Lille 1, 2016
Cited on pages 2, 99.

[*Rolland18*] Chloé Rolland et al. "Antibunched Photons Emitted by a Dc Biased Josephson Junction" (2018). arXiv: 1810.06217 [cond-mat, physics:quant-ph]
Cited on pages 2, 6, 99.

[*Roy18*] Ananda Roy and Michel H. Devoret. "Quantum-Limited Parametric Amplification with Josephson Circuits in the Regime of Pump Depletion" (2018). arXiv: 1801.10115 [cond-mat, physics:quant-ph]
Cited on pages 29, 33, 97, v–vi.

[*Sathyamoorthy16*] Sankar Raman Sathyamoorthy et al. "Simple, Robust, and on-Demand Generation of Single and Correlated Photons". *Phys. Rev. A* **93**, 063823 (2016),
Cited on page 2.

[*Shapiro63*] Sidney Shapiro. "Josephson Currents in Superconducting Tunneling: The Effect of Microwaves and Other Observations". *Phys. Rev. Lett.* **11**, 80–82 (1963),
Cited on page 27.

[*Souquet14*] J.-R. Souquet et al. "Photon-Assisted Tunnelling with Nonclassical Light". *Nature Communications* **5**, 5562 (2014),
Cited on pages 2, 6.

[*Tinkham04*] Michael Tinkham. *Introduction to Superconductivity*. 2. ed. Dover books on physics. Dover Publications, 2004
Cited on pages 25, 27, 30.

[*Vool17*] Uri Vool and Michel H. Devoret. "Introduction to Quantum Electromagnetic Circuits". *Int. J. Circ. Theor. Appl.* **45**, 897–934 (2017),
Cited on pages 29, ii.

[*Wallraff04*] Andreas Wallraff et al. "Strong Coupling of a Single Photon to a Superconducting Qubit Using Circuit Quantum Electrodynamics". *Nature* **431**, 162–167 (2004),
Cited on page 1.

[*Walls08*] D. F. Walls and G. J. Milburn. *Quantum Optics*. 2nd ed. Springer, 2008
Cited on page 33.

[*Weiss12*] Ulrich Weiss. *Quantum Dissipative Systems*. 4th ed. World Scientific, 2012
Cited on page 24.

[*Yin13*] Yi Yin et al. "Catch and Release of Microwave Photon States". *Phys. Rev. Lett.* **110**, 107001 (2013),
Cited on page 1.

[*Zeller69*] H. R. Zeller and I. Giaever. "Tunneling, Zero-Bias Anomalies, and Small Superconductors". *Phys. Rev.* **181**, 789–799 (1969),
Cited on page 3.

Appendices

Appendix A

Fluctuation-dissipation theorem

Contents

Let's consider a LC circuit, i.e. capacitor C and inductance L, in parallel, damped by an arbitrary admittance $Y_{\omega,\mathrm{damp}}(\omega)$. We consider two descriptions:

- A classical picture that results in equations of motion with an usual phenomenological damping model;
- A quantum picture in which the damping is pictured by an explicit bath Hamiltonian.

i Langevin equation

i.a Classical picture

First, current-voltage relations for each branch are written:

- $i_C \equiv C\,\partial_t u_C$
- $u_L \equiv L\,\partial_t i_L$
- $i_{\mathrm{damp}} \equiv Y_{t,\mathrm{damp}} * u_{\mathrm{damp}}$

Together with Kirchhoff's laws:

- $u_C = u_L = u_{\mathrm{damp}} = u$
- $i_C + i_L + i_{\mathrm{damp}} = i_t$

A classical Langevin equation emerges:

$$\partial_t^2 u + \omega_0\, Z_0\, Y_{t,\mathrm{damp}} * \partial_t u + \omega_0^2 u = \frac{1}{1/\omega_0 Z_0}\,\partial_t i_t \tag{A.1}$$

With $\omega_0 \equiv \sqrt{\frac{1}{CL}}$, $Z_0 \equiv \sqrt{\frac{L}{C}}$.

In the case of a purely resistive admittance, i.e. $Y_{t,\text{damp}} \equiv \frac{\delta}{R_\text{damp}}$, it corresponds to the classical equation of motion of a damped harmonic oscillator:

$$\partial_t^2 u + \frac{\omega_0}{Q}\partial_t u + \omega_0^2 u \;=\; \frac{1}{1/\omega_0 Z_0}\;\partial_t i_t \tag{A.2}$$

With a quality factor corresponding to $Q = \frac{R_\text{damp}}{Z_0}$. It discriminates the three different regimes of a damped harmonic oscillator – over-damped ($Q > 1/2$), critically damped ($Q = 1/2$) & under-damped ($Q < 1/2$).

The flux $\phi \equiv \int_{-\infty}^{t} u$ is more meaningful than u for our systems because the Josephson junction Hamiltonian is $\propto e^{i\frac{\phi}{\bar{\varphi}_0}} + \text{h.c.}$ [*Vool17*]. After integration, equation A.1 becomes:

$$\partial_t^2 \phi + \omega_0\; Z_0\, Y_{t,\text{damp}} * \partial_t \phi + \omega_0^2 \phi \;=\; \frac{1}{1/\omega_0 Z_0}\; i_t \tag{A.3}$$

An effective mass, m^*, is defined to fulfil the homogeneity equation $\left[\frac{1}{2} m^* \left[\partial_t \phi\right]^2\right] = \text{J} = \text{A V s}$, i.e. $[m^*] = \text{A s V}^{-1} = \text{s}\,\Omega^{-1}$, and so $m^* \equiv \frac{1}{\omega_0 Z_0}$ fulfil that equation. Finally, a full analogy with a classical mechanical harmonic oscillator can be pictured – table A.1.

Table A.1: Mechanical and LC circuit analogy

Mechanical picture	**LC circuit picture**
Mass m	Effective mass $m^* \equiv \frac{1}{\omega_0 Z_0}$
Position x	Flux ϕ
Spring constant k	$m^*\omega_0^2$
Restoring force $-kx$	$-m^*\omega_0^2\phi$
Impedance $Z_{t,\text{mecha}}$	Admittance $Y_{t,\text{damp}}$
Frictional force $Z_{t,\text{mecha}} * \partial_t x$	Ohm's law $Y_{t,\text{damp}} * \partial_t \phi$
Driving force	Driving current i_t
Kinetic energy $\frac{1}{2} m \left[\partial_t x\right]^2$	Capacitance energy $\frac{1}{2} m^* \left[\partial_t \phi\right]^2 = \frac{1}{2} C u^2$
Potential energy $\frac{1}{2} k x^2$	Inductance energy $\frac{1}{2} m^* \omega_0^2 \phi^2 = \frac{1}{2} L i_L^2$

Finally, the restoring force is extended with an arbitrary potential, $\mathcal{V}_\phi(\phi)$, and so:

$$\partial_t^2 \phi + \omega_0\; Z_0\, Y_{t,\text{damp}} * \partial_t \phi + \omega_0^2 \phi + \frac{1}{m^*}\left[\partial_\phi \mathcal{V}_\phi\right](\phi) \;=\; \frac{1}{m^*}\; i_t \tag{A.4}$$

Let's assume $\mathcal{F}_\omega\left[\left[\partial_\phi \mathcal{V}_\phi\right](\phi)\right] \equiv \frac{1}{L_\omega}\phi$. And from equations A.1 and A.4, u-response function $\chi_{\omega,ui_t} = Z_\omega$ and ϕ-response function $\chi_{\omega,\phi i_t}$ are derived:

$$\begin{aligned} \tfrac{1}{Z_\omega(\omega)} \;&\equiv\; \tfrac{i_{\omega,\text{drive}}}{u} \;&=\; Y_{\omega,\text{damp}}(\omega) + i m^* \omega \left[\tfrac{\omega_0^2 + 1/m^* L_\omega(\omega)}{\omega^2} - 1\right] \\ \chi_{\omega,\phi i_t}(\omega) \;&\equiv\; \tfrac{\phi}{i_{\omega,\text{drive}}} \;&=\; i\tfrac{Z_\omega(\omega)}{\omega} \end{aligned} \tag{A.5}$$

i.b Quantum picture

Previous notations are kept but now observable quantities are operators instead of vectors. Thanks to the analogy picture in table A.1, the Hamiltonian – excluding the dissipative aspect – is:

$$\mathcal{H}_{LC} \;\equiv\; \frac{1}{2} m^* \left[\partial_t \phi\right]^2 + \frac{1}{2} m^* \omega_0^2 \phi^2 \tag{A.6}$$

Applying Heisenberg equation of motion, we obtain the usual Hamiltonian of a harmonic oscillator with[1] $\partial_t \phi = \frac{q}{m^*}$:

$$\mathcal{H}_{LC} = \frac{1}{2m^*} q^2 + \frac{1}{2} m^* \omega_0^2 \phi^2 = \hbar\omega_0 \left(a^\dagger a + \frac{1}{2} \right) \tag{A.7}$$

With $a/a^\dagger \equiv \sqrt{\frac{m^*\omega_0}{2\hbar}} \left(\phi \pm i \frac{q}{m^*\omega_0} \right) = \sqrt{\frac{1}{2\hbar Z_0}} \left(\phi \pm i Z_0 q \right)$ as $\left[a, a^\dagger \right] = 1$, conversely $\phi = \phi_{\text{zpf}} \left(a^\dagger + \mathfrak{h.c.} \right)$ and $q = q_{\text{zpf}} \left(i a^\dagger + \mathfrak{h.c.} \right)$ with $\phi_{\text{zpf}} \equiv \sqrt{\frac{\hbar Z_0}{2}}$ & $q_{\text{zpf}} \equiv \sqrt{\frac{\hbar}{2Z_0}}$.

Now, the arbitrary potential is added back to the Hamiltonian[2]:

$$\mathcal{H}_{LC} \equiv \hbar\omega_0 a^\dagger a + \mathcal{V}_\phi \left(\phi \right) \tag{A.8}$$

The equation of motion is then:

$$\begin{aligned} \partial_t^2 \phi &= \tfrac{1}{m^*} \partial_t q &&= \tfrac{1}{i\hbar m^*} \left[q, \mathcal{H}_{LC} \right] \\ &&&= \tfrac{1}{m^*} \left(\tfrac{1}{i\hbar} \left[q, \hbar\omega_0 a^\dagger a \right] + \tfrac{1}{i\hbar} \left[q, \mathcal{V}_\phi \left(\phi \right) \right] \right) \\ \partial_t^2 \phi &&&= -\omega_0^2 \phi - \tfrac{1}{m^*} \left[\partial_\phi \mathcal{V}_\phi \right] \left(\phi \right) \end{aligned} \tag{A.9}$$

Which is consistent with equation A.4.

ii Fluctuation-dissipation relation

ii.a General case

Here we summarise [*Kubo66*]. First, a driving term $-\frac{1}{2} \{ i_t, \phi \}$, with i_t independent of the system, is added back in, so the full Hamiltonian of the driven system is:

$$\mathcal{H}_{\text{tot}} \equiv \mathcal{H}_{\text{env}} \underbrace{-\frac{1}{2} \{ i_t, \phi \}}_{\text{driving}} \tag{A.10}$$

Kubo studied the influence of the driving Hamiltonian on a system operator A, in the limit of small perturbations.

He shows that the A-response function, defined as the response when $i_t = \delta$, is $\chi_{t,Ai_t} \left(t \right) = \frac{1}{i\hbar} \Theta \left(t \right) \langle [\phi \left(0 \right), A \left(t \right)] \rangle$. Moreover, at thermal equilibrium – thermodynamic temperature β – in frequency domain, the response can be written as follows:

$$\begin{aligned} \chi_{\omega,Ai_t} \left(\omega \right) &= \mathcal{F}_\omega \left[\chi_{t,Ai_t} \right] \left(\omega \right) \\ &= \tfrac{1}{i\hbar} \int\limits_{\mathbb{R}_+} \langle [\phi \left(0 \right), A \left(t \right)] \rangle_\beta \; e^{i\omega t} \, \mathrm{d}t \\ &= \tfrac{1}{i\hbar \, \mathrm{Tr}\left(e^{-\beta \mathcal{H}_{\text{tot}}} \right)} \sum_{n,m} \int\limits_{\mathbb{R}_+} \langle n | \, \phi \left(0 \right) | m \rangle \langle m | \, A \left(0 \right) | n \rangle \; e^{i(\omega_m - \omega_n)t} \left[\, e^{-\beta\hbar\omega_n} - \, e^{-\beta\hbar\omega_m} \right] \, e^{i\omega t} \, \mathrm{d}t \\ &= \tfrac{i}{\hbar \, \mathrm{Tr}\left(e^{-\beta \mathcal{H}_{\text{tot}}} \right)} \sum_{n,m} \int\limits_{\mathbb{R}_+} \langle n | \, \phi \left(0 \right) | m \rangle \langle m | \, A \left(0 \right) | n \rangle \; e^{i(\omega_m - \omega_n)t} \left[\, e^{-\beta\hbar\omega_n} + \, e^{-\beta\hbar\omega_m} \right] \tfrac{1}{\coth(\beta\hbar\omega/2)} \; e^{i\omega t} \, \mathrm{d}t \\ \chi_{\omega,Ai_t} \left(\omega \right) &= \tfrac{2i}{\hbar \coth(\beta\hbar\omega/2)} \int\limits_{\mathbb{R}_+} \tfrac{1}{2} \langle \{ \phi \left(0 \right), A \left(t \right) \} \rangle_\beta \; e^{i\omega t} \, \mathrm{d}t \end{aligned} \tag{A.11}$$

This equation is the so-called *fluctuation-dissipation theorem*. It links the A-response function and the $A^\dagger$-(symmetrised) correlation function – i.e. $\frac{1}{2} \langle \{ \phi \left(0 \right), A \left(t \right) \} \rangle_\beta$:

[1] $[\phi, q] \equiv ih$

[2] The relations $\left[\phi, \hbar\omega_0 a^\dagger a \right] = i\hbar q/m^*$ and $\left[q, \hbar\omega_0 a^\dagger a \right] = -i\hbar m^* \omega_0^2 \phi$ still hold.

ii.b Flux-flux case

First, a straightforward derivation shows that a symmetrised auto-correlation function, e.g. when $A \equiv \phi$, for a stationary ergodic process is even, i.e. $\frac{1}{2}\left\langle\{\phi(0),\phi(t)\}\right\rangle_\beta = \frac{1}{2}\left\langle\{\phi(0),\phi(-t)\}\right\rangle_\beta$. Combined with equations A.5 and A.11 this result in:

$$\begin{aligned}
\frac{\mathrm{Re}[Z_\omega(\omega)]}{\omega} &= \mathrm{Im}\left(\chi_{\omega,\phi i_t}(\omega)\right) \\
&= \frac{1}{\hbar\coth(\beta\hbar\omega/2)}\left\{\int_{\mathbb{R}_+}\frac{1}{2}\left\langle\{\phi(0),\phi(t)\}\right\rangle_\beta\ e^{i\omega t}\,\mathrm{d}t + \int_{\mathbb{R}_+}\frac{1}{2}\left\langle\{\phi(0),\phi(t)\}\right\rangle_\beta\ e^{-i\omega t}\,\mathrm{d}t\right\} \qquad \text{(A.12)} \\
\frac{\mathrm{Re}[Z_\omega(\omega)]}{\omega} &= \frac{1}{\hbar\coth(\beta\hbar\omega/2)}\int_{\mathbb{R}}\frac{1}{2}\left\langle\{\phi(0),\phi(t)\}\right\rangle_\beta\ e^{i\omega t}\,\mathrm{d}t
\end{aligned}$$

Then, the inverse Fourier transform of equation A.12 is:

$$\mathcal{S}\left[\Gamma^\beta_{t,\phi\phi}\right](t) = \frac{1}{2\pi}\int_{\mathbb{R}}\underbrace{\frac{2\hbar\,\mathrm{Re}\left[Z_\omega(\omega)\right]}{\omega}\coth\left(\frac{\beta\hbar\omega}{2}\right)}_{\mathcal{S}[S_{\omega,\phi\phi}](\omega)\ \text{Symmetrised PSD}}e^{-i\omega t}\,\mathrm{d}\omega \qquad \text{(A.13)}$$

With $\left\langle\{\phi(0),\phi(t)\}\right\rangle_\beta = \mathcal{S}\left[\Gamma^\beta_{t,\phi\phi}\right]$. This equation is the form of the FDT applicable to a current driven circuit. For a voltage driven one, a similar relation involving charge and admittance can be derived.

Appendix B

Input output theory

Contents

The *input output relations* are derived in two steps:

- First, the quantisation of TLs shows how travelling field operators are defined from an infinite set of independent harmonic oscillators;
- Then, the input output relations themselves from a linearly coupled system & bath Hamiltonian.

Similar models of TL and coupling can be found [*Roy18*].

i Transmission line

The full continuous Hamiltonian of a TL is:

$$\mathcal{H}_{\mathrm{TL}} \equiv \frac{1}{2}\int_{\mathbb{R}_+} m^* \omega_0^2 \left[\partial_z \phi\right]^2 + m^* \left[\partial_t \phi\right]^2 \tag{B.1}$$

Where m^*, ω_0 & Z_0 are defined accordingly to table A.1.

After quantisation similar to appendix A, the Hamiltonian becomes:

$$\mathcal{H}_{\mathrm{TL}} = \frac{1}{2\pi}\int_{\mathbb{R}_+} \hbar v_\phi k_z \left[\left\{a^\dagger\left(k_z\right), a\left(k_z\right)\right\} + \left\{a^\dagger\left(-k_z\right), a\left(-k_z\right)\right\}\right] \mathrm{d}k_z \tag{B.2}$$

Where $a^\dagger\left(k_z\right)$ is the creation operator resulting from quantisation expressed in spacial frequency domain. v_ϕ is the phase velocity.

The equation of motion is then:

$$\begin{aligned} i\hbar\partial_t a\left(k_z\right) &\equiv \left[a\left(k_z\right), \mathcal{H}_{\mathrm{TL}}\right] \\ &= \tfrac{1}{2\pi}\int_{\mathbb{R}} \hbar v_\phi \left|k_z'\right| \left[a\left(k_z\right), \left\{a^\dagger\left(k_z'\right), a\left(k_z'\right)\right\}\right] \mathrm{d}k_z' \\ &= \int_{\mathbb{R}} \hbar v_\phi \left|k_z'\right| a\left(k_z'\right) \delta\left(k_z - k_z'\right) \mathrm{d}k_z' \\ i\hbar\partial_t a\left(k_z\right) &= \hbar v_\phi \left|k_z\right| a\left(k_z\right) \end{aligned} \tag{B.3}$$

Interpretation of equations B.2 and B.3 is straightforward: A semi-infinite TL is described by a continuous bath of non interacting modes – equation B.2; where a field can travel – equation B.3.

ii Input output model

ii.a Coupling model & Equation of motion

Now, the TL from equation B.1 can be inductively coupled to a flux $\phi_{\rm sys}$:

$$\mathcal{H}_{\rm tot} \equiv \mathcal{H}_{\rm env} + \underbrace{\frac{1}{2}\int\limits_{\mathbb{R}_+} m^*\omega_0^2\left[\partial_z\phi\right]^2 + m^*\left[\partial_t\phi\right]^2}_{\mathcal{H}_{\rm TL}} + \int\limits_{\mathbb{R}_+}\left\{\phi_{\rm sys}, \kappa_z\partial_z\phi\right\} \tag{B.4}$$

The same quantisation as before can be applied[1] , resulting in:

$$\begin{aligned}\mathcal{H}_{\rm tot} \equiv \mathcal{H}_{\rm env} &+\tfrac{1}{2\pi}\int\limits_{\mathbb{R}} v_\phi\left|k_z\right|\left[\tfrac{\left|k_z\right|}{Z_0}\phi\left(k_z\right)\phi\left(-k_z\right) + \tfrac{Z_0}{\left|k_z\right|}q\left(k_z\right)q\left(-k_z\right)\right]\mathrm{d}k_z \\ &+\tfrac{1}{2\pi}\int\limits_{\mathbb{R}}\left\{\phi_{\rm sys}, -ik_z\kappa_\omega\left(-k_z\right)\phi\left(k_z\right)\right\}\mathrm{d}k_z\end{aligned} \tag{B.5}$$

Note here that following [*Ford88*], this coupling is a linear-coupling/Ullersma model, that is equivalent to the independent-oscillator model after renormalisation. Moreover, it implies the system is subject to the *Quantum Langevin Equation* (QLE).

After substitutions $k_z \mapsto \omega/v_\phi$ and $\kappa_\omega\left(\omega/v_\phi\right)/v_\phi \mapsto \kappa_\omega\left(\omega\right)$, the resulting equation of motion[2] is consistent with equation A.4 and gives the following relation:

$$Z_0\left|\kappa_\omega\right|^2 = \mathrm{Re}\left[Y_{\omega,\rm damp}\right] \tag{B.6}$$

To go further, let's consider a system consisting of an anharmonic oscillator described by equation A.8, so two more equations of motion can be derived[3]:

$$\begin{aligned} i\hbar\partial_t b &= \overbrace{\hbar\omega_{\rm sys}b + \sqrt{\frac{1}{2\hbar Z_{\rm sys}}}\left[\partial_\phi\mathcal{V}_\phi\right]\left(\sqrt{\frac{\hbar Z_{\rm sys}}{2}}\left(b^\dagger + \mathfrak{h}.\mathfrak{c}.\right)\right)}^{\left[b,\mathcal{H}_{\rm env}\right]} \\ &\quad +\hbar\sqrt{Z_0Z_{\rm sys}}\ \tfrac{1}{2\pi}\int\limits_{\mathbb{R}}\mathrm{d}k_z\ i\,\mathrm{sgn}\left(k_z\right)\sqrt{\left|k_z\right|}\kappa_\omega\left(k_z\right)a^\dagger\left(k_z\right) + \mathfrak{h}.\mathfrak{c}. \\ i\hbar\partial_t a\left(k_z\right) &= \hbar v_\phi\left|k_z\right|a\left(k_z\right) + i\hbar\tfrac{\sqrt{Z_0Z_{\rm sys}}}{2}\,\mathrm{sgn}\left(k_z\right)\sqrt{\left|k_z\right|}\kappa_\omega\left(k_z\right)\left(b^\dagger + \mathfrak{h}.\mathfrak{c}.\right)\end{aligned} \tag{B.7}$$

ii.b RWA & Markov approximations

First, if the potential and source terms are thrown away, natural frequencies of b and $a\left(k_z\right)$ are respectively $\omega_{\rm sys} > 0$ and $v_\phi\left|k_z\right| > 0$. We then make a weak RWA approximation, i.e. we neglect counter-rotation terms proportional to $b^\dagger$ and $a^\dagger\left(k_z\right)$. Equations of motion are then:

$$\begin{aligned} i\hbar\partial_t b &= \left[b,\mathcal{H}_{\rm env}\right] - i\hbar\sqrt{Z_0Z_{\rm sys}}\ \tfrac{1}{2\pi}\int\limits_{\mathbb{R}}\mathrm{sgn}\left(k_z\right)\sqrt{\left|k_z\right|}\kappa_\omega\left(k_z\right)^*a\left(k_z\right)\mathrm{d}k_z \\ i\hbar\partial_t a\left(k_z\right) &= \hbar v_\phi\left|k_z\right|a\left(k_z\right) + i\hbar\tfrac{\sqrt{Z_0Z_{\rm sys}}}{2}\,\mathrm{sgn}\left(k_z\right)\sqrt{\left|k_z\right|}\kappa_\omega\left(k_z\right)b\end{aligned} \tag{B.8}$$

[1] The same CCR $\left[\phi\left(k_z\right), q\left(k_z'\right)\right] \simeq i\hbar\pi\delta\left(k_z + k_z'\right)$ and $\partial_t\phi q/m^*$ still holds, because the coupling does not involve $\partial_t\phi$.
[2] Algebra is tedious and can be found [*Ford88*; *Roy18*].
[3] Annihilation operator of the LC system is noted b to avoid confusion.

The free[4] and source terms of the solution of the second equation can be inserted in the first one:

$$
\begin{aligned}
& \tfrac{1}{2\pi}\int_{\mathbb{R}} \operatorname{sgn}(k_z)\sqrt{|k_z|}\kappa_\omega(k_z)^* a(k_z)\,\mathrm{d}k_z \\
\underset{\text{only free term}}{=} \quad & \tfrac{1}{2\pi}\int_{\mathbb{R}} \operatorname{sgn}(k_z)\sqrt{|k_z|}\kappa_\omega(k_z)^* \left[\mp a_{\text{ret/adv}}(\mp k_z)\right] e^{-iv_\phi|k_z|(t-t_0)}\,\mathrm{d}k_z \\
\underset{k_z\,\mapsto\,\omega/v_\phi}{=} \quad & \{t \mapsto \kappa_t(\pm t)\} * \underbrace{\left\{ t \mapsto \frac{1}{2\pi}\int_{\mathbb{R}_+} \sqrt{\frac{\omega}{v_\phi}} a_{\text{ret/adv}}\left(\frac{\omega}{v_\phi}\right) e^{-i\omega t}\,\mathrm{d}\omega \right\}}_{a_{\text{out/in}}}
\end{aligned}
$$

$$
\begin{aligned}
\underset{\text{only source term}}{=} \quad & \pm\tfrac{\sqrt{Z_0 Z_{\text{sys}}}}{2}\,\tfrac{1}{2\pi}\int_{\mathbb{R}} |k_z|\,|\kappa_\omega(k_z)|^2\,\mathcal{F}_\omega\left[[\delta_t * \{\tau \mapsto \Theta(\mp\tau)\}]\,b\right](v_\phi|k_z|)\; e^{-iv_\phi|k_z|t}\,\mathrm{d}k_z \\
\underset{k_z\,\mapsto\,\omega/v_\phi}{=} \quad & \pm i\sqrt{Z_0 Z_{\text{sys}}}\,\tfrac{1}{2\pi}\int_{\mathbb{R}_+} \left|\tfrac{1}{v_\phi}\kappa_\omega\left(\tfrac{\omega}{v_\phi}\right)\right|^2 (-i\omega)\,\mathcal{F}_\omega\left[[\delta_t * \{\tau \mapsto \Theta(\mp\tau)\}]\,b\right](\omega)\; e^{-i\omega t}\,\mathrm{d}k_z \\
\underset{\text{RWA}}{=} \quad & \pm i\sqrt{Z_0 Z_{\text{sys}}}\,\left[\{t \mapsto \Theta(\pm t)\}\left\{t \mapsto \int_{\mathbb{R}} \kappa_t(\tau)\,\kappa_t(\tau - t)\,\mathrm{d}\tau\right\}\right] * \partial_t b
\end{aligned}
\tag{B.9}
$$

Combining all together, it results in *input output relations* under weak RWA approximation:

$$
\begin{aligned}
i\hbar\partial_t b &= [b, \mathcal{H}_{\text{env}}] - i\hbar\sqrt{Z_0 Z_{\text{sys}}}\int_{-\infty}^{t} \kappa_t(t-\tau)\,a_{\text{out}}(\tau)\,\mathrm{d}\tau + \hbar Z_0 Z_{\text{sys}}\int_{-\infty}^{t} [\kappa_t * \mathcal{T}[\kappa_t]](t-\tau)\,\partial_t b(\tau)\,\mathrm{d}\tau \\
i\hbar\partial_t b &= [b, \mathcal{H}_{\text{env}}] - i\hbar\sqrt{Z_0 Z_{\text{sys}}}\int_{t}^{\infty} \kappa_t(\tau-t)\,a_{\text{in}}(\tau)\,\mathrm{d}\tau - \hbar Z_0 Z_{\text{sys}}\int_{t}^{\infty} [\kappa_t * \mathcal{T}[\kappa_t]](t-\tau)\,\partial_t b(\tau)\,\mathrm{d}\tau
\end{aligned}
\tag{B.10}
$$

Before applying Markov approximation, let's interpret $a_{\text{out/in}}$ by inserting free terms in the expression of q:

$$
\begin{aligned}
q(z,t) &= \tfrac{1}{2\pi}\int_{\mathbb{R}} i q_{\text{zpf}}\sqrt{|k_z|}\left[a^\dagger(-k_z,t) - a(k_z,t)\right] e^{-ik_z z}\,\mathrm{d}k_z \\
&= q_{\text{zpf}}\;\tfrac{1}{2\pi}\int_{\mathbb{R}_+}\mathrm{d}k_z\; i\left\{ -\sqrt{k_z}\;\underbrace{a(k_z,t)}_{a_{\text{adv}}(k_z)\;e^{-iv_\phi k_z t}}\; e^{-ik_z z} - \sqrt{k_z}\;\underbrace{a(-k_z,t)}_{-a_{\text{ret}}(k_z)\;e^{-iv_\phi k_z t}}\; e^{ik_z z}\right\} + \mathfrak{h.c.} \\
&\underset{k_z\,\mapsto\,\omega/v_\phi}{=} \tfrac{q_{\text{zpf}}}{v_\phi}\;\tfrac{1}{2\pi}\int_{\mathbb{R}_+}\mathrm{d}k_z\; i\left\{ \underbrace{-\sqrt{\frac{\omega}{v_\phi}}a_{\text{adv}}\left(\frac{\omega}{v_\phi}\right) e^{-i\omega(t+z/v_\phi)}}_{\frac{1}{2\pi}\int_{\mathbb{R}_+}\mathrm{d}k_z\;\to\;a_{\text{in}}(t+z/v_\phi)} + \underbrace{\sqrt{\frac{\omega}{v_\phi}}a_{\text{ret}}\left(\frac{\omega}{v_\phi}\right) e^{-i\omega(t-z/v_\phi)}}_{\frac{1}{2\pi}\int_{\mathbb{R}_+}\mathrm{d}k_z\;\to\;a_{\text{out}}(t-z/v_\phi)}\right\} + \mathfrak{h.c.} \\
q(z,t) &= q_{\text{in}}\left(t + \tfrac{z}{v_\phi}\right) - q_{\text{out}}\left(t - \tfrac{z}{v_\phi}\right)
\end{aligned}
\tag{B.11}
$$

So $a_{\text{out/in}}$ are the annihilation operators associated to the outgoing and incoming charge fields.

We now make the first Markov approximation, i.e. we neglect memory effects by assuming a purely resistive admittance in equation B.6: $\kappa_t \equiv \frac{\delta}{\sqrt{Z_0 Z_{\text{sys}} Q}}$. Moreover, the RHS can be approximated at first order: $a_{\text{out/in}} \mapsto \sqrt{\omega_{\text{sys}}}a_{\text{out/in}}$ & $\partial_t b \mapsto -i\omega_{\text{sys}} b$, i.e. not only counter rotating terms are neglected but their frequency is approximated as ω_{sys} at first order. This is the strong RWA approximation. Finally,

[4] With, arbitrarily, $a(k_z,t) = \mp a_{\text{ret/adv}}(\mp k_z)\; e^{-iv_\phi|k_z|t}$.

the equations of motion become:

$$\begin{aligned} i\hbar\partial_t b &= [b, \mathcal{H}_{\text{env}}] - i\hbar\sqrt{\tfrac{\omega_{\text{sys}}}{Q}}\, a_{\text{out}} - i\hbar\tfrac{1}{2}\tfrac{\omega_{\text{sys}}}{Q}\, b \\ i\hbar\partial_t b &= [b, \mathcal{H}_{\text{env}}] - i\hbar\sqrt{\tfrac{\omega_{\text{sys}}}{Q}}\, a_{\text{in}} + i\hbar\tfrac{1}{2}\tfrac{\omega_{\text{sys}}}{Q}\, b \end{aligned} \tag{B.12}$$

Those equations are the so-called *input output relations* under RWA and Markov approximations.

Appendix C

Auxiliary calculations

Contents

i Wiener-Khinchine theorem

General relations

In view of study the energy and power of a quadratic from, let's focus on the quantity $f_0^\dagger(t+\tau) f_1(t)$:

$$\begin{aligned} & \mathcal{F}_\omega\left[\tau \mapsto \mathcal{F}_\omega\left[t \mapsto f_0^\dagger(t+\tau) f_1(t)\right](\omega_t)\right](\omega_\tau) \\ = & \left[\left\{\omega_t \mapsto \mathcal{F}_\omega\left[\tau \mapsto \tfrac{1}{2\pi} e^{-i\omega_t\tau}\right](\omega_\tau)\, \mathcal{F}_\omega[f_0]^\dagger(-\omega_t)\right\} * \mathcal{F}_\omega[f_1]\right](\omega_t) \\ = & \left[\left\{\omega_t \mapsto \delta(\omega_t-\omega_\tau)\, \mathcal{F}_\omega[f_0]^\dagger(-\omega_t)\right\} * \mathcal{F}_\omega[f_1]\right](\omega_t) \end{aligned} \tag{C.1}$$

We suppose a stationary ergodic process, so that the average value is t-independent, it follows – with the previous expression where $\omega_t = 0$:

$$\begin{aligned} S_{\omega,f_0f_1} &\equiv \mathcal{T}\left[\mathcal{F}_\omega\left[\Gamma_{t,f_0f_1}\right]\right] \\ &= \mathcal{T}\left[\left\langle \mathcal{F}_\omega\left[\tau \mapsto f_0^\dagger(t+\tau) f_1(t)\right]\right\rangle\right] \\ S_{\omega,f_0f_1} &= \mathcal{F}_\omega[f_0]^\dagger \mathcal{F}_\omega[f_1] \end{aligned} \tag{C.2}$$

Hermitian auto-correlation case

Now let's assume $f_0 = f_1 = f$ is hermitian, i.e. $f^\dagger \equiv f$. Straightforwardly:

$$\mathcal{F}_\omega\left[\mathcal{S}\left[\Gamma_{t,ff}\right]\right] = \mathcal{S}\left[S_{\omega,ff}\right] = \left\{\mathcal{F}_\omega[f]^\dagger, \mathcal{F}_\omega[f]\right\} \tag{C.3}$$

Moreover, be a thermal equilibrium at thermodynamic temperature β, positive and negative frequency spectrum are related:

$$\begin{aligned} S^{\beta}_{\omega,ff}(-\omega) &= \int_{\mathbb{R}} \langle f(t) f(0)\rangle_{\beta}\ e^{i\omega t}\,\mathrm{d}t \\ &= \frac{1}{\mathrm{Tr}\left(\ e^{-\beta\mathcal{H}_{\mathrm{tot}}}\right)} \sum_{n,m} \int_{\mathbb{R}} \langle n|f(0)|m\rangle \langle m|f(0)|n\rangle\ e^{i(\omega_n-\omega_m)t}\ e^{-\beta\hbar\omega_n}\ e^{i\omega t}\,\mathrm{d}t \\ &= \frac{1}{\mathrm{Tr}\left(\ e^{-\beta\mathcal{H}_{\mathrm{tot}}}\right)} \sum_{n,m} \int_{\mathbb{R}} \langle m|f(0)|n\rangle \langle n|f(0)|m\rangle\ e^{-i(\omega_m-\omega_n)t}\ e^{-\beta\hbar\omega_m}\ e^{\beta\hbar\omega}\ e^{i\omega t}\,\mathrm{d}t \\ S^{\beta}_{\omega,ff}(-\omega) &= e^{\beta\hbar\omega} S^{\beta}_{\omega,ff}(\omega) \end{aligned} \tag{C.4}$$

ii P(E) properties

Exponential & correlation function

Let f an hermitian operator, i.e. $f^{\dagger} = f$. The following equation holds – thanks to the Wick theorem:

$$\begin{aligned} \partial_{\alpha}\left\langle\ e^{\pm i\alpha f(t)}\ e^{\mp i\alpha f(0)}\right\rangle(\alpha) &= \pm i\left\langle f(t)\ e^{\pm i\alpha f(t)}\ e^{\mp i\alpha f(0)}\right\rangle \mp i\left\langle\ e^{\pm i\alpha f(t)} f(0)\ e^{\mp i\alpha f(0)}\right\rangle \\ &= 2\alpha \underbrace{\left\{\langle f(t) f(0)\rangle - \langle f(0) f(0)\rangle\right\}}_{J_{t,f}(t)\ \equiv\ \Gamma_{t,ff}(t)-\Gamma_{t,ff}(0)} \left\langle\ e^{\pm i\alpha f(t)}\ e^{\mp i\alpha f(0)}\right\rangle \end{aligned} \tag{C.5}$$

Consequently:

$$\left\langle\ e^{\pm if(t)}\ e^{\mp if(0)}\right\rangle = e^{J_{t,f}(t)} \tag{C.6}$$

A similar derivation gives $\left\langle\ e^{\pm if(t)}\ e^{\pm if(0)}\right\rangle = e^{-J_{t,f}(t)}$.

Temperature asymmetry

Now, let's define $P^{\beta}_{f}(\hbar\omega_J) \equiv \frac{1}{h}\mathcal{F}_{\omega}\left[\ e^{J^{\beta}_{t,f}}\right](\omega_J)$ where thermal equilibrium at thermodynamic temperature β is assumed.

$$\begin{aligned} P^{\beta}_{f}(-\hbar\omega_J) &= \frac{1}{h}\int_{\mathbb{R}} \left\langle\ e^{\pm if(-t)}\ e^{\mp if(0)}\right\rangle_{\beta}\ e^{i\omega_J t}\,\mathrm{d}t \\ &= \frac{1}{h\,\mathrm{Tr}\left(\ e^{-\beta\mathcal{H}_{\mathrm{tot}}}\right)} \sum_{n,m} \int_{\mathbb{R}} \langle n|\ e^{\pm if(0)}|m\rangle\langle m|\ e^{\mp if(0)}|n\rangle\ e^{-i(\omega_n-\omega_m)t}\ e^{-\beta\hbar\omega_n}\ e^{i\omega_J t}\,\mathrm{d}t \\ &= \frac{1}{h\,\mathrm{Tr}\left(\ e^{-\beta\mathcal{H}_{\mathrm{tot}}}\right)} \sum_{n,m} \int_{\mathbb{R}} \langle m|\ e^{\mp if(0)}|n\rangle\langle n|\ e^{\pm if(0)}|m\rangle\ e^{i(\omega_m-\omega_n)t}\ e^{-\beta\hbar\omega_m}\ e^{-\beta\hbar\omega_J}\ e^{i\omega_J t}\,\mathrm{d}t \\ P^{\beta}_{f}(-\hbar\omega_J) &= e^{-\beta\hbar\omega_J} P^{\beta}_{f}(\hbar\omega_J) \end{aligned} \tag{C.7}$$

Minnhagen equation

First of all, in time domain:

$$\partial_t\ e^{J^{\beta}_{t,f}} = e^{J^{\beta}_{t,f}} \underbrace{\partial_t J^{\beta}_{t,f}}_{\partial_t\Gamma^{\beta}_{t,ff}} \tag{C.8}$$

It follows in frequency domain, together with equation C.4:

$$\begin{aligned} \nu_J P^{\beta}_{f}(h\nu_J) &= \int_{\mathbb{R}} P^{\beta}_{f}(h\nu_J - h\nu)\ \nu S^{\beta}_{\nu,ff}(-\nu)\ \mathrm{d}\nu \\ &= \int_{\mathbb{R}} P^{\beta}_{f}(h\nu_J - h\nu)\ \frac{\nu}{1+\ e^{-\beta h\nu}}\,\mathcal{S}\left[S^{\beta}_{\nu,ff}\right](\nu)\ \mathrm{d}\nu \end{aligned} \tag{C.9}$$

In the flux-flux correlation case, see equation A.13, and with $f \equiv \phi/\bar{\phi}_0$, it gives:

$$\nu_J P^{\beta}_{\phi/\bar{\phi}_0}(h\nu_J) = \int_{\mathbb{R}} P^{\beta}_{\phi/\bar{\phi}_0}(h\nu_J - h\nu) \underbrace{\frac{\mathrm{Re}\left[Z_\nu(\nu)\right]}{2\pi\,\bar{\phi}_0^2/\hbar}}_{R_Q} / 2 \frac{1}{1 - e^{-\beta h\nu}} \mathrm{d}\nu \tag{C.10}$$

This form is the so-called *Minnhagen equation*, it shows that thanks to the *fluctuation dissipation theorem* the probability function $P^{\beta}_{\phi/\bar{\phi}_0}$ is determined by the dissipative part of the electromagnetic environment $\mathrm{Re}\left[Z_\nu(\nu)\right]$.

Appendix D

List of publications

Dibyendu Hazra, N. Tsavdaris, Salha Jebari, Alexander Grimm, Florian Blanchet, F. Mercier, E. Blanquet, C. Chapelier, and Max Hofheinz. "Superconducting Properties of Very High Quality NbN Thin Films Grown by High Temperature Chemical Vapor Deposition". *Supercond. Sci. Technol.* **29**, 105011 (2016),

Alexander Grimm, Salha Jebari, Dibyendu Hazra, Florian Blanchet, Frédéric Gustavo, Jean-Luc Thomassin, and Max Hofheinz. "A Self-Aligned Nano-Fabrication Process for Vertical NbN–MgO–NbN Josephson Junctions". *Supercond. Sci. Technol.* **30**, 105002 (2017),

Alexander Grimm, Florian Blanchet, Romain Albert, Juha Leppäkangas, Salha Jebari, Dibyendu Hazra, Frédéric Gustavo, Jean-Luc Thomassin, Eva Dupont-Ferrier, Fabien Portier, and Max Hofheinz. "A Bright On-Demand Source of Anti-Bunched Microwave Photons Based on Inelastic Cooper Pair Tunneling" (2018). arXiv: 1804.10596 `[cond-mat, physics:physics, physics:quant-ph]`.

Dibyendu Hazra, Salha Jebari, Romain Albert, Florian Blanchet, Alexander Grimm, C. Chapelier, and Max Hofheinz. "Microwave Response and Electrical Transport Studies of Disordered s Wave Superconductor: NbN Thin Films" (2018). arXiv: 1806.03935 `[cond-mat]`.

Dibyendu Hazra, N. Tsavdaris, A. Mukhtarova, M. Jacquemin, Florian Blanchet, Romain Albert, Salha Jebari, Alexander Grimm, A. Konar, E. Blanquet, F. Mercier, C. Chapelier, and Max Hofheinz. "Superconducting Properties of NbTiN Thin Films Deposited by High-Temperature Chemical Vapor Deposition". *Phys. Rev. B* **97**, 144518 (2018),

Salha Jebari, Florian Blanchet, Alexander Grimm, Dibyendu Hazra, Romain Albert, Philippe Joyez, Denis Vion, D. Estève, Fabien Portier, and Max Hofheinz. "Near-Quantum-Limited Amplification from Inelastic Cooper-Pair Tunnelling". *Nature Electronics* **1**, 223–227 (2018),

Juha Leppäkangas, Michael Marthaler, Dibyendu Hazra, Salha Jebari, Romain Albert, Florian Blanchet, Göran Johansson, and Max Hofheinz. "Multiplying and Detecting Propagating Microwave Photons Using Inelastic Cooper-Pair Tunneling". *Phys. Rev. A* **97**, 013855 (2018),

Resumé

La photonique Josephson est un domaine récent de la physique à la croisée entre l'électrodynamique quantique en circuit et le blocage de Coulomb dynamique. Elle explique et étudie la possibilité pour une paire de Cooper de traverser une jonction Josephson polarisée en tension par effet tunnel inélastique, en dissipant la différence de potentiel électrique aux bornes de la jonction sous forme de photons émis dans l'environnement électromagnétique de la jonction.

Cette thèse s'arrête sur deux aspects de la photonique Josephson:

- La possibilité de contrôler la statistique des photons émis dans l'environnement, pour **générer des photons non-classiques**;
- La possibilité de stimuler l'émission de photons, ce qui permet d'**amplifier avec un bruit ajouté à la limite quantique**.

Pour fonctionner, ces dispositifs ne demandent qu'une simple tension continue servant à polariser la jonction Josephson. A terme ces dispositifs pourraient simplifier certaines mesures quantiques en remplaçant avantageusement des dispositifs micro-ondes existants plus difficiles à utiliser.

Nous avons étudié nos dispositifs avec deux théories, la théorie $P(E)$ et celle liant les flux de photons entrant et sortant, pour en tirer les caractéristiques de fonctionnement de nos dispositifs : taux d'émission, gain, bruit, bande passante, point de compression. Les dispositifs expérimentaux mesurés sont réalisés en nitrure de niobium en créant un environnement électromagnétique répondant à nos besoins. La possibilité de contrôler les processus photoniques que l'on veut en réalisant l'environnement électromagnétique adapté laisse la porte ouverte à de futures dispositifs : diverses sources non-classiques, amplificateurs large bande, détecteurs de photons.

Abstract

The recent field of Josephson photonics is about the interplay between circuit quantum electrodynamic and dynamical Coulomb blockade. It explains and studies the ability of a Cooper pair to inelasticity tunnel through a DC-biased Josephson junction by dissipating the Cooper pair energy in the electromagnetic environment of the junction in the form of photons.

This thesis focuses on two aspects of the Josephson photonics:

- Control over the statistics of the emitted photons with focus on **generation of non-classical photons**;
- Stimulated emission of photons leading to **amplification with added noise at the quantum-limit**.

These devices are powered with a simple DC voltage used to bias the Josephson junction. These devices could simplify quantum measurements hardware by replacing existing devices with large overhead.

We have studied our devices with two theories, P-theory and *input output theory*, to derive the characteristics of our devices: Photon rate, gain, noise, bandwidth, compression point. The measured samples are made of niobium nitride and the electromagnetic environment of the junction is engineered to fulfil our needs. The possibility to select the photonic processes at will by engineering the electromagnetic environment permits to imagine further devices: Other types of sources, wideband amplifiers, photon detectors.